Optical Remote Sensing of Snow on Sea Ice: Ground Measurements, Satellite Data Analysis, and Radiative Transfer Modeling

A

THESIS

Presented to the Faculty of the
University of Alaska Fairbanks
in Partial Fulfillment of the Requirements
for the Degree of

DOCTOR OF PHILOSOPHY

By

Xiaobing Zhou, B.S., M.S.

Fairbanks, Alaska
August 2002

UMI Number: 3059726

UMI®

ProQuest Information and Learning Company
300 North Zeeb Road
P.O. Box 1346
Ann Arbor, MI 48106-1346

Optical Remote Sensing of Snow on Sea Ice: Ground Measurements, Satellite Data Analysis, and Radiative Transfer Modeling

by

Xiaobing Zhou

RECOMMENDED: Keith Echelmeyer (W.D.H.)

Dr. Keith Echelmeyer

Dr. Martin O. Jeffries

Sharpton

Dr. Buck Sharpton

Dr. Knut Stamnes

Shusun Li

Dr. Shusun Li, Chairman, Advisory Committee

Douglas H Christensen

Department Chair, Geology and Geophysics

APPROVED: D Woodall

Dr. David M. Woodall
Dean, College of Science, Engineering and Mathematics

JR Kan

Dr. Joseph R. Kan, Dean, Graduate School

8-13-02

Date

ABSTRACT

The successful launch of the Terra satellite on December 18, 1999 opened a new era of earth observation from space. This thesis is motivated by the need for validation and promotion of the use of snow and sea ice products derived from MODIS, one of the main sensors aboard the Terra and Aqua satellites. Three cruises were made in the Southern Ocean, in the Ross, Amundsen and Bellingshausen seas. Measurements of all-wave albedo, spectral albedo, BRDF, snow surface temperature, snow grain size, and snow stratification etc. were carried out on pack ice floes and landfast ice. *In situ* measurements were also carried out concurrently with MODIS. The effect of snow physical parameters on the radiative quantities such as all-wave albedo, spectral albedo and bidirectional reflectance are studied using statistical techniques and radiative transfer modeling, including single scattering and multiple scattering. The whole thesis consists of six major parts. The first part (chapter 1) is a review of the present research work on the optical remote sensing of snow. The second part (chapter 2) describes the instrumentation and data-collection of ground measurements of all-wave albedo, spectral albedo and bidirectional reflectance distribution function (BRDF) of snow and sea ice in the visible-near-infrared (VNIR) domain in Western Antarctica. The third part (chapter 3) contains a detailed multivariate correlation and regression analysis of the measured radiative quantities with snow physical parameters such as snow density, surface temperature, single and composite grain size and number density. The fourth part (chapter 4) describes the validation of MODIS satellite data acquired concurrently with the ground measurements. The radiances collected by the MODIS sensor are converted to ground snow surface reflectances by removing the atmospheric effect using a radiative transfer algorithm (6S). Ground measured reflectance is corrected for ice concentration at the subpixel level so that the *in situ* and space-borne measured reflectance data are comparable. The fifth part (chapter 5) investigates the single scattering properties (extinction optical depth, single albedo, and the phase function or asymmetry factor) of snow grains (single or composite), which were calculated using the geometrical optical method. A computer code, GOMsnow, is developed and is tested against benchmark results obtained from an exact Mie scattering code (MIE0) and a Monte Carlo code. The sixth part (chapter 6) describes radiative transfer modeling of spectral albedo using a multi-layer snow model with a multiple scattering algorithm (DISORT). The effect of snow stratification on the spectral albedo is explored. The vertical heterogeneity of the snow grain-size and snow mass density is investigated. It is found that optical remote sensing of snow physical parameters from satellite measurements should take the vertical variation of snow physical parameters into account. The albedo of near-infrared bands is more sensitive to the grain-size at the very top snow layer (<5cm), while the albedo of the visible bands is sensitive to the grain-size of a much thicker snow layer. Snow parameters (grain-size, for instance) retrieved with near-infrared channels only represent the very top snow layer (most probably 1- 3 cm). Multi-band measurements from visible to near-infrared have the potential to retrieve the vertical profile of snow parameters up to a snow depth limited by the maximum penetration depth of blue light.

Table of Contents

List of Figures

List of Tables

ACKNOWLEDGMENTS

I would like to thank my thesis advisor, Dr. Shusun Li, for his expert advice on all aspects of this thesis: from ground measurements to radiative transfer modeling to satellite data analyses. He also taught me what Synthetic Aperture Radar (SAR) is and how to obtain interferograms to measure deformation (SAR Interferometry). I am very grateful to him for guidance, encouragement and enthusiastic support.

I would also like to thank the other thesis advisory committee members: Drs. Keith Echelmeyer, Martin Jeffries, Buck Sharpton, and Knut Stamnes for their advice on my graduate study, constructive comments, suggestions and insights on my thesis. Dr. Echelmeyer taught me what snow and ice are (Ice Physics), Dr. Stamnes taught me how radiation transfers in dispersive media (Radiative Transfer) while Dr. Sharpton taught me how to use radiation to "see" snow and ice (Remote Sensing). Special thanks to Dr. Jeffries for his critical review of the thesis, very helpful comments and suggestions, and editorial efforts in improving the quality of the thesis.

Thanks to Ms Kim Morris for providing the snow physical data, to Dr. Nazmi Z. El Saleous for ordering all the MODIS granules and coordinating the processing of the L1B products to generate Level 2 products. Gratitude also goes to Dr. Joey C. Comiso for his encouragement in research on remote sensing of snow and ice.

I am also very grateful for the logistical support furnished by the National Science Foundation and the Antarctic Support Associates personnel aboard the *R/V Nathaniel B. Palmer* for the three Antarctic cruises (NBP98-3, NBP99-1, and NBP00-1).

Thank you to Dr. Teruo Aoki, Dr. Hajo Eicken, Dr. Gary A. Maykut, Dr. Stephen G. Warren for helpful comments and subsequent improvements of manuscripts which are also part of the thesis.

Last, but not least, I wish to express my deep appreciation to my wife, Yan Fang and my children, Daoning and Marlene, for their love, support, and patience as I used almost every free moment during the past four years to concentrate on the thesis.

CHAPTER 1

Introduction

1.1 Optical Remote Sensing – A Useful Tool for Monitoring Snow and Sea Ice

Snow and ice are major water resources and a main component in the earth/ocean-atmosphere system. They play an important role in both hydrology and climate change. Snow cover and snow water equivalent (SWE) are important for runoff assessment, water resource management, and flood control. For instance, 50-90% of the annual Arctic precipitation and runoff is from snowfall [McNamara et al., 1998; Winther and Hall, 1999]. Snow albedo is the ratio of the reflected to the incident solar energy. Snow is the most reflective natural surface, and thus has the highest visible albedo (0.95). Depending on the snow conditions, snow albedo is also the most variable (0.2-0.95). Thus snow plays an important role in the energy balance between the Earth and the atmosphere.

Among advanced data collection technologies, satellite remote sensing has emerged as a very powerful and promising tool for monitoring, assessment, and management of snow cover both regionally and globally. Efficient monitoring of snow cover, SWE, snow depth, and snow surface albedo on continental and hemispheric scale is possible only by using satellite data. Snow surveys made by traditional methods involve much time and labor and are thus very scarce in regions that are remote and inaccessible like alpine regions and polar continents and seas. On the other hand, remote sensing offers an easy, time cost effective and accurate means for inventorying, surveying and mapping snow cover. The high reflectivity of snow makes it easily "seen" from space. Remote sensing can provide very useful data to study hydrological, geophysical and biological processes related not only to large-scale phenomenon, such as large-scale snow coverage and thus the large-scale variability of snow albedo for climate study and SWE assessment, but also to small-scale (a given basin size) phenomenon, such as snowline retreat in the snowmelt season, using high resolution satellite data. The spatial continuity and temporal repeat characteristics afforded by polar-orbiting satellites make remote sensing a useful tool for monitoring growth and decay of snow and ice. For instance, snow coverage derived from satellite images is widely applied for short-term and seasonal snowmelt runoff models [Rango and Martinec, 1979; Dey et al., 1983] used for forecasting runoff from snow-fed rivers.

Optical (visible and near-infrared, VNIR) sensors have been enticing from the very beginning of remote sensing due to their high resolution capacity, although atmospheric elements such as clouds frequently inhibit their application. With respect to spatial resolution, no means (thermal infrared and microwave) except synthetic aperture radar (SAR) can compete with them. Optical sensors have proved to be very useful for snow and ice monitoring due to the strong spectral reflectance contrast between snow-covered and snow-free regions. They have been used for mapping of the areal extent of snow since the early 1960's. Since then, the spectral, spatial and radiometric resolution of optical sensors, have improved considerably, together with the advancement of the science aspects of remote sensing. Optical remote sensing techniques are now widely used in oceanography, hydrology, agriculture, climate studies, glaciology, atmospheric science and meteorology.

The successful launch of the NASA Terra satellite on December 18, 1999 and the Aqua satellite on May 4, 2002, ushered in a new era of earth observation from space. The optical instrument, MODerate resolution Imaging Spectroradiometer (MODIS) (36 channels within VNIR and thermal infrared region, resolution varying from 250 to 1000 meters) is on both the Terra and Aqua satellites. On March 1, 2002, the European Space Agency (ESA) satellite Envisat was launched, with one main optical instrument MEdium Resolution Imaging Spectrometer (MERIS) (15 channels, spatial resolution of 300 meters) to add to the satellite fleet monitoring the Earth's environment from space.

In this thesis, the focus is on the interaction of VNIR radiation with snow cover on sea ice in the Southern Ocean (the Ross, Amundsen and Bellingshausen seas), though remote sensing of snow is of great interest on a broad sense.

1.2 Snow Cover on Sea Ice

Sea ice in the Arctic is covered by snow most of the year, while in Antarctica, it is covered by snow all year around. Sea ice is a very important component of the polar climatological system. Growth and decay of the ice extent and mass volume including especially the ice ridges [Weeks et al., 1988; Zhou and Li, 2000b] is becoming a major yardstick in monitoring polar climate change. Snow on sea ice is important for a couple of reasons, in particular for the mass and energy balance of sea ice. During winter, snow, due to its lower thermal conductivity than sea ice, acts as an insulating blanket, decreasing heat loss from the ocean to the atmosphere and thus retarding freezing on the bottom [Eicken, et al., 1995]. In summer, due to its higher albedo than sea ice, snow acts as a mirror, reflecting solar energy back to the atmosphere, and thus retarding the melting or decay of sea ice [Maykut and Untersteiner, 1971; Maykut, 1986]. In other words, snow reduces sea ice thickening in winter and thinning in summer. The snow cover on Arctic sea ice consists primarily of wind-blown, hard-packed snow composed of well-rounded grains with diameters of 0.25 – 0.50 mm and densities of 300-400 kg m^{-3} [Tucker et al., 1992]. Icy layers, resulting from melt-refreezing cycles, are quite common in the snowpack, and depth hoar can also be found occasionally at the base of the snow cover. The snow remains dry most of the year, but significant liquid water exists in snow during the summer – the snow melts completely in summer in the Arctic.

Research on snow on Antarctic sea ice is reviewed by Massom et al. (2001). The snow is heterogeneous [Sturm et al., 1998], with several distinct types of snow found inter-layered in a single stratigraphic column and sometimes two types of snow crystals (depth hoar and melt-grain clusters) commingled within a single layer. Ubiquitous meltwater percolation from the top of the snow pack and wicking of brine from the bottom result in zones of coarse-grained snow. Percolation columns and icy lenses are irregularly distributed both laterally and vertically in the winter and fall snowpack [Sturm et al., 1998]. In summer, flooding is more frequent due to depression of floes below sea level by a relatively thicker snow cover than in other seasons. The snow density is even more variable in summer (75-992 kg/m^3) than in fall (91-588 kg/m^3) [Morris and Jeffries, 2001; Jeffries et al., 1994]. The lowest values are for fine, soft and fresh snow. Fall snow crystals are characterized as rounded grains in chains and clusters with strong bonds, while summer snow crystals are dominated by melt clusters and melt-refreeze clusters [Morris and Jeffries, 2001]. Chains and clusters of single snow grains form composite grains. Both individual single snow grains and composite grains are found in the snowpack in the Ross Sea, but the individual single snow grains comprises only a small part of the snowpack [Morris and Jeffries, 2001].

"The International Classification for Seasonal Snow on the Ground" (ICSSG) [Colbeck et al., 1990] is adopted in this thesis for classification of snow type and snow-grain morphology in a snowpack. The definition of a grain in the ICSSG is "the smallest characteristic subunit of snow texture recognizable with a hand lens; it can consist of one or more crystals of ice". To discriminate the small single crystals from those of large clusters of grains and polycrystalline melt-freeze particles, which have distinctive remote sensing implications, "grains" are subdivided into two categories in this thesis: single grains and composite grains [Morris and Jeffries, 2001]. A single grain of snow refers to a single crystal [Bates and Jackson, 1980], while a "composite" grain of snow refers to well-bounded clustered single crystals (6cl) and melt-freeze polycrystals (6mf) in the ICSSG. For optical remote sensing of snow-covered sea ice, most of the signal comes from the snow cover. Snow coverage is also an indicator of the extent of snow on sea ice, especially for Antarctic sea ice which is snow-covered all-year round.

1.3 Optical Remote Sensing of Snow and Ice

Optical remote sensing in the visible and near infrared (VNIR) spectral regions is a unique remote sensing technique for mapping of snow surface albedo with applications in both snow hydrology and climate studies. Optical remote sensing has been an attractive technique since its first use. This is due to its high spatial resolution and the coincidence of its electromagnetic wave bands with the solar energy spectrum. As solar energy is the primary driving force of geophysical, hydrological, and biological processes on Earth, most of these processes can be investigated using remote sensing within the solar spectrum.

The present study focuses on the snow cover on sea ice floes in the Ross, Amundsen and Bellingshausen seas. Retrieval of the physical parameters of snow is the goal of remote sensing. The physical characteristics of the snow can be retrieved by remote sensing, because they determine the snow reflectance directly through the interaction of electromagnetic radiation with snow via absorption and scattering. To understand the optically remote sensed data, we have to understand the interaction processes of solar radiation with the snow cover. To achieve this goal, we first have to fully understand the physical characteristics of the snow cover, and the physical processes that control the snow physical parameters. Second, we have to understand the interaction of solar radiation with the snow physical parameters so that the reflected energy received by the space-based sensor can be quantified. Radiative quantities such as irradiance, radiance, albedo, spectral albedo, and bidirectional reflectance are basic parameters in the radiative theory that is used to achieve this goal. The interaction of electromagnetic radiation with dispersive media such as snow cover generally involves both single scattering theory to treat scattering and absorption by individual snow grains and radiative transfer theory to deal with multiple scattering in the snow medium consisting of a large collection of snow grains completely dispersed in space.

1.3.1 Snow Physical Parameters

Except for atmospheric effects, the signal received by a satellite sensor from a snow cover is determined by snow physical parameters such as snow depth, density, snow extent, snow grain size, snow water equivalent, impurities etc. The characteristics of winter snow cover on Weddell Sea and Eastern Antarctic sea ice were studied by Massom et al. (1997, 1998), and on Ross, Amundsen and Bellingshausen sea ice by Sturm et al. (1998). Summer and autumn snow covers were studied by Morris and Jeffries (2001) in the Ross Sea. In addition to the above-mentioned snow physical parameters, parameters of composite grains are also of interest because they constitute the main type of snow crystal in both summer and fall when individual single snow grains comprise only a small part of the snow pack [Morris and Jeffries, 2001]. The possible effect of large composite grains such as meltclusters, depth hoar crystals, etc. on optical remote sensing has yet to be determined.

1.3.1a Snow Extent

Snow coverage on land and ice is a primary concern in remote sensing [Dozier and Marks, 1987; Hall et al; 1995; 2000]. Snow coverage not only affects water volume equivalence of snow [Rango and Itten,1976], but also directly affects the area-averaged albedo. Knowledge of the snow coverage is vital for improving meso-scale to large-scale hydrological models, refining medium- and long-term weather forecasts, sea ice growth and decay models, and for improving general circulation models [Rango, 1985]. On both large-and small-scales, maps of snow extent through the snow season are used to forecast melt in the regions with or without appropriate ancillary ground data [Rango et al., 1977; Martinec and Rango, 1986]. Passive microwave instrument can be used to map the extent of snow, this capability is limited to dry snow. Optical remote sensing techniques have several advantages. First, the spatial resolution is high. Second, the criterion used to distinguish the snow-covered area from snow-free land is more reliable than that for microwave data because microwave signatures are more liquid-water dependent than visible and near-infrared channels [Walker and Goodison, 1993]. Thus, it has been suggested that passive microwave data be used in conjunction with VNIR data for the determination of snow coverage [Foster et al., 1984]. It has also been suggested that VNIR, infrared and microwave data be combined to improve snow cover mapping in various land areas under both clear and cloudy conditions [Tait et al., 1999; 2000].

1.3.1b Snow Grain Size

An individual snow grain (either single or composite) is treated as an isolated electromagnetic wave scatterer. In the scattering theory, the size of a scatterer is an important parameter in determining the absorption and scattering of the incident electromagnetic signal. The snow grain-size not only affects the single scattering albedo and absorption in the visible and near-infrared region, and thus the retrieval of all-wave albedo, but it also affects the emissivity of a snow-pack in the microwave region, and thus the retrieval of snow water equivalent and brightness temperature by microwave remote sensing techniques [Rott, 1987; Koike and Suhama, 1993]. Therefore, snow grain size is a very important parameter in remote sensing of snow [Wiscombe and Warren, 1980; Chang et al., 1981; Armstrong, et al., 1993].

In a dispersive medium such as a snow cover, the ice-air interface is the main boundary at which electromagnetic waves change propagation direction and polarization. A snow cover is an accumulation of ice crystals overlying on the Earth surface. A newly accumulated snow layer is composed of loosely packed snow flakes. In an older, metamorphosed snow layer, snow grains are in contact and often well bonded to each other [Grenfell and Warren, 1999]. For this case, the geometrically-equivalent sphere is defined as the sphere with the same surface-to-volume ratio as the bonded ice grains, and it has been used as the "optically-equivalent" grain size for the radiative transfer modeling of snow reflectance in the visible and near-infrared, thermal infrared and microwave regions [Dozier et al., 1989; Grenfell and Warren, 1999; Shi et al., 1993].

Snow grains within a snow cover change shape and grow in size due to metamorphism from the moment they are start to accumulate in the snowpack. When the temperature gradient is weak and the vapor flux rates are low, metamorphosed snow grains tend to have a smooth and rounded texture [Colbeck, 1982; Armstrong, 1985]. With large temperature gradients and associated vapor flux, snow will metamorphose to form large-grained "depth hoar" [Colbeck, 1987; 1990]. For summer snow cover on sea ice in the polar regions or late spring snow on the continents, the continuous process of melting and refreezing results in grain growth due to melt-freeze metamorphism [Colbeck, 1979; 1987], a process independent of the kinetic grain growth process in subfreezing snow. Snow grains in wet snow, where snow is liquid-saturated, are well rounded, uniform in size and cohesionless [Colbeck, 1979].

Snow grain size can be obtained by three methods: direct measurement, reflectance-inversion, and model-prediction.

Direct methods include stereology and the grid-lens method. Since the ice in a snowpack is all connected, snow grains are generally in contacts. The total volume, V, of ice in a snow matrix, and the total surface area, A, of the ice-air interface, can be measured using stereological techniques to obtain the equivalent spherical radius $r = 3V/A$ [Grenfell and Warren, 1999]. Theoretically, the surface area of ice crystals in a snow pack can be measured. But due to the highly irregular shapes typically encountered, no generally accepted method to determine the effective grain-size in a snow cover has evolved [Armstrong, et al., 1993]. Although attempts using stereology to determine snow grain-size have been reported [Dozier and Marks, 1987; Davis and Dozier, 1989; Shi et al., 1993], these methods may not be applicable for operational field measurements [Armstrong, et al., 1993]. For most snow fieldwork, visual estimates using millimeter grids or gridded cards and magnifying lenses or a microscope are still being widely used [Armstrong, et al., 1993; Nolin and Dozier, 2000; Morris and Jeffries, 2001]. Sieving also remains common [Bader et al., 1954; Bensen, 1962; Sturm, 1991; Sturm et al., 1993]. The International Association of Scientific Hydrology (IASH) International Classification for Seasonal Snow on the Ground [Colbeck et al., 1990] suggests that the observer take a "more or less homogeneous mass of snow and record the average size of its prevailing or characteristic grains, the size of the grain or particle being its greatest extension (diameter) measured in millimeters". Although simple, this method is found to provide consistent measurements of snow grain size and the results are sufficiently accurate for comparison with the grain size data retrieved from remotely sensed snow reflectance data [Nolin and Dozier, 2000].

The second method to obtain snow grain size is the reflectance-inversion technique. The retrieval of snow grains from remotely sensed reflectance data is closely related to this technique and is now very actively pursued. This method is based on the reflectance of snow in the near-infrared range, particularly across the wavelength range 1.0-1.3 μm, which is known to be sensitive to snow grain-size [Dozier, 1984, 1989; Hyvärinen and

Lammasniemi, 1987; Painter et al., 1998]. Wiscombe and Warren (1980) modeled the effects of grain size on snow spectral albedo using a two-stream model that was subsequently verified by the measurements of Grenfell et al. (1994). Early methods for estimating snow grain size from reflectance measurements have been qualitative [e.g. Hyvärinen and Lammasniemi, 1987; Dozier, 1984, 1989]. Techniques now adopted to map grain size from remotely sensed data exploit the sensitivity of snow reflectance to grain size in the near-infrared region [Dozier et al., 1981; Dozier and Marks, 1987; Carson et al., 1992; Nolin and Dozier, 1993, 2000; Bourdelles and Fily, 1993; Green and Dozier, 1996; Fily et al., 1997; Li et al., 2001]. Dozier et al. (1981), using the Wiscombe and Warren model and NOAA-6 AVHRR data, found that it was possible to determine snow grain-size from remote sensing data. But due to the limited sensitivity of the NOAA-6 AVHRR near-infrared band to snow grain size due to the bandwidth and spectral position, the retrieved results were not precise [Nolin and Dozier, 2000]. Later Dozier and Marks (1987) used Landsat Thematic Mapper (TM) data to retrieve grain size and classify snow-covered regions into relatively fine-grained new snow and older, coarser-grained snow. In an initial attempt to map the grain-size distribution across Antarctica, Carlson et al. (1992) focused on the region of characteristic water ice absorption features in the near-infrared region extending from 1.5 microns to 2.5 microns. Based on the fact that both theoretical and observed spectra show that the ratio of reflectivity at peaks and valleys varies with grain size, they used the ratio of signals at 1.5 and 1.7 microns to obtain the grain size map that was derived from Galileo spacecraft flyby data. Using the ratio of intensities provides a measure that is independent of sastrugi and other geometric effects, at least to a first approximation. Bourdelles and Fily (1993) mapped snow grain size using Landsat TM data over the Dumont D'Urville region of Antarctica. They combined the Wiscombe and Warren model and the 5S model "Simulation of the Satellite Signal in the Solar Spectrum" [Tanré et al., 1990] to calculate the apparent reflectance versus snow grain size for all the TM bands at the specified solar zenith angle and assuming the snow surface is Lambertian. Retrieval of apparent reflectance is thus converted to grain size by using the calculated one-to-one relationship between reflectance and grain size. Fily et al. (1997) computed the reflectance-grain size relations based on a bidirectional reflectance model and used the retrieved reflectance data from TM bands to obtain the grain sizes. To avoid the bands that are too sensitive to atmospheric conditions, Nolin and Dozier (1993, 2000) chose an AVIRIS band that sits around the ice absorption feature centered at 1.03 μm based on atmospheric transmittance, grain size sensitivity and amplitude of snow reflectance at this wavelength. To retrieve the optically-equivalent grain size from ground-based reflectance measurements, Davis et al. (1993) used a spectral band centered at 1.075 μm. The reflectance-grain size relations for specific solar illumination angles are calculated using the DIScrete-Ordinates Radiative Transfer (DISORT) model [Stamnes et al., 1988]. Snow reflectance retrieved from remotely sensed data is then inverted to yield quantitative estimates of snow grain size. Li et al. (2001) used multiple AVIRIS bands (0.86, 1.05, 1.24 and 1.73 μm) to retrieve snow grain-size and attributed the dependence of the retrieved grain-size on wavelength to the photon penetration depth. More studies with snow pack of various grain-sizes need to be done for this method to accurately derive the grain size from reflectance measurements. The effect of the vertical profile of snow grain-size on reflectance needs to be addressed, so that the vertical profile of snow grain-size can be retrieved from multi-spectral remotely sensed data rather than one grain-size for a natural snowpack, which is generally highly stratified.

The third method is model-prediction. Using a one-dimensional energy and mass transfer model, SNTHERM.89 [Jordan, 1991], Davis et al. (1993) tried to predict the growth of snow grains. The initial grain-size is input to the model and the grain-size is predicted from the model at a later time. This is an interesting method. But the evolution of a snowpack is too complicated, and thus more research is needed to improve the accuracy of the model prediction. This is why this method has not yet been widely used.

1.3.1c Snow Water Equivalent

The amount of water accumulated in a snowpack during a winter is very important in estimating the spring discharge of a specific river. It is especially important heavy and light snow years. Caution is taken to prevent floods in spring due to melt of snow and ice in heavy snow years and to ensure that there is enough water for agriculture and human use in light snow years. At present, the mapping the snow water equivalent (SWE), especially in winter, depends primarily on passive microwave techniques [Chang et al., 1987a,1987b; Mätzler, 1987; Walker and Goodison, 1993]. However, the effectiveness of microwave remote sensing of snow is limited in summer by the presence of liquid water within the snowpack. Liquid water alters the microwave emission characteristics such that internal absorption of the microwave radiation increases significantly and volume scattering decreases [Foster et al., 1984], because water is substantially more absorptive than ice in the microwave part of the spectrum. As a result, the typical passive microwave response to liquid water content is an increase in the observed brightness temperatures. In most cases, it is very difficult to discriminate wet or melting snow areas from snow-free land [Kunzi et al., 1982]. Therefore, a combination of VNIR and thermal infrared remote sensing techniques with microwave remote sensing is a very promising approach to study snow and ice [Tait et al., 1999].

1.3.1d Snowpack Depth

Snow depth, together with density, determines the snow water equivalent. As snow optical depth is proportional to the snow geometrical depth [Wiscombe and Warren, 1980], it plays an important role in snow surface reflectance if a snowpack is not optically semi-infinite, although snow thickness is a dummy variable when a snowpack is optically semi-infinite. Data on snow depth, water equivalent, and areal coverage play a fundamental role in snowmelt-runoff modeling, and are thus highly desirable in remote sensing of snow.

1.3.1e Snowpack Density

For new or recent snow cover, the density is generally small (108 kg m^{-3}). Aging and metamorphism increase snow density. A well-metamorphosed snowpack's density can approach that of randomly packed uniform ice spheres (580-600 kg m^{-3}). Densification due to gravity of the overlying snow can increase snow density to approximately 700-800 kg m^{-3}. When snow turns into glacial ice or snow-ice, the density reaches 800-830 kg m^{-3} [Sommerfeld and LaChapelle, 1970]. Density of snow in a snowpack varies from place to place depending on wind forces. For instance, a taiga snow cover generally has lower density (<250 kg m^{-3}) than a tundra snow density (>350 kg m^{-3}) because snowfalls are rarely accompanied by wind in the taiga zone [Sturm et al., 1993]. Large-scale average density of snowpack on sea ice in Antarctica varies from ~290 to 390 kg m^{-3} [Massom, et al., 2001]. Similar values are also found in the Arctic [Warren et al., 1999]. Snow density not only affects the snow thermal conductivity [Yen, 1981; Jordan, 1991; Sturm and Johnson, 1992; Brandt and Warren, 1997], but also the snow dielectric properties [Hallikainen and Winebrenner, 1992]. Snow density affects optical remote sensing through multiple scattering because the optical depth is proportional to snow density [Wiscombe and Warren, 1980]. Although snow density does not affect snow reflectance when the snowpack is semi-infinite, it does affect the semi-infinite depth of a snowpack for a particular wavelength.

1.3.2 Radiative Parameters

What an optical satellite sensor receives is the reflected or back-scattered solar radiation. For optical remote sensing, the energy received by the satellite sensor depends on the following: (1) the solar geometry (solar zenith angle, solar azimuth angle); (2) sensor viewing geometry (sensor zenith angle, sensor azimuth angle); (3) atmospheric properties such as the aerosol particle type, concentration, size and spatial distribution; (4) cloud particle types, concentration, size and spatial distribution; (5) vertical profiles and absorption spectrum of various gases (O_3, water vapor, etc.); and (6) the physical properties of the ground surface (snow grain-size, snow depth and density, snow stratigraphy, snow impurity composition). The interaction of electromagnetic radiation with the atmosphere or the ground surface is generally described in terms of radiative parameters including dimensional quantities such as radiance, spectral irradiance (spectral energy flux) or irradiance (energy flux), and dimensionless quantities such as bidirectional reflectance, spectral albedo and all-wave albedo.

1.3.2a Snow Bidirectional Reflectance

Reflectance is the ratio of reflected to incident flux or irradiance. The basic quantity that characterizes geometrically the reflecting properties of a surface is the bidirectional reflection distribution function (BRDF) [Nicodemus et al., 1977]. The BRDF characterizes the angular distribution of the reflected energy and thus the anisotropy of the reflecting surface, and is therefore a very important quantity in remote sensing. The anisotropy of snow is generally non-negligible. Knowledge of the BRDF can be used to correct the anisotropy of the ground surface when the satellite reflectance is converted to albedo. This correction involves the coupling of the surface BRDF and atmospheric processes (scattering and absorption by atmospheric gases, aerosol, clouds, etc.) [Vermote et al., 1997a]. Decoupling of the atmosphere from the target surface can be accomplished when the surface BRDF is known, and thus a more complete atmospheric correction can be made and the subsequent retrieved surface reflectance will be more accurate [Hu et al., 1999]. The BRDF, a derivative quantity, is useful primarily as an underlying concept and can not be measured directly because any instrument of truly infinitesimal solid angle can not obtain measurable amounts of radiant flux [Nicodemus et al., 1977]. But when the sensor's viewing solid angle is small enough, the BRDF can be measured approximately under very clear sky conditions [Grenfell et al., 1994; Zhou and Li, 2000a; Aoki et al., 2000; Li and Zhou, 2002a]. It can be modeled theoretically from radiative transfer [Thomas and Stamnes, 1999]. As all measurable reflectances [Nicodemus et al., 1977] can be derived from the BRDF, modeled BRDF results can be tested using the measured reflectances.

Early measurement of the bidirectional reflectance of snow was reviewed by Warren (1982). Since then, Taylor and Stowe (1984) developed empirical BRDFs for the snow-atmosphere system from Nimbus 7 satellite data. Kuhn (1985) measured the bidirectional reflectance of snow in Antarctica and an alpine snowpack at four wavelengths (0.45, 0.514, 0.75 and 1.0 μm). Steffen (1987) investigated the effects of snow grain-size and types on the bidirectional reflectance from measurements at selected wavelengths (0.5-0.6 μm) for flat snow surfaces in the Tienshan Mountains of China. Later, Steffen (1997) made the same observation in Greenland and showed anisotropic reflectance functions for various geometric conditions. Brandt et al. (1991) investigated the effect of sastrugi orientation on the BRDF at $\lambda = 0.9$ μm at the South Pole. Carlson and Arakelian (1993) measured bidirectional reflectance of the snowpack at Vostok, Antarctica, and found that the most anisotropic reflection in the principal plane was at $\lambda = 2.0$ μm as determined from data at $\lambda = 0.5$ to 2.3 μm. Grenfell et al. (1994) measured the BRDF at $\lambda = 0.9$ μm on a flat snowpack at South Pole. Warren et al. (1998) investigated the effect of surface roughness (sastrugi) on the BRDF at three wavelengths ($\lambda = 0.6$, 0.66, and 0.9 μm) at the South Pole from the point of view of satellite remote sensing. Aoki et al. (2000) made BRDF observations on a snowfield around Kitami in eastern Hokkaido, Japan and found that the anisotropic reflectance is most significant in the NIR region when $\lambda > 1.4$ μm. Based on the measurements of bidirectional reflectance of snow on sea ice, Li and Zhou (2002b) derived reciprocal kernel functions for snow BRDF.

The BRDF as a function of wavelength, grain-size, and illumination and viewing geometry was calculated by Li (1982) using Mie theory and the doubling method. Leroux et al. (1997, 1999) developed a polarized BRDF model using the doubling and adding method and found that the snow grain shape strongly affects the BRDF in the NIR. Leroux and Fily (1998) developed a BRDF model to study the effect of sastrugi. BRDF modeling of snow is being actively pursued [Li, 1982; Leroux and Fily, 1998; Leroux et al., 1999; Mishchenko, et al., 1999; Jin, et al., 1999], but no benchmarked computational algorithms are generally available.

1.3.2b Snow Spectral Albedo

Snow spectral albedo is the ratio of the reflected upwelling spectral irradiance to the downwelling incident spectral irradiance at the snow surface. Based on the concept of "biconical reflectance", spectral albedo is also called directional-hemispherical reflectance [Nicodemus et al., 1977], direct-beam albedo [Wiscombe and Warren, 1980] or "black-sky" albedo because the sky looks black when the incident radiation is directional. When the incident radiation is diffuse, it is called bihemispherical reflectance [Nicodemus et al., 1977], diffuse albedo [Wiscombe and Warren, 1980] or "white-sky" albedo because the sky looks white due to diffuse light. Factors that affect the spectral albedo include solar zenith angle, atmospheric optical properties, snow grain-size, density, snowpack thickness, liquid water content and cloud cover [Wiscombe and Warren, 1980], and impurities in the snowpack [Warren and Wiscombe, 1980; Warren, 1984b]. The dependence of the spectral albedo on snow grain-size has been well studied for grain-sizes below 1 mm [Nolin and Dozier, 1993], for which the Mie calculation of single scattering properties is appropriate [Wiscombe, 1980]. However, formation of composite grains (meltclusters, polycrystalline particle, icy lenses, depth hoar, percolation column) [Colbeck et al., 1990] often results in snow grain-sizes in a snowpack well above this limit, especially in the bottom snow layers in winter [Sturm et al., 1998], and anywhere in the snowpack in summer and fall [Morris and Jeffries, 2001]. The effect of these large ice crystals on snow reflectance is worth consideration (Chapter 3 and Chapter 6). The effect of snowpack stratigraphy on spectral albedo or reflectance of snow is much less studied (Chapter 6). Stratigraphy of the snow plays an important role in passive microwave emissivity [Bernier, 1987; Sturm et al., 1993].

1.3.2c Snow All-wave Albedo

Snow all-wave albedo is defined as the ratio of the solar energy flux reflected from the snow surface and incident on the surface. It is the integration of spectral albedo over the whole solar spectrum as follows

$$\alpha=\frac{\int\alpha_\lambda F_\lambda^{\downarrow}d\lambda}{\int F_\lambda^{\downarrow}d\lambda}=\frac{\int\left(F_\lambda^{\uparrow}/F_\lambda^{\downarrow}\right)F_\lambda^{\downarrow}d\lambda}{\int F_\lambda^{\downarrow}d\lambda}=\frac{\int F_\lambda^{\uparrow}d\lambda}{\int F_\lambda^{\downarrow}d\lambda} \tag{1.1}$$

where λ is the wavelength, α the all-wave albedo, α_λ the spectral albedo at wavelength λ, and $F_\lambda^{\downarrow}$ the downwelling spectral irradiance at the snow surface. From Equation (1.1) we can infer that all factors that affect the spectral albedo will affect the all-wave albedo. We can also see that the spectral distribution of the downwelling spectral irradiance $F_\lambda^\downarrow$ will also directly affect the all-wave albedo. Under cloudy and overcast conditions, the effect of clouds on the all-wave albedo is two-fold: it changes the spectral albedo by affecting the effective incident angle, and it changes the spectral distribution of the downwelling spectral irradiance. Reducing of the proportion of spectral irradiance in the near-infrared by clouds, where the spectral albedo of snow is lower than that in the visible, increases the all-wave albedo.

For climate studies, Earth's surface energy- and mass-balance, snow-melt and subsequent recharges in rivers, the albedo is an important parameter. Like the snow extent products, the all-wave albedo is another important product derived from remote sensing of snow and ice, due to its effect on the melting rate and surface energy balance. Retrieval of the snow-surface all-wave albedo from satellite measurements is a major task in optical remote sensing, but it is also challenging due to the strong dependence of the spectral albedo on the physical composition, topography, and stratigraphy of the snow surface [Knap et al., 1999]. There is no obvious way of deriving the all-wave (broadband) albedo from narrowband spectral albedo measurements. Nevertheless research on the conversion from satellite-measured narrowband spectral albedo to all-wave broadband albedo continues [Brest and Goward, 1987; Brest, 1987; Duguay and LeDrew, 1991, 1992; Gratton, 1993; Knap, et al., 1999]. These conversions are mostly empirical, with the relationship between all-wave albedo and individual narrowband albedos established on the basis of statistical multivariate regression analysis of the ground-based measurements of both all-wave albedo and simulated satellite narrowband albedos or by use of weighting functions [Duguay and LeDrew, 1992; Gratton, 1993]. One shortcoming is that there should be a specific relationship for a particular surface feature. Because of this, understanding the spectral structure of the albedo of a ground surface cover such as snow is very important. Generally the spectral albedo of snow increases from ultraviolet to visible, then decreases from the visible to the near-infrared. However, the study of the fine spectral structure of snow spectral albedo is far from complete. Differences in snow grain-size, snow water equivalent, snow depth, stratification, impurity content etc. lead to a great diversity of spectral albedo curves (Chapter 6). For snow or ice, the diversity of spectral albedo is often found to be too high to be described by one generalized spectral albedo curve [Knap et al., 1999]. This renders very difficult the retrieval of all-wave albedo from narrowband spectral albedo from satellite data. To increase the reliability of the empirical relationships between all-wave albedo and individual narrowband albedos established by statistical multivariate regression analysis of the ground-based measurements of all-wave albedo and simulated satellite narrowband albedos, it is necessary to

- Establish a complete global database of all-wave albedo (Chapter 2), so that the statistical analysis is based on a more complete data set. For spectral albedo, previous measurements based on a few bands should be replaced with instruments with much higher spectral resolution [Zhou et al., 2001];
- Accurately validate reflectance measured by satellite optical sensors, especially for newly-launched satellite sensors (Chapter 4).

Through efforts to establish a complete global database of all-wave albedo and high spectral-resolution spectral albedo of snow by ground measurements, modeling study and reflectance products validation, all-wave albedo products are expected to become more accurate and thus to provide more reliable inputs to snowmelt modeling and climate studies as well.

The remainder of the thesis is organized as follows:

Chapter 2 describes the instrumentation and *in situ* measurement of albedo, spectral albedo and bidirectional reflectance. Comparison of instruments is conducted to test the accuracy of the measurements. Ground measurements of radiation are also compared with modeling results to assess the difference between the measurements and the calculations using an established model.

Chapter 3 discusses snow physical parameters and correlation of these parameters with all-wave albedo. Spatial variation of all-wave albedo and the physical parameters of the snowpack where the albedo was measured are discussed using statistical techniques.

Correlation between albedo and the parameters of single snow grains and composite grains is discussed.

Chapter 4 presents the techniques and difficulties in validating the MODIS reflectance products of snow and sea ice. Accurate location of *in situ* measurement site, atmospheric correction, *in situ* reflectance measurement, ice concentration estimate and ice concentration correction of the *in situ* measurements are discussed.

Chapters 5 and 6 are dedicated to radiative transfer modeling of solar radiation in a snowpack. Chapter 5 focuses on the calculation of single scattering properties for large snow grains, such as snow composite grains, whose size parameter is beyond the publicly available Mie code's capability, in the context of the geometrical optics method. The resulting radiative properties of individual snow grains are used in Chapter 6. Chapter 6 discusses the effect of the vertical heterogeneity of a snowpack on the snow reflectance, considering multiple scattering coupled with the single scattering parameters. Comparison with ground measurement is also given.

A summary of the results and prospects for future work are given in Chapter 7.

CHAPTER 2*

All-wave Albedo, Spectral Albedo and BRDF of the Snow on Summer Sea Ice

ABSTRACT. All-wave albedo, spectral albedo and bidirectional reflectance distribution function were measured over snow-covered pack-ice floes during summer 1999 (January and February) in the Ross sea, Antarctica. Temporal variation of the all-wave albedo and the spectral albedo was measured from the northern edge to the southern edge of the pack ice along three lines of longitude: 165°W, 150°W, and 135°W. Snow depth, snow-cover stratification, snow-temperature profiles, and grain-size and morphology were also documented. It was observed that daily-averaged albedos varied from 0.70 to 0.86 for cloudy conditions over the pack ice. Only two sets of daily-averaged albedo were collected for clear-sky conditions (0.788 and 0.825). Albedo was lower at the marginal edges of the pack ice than in the central pack ice. Albedo was higher over the southern part of the central pack ice than the northern part. Clear- and cloudy-sky albedos measured on the same site indicate that the average increase in albedo due to clouds is 1.4% (maximum 4.0%). Spectral albedos of the pack-ice floes were similar under clear-sky and cloudy conditions. Both are mainly controlled by the snow grain size (see chapter 6), especially in the top snow layer. All-wave albedo derived from measured visible and near-infrared spectral albedo, with extrapolation to ultraviolet and shortwave infrared regions for both clear- and cloudy-sky conditions, agrees well with all-wave albedo from direct measurements.

---

* This chapter is based on material published by Zhou et al. (2001) and Zhou and Li (2000a).

2.1 Introduction

Spectral albedo is the ratio of the upwelling spectral irradiance reflected by the surface to the downwelling incident spectral irradiance at the surface. All-wave albedo is the integral of spectral albedo over the whole solar spectrum. It is a major variable in controlling the energy budget of sea ice, and an important tuning parameter in modeling sea ice-atmosphere interaction and global warming. Any reduction of the surface albedo of snow and sea ice means more absorption of solar radiation, which tends to increase the temperature at the surface. Absorption of short-wave radiation can result in internal melting and an increase of liquid-water content, changing the surface characteristics and internal structure of the snow cover [Grenfell and Maykut, 1977]. Accompanying the absorption of solar radiation is metamorphosis of snow crystals, which results in larger grain size and a decrease of the number density of snow grains. All of these factors will contribute to a decrease of the snow albedo.

To accurately retrieve the earth surface features from NASA moderate resolution imaging spectrometer (MODIS) data, the atmospheric and surface anisotropic effects must be corrected. This correction involves the coupling of the surface bidirectional reflectance distribution function (BRDF) and atmospheric processes (scattering and absorption by atmospheric gases, aerosol, clouds, etc.) [Vermote et al., 1997b]. Decoupling of the atmosphere from the target surface can be accomplished when the surface BRDF is known, and thus more complete atmospheric correction can be made and the subsequent retrieved surface reflectance will be more accurate [Hu et al., 1999]. BRDF is also the kernel used to obtain the directional-hemispherical reflectance ("black-sky" albedo) and bihemispherical reflectance ("white-sky" albedo) that are important parameters in climate studies. The radiance emerging from a ground pixel and received at a specific band by a narrow-field-of-view optical sensor deployed in space is from a particular direction. The spectral albedo at a specific wavelength is the ratio of the upwelling spectral irradiance, which is the integral of the reflected radiance over all angles, and the downwelling spectral irradiance. Thus, to retrieve spectral albedo from the radiance measured by a satellite sensor at only one angle, it is imperative to know the ground surface BRDF so that integration over all angles can be performed. Once the spectral albedo of a specific waveband is retrieved, the all-wave albedo, can be obtained by narrowband-to-broadband conversion [Brest and Goward, 1987; Li and Garand, 1994; Knap et al., 1999].

The all-wave albedo of the open ocean is much smaller than that of the snow and sea-ice cover. Approximately 85-95% of the incident solar radiation is absorbed by the open ocean, while 30-50% or less is absorbed by a snow and sea-ice cover [Washington and Parkinson, 1986]. Thus, during the summer season, a reduction of the snow and sea-ice albedo due to snow metamorphosis and possible removal of the snow cover enhances the absorption of solar energy. This results in thinning and breaking-down of ice floes, and reduction of ice concentration and ice extent, which will further reduce the area-averaged albedo. On the other hand, an increase in surface albedo due to freezing of sea water means more solar energy is reflected back to the atmosphere, resulting in less energy input into the sea ice or ocean. This results in a higher probability of more freezing of ocean water in polar regions, and an increase in the areal ice coverage and possibly snow and sea ice thickness, which will produce a further increase in the area-averaged albedo. The positive feedback of the surface albedo to changes in atmospheric conditions makes the snow and sea-ice in polar regions an important subject for weather prediction and global warming studies.

In summer, the patterns of sea ice and snow decay are different in the Antarctic as compared with the Arctic [Fetterer and Untersteiner, 1998; Andreas and Ackley, 1982]. In the Arctic, melt ponds form as snow melts and meltwater accumulates on the ice surface. Decay of snow and ice cover is mainly from the top of the cover and from the sides. In the Antarctic, melt ponds are rarely observed [Arctowski, 1908; Wordie, 1921; Spichkin, 1967; Ackley, 1979]. As a consequence, the surface albedo of the Antarctic sea ice is close to the typical albedo value of snow-covered ice all year round. Antarctic sea ice albedo shows large variation due to the spatial complexity and variability of the surface even within the same region.

Although many albedo studies have been carried out in the Arctic [Hanson, 1961; Chernigovskii, 1966; Langleben, 1969,1971; Grenfell and Maykut, 1977; Grenfell and Perovich, 1984; De Abreu and others, 1995] and Antarctic [Liljequist, 1956; Hanson, 1960; Hoinkes, 1961; Weller, 1968; Kuhn et al., 1977; Carroll and Fitch, 1981; Yamanouchi, 1983; Grenfell and others, 1994; Allison and others, 1993], the data obtained are not sufficient for the global circulation model (GCM) study. The processes affecting the snow surface albedo are still only qualitatively known, and the available albedo data on regional and temporal differences are too sparse and insufficient to validate any albedo modeling efforts [Fetterer and Untersteiner, 1998]. Most of the albedo measurements made in Antarctica are from continental sites. There are few datasets of all-wave albedo and spectral albedo available for the Southern Ocean [e.g., Allison et al., 1993], and even fewer for the western Antarctic sea ice, including the pack ice in the Ross Sea. Consequently, an effort was made to measure the albedo during a summer cruise aboard the US research vessel *Nathaniel B. Palmer* in the Ross Sea in January and February 1999. Other parameters such as snow surface temperature, snow depth and snow grain-size were also routinely measured. In addition, one to two snow pits were dug at each of the ice-floe stations, and precise measurements of snow depth, stratigraphy, density, grain-size and morphology, salinity and temperature were recorded [Morris and Jeffries, 2001]. Bidirectional reflectance distribution function (BRDF) was measured in the Ross and Amundsen seas in February and March 2000 (see also chapter 4). The focus of this chapter is on the data of the 1999 cruise.

2.2 Study Area, Instrumentation and Methods

2.2.1 Study Area

The cruise route is shown in Figure 2.1. The sea-ice cover in the Ross Sea is primarily first-year pack ice. Sea ice and its snow cover were taken as the primary platform for albedo measurements. Temporal variation of the all-wave albedo and spectral albedo was measured from the northern edge to the southern edge of the pack ice along three lines of longitude: 165°W, 150°W, and 135°W. Albedo measurements were carried out on 24 first-year ice-floe stations and one land-fast ice site (station 9).

2.2.2 Instrumentation and methods

The all-wave albedo and spectral albedo data discussed in this chapter include data for both cloudy and clear-sky conditions. Almost all the measurements were carried out under cloudy sky conditions: only two sets of albedo data were obtained under very clear-sky conditions (station 5 and station 9). Downwelling solar irradiance was measured together with the all-wave albedo. Most measurements of all-wave albedo and spectral albedo were carried out from 1000 to 1600 h local solar time when the solar zenith angle was smallest. This choice was optimal for the measured results since the uncertainties of both measurement and model calculation are minimized [Schwander et al., 1999]. As the all-wave albedo generally varies considerably with time, depending on the cloud conditions (see section 2.2.3), the two computers used for spectral albedo and all-wave albedo data collection were synchronized daily with the well-calibrated GMT clock on the ship. Datasets were time-stamped so that comparisons between the all-wave albedo retrieved from the spectral albedo and the all-wave albedo measured directly were possible.

2.2.3 All-wave Albedo

The total albedo (or all-wave albedo) was measured using two EPPLEY broadband, precision spectral pyranometers (PSPs) whose wavelength sensitivity was 0.2-4.0 μm. The two pyranometers were installed in the middle of a slender 2.2 m long aluminum bar and suspended about 1.4 m above the snow surface. Ninety-nine per cent of the upwelling irradiance received by the downward-looking pyranometer was from a ground field of view (GFOV) of 20 m. The glass domes of the pyranometers were cleaned before each deployment. As the results from the pyranometers are sensitive to the level of the instruments, care was taken to keep both pyranometers level. One PSP measured the downwelling irradiance and the other the upwelling reflected irradiance. The two

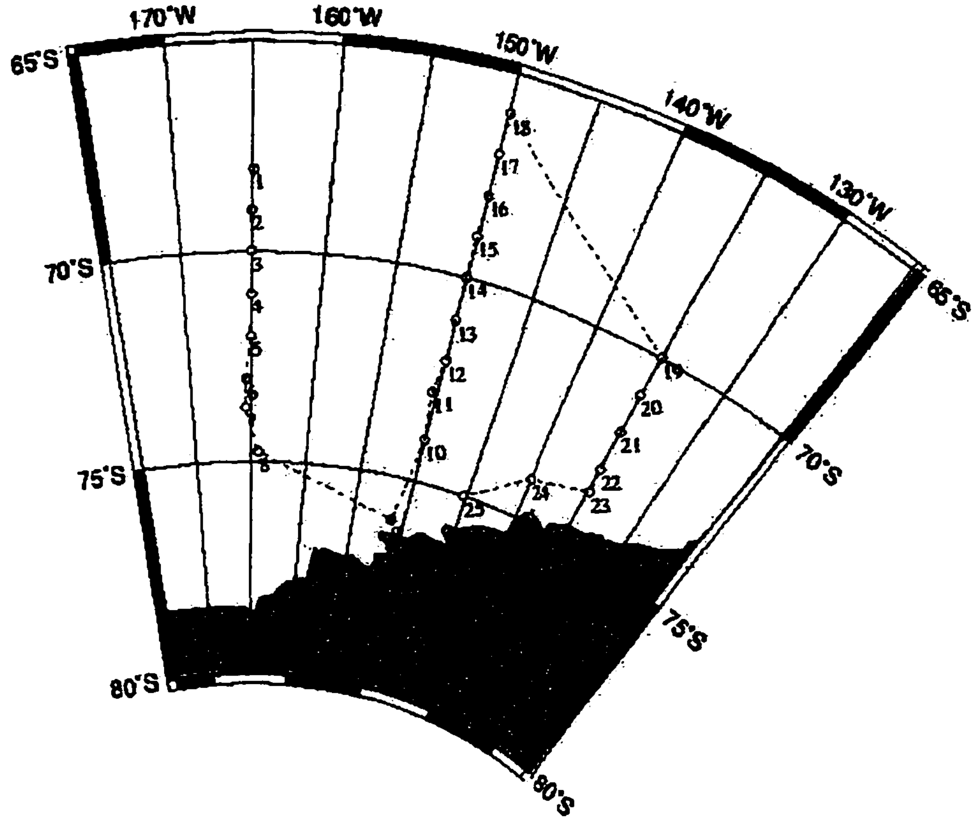

Figure 2.1 The cruise track of R/V *Nathaniel B. Palmer* and albedo station locations during the summer cruise in the Ross Sea, Antarctica (January and February 1999). The ice station number is shown. The numbered circles show the location of the ice station. See Table 2.1 for corresponding days of year.

pyranometers were simultaneously scanned every second, and the data saved at time intervals ranging from one second to several minutes, depending on the deployment period, using a CR10X datalogger. The save-time-interval (STI) was generally 20-60 s, although a 1s interval was sometimes used to study temporal variations of the all-wave albedo with high temporal resolution. The data stored were the average of the scans during the STI.

Time series of downwelling solar irradiance ($F\downarrow(t)$) were derived from the upward-looking pyranometer by converting the direct readings of voltage to flux unit (Wm^{-2}). Likewise, the upwelling irradiance ($F\uparrow(t)$) was obtained from the readings of the downward-looking pyranometer, i.e.

$$F_{\downarrow}(t)=V_U(t)/S_U,\ F_{\uparrow}(t)=V_D(t)/S_D \tag{2.1}$$

where $V_D(t)$ and $V_U(t)$ are the time series of the readings in units of millivolts (mV) from the downward-looking and upward-looking pyranometers, respectively, and S_D and S_U are the sensitivities in units of $mVW^{-1}m^2$ of the downward-looking and upward-looking pyranometers, respectively. Thus the time series of all-wave albedo ($\alpha(t)$) were obtained from

$$\alpha(t)=\frac{F_{\uparrow}(t)}{F_{\downarrow}(t)}=\frac{V_D(t)}{V_U(t)}\cdot\frac{S_U}{S_D} \tag{2.2}$$

2.2.4 Spectral Albedo

Spectral albedo in the visible/near-infrared (VNIR) region was measured using a high-spectral-resolution fiber-optic spectroradiometer manufactured by Analytical Spectral Devices, Inc. (ASD). The sensor measures spectral reflectance and spectral radiance between 333.65 nm and 1064.9 nm in 512 channels, with a spectral resolution of 3 nm. The spectral albedo was measured using a flux sensor (or a remote cosine receptor (RCR) in the manufacturer's terminology) connected to the spectroradiometer by a fiber-optic cable. The base of the RCR has two built-in bubbles for horizontal alignment of the receptor. The RCR was mounted at one end of a slim level bar (about 60 cm long), with the other end attached to a tripod so that the receptor was about 40 cm from the snow surface. However, for most of the measurements of upwelling irradiance, the bar was held by hand with the RCR about 30 cm above the snow surface. Care was taken to insure that the RCR remained level during measurement of downwelling irradiance or upwelling irradiance. The spectral noise values - the electronic noise level of each of the 512 silicon photodiode detectors of the spectroradiometer - were collected before the sensors were exposed to any illumination, and were automatically subtracted from the data during the measurement. The spectral albedo was acquired by measuring the downwelling irradiance, followed immediately by measuring the upwelling irradiance using the RCR. Data were recorded by a mini-computer that was attached to the spectroradiometer. To reduce system errors and errors caused by the fluctuations of the radiation field, several samples (each being the average of 10 scans) were collected for both upwelling and downwelling spectral irradiances.

For a Lambertian surface, 99% of the upwelling irradiance that the cosine sensor receives comes from angles between 0° (nadir) and 82°, i.e. within a GFOV of 2.135 - 2.846 m radius for a height of 30-40 cm above the surface. As the RCR optic and level bar are small and the level bar was always pointed towards the solar azimuth under sunny conditions, the shadowing effects should be negligible. For a height of 30-40 cm, 89.4-83.2% of the upwelling irradiance the RCR received was from the central part of the GFOV, with minimal shadowing effect from personnel. The shadowing effect due to personnel is estimated to be 1.1-1.8% under overcast sky conditions.

2.2.5 *Bidirectional Reflectance Distribution Function*

Clear-sky BRDF of snow cover on sea ice $\rho(\theta_i, \theta_v, \phi, \lambda)$ is defined as the ratio of the spectral radiance $I_v(\theta_i,\theta_v,\phi,\lambda)$ in the viewing direction to the downwelling direct-beam spectral irradiance $F_{\downarrow}(\theta_i,\lambda)$ for wave band λ, i.e.

$$\rho(\theta_i,\theta_v,\phi,\lambda)=\frac{dI_v(\theta_i,\theta_v,\phi,\lambda)}{dF_{\downarrow}(\theta_i,\lambda)} \tag{2.3}$$

where θ_i is the solar zenith angle, 0_v the viewing zenith angle (VZA), and ϕ the viewing azimuthal angle. The BRDF defined above is presented in a coodinate system with the principal plane (vertical plane intersecting the sun) taken as the reference plane (ϕ=0) without loss of generality, due to the symmetry in the azimuthal direction of the sun.

To avoid errors caused by both the radiance sensor and the irradiance sensor, a Lambertian white reference panel was used. Supposing BRDF of the white reference panel is $\rho'(\lambda)$, then

$$\rho'(\lambda)=\frac{dI'_v(\theta_i,\theta_v,\phi,\lambda)}{dF_i(\theta_i,\lambda)} \tag{2.4}$$

where $I'_v(\theta_i,\theta_v,\phi,\lambda)$ is the radiance reflected by the Lambertian white reference panel. In fact, it is independent of the viewing angle (zenith and azimuth), thus $I'_v(\theta_i,\theta_v,\phi,\lambda)=I'_v(\theta_i,\lambda)$. Eliminating the incident spectral irradiance in (2.3)-(2.4), the BRDF of snow cover on sea ice takes the form of

$$\rho(\theta_i,\theta_v,\phi,\lambda)=\frac{dI_v(\theta_i,\theta_v,\phi,\lambda)}{dI'_v(\theta_i,\lambda)}\rho'(\lambda) \tag{2.5}$$

where $\rho'(\lambda)$ is also the calibration data of the white reference panel, and is usually given as the product of π and the BRDF of the Lambertian white reference panel. $dI'_v(\theta_i,\lambda)$ was measured at the viewing nadir from the Lambertian white reference, and $dI'_v(\theta_i,\theta_v,\phi,\lambda)$, the radiance reflected by the target surface, was measured at any viewing angle. Thus BRDF obtained from (2.5) and shown in the following is the product of π and the BRDF defined in (2.3). From (2.5) we can see that the error in BRDF stems mainly from the white reference. Systematic errors caused by the radiance sensor are mostly cancelled by the radiance division.

The arguments above are based on the assumption that the downwelling spectral irrdiance and the reflected radiance are independent of time. This is a good approximation to the real case when the measurement of a whole set of BRDF is completed under clear-sky conditions and completed in a short period of time.

BRDF of the snow surface on sea ice was measured using a visible/near infrared (VNIR) spectroradiometer. The instrument has 512 channels in the VNIR wavelength region (333.65 – 1064.90 nm) with a spectral resolution of 3 nm, in which 16 of the 36 channels of MODIS are covered. The spectral bidirectional reflectance was measured using a fore-optical sensor with a field-of-view (FOV) of 3°. The spectral noise values of the instrument (dark currents) were collected before the white reference measurement. Radiance reflected from the white reference was collected at the viewing nadir. Dark current was collected once again before the subsequent collection of radiance reflected by the snow cover on sea ice at all the viewing angles and subtracted from the radiance data. The resultant radiance at each viewing angle was divided by the radiance data of the white reference at the viewing nadir to obtain the BRDF of snow cover on sea ice. At a fixed viewing zenith angle (VZA) (initially 0°), measurements were carried out in azimuth direction at 10° intervals from the forward direction of the principal plane (azimuth angle ϕ=0°) to the backward direction of the principal plane (azimuth angle ϕ=180°). The VZA was then increased by 10° and the measurements repeated up to a VZA of 80°. The measurements in a full BRDF set thus form a half-hemisphere that contains both forward and backward reflectance. The whole procedure took 15-20 minutes, which is short enough for the change of illumination condition due to change of solar zenith angle to be considered negligible. As the shadow of the sensor itself affected the results around the backward azimuth (ϕ=180°) when the VZA was small, only results up to the 170° azimuth in the half plane are shown.

2.2.6 Snow surface temperature

As the top 5 cm of the snow largely determines the albedo [Grenfell et al., 1994], the skin temperature on the snow surface was measured using a non-destructive method. An Exergen Model D-501-RS Infrared Microscanner [Li and others, 1999] was used to measure the skin temperature. To eliminate the effects of sky temperature and the surface emissivity on the temperature measurement, the head of the scanner is placed very near, but not touching, the surface to protect the sensor. This forms a blackbody cavity between the snow surface and the surface of the microscanner, so that the measured temperature is the physical temperature of the skin of the snow surface. The microscanner is precise (±0.1°C) and quick in acquiring skin temperature data. Skin temperature data discussed in this chapter are exclusively from the microscanner.

2.3 Characteristics of Snow Surface on Sea Ice

Pack ice in the Ross Sea is covered by snow all year around. Even in summer, new snow was observed to fall on top of the old snow, although it metamorphosed very quickly under solar irradiation. Icy layers, melt clusters and ice lenses were ubiquitous in the snow cover due to melt and refreeze cycles. During the 1999 summer cruise, 25 ice floes were extensively examined and more ice floes were checked visually from the ship's bridge during the hourly ice observations: no melt ponds were observed. The conspicuous rotten edges of almost all of the ice floes indicate that the decay of the sea ice occurred at the bottom and lateral edges of the ice floe. Temporary wetting of the top snow layer was due to short periods of surface snow melting by solar heat, or by sea water splashed up onto the ice floe surface.

The snow surface temperature varied between -0.3°C and -3.8°C, which is consistent with our observation that no slush or melt ponds were observed on the snow surface of any ice floe. The difference in surface temperature on a single ice floe was as much as 1.9°C on station 11 (January 15), and as little as 0.5°C on station 7 (January 10). Snow surface temperature seemed to be primarily affected by the air temperature [Li and others, 1999] with no observation of correlation between snow depth and snow surface temperature.

2.4 Measured Results of All-wave Albedo and BRDF of Snow Surface on the Sea Ice

2.4.1 Spatial Variation of All-wave Albedo

Daily-averaged all-wave albedo at all the stations is shown in Figure 2.2a. The average skin temperature of the snow surface on each floe is shown in Figure 2.2b. The three sections enclosed by dashed lines correspond to the three legs of the cruise (Figure 2.1). The stations at the ends of each leg (stations 1, 8; 9, 18; 19, 25) were at the marginal edges of the pack ice. Albedos at the margins of the pack ice were lower than those in the central pack ice.

The daily-averaged albedos, the Julian dates and the positions at which they were acquired together with the variation range are summarized in Table 2.1. Because clouds deplete the longer wavelengths, the spectral distribution of downwelling irradiance is altered such that snow albedo is generally greater under overcast than under clear-sky. Variations of cloud conditions (types, thickness, and extent, etc.) can also affect overcast albedos [Grenfell and Maykut, 1977]. From the albedo values shown in Table 2.1, we can see that daily-averaged albedo varied from 0.700-0.857, depending on the snow surface conditions and cloud conditions. The highest value was obtained on station 22 (January 29) on an ice floe where there was a surface layer of about 0.6cm of recent snow, with an average grain diameter about 0.2mm. The lowest value was obtained at station 1 (January 4) on a relatively small ice floe (about 20 m in diameter) at the northern edge of the pack ice. The range in albedo for the pack ice is similar to that obtained from the first-year sea ice in the East Antarctica (0.65-0.85) [Allison et al., 1993].

The relationships between latitude and albedo and between latitude and snow surface temperature of ice floes in the central pack under cloudy skies are shown in Figure 2.3. Data from the most southerly and northerly ice stations (stations 1, 8; 9, 18; 19, 25) along each of the three legs, and the data taken under clear-sky conditions (station 10) are excluded. Measurements on station 5 were made under both clear and cloudy periods. The albedo shown in Figure 2.3 for this ice floe is the averaged value over the cloudy period. It can be seen that the albedo increases with latitude (Figure 2.3a), while snow surface temperature decreases with latitude (Figure 2.3b). The higher albedo at the more southerly stations is associated with the lower snow surface temperatures and the resulting lower liquid-water content, together with smaller effective grain-size in the upper portion of the snow (see chapter 6).

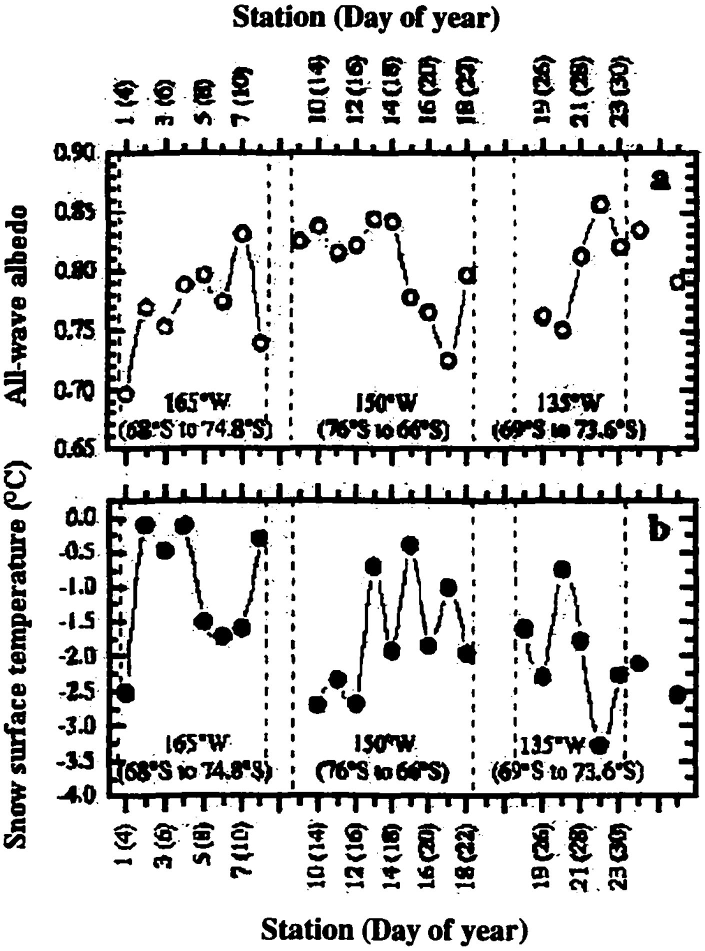

Figure 2.2 Daily averaged all-wave albedo (a) and area-averaged snow surface temperature (b) versus time and latitude.

2.4.2 Temporal Change of All-wave Albedo

A time series of irradiance and all-wave albedo measured at station 5 (January 7-8, 1999) is shown in Figure 2.4. From midmorning local solar time (~1000 h) until almost noon, the sky was clear. The measured irradiance increased smoothly with increasing solar elevation, but the albedo did not change significantly. At 23:24 GMT (1124 h, local time), it became cloudy, with the clouds moving rapidly over the ice floe while the snow

Table 2.1 All-wave albedo of snow on sea ice in the eastern Ross Sea, January-February, 1999 (data in parentheses are for clear sky)

Station No. (Day No.)	*Latitude, Longitude*	*Average*	*Minimum*	*Maximum*
	First leg along ~165°W			
1(4)	68°S, 165°W	0.700	0.692	0.721
2(5)	69°S, 165°°W	0.769	0.741	0.808
3(6)	70°S, 165°W	0.754	0.729	0.774
4(7)	71°S, 165°W	0.788	0.752	0.825
5(8)	72°S, 165.1°W	0.799(0.788)	0.784(0.788)	0.820(0.789)
6(9)	73°S, 165.4°W	0.774	0.747	0.803
7(10)	73.7°S, 165.5°W	0.832	0.819	0.855
8(11)	74.8°S, 164.4°W	0.740	0.706	0.781
	Second leg along ~150°W			
9(13)	76°S, 151.3°W	(0.827)	(0.814)	(0.830)
10(14)	74°S, 150°W	0.838	0.760	0.886
11(15)	72.8°S, 150.4°W	0.816	0.785	0.855
12(16)	72°S, 150°W	0.822	0.795	0.861
13(17)	71°S, 150°W	0.845	0.829	0.863
14(18)	70°S, 150°W	0.842	0.785	0.871
15(19)	69°S, 150°W	0.778	0.765	0.799
16(20)	68°S, 150°W	0.766	0.725	0.802
17(21)	67°S, 150°W	0.731	0.681	0.777
18(22)	66°S, 149.9°W	0.797	0.774	0.837
	Third leg along ~135°W			
19(26)	70°S, 135°W	0.763	0.747	0.779
20(27)	71°S, 135.1°W	0.751	0.735	0.787
21(28)	72°S, 135°W	0.813	0.793	0.830
22(29)	73°S, 135°W	0.857	0.846	0.871
23(30)	73.6°S, 134.9°W	0.821	0.772	0.844
24(31)	74°S, 140°W	0.847	0.812	0.867
25(33)	75°S, 145.3°W	0.791	0.775	0.820

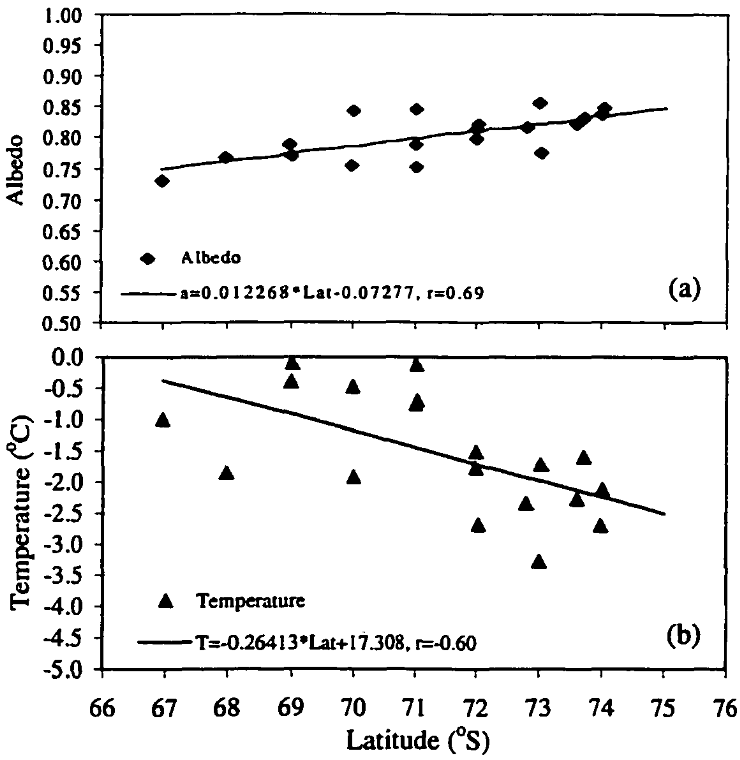

Figure 2.3 Pack ice albedo and surface temperature values under cloudy sky conditions. The linear regression shows the relationship between (a) average albedo and latitude, and (b) average snow surface temperature and latitude. Stations at the pack ice edge and on landfast ice are excluded from this analysis.

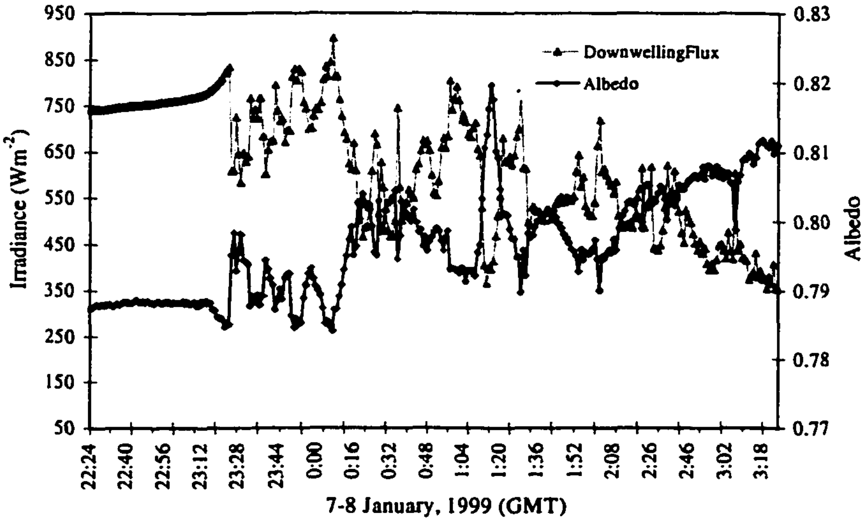

Figure 2.4 Time series of the downwelling irradiance and all-wave albedo measured on January 7-8, 1999 during clear and cloudy sky conditions. The station was at 72°00.106' S, 165°03.242' W. The snow depth was about 39cm.

surface conditions (topography, temperature, etc.) remained almost the same. Clear and cloudy periods can be separated by the sudden change in downwelling irradiance (Figure 2.4). Even before the cloud covered the site completely, the cloud scattered more light into the site without blocking the direct solar beam. This caused the irradiance to increase slightly before it decreased abruptly as the cloud blocked direct sunlight to the site. When there were variations in the incident radiation due to changes in cloud conditions, the change of albedo was exactly opposite to that of downwelling irradiance, i.e. as downwelling irradiance increased, albedo decreased. The average irradiance and albedo during the period of most stable clear-sky conditions (22:30 to 23:10 GMT) and during the cloudy period are shown in Table 2.2, along with the irradiance fluctuation ranges during the two periods. From Table 2.2, we can see that the downwelling irradiance decreases by almost 23% due to the clouds. The increase of the average albedo due to clouds is about 1.4% relative to the average clear-sky albedo. The largest increase in albedo, which corresponded to the thickest cloud cover during the data acquisition, is 4.0%. The increase of albedo due to clouds is a strong function of the cloud type, coverage and thickness. Visible-enrichment of the radiation incident on the snow surface due to the cloud cover, and thus the increase of all-wave albedo, depends on the types and thickness of the clouds [Grenfell and Maykut, 1977]. Although increases of albedo due to clouds are smaller than those observed by Liljequist (1956) at Maudheim (5-10%), Hanson (1960) at the South Pole (5-7%), and Weller (1968) at Mawson (11%), they are reasonable, considering the broad temporal and spatial variability of the cloud coverage and thickness. Cloud also affects spectral albedo through conversion of direct radiation into diffuse radiation and thus altering the effective incident zenith angle of solar radiation [Wiscombe and Warren, 1980]. The purely diffuse solar radiation has an effective incident zenith angle of about 50°. Based on the dependence of spectral albedo on solar zenith angle: the larger the zenith angle, the higher the albedo, and the effect of cloud on spectral albedo is negligible if the solar zenith angle is about 50°; cloud increases the spectral albedo if the solar zenith angle is < 50°; cloud will decrease the spectral albedo if the solar zenith angle is > 50°.

Table 2.2 Downwelling irradiance and albedo for clear and cloudy periods, 7-8 Jan. 1999

Sky Conditions	Irradiance (Wm^{-2})		Albedo	
	Average	Range	Average	Range
Clear	753.59	741.22~769.78	0.788	0.7877~0.7886
Cloudy	580.29	352.71~896.06	0.799	0.7841~0.8197

2.4.3 Bidirectional Reflectance Distribution Function (BRDF)

For the 1999 cruise, BRDF was measured on 30 daily stations (ice floes), but only two sets of BRDF were collected under clear-sky conditions. For comparison, one BRDF data set from the 2000 cruise, which covered the Ross, Amundsen and Bellingshausen seas (see chapter 4) is included in this section. Here we present and compare two typical sets of clear-sky BRDF. One was collected on January 8, 1999 at 72°00.106' S, 165°03.242' W on a first year ice floe (ice floe 1). The other was collected on February 19, 2000 at 76°04.994'S, 152°34.049'W on a ridged multiyear ice floe (ice floe 2). For ice floe 1, the snow surface was very flat and the average snow grain size at the top was about 0.4 mm. No ice crystal clusters were observed at the snow surface. The snow surface temperature was -1.5 °C and the snow depth at the measuring site about 39cm. At ice floe 2, there was a refrozen icy layer on the snow surface. Ice crystal clusters were visible on the surface. Areas between ice clusters were filled with wind-packed white snow. The snow surface temperature at this site was -5°C and the snow depth at the measuring site about 67cm. Compared with ice floe 1, the surface of ice floe 2 was much rougher and more heterogeneous.

From a complete set of BRDF measurements, the BRDF for the 16 MODIS channels was retrieved from the data set, using interpolation when necessary. To see the BRDF patterns of these channels, 4 channels are used as representatives. They are: 443nm (band 9) representing the blue channel, 551nm (band 11) representing the green channel, 645nm (band 1) representing the red channel, and 905nm (band 17) representing the near-infrared for which the atmospheric Raleigh scattering would be negligible.

The BRDF patterns on ice floe 1 obtained on January 8, 1999 and ice floe 2 on February 19, 2000 are shown in Figure 2.5 and Figure 2.6 respectively. Azimuthal

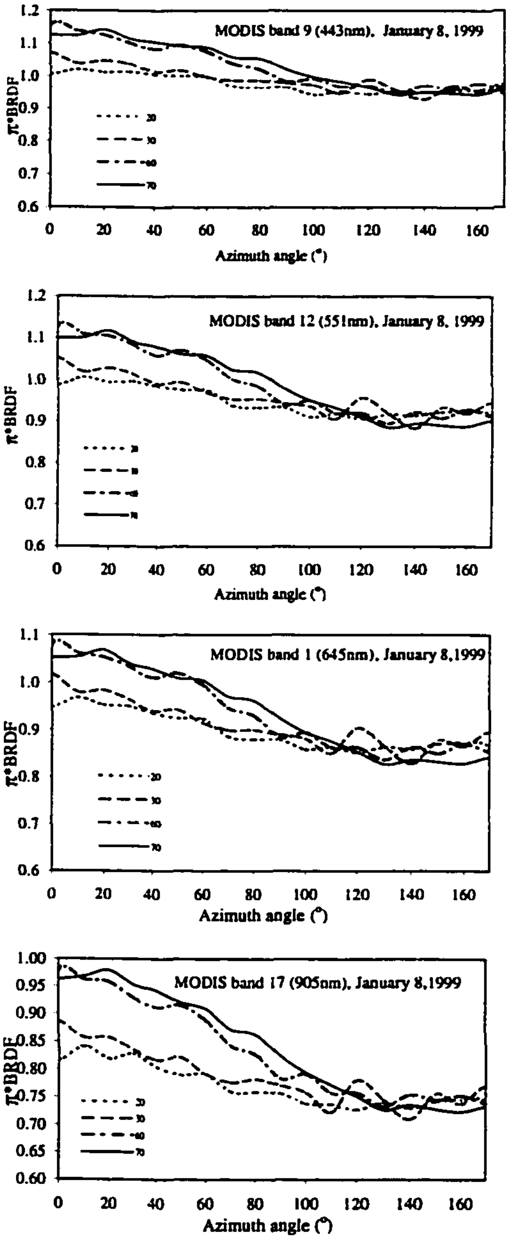

Figure 2.5 BRDF patterns obtained on January 8, 1999 at 72°00.106' S, 165°03.242' W on a first-year pack ice floe. BRDF patterns for MODIS band 9 (blue), band 12 (green), band 1(red), and band 17 (near-infrared) are Shown.

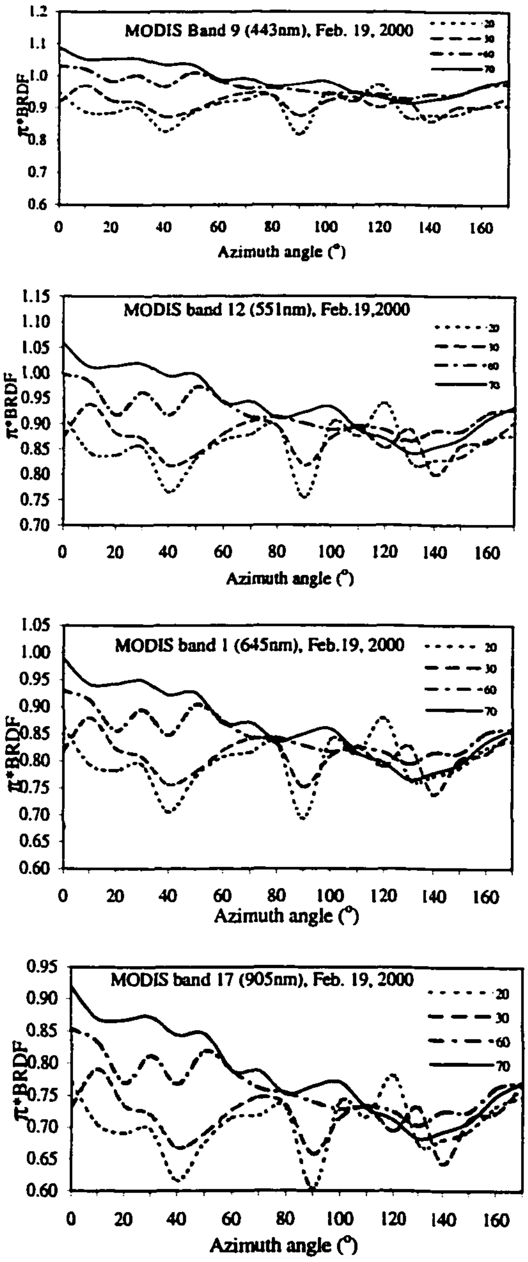

Figure 2.6 BRDF patterns obtained on February 19, 2000 at 76°04.994'S, 152°34.049'W on a multiyear ice floe. BRDF patterns for MODIS band 9 (blue), band 12 (green), band 1(red), and band 17 (near-infrared) are Shown.

distributions of the bidirectional reflectance are given for two groups of VZAs: small angle group (20°and 30°) and large angle group (60° and 70°). Such a selection allows investigation of the difference of the BRDF patterns between small VZAs and large VZAs.

2.5 Evaluation of Measured Albedo and Spectral Albedo

2.5.1 Measured albedo compared to calculated all-wave albedo

To access the difference between the measurements of solar radiation for the albedo calculation with publicly accepted theory, we compared the measured values with model calculations. The clear-sky measurements taken at ice station 9 (January 12-13) were used for this analysis. This station was the southernmost station of the cruise and also the only station on landfast ice. At the beginning of the station occupation, the air temperature was –5.4°C and the snow surface temperature was –4.0°C. The downwelling irradiance and all-wave albedo are shown in Figure 2.7. The downwelling irradiance decreased continuously until the end of the measurements as the solar elevation angle decreased after local noon. However, the albedo did not change significantly. During the last third of the measurement period, the albedo decreased slightly.

Because the atmosphere was clear, we use a simple solar-zenith-angle model to calculate irradiance values for this time period to test the correctness of the irradiance measurements. Supposing at starting time t_0 the theoretical value of irradiance $F'{\downarrow}(t_0)$ is exactly the same as the measured value $F{\downarrow}(t_0)$, then for any time t later, the theoretical irradiance value is

$$\begin{aligned} F'_{\downarrow}(t) &= \frac{\cos[\theta(t)]}{\cos[\theta(t_0)]} F'_{\downarrow}(t_0) \exp\{-\tau[\sec^{-1}\theta(t) - \sec^{-1}\theta(t_0)]\} \\ &= \frac{\cos[\theta(t)]}{\cos[\theta(t_0)]} F_{\downarrow}(t_0) \exp\{-\tau[\sec^{-1}\theta(t) - \sec^{-1}\theta(t_0)]\} \end{aligned} \tag{2.6}$$

where $\theta(t)$ is the solar zenith angle at time t, and τ is the apparent bulk optical depth of the clear-sky atmosphere. The atmospheric turbidity or optical depth at 0.5μm shows very small values in the Antarctic. Values of about 0.02 were reported at coastal stations, 0.018 at Mauna Loa, Hawaii and 0.012 at the South Pole [Shaw, 1982; Matsubara, 1983]. These values are the lowest limits at the corresponding stations and much higher optical depths were reported following volcanic eruptions [Shiobara et al., 1986; Herber, 1996]. Based on the results of Wendler (1986) and Li et al. (1987), τ is chosen to be 0.08. The solar-zenith-angle model devised by Woolf (1968) was used to calculate the temporal variation of solar zenith angle. The results of the calculated surface solar irradiance with and without atmospheric attenuation are compared with actual measurements in Figure 2.7. For the case of no atmospheric attenuation (τ=0), the maximum deviation of the calculated from the measured surface solar irradiance is 1.43% and occurs at 1:27:40GMT on January 13 when the measured value is 548.2 Wm^{-2} and the calculated value is 556.0 Wm^{-2}. For the case τ=0.08, the maximum deviation of calculated from the measured surface solar irradiance is 0.26% and occurs at 1:22:00 GMT on January 13 when the measured value is 554.0 Wm^{-2} and the calculated value is 552.5 Wm^{-2}. This comparison demonstrates that even using a simple approximation there is good agreement between measured and calculated values, especially when the atmospheric attenuation is considered. Nevertheless, an effort is being made to model albedo using a more complicated radiative transfer method (cf. Chapter 6).

2.5.2 Comparison of All-wave Albedo and Spectral Albedo Measurements

Spectral albedo (α_λ) was measured simultaneously with all-wave albedo. In order to determine how well these two sets of measurements agree, all-wave albedos derived from spectral albedo data were compared to the measured values. First, the spectrally-averaged visible and near-infrared (333.65–1064.9 nm) albedo (α_{vnir}) is obtained from

$$\alpha_{vnir} = \frac{\int_{333.65}^{1064.9} \alpha_\lambda F_\lambda^{\downarrow} d\lambda}{\int_{333.65}^{1064.9} F_\lambda^{\downarrow} d\lambda} = \frac{\sum_{i=1}^{512} \alpha_i F_i^{\downarrow} \Delta\lambda_i}{\sum_{i=1}^{512} F_i^{\downarrow} \Delta\lambda_i} \tag{2.7}$$

where α_i, $F_i^{\downarrow}$ and $\Delta\lambda_i$ are the albedo, downwelling irradiance and bandwidth of the ith channel of the 512 channels of the spectroradiometer, respectively. The all-wave albedo

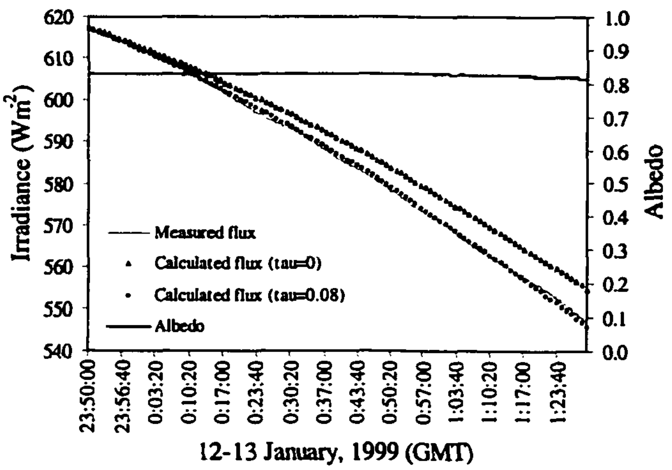

Figure 2.7 Comparison of time series of the downwelling irradiance and all-wave albedo measured on January 12-13, 1999 during clear-sky conditions and calculated irradiance with atmospheric attenuation (τ=0.08) and without atmospheric attenuation (τ=0). The station was at 76°01.287'S, 151° 16.012'W, with a multi-year snow cover of about 154cm thickness.

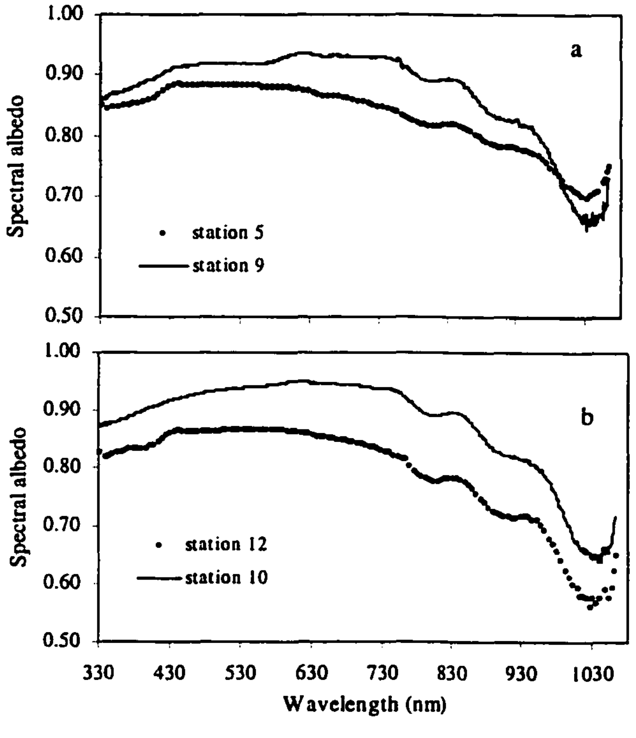

Figure 2.8 (a) Spectral albedos under clear-sky conditions obtained at station 5 (January 8, 1999) and station 9 (January 13, 1999). (b) Spectral albedos under cloudy conditions obtained at station 10 (January 14, 1999) and station 12 (January 16, 1999).

α_{int} can be estimated through integration over the measured VNIR spectral albedo with extrapolation to the unmeasured spectral regions for clear-sky conditions:

$$\alpha_{int} = \left\{ \int_{280}^{334} F_\lambda^{\downarrow} \alpha_{334} d\lambda + \int_{334}^{1060} F_\lambda^{\downarrow} \alpha_\lambda d\lambda + \int_{1060}^{4000} F_\lambda^{\downarrow} \frac{(\alpha_{1060} + 0.07)}{2} d\lambda \right\} / \int_{280}^{4000} F_\lambda^{\downarrow} d\lambda \qquad (2.8)$$

where $\alpha_\lambda = \alpha_{334}$ is assumed for $\lambda < 334$ nm and $\alpha_\lambda = (\alpha_{1060} + 0.07)/2$ is assumed for $\lambda > 1060$ nm [Allison and others, 1993]. Other values of α_λ within $\lambda \in [334, 1060]$ are the measured spectral albedo and $\alpha_\lambda = 0.07$ is the albedo of open water. Equation (2.8) provides a method for deriving α_{int} from the measured spectral albedo when the proportions of the downwelling irradiance in the ultra-violet (UV), VNIR and short-wave infrared (SWIR) spectral regions are known. The proportions of downwelling clear-sky spectral irradiance in different wavelength regions is calculated using the radiative transfer algorithm of Stamnes et al. (1988).

To derive the all-wave albedo from the measured spectral albedo for cloudy conditions, the proportion of the downwelling SWIR irradiance was calculated by subtracting the UV and VNIR irradiance from the all-wave irradiance. Compared with near-infrared radiation, the effects of clouds on the ultraviolet radiation are negligible, so the spectral irradiance $F_\lambda^{\downarrow}$ in the UV wavelength region between 280-334 nm was taken to be the corresponding clear-sky downwelling spectral irradiance calculated using the radiative transfer algorithm [Stamnes and others, 1988]. Within the VNIR wavelength region, we used the measurements from the ASD spectroradiometer. The all-wave downwelling solar flux was measured by the upward-looking pyranometer (PSP). To account for the difference in the sensitivities between the PSP pyranometer and the ASD spectroradiometer, we define instrument-dependent parameters κ_1 and κ_2 to relate the measured downwelling solar irradiance F^{PSP} and spectral irradiance $F_{\lambda,ASD}^{\downarrow}$ with the theoretical spectral irradiance $F_\lambda^{\downarrow}$ derived from the radiative transfer model for clear-sky conditions.

$$\kappa_1 = \frac{F^{PSP}}{\int_{280}^{4000} F_\lambda^{\downarrow} d\lambda}, \quad \kappa_2 = \frac{\int_{334}^{1060} F_{\lambda,ASD}^{\downarrow} d\lambda}{\int_{334}^{1060} F_\lambda^{\downarrow} d\lambda} \tag{2.9}$$

For the ideal case, $\kappa_1 = \kappa_2 = 1$. For the pyranometer and the spectroradiometer, we use $\kappa_1 = 1.128$ and $\kappa_2 = 0.883$, as obtained using a clear-sky case at station 5 (January 8, 1999). Then the equivalent of Equation (2.8) takes the form,

$$\begin{aligned}\alpha_{int} &= \kappa_1 \alpha_{334} \int_{280}^{334} \frac{F_\lambda^{\downarrow}}{F^{PSP}} d\lambda + \frac{\kappa_1}{\kappa_2} \int_{334}^{1060} \frac{F_{\lambda,ASD}^{\downarrow} \alpha_\lambda}{F^{PSP}} d\lambda \\ &+ \frac{(\alpha_{1060} + 0.07)}{2} \left(1 - \kappa_1 \int_{280}^{334} \frac{F_\lambda^{\downarrow}}{F^{PSP}} d\lambda - \frac{\kappa_1}{\kappa_2} \int_{334}^{1060} \frac{F_{\lambda,ASD}^{\downarrow}}{F^{PSP}} d\lambda \right)\end{aligned} \tag{2.10}$$

Spectral albedo obtained under clear-sky conditions at station 5 (January 8, 1999) on pack ice and at station 9 (January 13, 1999) on landfast ice are shown in Figure 2.8a. Spectral albedos obtained under cloudy sky conditions at station 10 (January 14, 1999) on central pack ice and at station 12 (January 16, 1999) are shown in Figure 2.8b. The snow characteristics, solar zenith angle and albedo values are summarized in Table 2.3.

Table 2.3 Snow parameters and retrieved albedos for selected sites where spectral albedo was measured in 1999.

Parameters	Clear sky		Cloudy sky	
	Station 5	Station 9	Station 10	Station 12
Surface temperature (°C)	-1.5	-4.0	-2.3	-1.4
Snow depth (cm)	39	154	34	22
Snow grain size (mm)	0.4	0.1	0.3-1.0	0.2-1.0
Snow density (kgm^{-3})	320	--	330	390
Solar zenith angle (°)	50	55	51	50
α_{vnir}	0.847	0.892	0.900	0.820
α_{int}	0.773	0.797	0.838	0.786
α	0.788	0.829	0.834	0.818
$\Delta_1 = \alpha_{vnir} - \alpha$	0.059	0.063	0.066	0.002
$\Delta_2 = \alpha_{int} - \alpha$	-0.015	-0.032	0.004	-0.032
$\Delta_3 = \alpha_{vnir} - \alpha_{int}$	0.074	0.095	0.062	0.034

At station 5, the snow surface was made up of melt clusters ranging from 0.3-0.6mm, with an average grain size (D) of 0.4mm and density $\rho = 320$ kg m^{-3} for the surface layer

(6cm). At station 9, the snow surface was wind packed and icy and made up of 0.1mm grains. No snow density data are available at this station. Although the sky was clear when the spectral albedo was measured at station 5 and 9, it was much clearer at station 9 than at station 5 (see Figure 2.4 and Figure 2.7). There was a very thin but stable layer of cirrus clouds at station 5 during the clear period in the day. From Figure 2.8a we can see that the spectral albedo is smaller at station 5 than at station 9 until the wavelength exceeds 994nm. This was mainly due to the smaller grain size (D=0.1 mm) at station 9 [Dozier, 1989; Wiscombe and Warren, 1980].

The surface of the ice floe at station 10 was rough. Snow depth across the floe was horizontally very inhomogeneous, ranging from 3cm to 60cm. The grain size of the top 1cm layer was D=0.3mm, with coarse-grained snow (D=1mm) directly below. Average density for the surface layer (6cm) was ρ = 330 kgm^{-3}. The snow surface at station 12 was flatter than at station 10. On the very top of the snow cover was a 0.5 cm thick layer of recent snow with D = 0.2mm, under which there was a cemented icy layer of 3cm with D = 0.6mm. Under the icy layer were clusters of rounded particles of grain size D = 1mm. The average density of the upper 6 cm was ρ = 390 kg m^{-3}. The larger spectral albedo at station 10 (Figure 2.8b) is mainly due to the finer grain size (D=0.2 mm) of the top layer. The relationship of albedo with snow grain-size is explored in more detail in chapters 3 and 6.

Derived all-wave albedo values (α_{int}) using Equations (5) and (7) for stations 5, 9, 10, 12 are listed in Table 2.3. The differences between α_{vnir} and α_{int} are smaller (3.4-6.2%) for cloudy than under clear-sky conditions (7.4-9.5%) because the SWIR proportion was smaller under cloudy conditions. For example, at station 10, the SWIR accounts for only 7.6% of the total downwelling irradiance, but at station 5 where the sky was clear, the SWIR accounts for 19.1% of the total downwelling radiation.

The difference between the measured all-wave albedo α and those derived from measured VNIR spectral albedo is within ±3.2%. Because the all-wave albedo and the spectral albedo were measured on the same ice floes, yet at separate locations, these results seem reasonable given the uncertainties associated with spectral extrapolation (cf. section 2.5.2).

2.6 Discussion and Conclusions

The current investigation has focused on regional all-wave and spectral albedo measurements of the snow cover on the austral summer sea ice in the Ross Sea. No obvious correlation between snow thickness and skin temperature of the snow surface emerged from our data. The snow surface temperature was primarily correlated with air temperature [Li and others, 1999].

Compared with small viewing zenith angles (VZAs), the azimuthal distribution of bidirectional reflectance of large VZAs shows much smoother behavior. Fluctuation of the reflectance-azimuth curves for smaller VZAs is due to the small footprint of the sensor that was mounted on a tripod with a height of 0.8m. This results in higher resolution and more accurate surface feature identification at smaller VZAs. For any VZA, the reflectance-azimuth curve reveals a minimum at some azimuth angle between 100° and 140°. Largest reflectance occurs around the principal plane for moderate to large VZAs. This is primarily attributed to the strong forward scattering processes of the snow grains (see section 5.4.2) in the snow layer and secondly to surface reflection of the refrozen surface icy layer. The up-curled tails of the reflectance-azimuth curves are presumably related to reflection from back facing part of undulating snow surface.

Sensitivity of bidirectional reflectance to the VZA is strongest around the principal plane ($\phi=0$). Consistent with surface roughness and heterogeneity observations, the BRDF patterns of the snow cover, which had an icy layer and refrozen clusters on the surface on a ridged ice floe (February 19, 2000), show much more anisotropy than the ice floe with a flat and more homogeneous snow cover (January 8, 1999).

The measured all-wave downwelling irradiance agreed well with a simple approximation using solar zenith angle and bulk optical thickness for clear-sky conditions. Measured irradiance has not been compared with calculations for overcast conditions, due to lack of quantitative cloud-cover data. Albedo varied greatly

(0.70-0.86) between different places in the Ross Sea. This large variation in albedo has also been observed in the first-year pack ice in East Antarctica (0.65-0.85) [Allison et al., 1993]. Clear- and cloudy-sky albedos measured at the same site indicate that the average increase due to clouds is 1.4%, with the largest increase being 4.0%.

All-wave albedos were observed to be lower at the margin of the pack ice than in the central pack ice. This may due to larger grain-size at the margin than in the central pack ice (cf. chapters 3 and 6). Over the central pack ice, it was observed that the higher the latitude, the lower the snow surface temperature and the higher the all-wave albedo.

There was no major difference between spectral albedos under clear-sky and cloudy conditions. Both are mainly controlled by the snow grain-size, especially the snow grain-size of the top snow layer (cf. chapter 6). All-wave albedo calculated from direct measurements of all-wave irradiance agreed well with those derived from integration of visible and near-infrared spectral albedo which included extrapolation to UV and SWIR regions for both clear- and cloudy-sky conditions. This indicates that our all-wave and spectral albedo measurements are reliable.

Acknowledgments

For the research work involved in this chapter, we are very grateful for the logistical support furnished by the National Science Foundation and the Antarctic Support Associates personnel aboard the *R/V Nathaniel B. Palmer*. We also sincerely appreciate the support of Dr. Martin O. Jeffries, Chief Scientist of the NBP99-1 cruise, who always gave us the opportunity to be the first to occupy the ice floe before other activities which might have disturbed the surface of snow and sea ice. The research activities involved in this chapter were supported by the National Aeronautics and Space Administration (NASA) under grant NAG5-6338 and by National Science Foundation under grant OPP9614844.

CHAPTER 3

Spatial Variation of, and Correlations among, Snow Surface Albedo and Physical Parameters of Summer Snow Cover on Sea Ice in the Ross Sea, Antarctica

ABSTRACT. Surface albedo of austral summer snow cover on sea ice was measured in the Ross Sea during a cruise in January-February, 1999. Concurrent measurements of physical parameters of the snow cover such as composite snow grain-size, single snow grain-size, snow density, snow surface temperature, and snow stratification were carried out. Based on these *in situ* measurements, three statistically-averaged grain-size models (equal grain number model, size distribution integrated average model and effective size model) are used for the correlation analyses between the albedo and the snow grain-size for two categories (composite grain-size and single grain-size). Spatial variation analyses of the snow albedo and the snow physical parameters show that on the pack ice in the Ross Sea there are notable latitudinal variations in the snow surface albedo and the snow physical parameters. As the ship moved southward through the pack ice: the snow surface temperature decreased; the albedo increased; the snow density decreased; the snow composite grain-size decreased; and the number density of composite grains increased. Correlations between the albedo and the snow physical parameters show that the summer snow albedo is more sensitive to the snow cluster (or composite) grain-size than the single snow grain-size for the top 9 cm of the snow cover: the larger the snow composite grain-size, the lower the albedo. Multivariate linear regression analyses show that for a homogeneous snow cover of 9 cm thickness, the top layer (0-3 cm) contributes approximately 86.9% to the albedo while the second layer (3-6 cm) accounts about 10.7%, with the remainder (2.4%) contributed by the third layer (6-9 cm). Correlation analyses

between the albedo and the composite grain number density show that for the top 9 cm of the snow cover, the albedo is strongly correlated with the composite grain number density: the larger the number density of composite grains of the snow surface layer, the higher the albedo. The same analyses for the single grain-size and single grain number density show that there is no significant correlation between the albedo and the single grain-size or between the albedo and the single grain number density. From the correlation analyses between albedo, the snow surface temperature and the composite grain-size, it is found that the lower the surface temperature and the smaller the surface composite grain-size, the higher the albedo.

3.1 Introduction

Reflectivity of a dispersive medium is determined primarily by two processes: absorption and scattering. Absorption is governed by chemical composition that determines the complex refractive index or the dielectric permittivity tensor of scatterers and the depth of the light-absorbing layer. From the point of view of scattering theory, particles (scatterers) in a light-scattering layer are characterized by their number density, shape, orientation, size, structure (uniform or non-uniform) and chemical composition [Bohren and Huffman, 1983]. For snow cover, if the particles are optically represented as spheres [Grenfell and Warren, 1999], the spectral reflectivity will be determined mainly by the snow grain-size, number density, thickness (within the light-absorbing/scattering layer), impurities, and stratigraphy (cf. chapter 6). Spectrally integrated reflective properties of snow, such as all-wave albedo, depend significantly on the spectral characteristics of the incident radiation and snow physical properties. Parameters affecting the incident radiation include solar zenith angle [Dirmhirn and Eaton, 1975; Warren, 1982], cloud type, thickness and distribution [Male and Granger, 1981; Warren, 1982], and atmospheric parameters such as precipitable water, aerosol, and ozone content. For a specified incoming radiation, all-wave albedo of snow depends on snow grain-size [Wiscombe and Warren, 1980; Grenfell et al., 1994], impurities [Warren and

Wiscombe, 1980; Conway et al., 1996], wetness, density and composition, snowpack thickness, and surface roughness [Dirmhirn and Eaton, 1975; Warren et al., 1998; Leroux and Fily, 1998].

Wetness of snow is believed to affect the grain-size by accelerating the metamorphism and ice-ice bond between single snow grains [Colbeck, 1986; Colbeck et al., 1990]. Liquid water in snow replaces air between snow grains and thus increases the effective grain-size due to similarity of refractive index of liquid water with ice in the solar spectrum [Wiscombe and Warren, 1980]. For a specific size distribution of a snow cover, the number density distribution is determined by the snow density. When the evolution history of grain-size distribution is given, the number density distribution can be determined.

Snow on sea ice is typically characterized in terms of its thickness and spatial distribution, texture, stratigraphy, density, shape and size of snow grains, wetness, salinity, and thermal conductivity [Massom, et al., 2001]. For snow cover on sea ice in summer, frequent wetting or dampening of the snow by melting, flooding and incorporation of brine from the snow-ice interface often changes the snow grain-size, snow stratigraphy and density. Wetting/dampening with a low water content resulting from melting, flooding, and percolation, which is often the case of snow cover on Antarctic sea ice, holds the individual snow crystals together by ice-ice bonds to form clusters of rounded crystals [Colbeck, 1982; 1986]. Subsequent refreezing results in coarse, rounded polycrystalline snow grains. Due to frequent melt-refreezing cycles, summer snow cover on Antarctic sea ice is characterized by ubiquitous icy clusters, ice lenses, ice layers, and percolation columns, with grain-size on the order of 1cm [Haas et al., 2001; Morris and Jeffries, 2001]. Centimeter-scale icy nodules in snow were also observed in winter after surface melting due to warm storms and subsequent refreezing [Massom et al., 1997, 1998].

Although many studies have been carried out on the interaction of solar radiation with snow, the transmission and absorption of solar radiation is not fully understood [Davis et al., 1993]. To better understand the relationship between the snow surface albedo and the snow physical parameters, especially the possible impact of the formation of composite grains on optical remote sensing signatures, correlation between the snow surface albedo and snow physical parameters is the primary purpose in this chapter. In section 3.2, the cruise to the Ross Sea and measurements of albedo and snow physical parameters are described. In section 3.3, statistical methods to analyze the spatial variation of, and correlations among albedo and snow physical parameters are elucidated. Section 3.4 describes the spatial variation of albedo and snow physical parameters. Correlations between albedo and snow physical parameters are shown in section 3.5. Multiple correlation and regression analyses of albedo with composite grain-size and composite grain number density are given in section 3.6. Analyses and discussion are given in section 3.7. Conclusions are drawn in section 3.8.

3.2 Field Programs

Albedo measurements and snow pit work were made during a summer cruise to the Ross Sea, Antarctica, in January and February, 1999. The cruise track and the ice stations are shown in Figure 3.1. The albedo was measured at each ice station along with snow physical parameters that included the snow density, snow composite grain-size, snow single grain-size, and snow surface temperature. Altogether, 25 sets of albedo data were collected. All-wave albedo was measured with two EPPLEY broad-band precision spectral pyranometers. Time series of downwelling and upwelling solar irradiances were received by the upward-looking and downward-looking pyranometers, respectively. Data were collected and stored using a CR10X datalogger, so that at any moment, the albedo was obtained as the ratio of upwelling irradiance to down-welling irradiance. The detailed description of the instrumentation and intra-instrument comparisons were given elsewhere [Zhou, et al., 2001]. The albedo data for this study is the averaged value over the measuring time at each measurement site. The temperature on the snow surface (skin temperature) under the pyranometer at each albedo site was taken using an Exergen Model D-501-RS Infrared Microscanner [Li, et al., 1999].

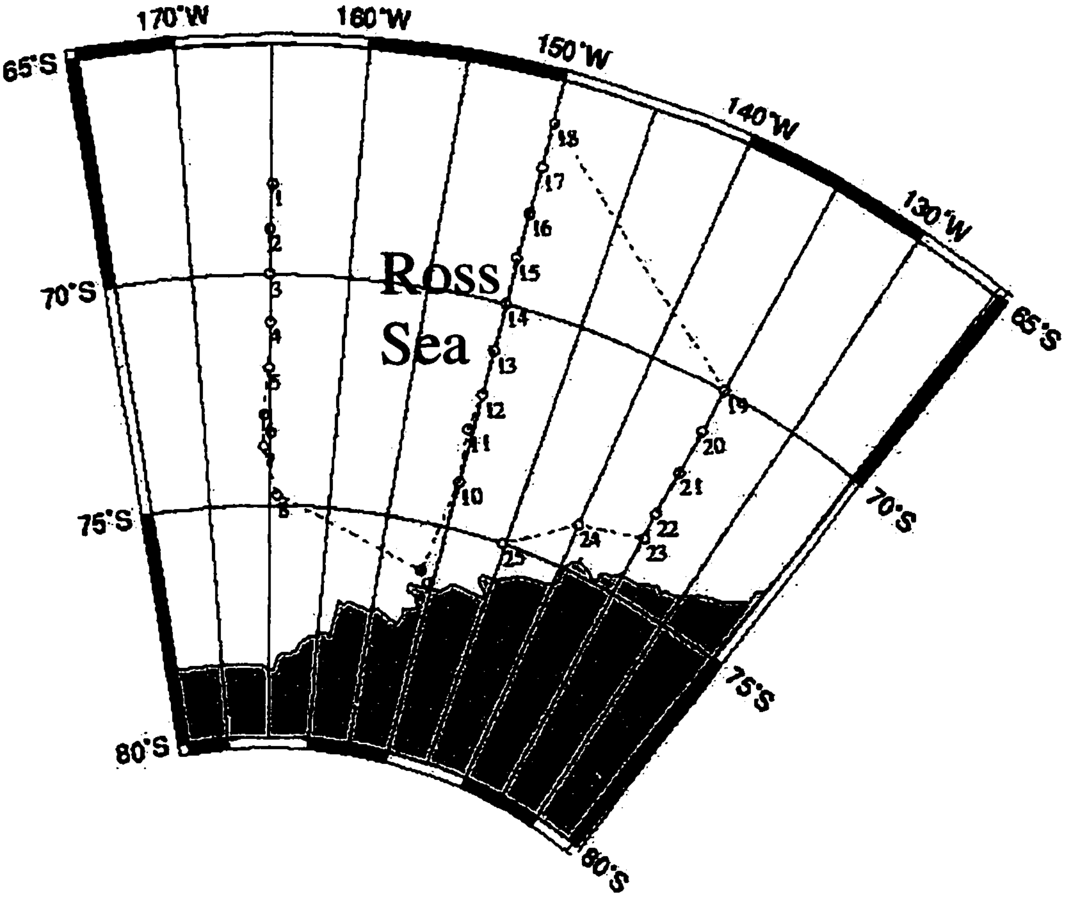

Figure 3.1 The route of R/V Nathaniel B. Palmer during a summer cruise in the Ross Sea, Antarctica (January and February, 1999). The number indicates the ice station number where albedo and snow pit work were carried out.

A snow pit was dug in the vicinity (5-10 m) of the albedo measurement site at each ice station. Snow samples of 100 cm^3 each were taken at 3 cm intervals from the snow surface to the underlying sea ice surface. Both composite snow grain and single snow grain-sizes (long dimension and short dimension) were measured using a petrographic microscope. If the particle is a sphere, the long dimension equals the short dimension. The mass of each snow sample was measured and the density was calculated. Individual snow grains in the snow sample were described in terms of shape and general appearance using standardized terms, i.e., facets, striates, melt clusters, chains of grains, etc., and the relative proportion (percentage) of each particle type with mean radius, $<r>$, was determined [Morris and Jeffries, 2001; Colbeck et al., 1990]. The grain-size distribution was measured by sieving [Sturm and Benson, 1997; Sturm, et al., 1998]. As almost all of the snow samples had undergone cycles of thawing, flooding and freezing, from which single-grain clusters and melt-freeze grains formed [Colbeck, 1979; 1982], the particles of the field samples could be divided into two categories: the overall centimeter-order size of the larger, composite grains such as meltclusters, and the millimeter-order size of the grains that made up the meltclusters [Morris and Jeffries, 2001]. In the following discussion, the snow composite grains refer to the former and the snow single grains refer to the latter.

3.3 Analysis Methods

Snow physical parameters (composite grain-size, single grain-size, density, and the relative proportion of each particle type with mean radius $<r>$) were measured at intervals of 3 cm. The vertical profile of these parameters is thus described in terms of layers, each layer being 3 cm thick. Snow particles of each type and size are taken as spheres with radius equal to one fourth of the sum of lengths of the long and short axes of the snow particle type within each layer, and are assumed to be uniformly distributed in the layer. In a light-scattering layer snow particles are characterized by means of their number density and grain-size. For the following analysis, three models of effective average grain-size are used.

The first model is the equal-number-density average grain-size, i.e., weight and snow grain number in unit volume are kept constant in calculating the average grain-size. For the jth layer (j=1 is the top 3 cm layer), the equal-number-density average composite grain-size or single grain-size (EN model) is

$$\left\langle r_j^{EN} \right\rangle = \frac{1}{\sqrt[3]{\sum_i \frac{p_{j,i}}{r_{j,i}^3}}} \tag{3.1a}$$

where $r_{j,i}$ is defined as one fourth of the sum of lengths of the long and short axes of the ith snow particle type within the jth layer, and $p_{j,i}$ is the relative weight percentage of the ith snow particle type to the whole sample of each category (composite grain or single grain) in the jth layer.

The second model is the size-distribution-integrated average grain-size. The distribution-integrated average composite grain-size or single grain-size (DI model) is

$$\left\langle r_j^{DI} \right\rangle = \frac{\int r f_j(r) dr}{\int f_j(r) dr} = \sum_i \left(\frac{p_{j,i}}{r_{j,i}^2} \right) \Bigg/ \sum_i \left(\frac{p_{j,i}}{r_{j,i}^3} \right) \tag{3.1b}$$

where $f_j(r)$ is the snow particle size distribution function in the jth layer.

The third model is the effective radius (EFF model), which is proportional to the volume/surface area ratio.

$$\left\langle r_j^{EFF} \right\rangle = \frac{\int r^3 f_j(r) dr}{\int r^2 f_j(r) dr} = 1 \Bigg/ \left(\sum_i \frac{p_{j,i}}{r_{j,i}} \right) \tag{3.1c}$$

Hansen and Travis (1974) found that dispersive media with different particle size distributions, but the same values of effective radius, have approximately the same light scattering and absorption characteristics. In this chapter, we will look into the correlation between albedo and each of these statistically averaged radii.

For the top n layers (n=1 is the top 3 cm snow layer), the equal-number-density average grain-size for each category (composite or single grain-size) is

$$\bar{r}_n^{EN} = \left(\frac{\sum_{j=1}^{n} \rho_{j,snow}}{\sum_{j=1}^{n}\sum_{i} \frac{p_{j,i}\rho_{j,snow}}{r_{j,i}^{3}}} \right)^{1/3} \tag{3.2a}$$

The size-distribution-integrated average grain-size and the effective grain-size for the top n layers for either composite grains or single grains are given by Equation (3.2b) and (3.2c) respectively

$$\bar{r}_n^{DI} = \left(\sum_{j=1}^{n} \frac{\rho_{j,snow}}{\langle r_j^{DI}\rangle^{2}}\right) \Bigg/ \left(\sum_{j=1}^{n}\frac{\rho_{j,snow}}{\langle r_j^{DI}\rangle^{3}}\right) \tag{3.2b}$$

$$\bar{r}_n^{EFF} = \frac{\sum_{j}^{n} \rho_{j,snow}}{\sum_{j}^{n}\sum_{i} \frac{p_{j,i}\rho_{j,snow}}{r_{j,i}}} \tag{3.2c}$$

where $\rho_{j,snow}$ is the snow density of the jth layer.

When the average composite grain-size and single snow grain-size are obtained from Equations (3.1) and (3.2), the average number density of snow grains in the jth layer for each category can be calculated by

$$n_j^k(\langle r\rangle) = \frac{3\rho_{j,snow}}{4\pi\rho_{ice}\langle r_j^k\rangle^{3}} \tag{3.3a}$$

where ρ_{ice} is the density of pure ice, k= EN,DI or EFF, and $\langle r_j^k\rangle$ are given in Equation (3.1). The average number density of snow grain within the top n layers takes the form

$$n_n^k(\bar{r}) = \frac{3\sum_{j=1}^{n} \rho_{j,snow}}{4\pi n\rho_{ice}\left(\bar{r}_n^k\right)^{3}}, \tag{3.3b}$$

where $\langle \bar{r}_n^k\rangle$ (k = EN, DI or EFF) are given by Equation (3.2).

Regression analyses of the spatial variation of albedo and snow physical parameters, and correlation analyses between albedo and surface temperature, composite grain-size, single snow grain-size, density and snow grain number density are made against a null hypothesis that a relation does not exist between them. Correlation coefficients (R) are then calculated using Pearson's product-moment correlation statistical method [Pearson and Hartley, 1966]. A correlation coefficient R indexes two properties of a linear relationship of two data sets: the absolute value of R indicates the magnitude of the correlation of the linear relationship, and the sign of R indicates the direction of the relationship, whether the variables vary together (positively) or if they vary inversely (negative). An R value is tested against the null hypothesis that R =0. This yields a value that can be interpreted as the probability (p) that the obtained correlation coefficient could occur by sampling error. This process is implemented using a t test, where t is calculated using

$$t = \frac{|R|\sqrt{n-2}}{\sqrt{1-R^2}} \tag{3.4}$$

where n is the number of pairs of samples of the two variables whose relationship is to be tested [Williams, 1992]. Based on the t value calculated, p is obtained for a specific R by looking up the table of percentage points of the t distribution [Pearson and Hartley, 1966]. The significance of a correlation is defined here as

$$s = 100\%-100\cdot p\% \tag{3.5}$$

By the common practice of statistics, the level of probability for the rejection of the null hypothesis R = 0 is set to be p = 0.05. This means that a correlation is significant only when $s \geq 95\%$. In the following, this criterion is used to determine whether a correlation between two quantities under test is significant or not.

When two quantities are significantly related according to the correlation analyses, regression analyses are further attempted to predict the nature of the relationship between the two data sets. Linear, polynomial of order 3, logarithmic, power and exponential regression methods are all used to select the best fitting, based on the largest coefficient of determination (r^2). A value of r^2 between 0 and 1 represents a percentage ($100\cdot r^2$) of the variance of the dependent variable that can be explained by the model function (regression equation) of the predictor variables. For a pure linear relation, $r^2 = R^2$. A coefficient of determination value closer to 0 indicates that the regression does not match the original data set at all; a value of r^2 close to 1 indicates increasing accuracy in the trend line, thus increasing accuracy in prediction.

3.4 Spatial Variations of Albedo and Snow Physical Parameters

On the NBP 99-1 cruise to Ross sea, ice stations were occupied from the northern edge to the southern edge of the pack ice along three lines of longitude, 135°W, 150°W and 165°W at approximately one degree latitude intervals along each leg. Seven to ten ice stations were made along each meridian, but only 3 ice stations along each latitudinal parallel [see Figure 3.1]. This offers the opportunity to look into the spatial variation of albedo and snow physical parameters in the latitudinal direction. Twenty-five data sets of all-wave albedo were obtained, out of which 19 data sets of the central pack ice are used for the analysis. The ice stations at the ice edges generally had very low ice concentration, and thus are excluded from the analysis.

Snow grains of the top 3 cm at station 24 (Julian day 31) were all single snow grains without meltclusters. Thus there are 18 data sets of composite grain-size corresponding to the albedo data sets in the central pack ice. For stations where the snow was not thick enough for multi-layer analysis, the data sets will be reduced accordingly. Snow depth was greater than 9 cm at all stations, and only 3 stations have snow depth less than 12 cm.

Correlation coefficients and significance values of albedo, surface temperature and density of the top 3 cm snow with latitude are shown in Table 3.1. Albedo is positively correlated with latitude, while surface temperature and density of the top 3 cm snow are negatively correlated with latitude. No significant correlation ($s < 95\%$ for 6-9 cm snow layer) between density of the snow below the top 3 cm and latitude is found. Significance values of the correlations between albedo and latitude, and surface temperature and latitude are larger than 99%. Significance for the correlation between snow density of the top 3 cm and latitude ($95\% < s < 98\%$) is less than those of albedo and temperature versus latitude, but it is still significant at 95%. These correlations demonstrate that over the pack ice, snow surface albedo increases with latitude, while surface temperature and snow density of the top 3 cm decrease.

Table 3.1 Correlation coefficients and significance values of albedo, surface temperature, and density of the top 3 cm of snow as a function of latitude

	Albedo	Temperature	Density (top 3cm)
Latitude	$R = 0.699$ $s > 99\%$	$R = -0.747$ $s > 99\%$	$R = -0.486$ $95\% < s < 98\%$

Latitudinal variations of albedo, surface temperature and density of the top 3 cm of snow from the northern edge to the southern edge of the pack ice are shown in Figures 3.2a-3.2c. The solid lines are the regression-based trend lines. Polynomial regression results in the best coefficient of determination. Predictive relations of albedo, surface temperature and density of the top 3 cm of snow with latitude (L) are

$$\alpha = 6.0\times10^{-4}L^3 - 0.1317L^2 + 9.3419L - 220.3, \quad r^2 = 0.5088 \tag{3.6}$$

$$T = -0.2641L + 17.308, \quad r^2 = 0.3551 \tag{3.7}$$

$$\rho = -0.6621L^3 + 138.3L^2 - 9639.2L + 224447, \quad r^2 = 0.2541 \tag{3.8}$$

where α is the all-wave albedo, T is the surface temperature in °C, ρ is the snow density in kg m^{-3} of the top 3 cm, L (positive) is latitude in degrees. Although the density is correlated with latitude, regression Equation (3.8) does not fit the measured data set very closely. The other two relations do fit well with the *in situ* data.

The correlations between latitude and the average composite grain-size of the top 3 cm of the snow cover calculated with the three size models indicate that best correlation coefficient (R = -0.702) is from the DI model. The correlations between latitude and the average composite size of the top 3 cm of the snow cover for the other two average grain-size models are similar, except there are slightly lower correlation coefficients (R = -0.701 for EN model; R = -0.698 for EFF model). The maximum difference of correlation coefficient between the DI model and EFF model is only 0.6%. Statistically, average composite grain-sizes from the three models are all significantly correlated with latitude, with significance s > 99%. Latitudinal variation of the average composite grain-size from

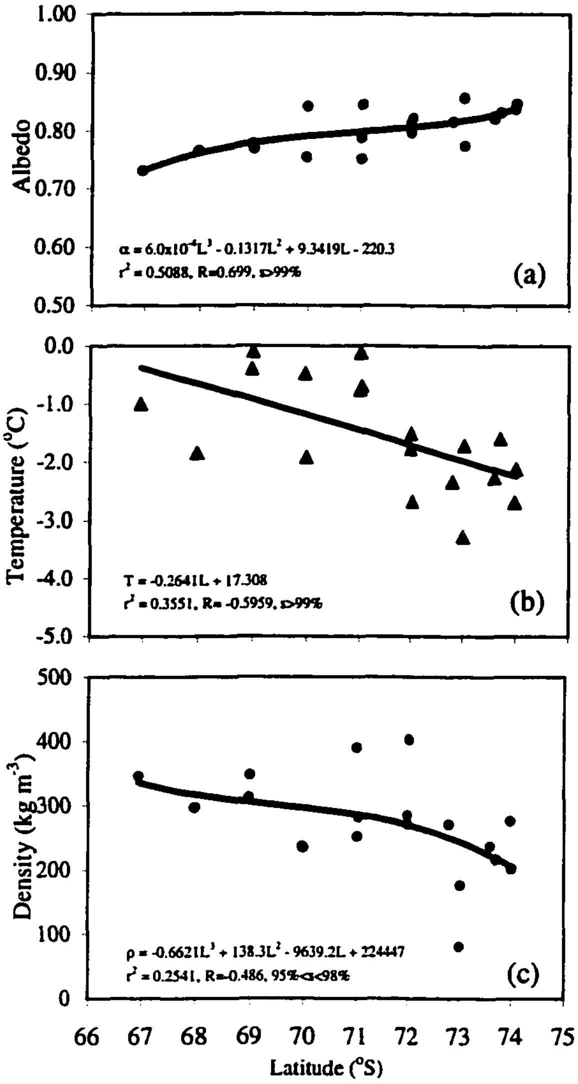

Figure 3.2 Variation of albedo (a), surface temperature (b), and snow density (c) of the top 3cm of snow with respect to the latitude in the pack ice of Ross Sea.

the DI model is shown in Figure 3.3a. The solid lines are the regression-based trend lines. Polynomial regression results in the best coefficient of determination. Predictive relations between average composite grain-size and latitude for the three average size models are given by

$$\left\langle r_1^{EN} \right\rangle = -1.9\times10^{-3}L^3 + 0.4161L^2 - 30.286L + 735.17, \quad r^2 = 0.6926 \tag{3.9a}$$

$$\left\langle r_1^{DI} \right\rangle = -1.7\times10^{-3}L^3 + 0.367L^2 - 27.481L + 669.68, \quad r^2 = 0.6908 \tag{3.9b}$$

$$\left\langle r_1^{EFF} \right\rangle = -2.1\times10^{-3}L^3 + 0.4595L^2 - 33.333L + 806.29, \quad r^2 = 0.6912 \tag{3.9c}$$

The statistical results are shown in Table 3.2, where correlation coefficients, values of the sampling statistic t, the number of sample size n are included. All these values are used to calculate the probability p and significance s, which are also shown in Table 3.2. Correlation coefficients of the average composite grain-size in different depth layers from the three size models are shown in Table 3.3. For any average size model of the three, the correlation coefficients of the composite grain-size in the second layer (3-6 cm from top) and third layer (6-9 cm from top) decrease with latitude, and the average composite grain-size is no longer correlated with latitude ($s < 90\%$). Correlation between composite grain-size and latitude is observed only for the top 3 cm of snow.

Snow composite grain number density in each layer can be calculated using Equation (3.3a). Correlation coefficients and significance values between latitude and composite grain number density of any depth layer of the top 3 layers are given in Table 3.4. The best correlation coefficient is $R = 0.390$ for the top 3 cm snow from the DI model, with significance $80\% < s < 90\%$. No correlation between composite grain number density in any depth layer and latitude is found to be significant.

The average single grain-size in each layer is calculated using Equations (3.1a-3.1c). Correlation analyses of the single grain-size in any of the top 4 layers (up to 12 cm) with latitude show that the best significance ($s < 50\%$) is from 3-6 cm and 9-12 cm layers. For the top 3 cm layer, the significance is $s < 20\%$. For the purpose of comparison with composite case, the correlation between the distribution-integrated average single grain-size of the top 3 cm snow cover and latitude is shown in Figure 3.3b. Correlation analyses show that single grain-size does not correlate with latitude.

Table 3.2 Statistics for the correlation between composite average grain-size within the top 3cm of snow cover from the three average size models as a function of latitude

EN model $\langle r^{EN} \rangle$	DI model $\langle r^{DI} \rangle$	EFF model $\langle r^{EFF} \rangle$
$R = -0.701$ $n = 17$ $t = -3.808$ $p < 0.01$ $s > 99\%$	$R = -0.702$ $n = 17$ $t = -3.817$ $p < 0.01$ $s > 99\%$	$R = -0.698$ $n = 17$ $t = -3.773$ $p < 0.01$ $s > 99\%$

Table 3.3 Significance values and correlation coefficients between composite average grain-size and latitude within different layers for the three average size models

Snow depth	EN model $\langle r^{EN} \rangle$	DI model $\langle r^{DI} \rangle$	EFF model $\langle r^{EFF} \rangle$
0-3 cm	$R = -0.701$ $s > 99\%$	$R = -0.702$ $s > 99\%$	$R = -0.698$ $s > 99\%$
3-6 cm	$R = -0.401$ $80\% < s < 90\%$	$R = -0.404$ $80\% < s < 90\%$	$R = -0.397$ $80\% < s < 90\%$
6-9 cm	$R = -0.373$ $80\% < s < 90\%$	$R = -0.375$ $80\% < s < 90\%$	$R = -0.372$ $80\% < s < 90\%$

Table 3.4 Significance values and correlation coefficients between composite grain number density and latitude within different layers for the three average size models

Snow depth	EN model $\langle n^{EN} \rangle$	DI model $\langle n^{DI} \rangle$	EFF model $\langle n^{EFF} \rangle$
0-3 cm	$R = 0.379$ $80\% < s < 90\%$	$R = 0.390$ $80\% < s < 90\%$	$R = 0.362$ $80\% < s < 90\%$
3-6 cm	$R = 0.376$ $80\% < s < 90\%$	$R = 0.379$ $80\% < s < 90\%$	$R = 0.373$ $80\% < s < 90\%$
6-9 cm	$R = 0.339$ $80\% < s < 90\%$	$R = 0.341$ $80\% < s < 90\%$	$R = 0.33$ $80\% < s < 90\%$

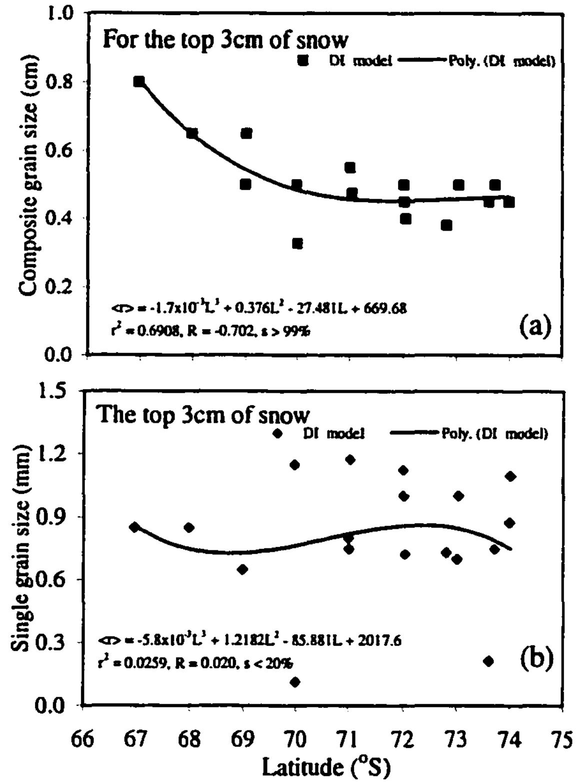

Figure 3.3 Longitudinal variation of composite grain-size (a) and single grain-size (b) of the top 3cm of snow. With increase of latitude, snow composite grain-size shows a negative correlation, while no correlation is found between single grain-size and latitude for the top 3 cm of snow.

Snow single grain number density in each layer can be calculated using Equation (3.3a). Correlation coefficients and significance values of the top 3 layers are given in Table 3.5. The best correlation coefficient (R = -0.3517) is from the EFF model of the third layer (6-9 cm from top), with significance 80% <s < 90%. No correlation between single grain number density in any layer and latitude is significant.

3.5 Correlations and Regressions between All-wave Albedo and Snow Physical Parameters

From electromagnetic scattering theory, once the size of the scatterer is specified, temperature is not a basic physical quantity that affects the scattering and absorption of electromagnetic energy by dispersive media [Bohren and Huffman, 1983]. However, an increase of snow grain-size due to metamorphism is a strong function of the temperature [Wiscombe and Warren, 1980]. Nineteen data sets of albedo and surface temperature were obtained in the central pack ice of the Ross Sea. The correlation coefficient is R = -0.635. The conclusion that all-wave albedo is related to snow surface temperature is justified by the high correlation significance value (s > 99%). Variation of snow surface albedo with surface temperature is shown in Figure 3.4a, where a regression-based trend curve is also shown. The predictive relation between albedo and surface temperature resulting from polynomial regression analysis is

$$\alpha = 5.8\times10^{-3}T^3 + 0.0351T^2 + 0.0317T + 0.7816, \qquad r^2 = 0.4347 \tag{3.10}$$

where T is in °C. Negative correlation between albedo and temperature indicates that with an increase in temperature, all-wave albedo decreases.

Variation of composite grain-size of the top 3 cm of snow with surface temperature is shown in Figure 3.4b. Seventeen data sets of composite grain-size were obtained in the central pack. Of the 19 albedo sites, two sites had no composite snow grains in the top 3 cm of snow. Correlation analysis between composite grain-size of the top 3 cm of snow and surface temperature shows that composite grain-size is correlated with surface temperature, with significance 95% < s < 98%. The best coefficient (R = -0.526) is from

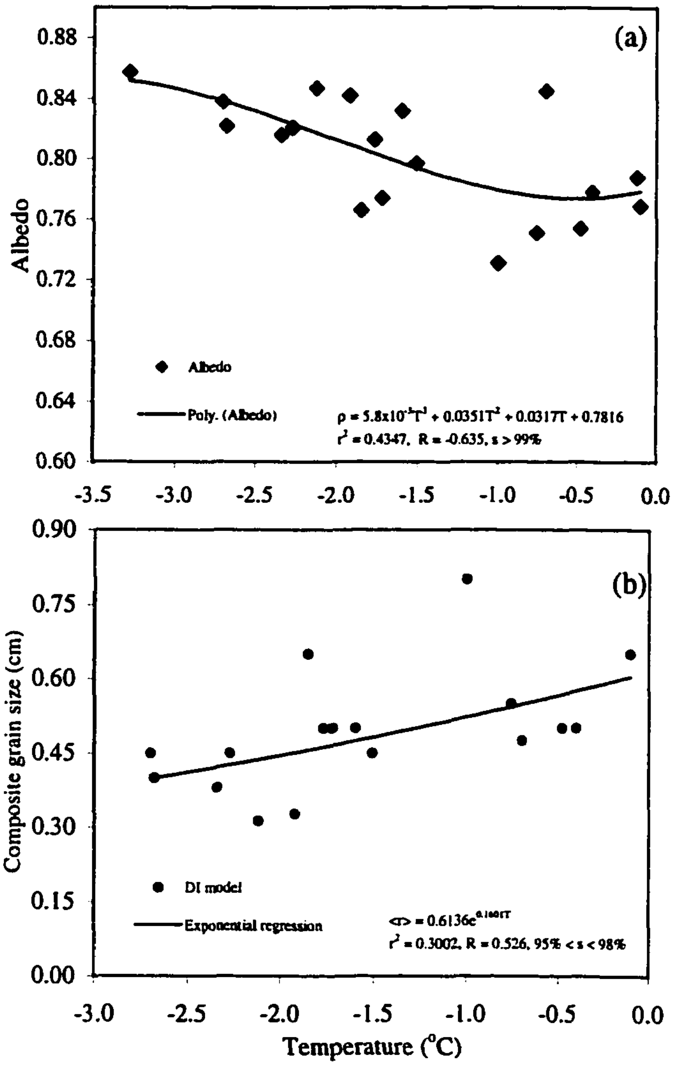

Figure 3.4 Snow surface all-wave albedo (a), and composite grain-size of the top 3 cm of snow (b) versus snow surface temperature. Albedo is quite significantly correlated with snow surface temperature. Composite grain-size of the top snow layer is also related to snow surface temperature.

the DI model and the closest fitting is an exponential regression. The predictive relation is

$$\bar{r}_1^{DI} = 0.613e^{0.1601T}, \quad r^2 = 0.300 \tag{3.11}$$

Albedo correlations with composite grain-size and composite grain number density are analyzed with respect to multiple layers, so that the effect of snow depth on albedo can be investigated. The average grain-sizes (both composite or single) within multiple layers are calculated using Equations (3.2a-3.2c). The number density of each layer and multiple snow layers are evaluated from Equations (3.3a-3.3b), respectively, using the three average size models. Snow density was the measured data and the average grain-sizes in each layer are calculated from Equations (3.1a-3.1c), as was done in section 3.3.

Table 3.5 Significance values and correlation coefficients between single grain number density and latitude within different layers for the three average size models

Snow depth	EN model $\langle n^{EN} \rangle$	DI model $\langle n^{DI} \rangle$	EFF model $\langle n^{EFF} \rangle$
0-3 cm	R = -0.119	R = -0.220	R = -0.236
	20%<s< 50%	50%<s< 80%	50%<s< 80%
3-6 cm	R = -0.048	R = 0.100	R = -0.100
	s< 20%	20%<s< 50%	20%<s< 50%
6-9 cm	R = 0.293	R = 0.228	R = 0.352
	50%<s< 80%	50%<s< 80%	80%<s< 90%

Variation of albedo with composite grain-size for various depths of snow is shown in Figure 3.6. For the top 3 cm of snow, albedo is strongly correlated (s > 99%) with the average composite grain site calculated with all three models: albedo decreases with increase of composite grain-size. The predictive relations between albedo and composite grain-size for the three average size models are

$$\alpha = 0.4946\left(\bar{r}_1^{EN}\right)^3 - 0.6642\left(\bar{r}_1^{EN}\right)^2 + 0.0135\bar{r}_1^{EN} + 0.8946, \quad r^2 = 0.624 \tag{3.12a}$$

$$\alpha = 0.7198\left(\bar{r}_1^{DI}\right)^3 - 1.059\left(\bar{r}_1^{DI}\right)^2 + 0.238\bar{r}_1^{DI} + 0.8527, \quad r^2 = 0.627 \tag{3.12b}$$

$$\alpha = 0.7085\left(\bar{r}_1^{EFF}\right)^{-0.1674}, \quad r^2 = 0.619 \tag{3.12c}$$

The best correlation coefficient (R = -0.788) between albedo and composite grain-size for the top 3 cm snow is from the DI model, but the differences between DI model and other two are very small (R = -0.785 and -0.781 for EN model and EFF model respectively). For the top 6 cm of snow, the EN model gives the best coefficient (R = -0.723, s > 99%) and for snow depth larger than 6 cm, the EFF model gives the best results (R = -0.660, s > 99%). Significant correlation between albedo and composite grain-size remains up to 9 cm depth, but the correlation coefficients decrease with snow depth. This tendency is shown in Figure 3.5a, along with the regression equation. A polynomial regression analysis is performed for the correlation coefficient values and snow depths shown in Figure 3.5a. The average composite grain-size data used to calculate the correlation coefficients shown in Figure 3.5a are from the EFF model, because it generates the best correlation coefficients with snow depth up to 9 cm. The correlation significance decreases rapidly with the increase of snow depth. For snow depth greater than 9 cm, significance decreases to less than 95%, which indicates that a relationship is no longer justified. Further increase of snow depth has little effect on albedo. This indicates that snow depth approaches optically semi-infinite for all-wave albedo if the depth exceeds 9 cm (cf. chapter 6). Relationships between albedo and the average composite grain-size for different depths of snow (up to 9 cm) are shown in Figures 3.6a-3.6c, where solid curves are the regression-based trend lines. The best coefficient of determination is from the power regression method for the top 3 cm of snow. However, for snow depth of 6 cm and 9 cm from the top, the best coefficient of determination is from the third-order polynomial regression method.

Snow composite grain number density is calculated based on the average composite grain-size for a specific depth of snow. For the top 3 cm of snow, the best correlation results (R = 0.663, s > 99%) between albedo and composite grain number density are from the DI model. However, for the top 6 cm snow, the best correlation results (R = 0.574, 95% < s < 98%) are from the EN model, and for the top 9 cm of snow, they are from the EFF model (R = 0.529, 95% < s < 98%). For the top 3 cm of snow, relations between albedo and composite grain number density for the three models are

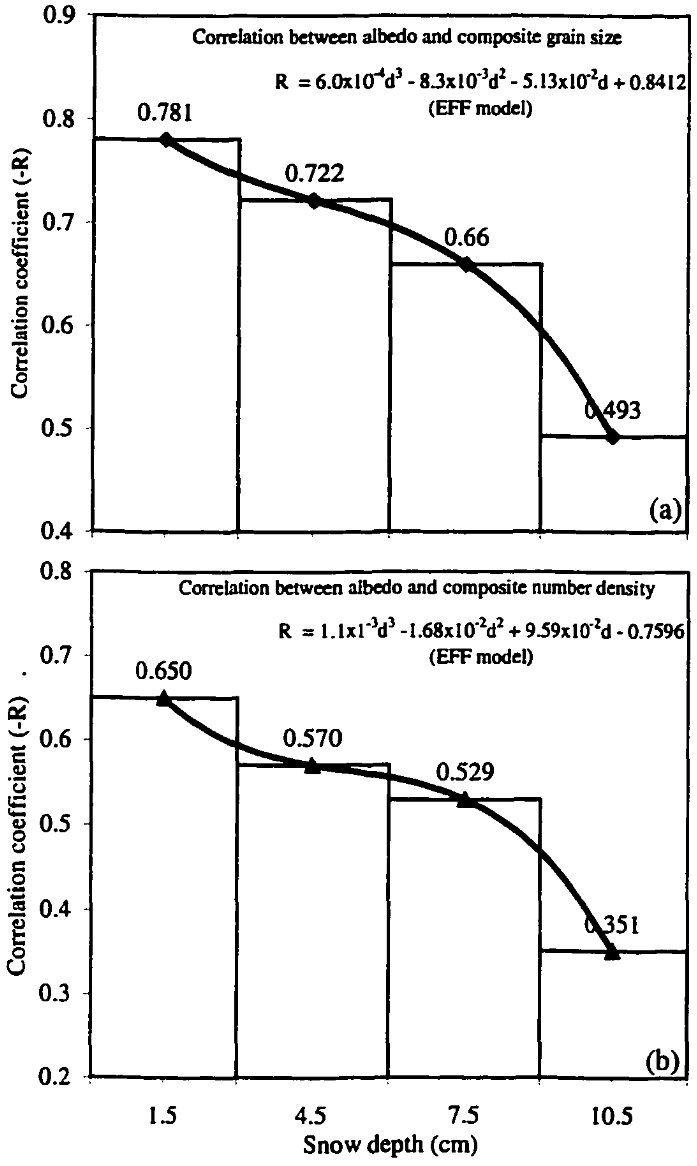

Figure 3.5 (a) Correlation coefficients between albedo and snow composite grain-size (from the EFF model) versus snow depth. The solid curve is the polynomial regression line. d is the snow depth (in cm). (b) Same as (a) but for the correlation between albedo and composite grain number density.

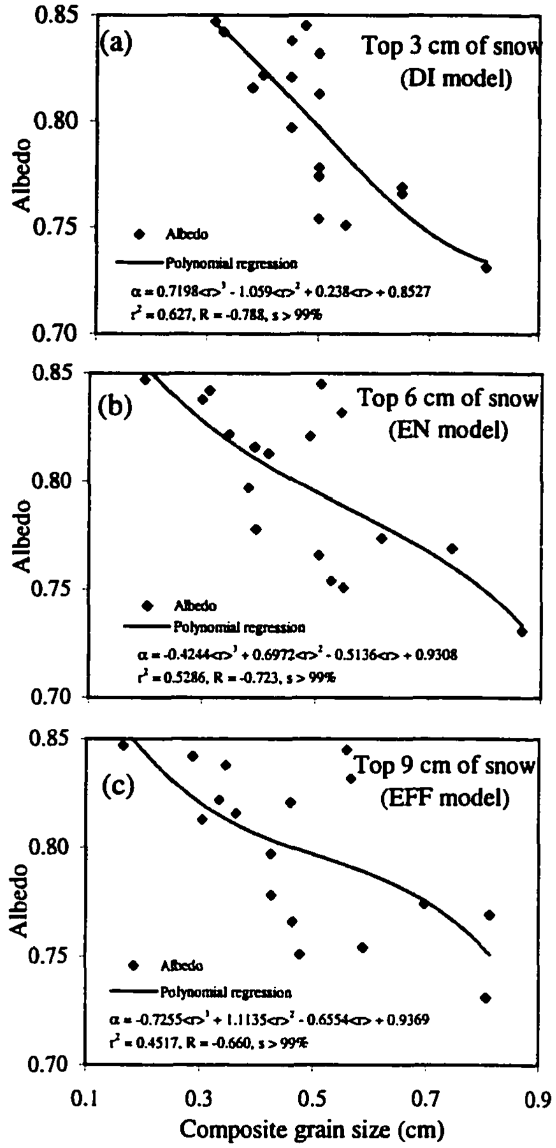

Figure 3.6 Variation of albedo with snow composite grain-size for various depths of snow. (a), (b), and (c) are for snow depth d = 3 cm, 6 cm, and 9 cm, respectively. Albedo is significantly correlated with snow composite grain-size for snow depth up to 9 cm. Solid curves are the regression-based trend lines. The eest results (largest correlation coefficients) shown here are from the DI model for d = 3cm, the EN model for d = 6cm, and the EFF model for d = 9 cm.

$$\alpha = 5.291\times10^{-2} n_1^{EN} + 0.760, \quad R = 0.660 \tag{3.13a}$$

$$\alpha = 4.900\times10^{-2} n_1^{DI} + 0.762, \quad R = 0.663 \tag{3.13b}$$

$$\alpha = 5.604\times10^{-2} n_1^{EFF} + 0.759, \quad R = 0.650 \tag{3.13c}$$

From any of the three average size models, it is found that for each depth of snow that is less than 9 cm, the albedo is significantly correlated with composite grain number density: the larger the number density, the higher the albedo. However, the correlation coefficient between albedo and composite grain number density decreases with snow depth. This decreasing tendency is shown in Figure 3.5b, where the regression equation and the corresponding coefficient of determination r^2 are also shown. Of the three average size models, the EFF model generates the best correlation coefficients between albedo and composite grain-size for snow depth larger than 6 cm. Computation of number density to obtain the coefficients shown in Figure 3.5b is thus done based on the EFF model. With snow depth greater than 9 cm, significant correlation is no longer observed (significance $s < 80\%$). As the significance of correlation is well below 95% for snow depth larger than 9 cm, correlation coefficients for snow depth larger than 9 cm do not indicate any correlation between the two parameters.

Relationships between albedo and the composite grain number density for various depths of snow (up to 9 cm) are shown in Figures 3.7a-3.7c, where solid curves are the regression-based trend lines. The best coefficient of determination is from the polynomial regression method for the top 3 cm and 6 cm of snow (Figures 3.7a and 3.7b). For snow depth of 9 cm from the top, the best coefficient of determination is from the power regression method (Figure 3.7c).

The same analyses for composite grains are used to analyze the correlation among albedo and single grain physical parameters. There is no correlation between single grain-size of the top 3 cm of snow and latitude for the largest correlation coefficient ($R = 0.088$) and significance is $20\% < s < 50\%$ for the EFF model. The same analyses for the other 3 layers (to a depth of 12 cm) confirm that no correlation exists between single grain-size in any layer of the top 12 cm of snow and latitude. The best correlation coefficient and significance value for single grain-size of the top 3 cm of snow and snow

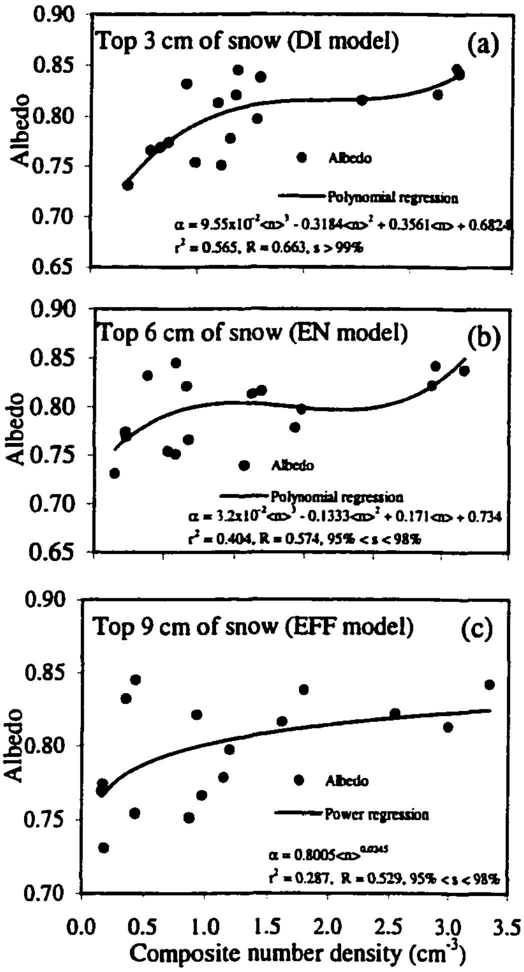

Figure 3.7 Correlation between albedo and snow composite grain number density for various depths of snow. (a), (b), and (c) are for snow depth d = 3 cm, 6 cm, and 9 cm, respectively. Albedo is significantly correlated with snow composite grain number density for snow depth up to 9 cm. Below that no correlation is found. The best results (largest correlation coefficients) shown here are from the DI model for d = 3cm, the EN model for d = 6cm, and the EFF model for d = 9 cm.

surface temperature are from the DI model: $R = 0.304$, $50\ \% < s < 80\%$, which shows that single grain-size of the top snow layer is not related to the surface temperature. Correlation analyses between single grain number density of multiple layers of 3 cm, 6 cm, 9 cm and 12 cm depth and latitude show that no relationship exists. The best correlation coefficient and significance ($R = -0.236$, $50\% < s < 80\%$) between the single grain number density and latitude are from the EFF model for the top 3 cm of snow. The same analyses using albedo in place of latitude show that albedo does not strongly correlate with single grain-size and number density at any depth. This conclusion can be drawn because all three different average size models lead to the same results.

Correlation analyses of albedo with average snow density for snow depth up to 15 cm show that no correlation exits between albedo and density. For example, the correlation coefficient of albedo and snow density of the top 3 cm is $R = -0.373$, with significance $80\% < s < 90\%$. For the top 9 cm snow, $R = -0.389$, $80\% < s < 90\%$. All the results indicate that no correlation exists between albedo and snow density. These results support the conclusion made by Bohren and Beschta (1979) that snow albedo is, at most, weakly dependent upon snow density, although snow densification in their case was made by mechanical methods, while here the densification of snow was obviously due to various metamorphose and meteorological processes (e.g. wind packing, etc.).

The effect of solar zenith angle is shown in Figure 3.8a. Because the albedo measurements were carried out around local solar noon, the solar zenith angle is the solar zenith angle at local noon, which is calculated using the solar-zenith-angle model [Woolf, 1968]. A correlation coefficient $R = -0.64$ with significance $s > 99\%$ indicates the correlation is very significant. Decrease of albedo with increase of cosine of the solar zenith angle is well represented by the linear fitting function. Decrease of albedo with cosine of the solar zenith angle has been observed previously in Antarctica [Liljequist, 1956; Rusin, 1961; Carrol and Fitch, 1981]. The reason that the all-wave albedo increases with the zenith angle is that the energy component in the vertical direction of a photon is less when the zenith angle is larger, resulting in less penetration depth and less probability of being absorbed, and thus a greater chance of escaping the snow surface.

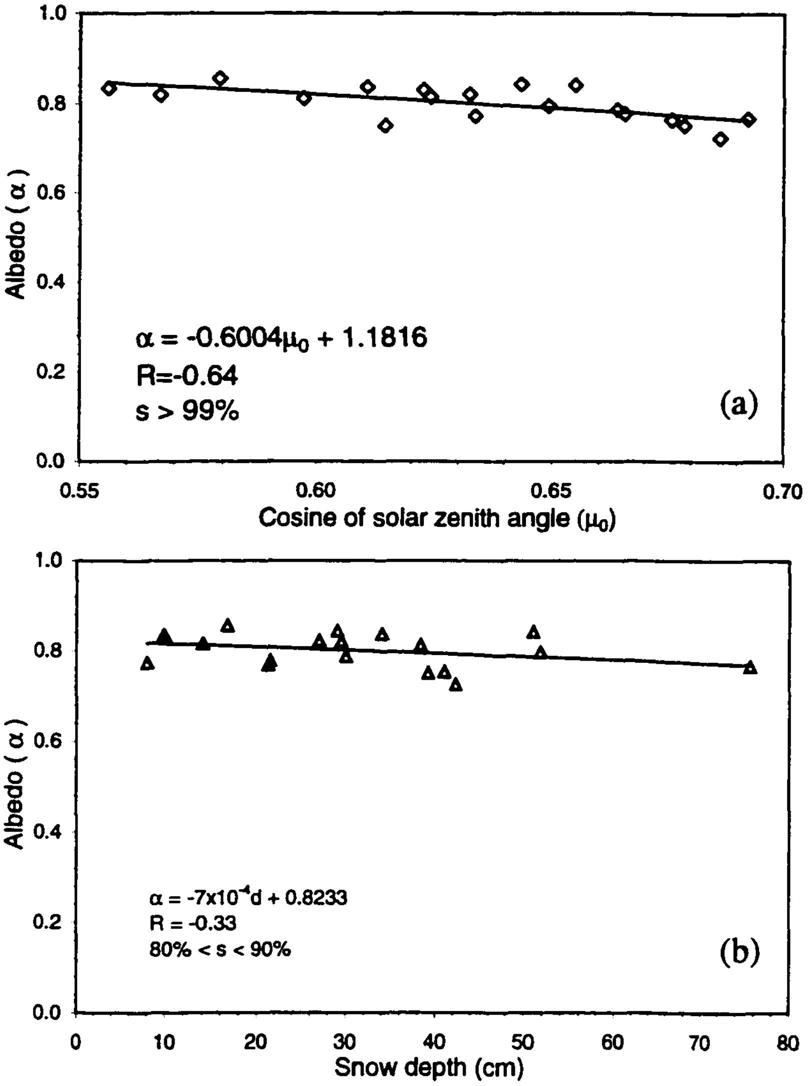

Figure 3.8 (a) Albedo (α) versus cosine of the solar zenith angle (μ_0). The correlation coefficient, R = -0.64, is significant at the s > 99% level. (b) Albedo versus (α) snow depth (d). The correlation coefficient, R = -0.33, is not significant at the 80 < s < 90% level.

The relationship between albedo and snow depth is also worthy of discussion. Figure 3.8b shows the albedo versus snow depth. Of the 19 snow data sets, the lowest mean snow depth is 8.0 cm at station 6 (day 9), and the greatest snow depth is 75.6 cm at station 16 (day 20). There were only three stations with snow depth less than 10 cm. From the above analyses, we have seen that albedo is significantly correlated with physical parameters within the top 9 cm snow, while these parameters within deeper snow layers are not very albedo. Although the snow semi-infinite depth can not be accurately determined from the statistical analyses, if we take the top 10 cm as the most important snow depth in determining the snow albedo, then it is not difficult to understand that the albedo is not significantly correlated with snow depth because most sites have snow deeper than 10 cm. For the three sites that the snow depth was less than 10 cm, albedo did increase with increase of depth.

3.6 Multivariate Correlations of Albedo with Grain-size and Number Density

The results in section 3.5 show that albedo is strongly correlated with composite grain-size, and also strongly correlated with composite number density for snow depth up to 9 cm. To assess the effect of the composite grain-size and number density of different layers on albedo, and the degree to which composite grain-size and number density together affect the albedo, multivariate regressions are made.

First, let's analyze the correlation between the composite grain-size and number density before the degree to which composite grain-size and number density together relate to the albedo can be assessed using multivariate regression methods.

Relations of composite grain-size with composite grain number density for three depths of snow are shown in Figures 3.9a-3.9c. For snow depth of 3 cm, the DI model gives the best correlation coefficient (R = -0.832 with significance s > 99.9%). For the top 6 cm snow, the EFF model also gives the best correlation coefficient (R = -0.840, with s > 99.9%). For the top 9 cm, which from section 3.5 we know is the important depth for albedo, the EFF model gives the best correlation coefficient (R = -0.856, with s > 99.9%). Results from all three size models show that composite grain-size is strongly

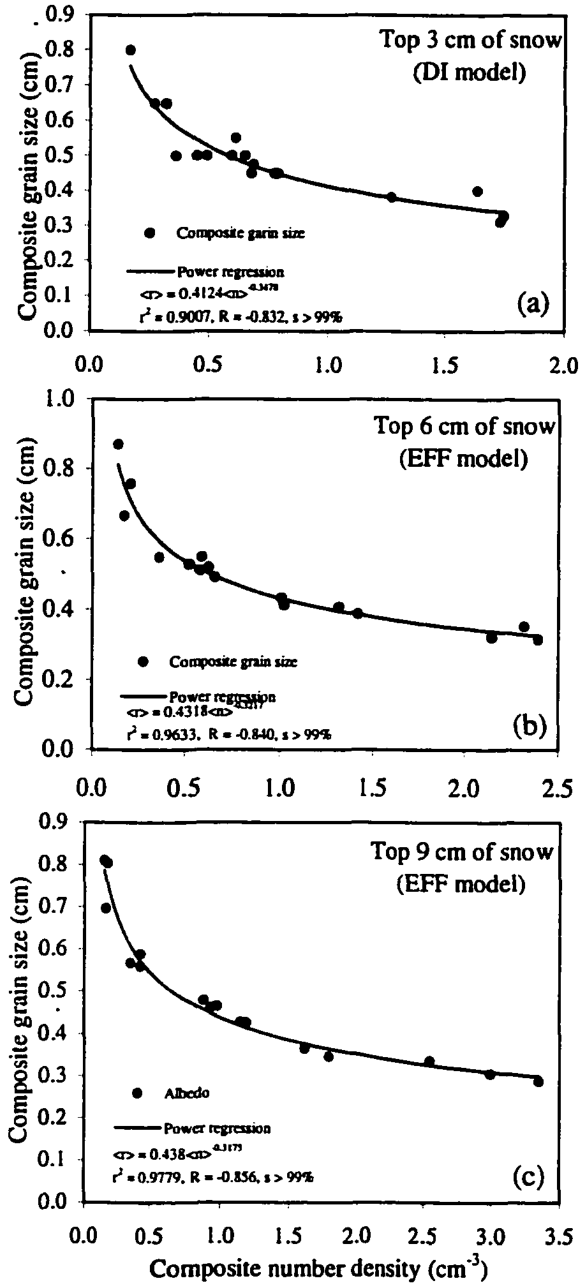

Figure 3.9 Correlation between composite grain-size and snow composite grain number density for various depths of snow. (a), (b), and (c) are for snow depth d = 3 cm, 6 cm, and 9 cm respectively. Composite grain-size is strongly correlated with snow composite grain number density for snow depth up to 9 cm. The best results (largest correlation coefficients) shown here are from the DI model for d = 3cm, the EFF model for d = 6cm and d = 9 cm.

correlated with composite grain number density for multiple snow layers up to 9cm depth. Various regression analyses show that power regression results in the best fit for snow depth ranging from 3 cm to 9 cm. For the three different depths of snow, the relations between composite grain-size and composite grain number density are

$$\bar{r}_1^{DI} = 0.4124\left(n_1^{DI}\right)^{-0.3478}, \quad r^2 = 0.901 \tag{3.14a}$$

$$\bar{r}_2^{EFF} = 0.4318\left(n_2^{EFF}\right)^{-0.3217}, \quad r^2 = 0.963 \tag{3.14b}$$

$$\bar{r}_3^{EFF} = 0.4380\left(n_3^{EFF}\right)^{-0.3175}, \quad r^2 = 0.978 \tag{3.14c}$$

From the above analyses and those of section 3.5, we can see that the for the top 3 cm of snow, the DI model generally gives the best correlation among albedo, composite grain-size and composite grain number density. But for snow deeper than 6 cm, the EFF model gives the best results. For snow of 3 to 6 cm, the EN model gives the best coefficients for correlation between albedo and composite grain-size and number density, while the EFF model results in the best coefficient for the correlation between albedo and composite grain-size and composite grain number density. This layer (3-6 cm) appears to be a transition layer for the applicability of the EFF model for snow cover greater than 3 cm deep. For snow depth greater than 9 cm, albedo is no longer correlated with the snow parameters. In the following discussion for the multiple correlation of albedo with composite grain-size and number density, we use the DI model when the snow cover is less than 3 cm, while the EFF model is used for snow depth larger than 3 cm.

Multivariate regressions show that the multiple correlation coefficients $R_{\alpha,<r><n>}$ of composite grain-size (<r>) and number density (<n>) with albedo (α) for snow depth d = 3 cm, 6 cm and 9 cm are 0.788, 0.682 and 0.608 respectively. The statistical significance of the multiple correlation is tested by use of an F-test [Pearson and Hartley, 1966]. F is computed with k and (n - k - 1) degrees of freedom,

$$\begin{aligned} F &= \frac{R^2/k}{\left(1-R^2\right)/(n-k-1)} \\ &= \frac{R^2_{\alpha,<r><n>}/2}{(1-R^2_{\alpha,<r><n>})/(n-3)} \end{aligned} \tag{3.15}$$

where k = number of terms in the multiple regression equation, excluding the constant. For this particular regression, degrees of freedom d.f. = k/(n-k-1) = 2/14. F = 11.5, 6.10, and 4.11 for snow depth d = 3cm, 6cm, and 9cm, respectively. With the d.f. number and F values, we obtain that a significance of 99.5% < s < 99.9% for the top 3 cm of snow, 97.5% < s < 99% for the top 6 cm of snow, and 95% < s < 97.5% for the top 9 cm of snow. These indicate that the multiple correlation is significant and there is a relationship between albedo and composite grain-size and number density for snow depth up to 9 cm.

The multiple regression equation of albedo (α) with composite grain-size <r> and number density <n> is

$$\alpha = a + b_{<r>\alpha,<n>} < r > + b_{<n>\alpha,<r>} < n > \tag{3.16}$$

where the coefficients a, b are given as

$$a = M_{\alpha} - b_{<r>\alpha,<n>} M_{<r>} - b_{<n>\alpha,<r>} M_{<n>}$$

$$b_{<r>\alpha,<n>} = \frac{S_{\alpha}}{S_{<r>}} \frac{R_{<r>\alpha} - R_{<n>\alpha} R_{<r><n>}}{1 - R^2_{<r><n>}}$$

$$b_{<n>\alpha,<r>} = \frac{S_{\alpha}}{S_{<n>}} \frac{R_{<n>\alpha} - R_{<r>\alpha} R_{<r><n>}}{1 - R^2_{<r><n>}}$$

in which $R_{xy} = R_{yx}$ ($x \neq y$ and x, y = α, <r>, <n>) is the correlation coefficient between parameters x and y [Williams, 1992]. M_x and S_x are the mean value and the standard deviation of the distribution of x, respectively. Therefore, the multiple regression equations of albedo with composite grain-size and number density for snow cover of 3 cm, 6 cm and 9cm depth are

$$\alpha = 0.9155 - 0.2372<r> + 1.7924\times10^{-3}<n>, \quad d = 3\text{ cm} \tag{3.17a}$$

$$\alpha = 0.8794 - 0.1602<r> + 1.7744\times10^{-4}<n>, \quad d = 6\text{ cm} \tag{3.17b}$$

$$\alpha = 0.8593 - 0.1288<r> + 1.0869\times10^{-3}<n>, \quad d = 9\text{ cm} \tag{3.17c}$$

where <r> is in units of cm and <n> in units of cm^{-3}. According to the statistical practice, a squared multiple correlation coefficient tells us what proportion of the variance of the predicted variable (albedo) is accounted for by the two predictor variables (composite grain-size and number density). From the following equation [Williams, 1992]

$$R^2_{\alpha,<r><n>} = \left(\frac{R_{<r>\alpha} - R_{<n>\alpha} R_{<r><n>}}{1 - R^2_{<r><n>}} \right) R_{<r>\alpha} + \left(\frac{R_{<n>\alpha} - R_{<r>\alpha} R_{<r><n>}}{1 - R^2_{<r><n>}} \right) R_{<n>\alpha} \tag{3.18}$$

we can determine that for the top 3 cm of the snow cover, approximately 60% of the prediction of albedo (total 62%) is attributable to composite grain-size alone and approximately 2% is due to the addition of the composite grain number density. Even for the top 9 cm of snow, approximately 35.4% of the prediction of albedo (total 37%) is due to composite grain-size alone and 1.6% is due to the addition of number density. Although albedo is correlated with both composite grain-size and composite grain number density, the contributions from composite grain-size are dominant. The high correlation coefficient between the composite grain-size and composite number density results in a relatively small contribution by the addition of composite grain number density.

In section 3.5, it was found that for snow ≥ 9 cm, the EFF model results in the best correlation between albedo and composite grain-size or number density. Now let's use the EFF model to investigate the effect of composite grain-size and number density in different layers on albedo using the multiple linear regression method. For all ice stations where the snow cover was more than 9cm deep, correlation analyses of albedo with composite grain-size in each layer (0-3cm, 3-6 cm and 6-9 cm layers) show that albedo is correlated with composite grain-size in each layer. For the 0-3 cm layer, R = -0.781 with s > 99.9%; for the 3-6 cm layer, R = -0.632 with 95% < s < 99%; and for the 6-9 cm layer, R = -0.491 with 95% < s < 98%. Multiple linear regression equations for albedo with composite grain-size and number density are given as

$$\alpha = a_0 + b_{0-3} < r_{0-3}^{EFF} > + b_{3-6} \left\langle r_{3-6}^{EFF} \right\rangle + b_{6-9} \left\langle r_{6-9}^{EFF} \right\rangle \tag{3.19a}$$

Regression analyses of the data sets with snow depth d ≥ 9 cm give a multiple regression equation of albedo with composite grain-size

$$\alpha = 0.9197 - 0.2187 < r_{0-3}^{EFF} > -2.707 \times 10^{-2} \left\langle r_{3-6}^{EFF} \right\rangle + 5.985 \times 10^{-3} \left\langle r_{6-9}^{EFF} \right\rangle \tag{3.19b}$$

with a multiple correlation coefficient R = -0.786. From Equation (3.15), we have F = 7.02. With d.f. = 3/13, we obtain that a significance of 99% < s < 99.5%. This indicates that the multiple regression relation (3.19) is significant for fitting the field data sets. From $|b_{0\text{-}3}|$: $|b_{3\text{-}6}|$: $b_{6\text{-}9}$ $\approx 36.5 : 4.5 : 1$, we can see that the contribution of the top layer (0-3 cm) is 36.5 times that of the third layer (6-9 cm) and the contribution of the second layer (3-6 cm) is 4.5 times that of the third layer if the average composite grain-size of all the three layers is the same.

For all ice stations where snow cover was more than 9cm deep, correlation analyses of albedo with composite grain number density in each layer (0-3cm, 3-6 cm and 6-9 cm layers) show that albedo is correlated with composite grain number density only for the top two layers. For the 0-3 cm layer, R = 0.606 with 98% < s < 99%; for the 3-6 cm layer, R = 0.508 with 95% < s < 98%; and for the 6-9 cm layer, R = 0.312 with 50% < s < 80%. Multiple linear regression equations for albedo with the composite grain number density is given as $\alpha = c_0 + d_{0-3} < n_{0-3}^{EFF} > +d_{3-6}\left\langle n_{3-6}^{EFF} \right\rangle$.

Regression analyses of the data sets with snow depth d ≥ 6 cm give a multiple regression equation of albedo with composite grain number density

$$\alpha = 0.7611 + 4.1911\times10^{-2} < n_{0-3}^{EFF} > +4.9676\times10^{-3}\left\langle n_{3-6}^{EFF} \right\rangle \tag{3.20}$$

with the multiple correlation coefficient R = 0.621. With the same analyses of multiple regression as for the case of albedo versus composite grain-size, we obtain F = 4.08 and a significance of 95% < s < 97.5%. This indicates that the multiple regression relation (3.20) is significant. From $|d_{0\text{-}3}|$: $d_{3\text{-}6} \approx 8.4: 1$, we can see that contribution of composite grain number density from the top layer (0-3 cm) is 8.4 times that of the second layer (3-6 cm) if the average composite grain number density of all layers is the same. If, as has been done for the albedo versus composite grain-size for all the top three layers, multiple regression (3.20) is also carried out for all the top three layers, the resulting in correlation coefficient R = 0.630 and significance 75% < s < 90%, indicates that regression of albedo for all the three layers in not significant. This occurs due to the non-correlation of albedo with the composite grain number density in the third layer (6-9 cm).

3.7 Discussions

Albedo at the ice edges, especially in the northern marginal ice zone of the pack ice, is lower than the central pack. Away from the northern ice edge, albedo increases as snow composite grain-size decreases southward in the central pack ice. Snow surface temperature decreases with latitude from north to south in the pack ice. Formation and growth of composite grains may experience the following processes:

Single grains grow before they bond together to form composite grains. The usual metamorphosis mechanisms control such a growth [Colbeck, 1982]. Spatial temperature differences can cause metamorphism at different rates: higher temperature will lead to coarser single snow grains.

Formation of composite grains from single grains: when liquid water content in a snowpack increases due to melting or flooding, single ice grains tend to bond each other to form clustered rounded grains (6cl) [Colbeck, 1990]. Such clusters form to minimize surface free energy [Colbeck, 1979]. At this stage, single grains are held together by large ice-to-ice bonds with liquid water in internal veins among multiple crystals without melt-refreeze cycles. Because water has similar refractive index as ice, water in the internal veins acts in the same role as ice in absorbing and scattering solar radiation. Thus a cluster (or a composite grain) of single grains acts like a single large ice grain rather than a system of the individual single grains that make up the cluster in its interaction with the solar radiation. If these clusters are refrozen, the clusters will form rounded poly-crystals or also called melt-freeze polycrystals (6mf) [Colbeck, 1990].

Growth of the composite grains can be in two ways. The first way is that more single grains are bonded to the original composite grains. This process is mainly controlled by the minimization of the surface energy [Colbeck, 1979]. The second way is that the composite grain acts just like a single ice crystal and grows due to various kinds of metamorphism, dependent on meteorological conditions and liquid water content. These two mechanisms may work together, or one plays a major role over the other, depending on the external conditions.

In the marginal ice zones, especially the northern edge of the pack ice in the Ross Sea, wave-ice interaction can often break up the existing ice floes into smaller floes. Waves and ocean currents can operate harmonically to tilt the smaller ice floes and thus flood the ice surface and/or remove much of the loose part of the snow cover. These phenomena are very common in the marginal ice zone all year round [Wadhams et al., 1987; Massom et al., 1997, 1998, 2001]. Flooding occurs more frequently at the marginal ice zones, especially the northern edges, although sometimes long-period swells penetrate deeply into the inner pack and flood the interior ice floes [Squire et al., 1986; Worby, et al., 1996; Morris et al., 1998]. Sea ice flooding is observed to occur more frequently in summer [Drinkwater and Lytle, 1997; Jeffries et al., 2001], probably due to basal melt by higher oceanic heat flux [McPhee et al., 1996], compared with other seasons, or may simply be due to the increasing snow load. Flooding and melting can cause temporary liquid-saturated snow or wet snow, which in turn generates well-rounded ice crystals. Saturated or very wet snow (wetness > 8%, funicular regime) before drainage and refreezing is characterized by single grain-boundary melting, rapid grain rounding and rapid single grain growth [Colbeck, 1980]. When the liquid water in the upper layers due to melting or flooding is drained due to gravity, wetness in the snow will decrease to below 8% (pendular regime). At this stage, the tightly packed single-grain clusters (6cl) appear. Single-grain clusters also appear due to increase of liquid water from the flooded snow-ice interface by capillary actions. Percolation during drainage increases the wetness in the lower part from the surface and capillarity increases the wetness of the snow layer above the flooded ice-snow interface of the snow cover up to a significant scale of the whole snowpack. This can furnish the probability that a pendular regime can be available within the whole snowpack, providing the environment needed for the single-grain clusters to form. The data collected during NBP99-1 cruise show that snowpacks on all ice stations are composed of composite grains from top to bottom, except the snowpack of one station, of which the top 3 cm snow of the snowpack was not composed of composite grains. Single-grain clusters (6cl) appear in the wet (wetness 3-8%) snow. Subsequent refreezing produces polycrystalline particles (6mf). Latitudinal variation of snow composite grain-size from north to south may indicate the spatial variation of wetting/dampening /flooding.

Growth of single snow grains is a direct result of temperature and/or temperature gradient-related metamorphism [Colbeck, 1982]. Single grain-size generally increases with increasing temperature [Sommerfeld and LaChapelle, 1970]. Thus it is expected that the single grain-size should also be related to temperature. However, our data analyses indicate that no correlation exists between the single grain-size of the top 3 cm of snow and the surface temperature. This may suggest that the growth of single grains at the top snow layers before they form composite grains is very limited due to the possibility that they did not experienced the funicular regime period during which the single grains grow quickly possible, and thus they may form composite grains directly through pendular regime. This agrees with our observation that very wet snow or saturated snow is seldom observed at the top of snow during the NBP 991 cruise. Once the melt-freeze poly-crystals (also called melt-refreeze clusters) (6mf) are formed, single grains are bounded rigidly within the melt-refreeze clusters due to single grain boundary adhesion. Thus, the growth of a single grain with increase of temperature may be inhibited due to the seal-off of the channels of the vapor flux. Mass transfer channel is hindered for the internal single grains of a melt-refreeze cluster. A single grain in the interior of a composite grain with no free air surface can be easily in thermo-equilibrium with the rest of the composite grain [Colbeck, 1979]. The heat and mass flows among the single grains inside the composite grain are greatly reduced by the absence of a liquid path. Therefore, the change of the single grain-size due to the temperature-related metamorphism is greatly reduced. This might explain why the single-grain-size is not observed correlated with temperature in the summer pack ice of the Ross Sea.

The significant correlation between the composite grain-size and surface temperature observed may indicate that the composite grain-size when the composite grain is formed from single grains is a strong function of temperature. Once the melt-refreeze cluster is formed, acting as a single unit, it will grow with temperature [Sommerfeld and LaChapelle, 1970].

Correlation analyses of albedo with the composite grain-size and albedo with the composite grain number density show that the correlation is significant for snow depth less than 9 cm. This may be due to the fact that the all-wave albedo has reached the saturated value when the snow depth is greater than 9 cm (cf. chapter 6). For all the snow samples up to 9cm depth, the average density is 322.7 kg m^{-3}. The semi-infinite depth for visible light to be saturated maybe deeper than 9 cm, but the semi-infinite depth for near-infrared wavelength is well below 9 cm for the composite grain-size [Warren and Wiscombe, 1980] (cf. chapter 6). Measurements on snow and glacier ice showed that all-wave albedo is generally closer to the near-infrared (0.76-0.90 μm) albedo than visible (0.52-0.60 μm) albedo, and thus the all-wave albedo can even be fitted fairly well with a function of only near-infrared albedo, which indicates that high reflectance in the visible is to a large extent compensated by low reflectance in the near-infrared (cf. Chapter 6). The all-wave albedo seems to be more or less represented by near-infrared (0.7-1.0 μm) albedo, which 9 cm snow is deep enough to be treated as semi-infinite [Knap et al., 1999]. This is also consistent with our observation that all-wave albedo is not significantly correlated with snow layers that are deeper than 9 cm. For all-wave albedo, 10 cm seems to be the most important thickness can also be seen from Grenfell et al.'s (1994) description of dependence of albedo on snow physical properties: "The albedo of a homogeneous snowpack depends on the size and shape of the grains, the angular distribution of the incident radiation field, the concentration of absorbing impurities, the surface roughness, and for layers less than about 10 cm thick, on the thickness of the layer and the reflectance of the underlying surface."

It is observed that the snow composite grain size of the top 3 cm of snow decreases with latitude from north to south. The composite grain number density is not correlated with latitude, but it is strongly correlated with albedo. For each depth of snow that is less than 9 cm, the albedo is significantly correlated with composite grain number density: the larger the number density, the higher the albedo. This is because larger composite grain number density is associated with smaller composite grain-size (section 3.6), thus larger single scattering albedo [Bohren and Barkstrom, 1974]. Multiple correlation of albedo with composite grain-size and number density show that albedo does have a relationship with both composite grain-size and number density. However, evaluation of contributions of predictor variables indicates that for prediction of albedo, grain-size is the dominant factor, and the effect of number density is masked by the effect of composite grain-size due to the high correlation between the two factors.

3.8 Conclusions

Spatial variation analyses of all-wave albedo, snow surface temperature, snow composite grain-size, composite grain number density, single grain-size, and single grain number density with latitude show that albedo increases, and temperature and snow density decrease with latitude from north to south in the central pack ice of the Ross Sea. Composite grain-size within the top 3 cm of snow is strongly correlated with latitude: the higher the latitude, the smaller the composite grain-size. For snow layers below the top 3 cm, no correlation is found between composite grain-size and latitude. No correlation between single grain-size and single grain number density at any depth is observed with latitude. Composite grain-size of the top 3 cm of snow is positively correlated with snow surface temperature, while single grain-size of the top 3 cm of snow is not.

Correlation regression analyses between albedo and snow surface temperature show that albedo decreases with increase of surface temperature in the austral summer pack ice. Composite grain-size is observed to positively correlate with snow surface temperature: the higher the surface temperature, the larger the composite grain-size. No such correlation is found for the single grain-size. Within snow up to 9 cm deep, albedo is strongly correlated with snow composite grain-size and number density: the larger the composite grain-size, the lower the albedo; the higher the number density, the higher the albedo. For the top snow layer (depth ≤ 3 cm), the best correlation results from the distribution-integrated average size model (DI), while for the lower snow layers (≥ 3 cm), the effective-radius average size model (EFF) generates the best results. However, the same analyses for the single grains show that no significant correlations are observed between albedo and single grain-size and single grain number density at any depth of snow on sea ice in summer. This indicates that formation of composite grains (clusters of single snow crystals) not only has a significant effect on the surface electromagnetic signature in microwave remote sensing [Comiso, 1983; Garrity, 1992], but also affects the absorbing and scattering properties within the solar spectrum. The density of the top 3 cm of snow decreases with increasing latitude from north to south in the ice pack. However, albedo is not observed to correlate with snow density (densification), corroborating previous experimental [O'Brien and Munis, 1975; Bohren and Beschta, 1979] and theoretical [Bohren and Barkstrom, 1974] conclusions. Strong correlation of albedo with composite grain-size and number density instead of single grain-size and number density indicates that grain bonds, whose effect on albedo has not been well investigated yet, may play an important role in determining optical properties of summer snow such as albedo, by formation of large composite grains from small single grains. It is also observed that albedo decreases with the cosine of the solar zenith angle. Because snow depths at all except 3 sites were more than 10 cm deep, albedo was not observed to significantly correlate with snow depth. But for the 3 sites with snow depth less than 10 cm, albedo does increase with snow depth. This is consistent with other observations that albedo significantly correlates with snow composite grain-size and number density within only the top 9 cm of snow. Multiple correlation and regression analyses and evaluation of contributions of predictor variables based on multiple-correlation coefficients indicate that contribution to the prediction of albedo is dominated by composite grain-size. The effect of the composite grain number density is masked by the effect of the composite grain-size due to the strong correlation between the composite grain-size and number density. Multivariate linear regression analyses of albedo with composite grain-size within multiple layers show that for a homogeneous snow cover 9 cm thick, the variation of albedo due to change in grain-size can be explained as follows: the top layer (0-3 cm) contributes approximately 86.9%, while the second layer (3-6 cm) accounts for about 10.7%, with the other (2.4%) contributed by the third layer (6-9 cm). Thus, the top 6 cm snow is the most important (97.6%) for the optical properties of snow.

ACKNOWLEDGMENTS

We are very grateful for the logistical support provided by the National Science Foundation and the Antarctic Support Associates personnel on board the *R/V Nathaniel B. Palmer*. Snow pit work was conducted by Kim Morris and her group. The research involved in this chapter was supported by the National Aeronautics and Space Administration under grant NAG5-6338 and by the National Science Foundation under grant OPP9614844.

CHAPTER 4*

Comparison between *In Situ* and MODIS-derived Spectral Reflectances of Snow and Sea Ice in the Amundsen Sea, Antarctica

ABSTRACT. The spectral albedo and directional reflectance of snow and sea ice were measured on various sea ice types, including nilas, grey ice, pancake ice, multi-year pack ice, and landfast ice in the Ross, Amundsen and Bellingshausen seas during a summer cruise in February through March 2000. Measurements were made using a spectroradiometer that has 512 channels in the visible and near-infrared (VNIR) region in which 16 of the 36 bands of the Moderate Resolution Imaging Spectroradiometer (MODIS) are covered. Directional reflectance is also retrieved from the MODIS radiometrically calibrated data (Level 1B) concurrently acquired from the first NASA Earth Observing System (EOS) satellite, Terra. The locations of the ground ice stations are identified accurately on the MODIS images, and the spectral albedo and directional reflectance values at the 16 VNIR MODIS bands are extracted for those pixel locations. MODIS-derived reflectance is then corrected for the intervening atmosphere whose parameters are retrieved from the MODIS atmospheric profiles product (MOD07_L2) for the same granule. The corresponding spectral albedo and directional reflectance with the same viewing geometry as MODIS are derived from our ground-based spectroradiometer measurements. Because the footprint of the ground spectroradiometer is much smaller than the pixel sizes of MODIS images, the averaged spectral reflectance and albedo in the vicinity of each ice station are simulated for the corresponding MODIS pixel from the

---

* This chapter is based on material published by Zhou and Li (2002a) and material to be published by Zhou and Li (2002c).

ground spectral measurements by weighing over different surface types (various ice types and open water). An accurate determination of ice concentration is important in deriving ground reflectance of a simulated pixel from *in situ* measurements. The best agreement between the *in situ* and MODIS measurements was found when the ice had 10/10 ice concentration (discrepancy range 0.2-11.6%, average 4.8%) or when one ice-type was dominant (discrepancy range 0.8-16.9%, average 6.2%). The more homogeneous the ice surface and the less variable the ice topography, the more comparable the *in-situ* and satellite-derived reflectance is expected to be.

4.1 Introduction

The albedo of snow and ice in the polar regions is a sensitive variable in the study of climate. Because the energy stored at the earth's surface and in the atmosphere comes primarily from solar radiation, albedo is an important boundary condition for the energy exchange between the atmosphere and the earth [Sellers, 1969]. As satellites can provide temporally repetitive coverage and spatially continuous data in the polar regions that are not easily accessible for ground-based measurements, monitoring the surface for the climate change study depends increasingly on satellite remote sensing [Lucht *et al.*, 2000a; 2000b; Stroeve *et al.*, 2001; 1997]. The spectral albedo for Advanced Very High Resolution Radiometer (AVHRR) channels 1 and 2 was obtained from bi-directional reflectance data assuming snow reflection is isotropic [Haefliger *et al.*, 1993]. Surface all-wave albedo was obtained from narrow-band reflectance measurements converted into a broadband albedo (0.3-4.0 μm) with atmospheric correction but without anisotropic correction [Knap and Oerlemans, 1996; De Abreu *et al.*, 1994; Li and Leighton, 1992; Saunders, 1990; Gutman, 1988; Wydick *et al.*, 1987], and with both atmospheric and anisotropic corrections [Knap *et al.*, 1998]. Comparisons of satellite-derived and *in situ* reflectance were carried out on an ice sheet [Stroeve *et al.*, 1997], landfast first-year sea ice [De Abreu *et al.*, 1994] and glaciers [Hall *et al.*, 1989; 1990].

A direct comparison between satellite-derived and *in situ* measurements is generally difficult when the ground surface is very heterogeneous. For instance, the difference is as large as 30% [Hall *et al.*, 1992] for glacier ice during summer melt and 11% for an ice sheet with 20% melt pond coverage [Stroeve *et al.*, 1997]. Comparison of satellite sensor data with *in situ* measurement over pack ice in polar seas is even more difficult for two reasons. First, the pack ice in polar seas is a dynamic surface which is in constant motion and deformation, and thus no "permanent" ground truth exists. Second, sea ice is very heterogeneous and a satellite pixel generally covers more than one ice type and different types of ice have distinctive reflectivity. To overcome these difficulties, our strategy is as follows:

a) *In situ* measurements are completed as exactly concurrent as possible with the MODIS overpasses to avoid "ground truth" shift due to ice motion. At each ice station on which the reflectance measurement is concurrent with the Terra satellite overpass, the ice types and ice concentration are coincidentally observed and recorded with *in situ* reflectance observations.

b) Using the small angle approximation [Nishihama *et al.*, 1997] and the direct matching algorithm [Patt *et al.*, 1997] to improve the navigation accuracy. To accurately and quickly locate the ground site in the imagery, the scan and frame numbers (line and column position) of a ground site are first estimated using the small angle approximation. Then, the accurate location is identified using the direct matching algorithm.

c) Using ice concentration and reflectance of various ice types to correct the ground measurement over a small area. Measurements of reflectance are carried out on as many ice types as possible that cover the main ice types encountered along the ship-track during the cruise.

The use of MODIS data to retrieve ground surface geophysical and biophysical parameters requires atmospheric correction so that the top of the atmosphere (TOA) radiance can be converted to the actual ground surface reflectance. The ground surface reflectance with atmospheric effects corrected is an estimate of the surface reflectance for the given atmospheric condition based on the TOA radiance received by the satellite sensor. Adequate atmospheric correction requires an accurate description of the profile of the variable constituents of the atmosphere that influence the TOA radiance received by the satellite sensor, and correct modeling of the absorption and scattering of solar radiation by the atmosphere. Two methods are generally used for the atmospheric corrections. One is correction schemes based on satellite-measured radiances at the top of atmosphere [Reijmer *et al.*, 2001; Dave and Gazdag 1970]. The baseline of this kind of scheme is the attenuation of the solar radiance due to intervening atmosphere is exponentially attenuated [Reijmer *et al.*, 2001; Schlatter, 1972; Liljequist, 1956]. The attenuation coefficient or the optical depth is obtained beforehand by comprehensive radiative transfer models [Koepke, 1989; Dozier and Marks, 1987] so that atmospheric correction is possible. The accuracy depends on the correctness of the optical depth for the correction. This method is widely used for its simplicity, especially for clear sky conditions [Zhou *et al.*, 2001; Knap and Oerlemans, 1996; De Abreu *et al.*, 1994; Hall *et al.*, 1990]. The other method for atmospheric corrections is comprehensive radiative transfer models such as 6S [Vermote *et al.*, 1997a; 1997b; Tanré *et al.*, 1992], STREAMER [Key and Schweiger, 1998], LOWTRAN [Kneizys *et al.*, 1988], and MODTRAN [Kneizys *et al.*, 1996], which consider gas absorption and scattering by the main components of the atmosphere.

The MODIS instrument on the Terra satellite was designed to provide improved monitoring of the earth for land, ocean, and atmospheric research and to meet the needs of global change research. MODIS data products are categorized into five levels in order of increasing level of processing. Level 1B (L1B) products are generated from the raw instrument data (Level 0) by appending geolocation and radiometric calibration data. Multiple onboard calibration systems are used in the MODIS instrument to ensure a calibration accuracy of 2% relative to the solar radiance [Guenther *et al.*, 1998]. The MODIS surface reflectance product, MOD 09 is a seven band-product computed from MODIS L1B land bands 1, 2, 3, 4, 5, 6 and 7. Although the products are atmospherically corrected, only three bands are covered by the spectrometer (330-1060 nm) we used, which covers 16 bands of the 20 MODIS VNIR bands. Thus, we used the L1B product, and the atmospheric corrections for the 16 VNIR MODIS bands covered by the ground-based spectrometer were accomplished using 6S radiative transfer code as described bellow.

In this chapter, a comparison is made between the 1km MODIS-derived surface reflectance and that measured *in situ* concurrently on the snow and sea ice surface. With validation of MODIS sea ice products as the primary purpose, we participated in a cruise to the Ross, Amundsen and Bellingshausen seas, Antarctica, aboard the *R/V Nathaniel B. Palmer* in February and March, 2000 (Figure 4.2). Measurements were made at 22 ice stations. Among the 22 daily measurements, 3 measurements (3 Julian days shown in Figure 4.2) were under very clear sky conditions. All these sites are in the Amundsen Sea and are chosen for detailed comparison and analyses in this study.

4.2 Matching Algorithm of a Ground Station Position within a MODIS Image Granule

The MODIS data sets used for this comparative study are the MODIS L1B 1km earth-view (EV) product [Guenther *et al.*, 1998] and the MODIS Atmospheric Profiles product (MOD07_L2) [Menzel and Gumley, 1998]. Both products are stored in granules that are derived from approximately five minutes of continuous instrument data in the Hierarchical Data Format for Earth Observing System (HDF-EOS). Reflectance of the ground surface is retrieved from the L1B products and the atmospheric parameters for atmospheric correction are retrieved from the MOD07_L2 products for the same granule.

For satellite measurements to be comparable with the ground measurements, one important step is to correctly locate the ground site in the imagery. For MODIS L1B 1km products, the scientific data sets (SDSs) are generally 2030 (scan lines) x 1354 (frames). These data were not geometrically rectified and registered to a conventional map projection, thus the ground size of a pixel changes with pixel location. Data collected at nadir have a nominal spatial resolution of 1km and become coarser with distance off nadir. The ground instantaneous spatial resolution expands by a factor of four towards the end of each scan (±55°) due to the earth curvature, as viewed from the satellite altitude of

705 km. In this chapter, when a pixel is referred to the ground surface, it is referred to the ground field of view of a single detector sample from one of the 1km nadir spatial resolution MODIS bands. The geographical data sets in the L1B products are used for the geolocation of the ground site in the imagery. For each ground pixel in MODIS L1B products, the ground height and zenith angles are measured with respect to the local ellipsoid normal, and the azimuth angles are relative to local geodetic north.

The MOD07_L2 product consists of total-ozone burden, atmospheric stability, temperature and moisture profiles, and atmospheric water vapor. All of these parameters are produced at 5 × 5 km pixel spatial resolution when at least 9 of the 25 1km sub-pixels are cloud-free. Thus, the corresponding geographical data set for a granule is 406 (lines) x 271 (frames), each point representing a 5x5 pixel subset in the L1B SDSs. The mapping relationship between the MODIS L1B product and MOD07_L2 product for the same granule is given by

$$\begin{aligned} n_s &= 5(n_s^{'} - 1) + 3 \\ n_f &= 5(n_f^{'} - 1) + 3 \end{aligned} \tag{4.1}$$

where n_s and n_f are the scan line number and frame number in the SDSs of L1B product and $n_s^{'}, n_f^{'}$ are the line number and frame number in the corresponding geographical data sets in MOD07_L2 product for the same granule.

The retrieval processes of pixel location for the ground sites includes the following main steps:

i) Estimating the approximate scan line number and frame number of the pixel that contains the ground measurement site. This is accomplished by an inverse mapping algorithm such that for a given ground point in geodetic coordinates (latitude and longitude) the matching pixel within a MODIS imagery granule [Nishihama *et al.*, 1997] will be found.

ii) Extracting a small candidate pixel patch around the estimated pixel obtained in the first step.

iii) Applying a direct match method to accurately locate the pixel that contains the measurement site [Patt *et al.*, 1997]. If the optimal pixel lies at the edge of the patch, shift the patch so that it centres at the newly optimal pixel. This process continues until the optimal pixel lies inside the patch.

Once the pixel is found, WebWinds (an interactive science data visualization system) [Elson *et al.*, 2000] is used to display the scaled integer (SI) for all the bands of the pixel. The reflectance is then calculated using the procedure described in section 4.1

Figure 4.1 shows the flow chart of the processing methodology to locate ground station position in the MODIS imagery granule. Details of the main steps are illustrated in the following subsections.

4.2.1 Estimation of the Pixel Location of a Ground Station in a MODIS Granule

This step is necessary to reduce errors in the matching algorithm to locate the ground control point. Based on the estimated pixel position, a small candidate pixel patch centred on the estimated pixel is set up. This way, the real pixel of the ground station can be found correctly and quickly.

Supposing the geodetic coordinates of a ground station at which the ground measurement is carried out are (θ_g, φ_g), where θ_g = latitude in degrees and φ_g = longitude in degrees, the normalized unit vector of the ground point is defined as

$$\vec{v} = (\cos\theta_g \cos\varphi_g, \cos\theta_g \sin\varphi_g, \sin\theta_g) \qquad (4.2)$$

If the unit vectors of the four corner pixels which are defined as the first frame of the first scan line (1), the last frame of the first scan line (2), the first frame of the last scan line (3) and the last frame of the last scan line (4) in the MODIS granule are

$$\vec{v}(i) = (\cos\theta_i \cos\varphi_i, \cos\theta_i \sin\varphi_i, \sin\theta_i) \quad (i = 1, 2, 3, 4) \qquad (4.3)$$

then, the scan number for the location of ground site $\vec{v}$ is estimated from the small angle approximation to be

$$n_s = N_s\left(0.5 + \frac{\vec{v}\cdot\left(\vec{v}_{n1} + \vec{v}_{n2}\right)}{\vec{v}_{c2}\cdot\vec{v}_{n1} - \vec{v}_{c1}\cdot\vec{v}_{n2}}\right) \qquad (4.4a)$$

with

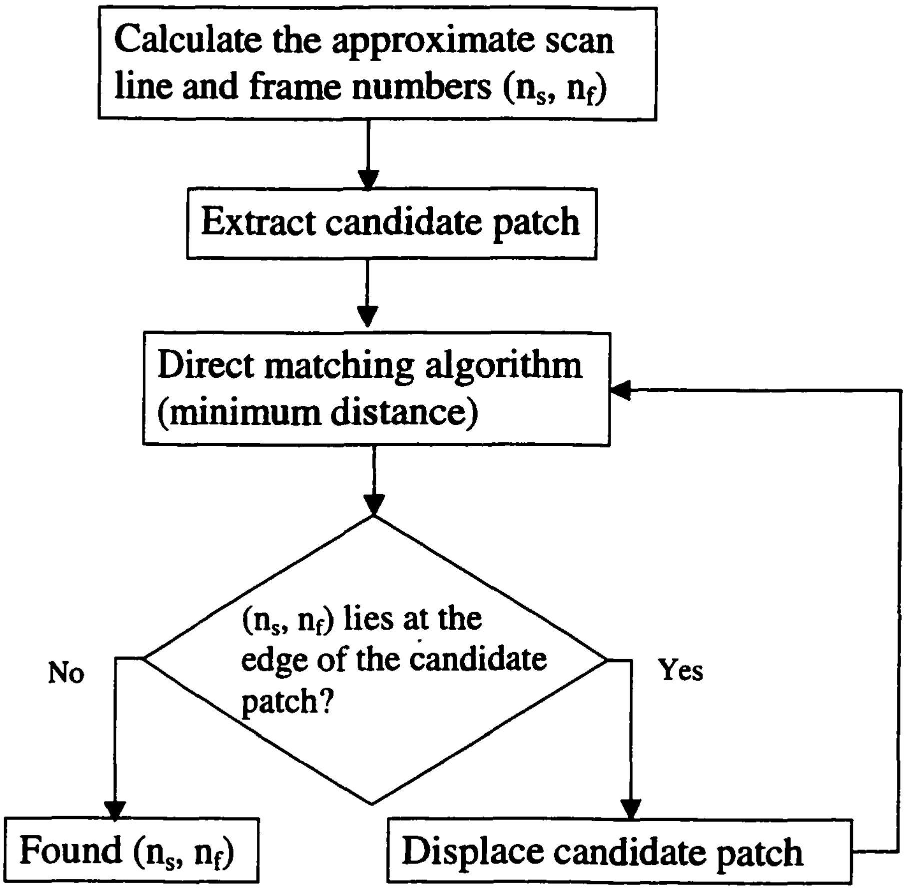

Figure 4.1 Flow chart for matching a ground station in the MODIS image granule.

$$\vec{v}_{n1} = \frac{\vec{v}(2)\times\vec{v}(1)}{\left|\vec{v}(2)\times\vec{v}(1)\right|},\quad \vec{v}_{n2} = \frac{\vec{v}(4)\times\vec{v}(3)}{\left|\vec{v}(4)\times\vec{v}(3)\right|},\quad \vec{v}_{c1} = \frac{\vec{v}(2)+\vec{v}(1)}{\left|\vec{v}(2)+\vec{v}(1)\right|},\quad \vec{v}_{c2} = \frac{\vec{v}(4)+\vec{v}(3)}{\left|\vec{v}(4)+\vec{v}(3)\right|}$$

where N_s is the total scan lines in the granule [Nishihama *et al.*, 1997].

The frame (sample) number is estimated as

$$n_f = N_f/2 + 705\cdot\tan^{-1}\left(\frac{\sin\alpha}{r/R-\cos\alpha}\right) \tag{4.4b}$$

with

$$\alpha = \sin^{-1}\left(\frac{\vec{v}\cdot\left(\vec{v}_{c1}\times\vec{v}_{c2}\right)}{\left|\vec{v}_{c1}\times\vec{v}_{c2}\right|}\right),$$

where r is the distance from the earth centre to the spacecraft and R is the local radius of the Earth. N_f is the total frame (sample) number in the granule. The number 705 is the number of frames in a MODIS granule covered by a unit radian in scanning angle.

The geodetic coordinates of ground measurement site are given by the Global Positioning System (GPS) aboard the research vessel. The latitude and longitude of the four corners in the MODIS imagery granule are given in the geolocation data sets. Using Equation (4.4), the position of the ground site in the imagery granule is estimated.

4.2.2 Direct Matching

Once the station pixel (n_s, n_f) is estimated, a candidate square patch consisting of 11x11 pixels, centred on (n_s, n_f), is extracted from the imagery granule. The direct matching algorithm is used to find the exact pixel that contains the ground station [Patt *et al.*, 1997]. The ground distance between the station and the centre of each pixel in the patch is calculated by

$$S = R\cos^{-1}\left[\sin\theta_t\sin\theta' + \cos\theta_t\cos\theta'\cos\left(\varphi_t-\varphi'\right)\right] \tag{4.5}$$

where (θ', φ') define the geographical location of the candidate pixels within the patch. The direct algorithm is used to find the nearest pixel to the ground station position. However, if the optimal pixel in the current search lies at the edge of the patch, the patch is displaced to the centre of the current optimal pixel and the matching process is run again until the optimal pixel lies within the candidate patch. This way, the found pixel is the pixel that contains the ground station.

The above methodology is applied to the three MODIS L1B 1km granules. The pixels found to match the ground stations and the distances between the station position and the centre of the pixel are shown in Table 4.1. The design of the Earth location algorithm that generated the Earth location data was guided by the accuracy requirement that the Earth location data are accurate to 0.1 pixel [Nishihama *et al.*, 1997]. The geolocation error is expected to be 100m for the nadir pixels. As the spatial resolution of the pixel at nadir is 1km, off nadir pixels have coarser spatial resolution. Since the distance between the ground site and the centre of the image pixel is less than 0.707 km for the image granules of day 65 and day 70, it is evident that the ground stations lie well within the pixels. For the day 78 granule, the distance is over 1km. Considering that the pixel is very much off nadir and the pixel size is larger than 2km, the ground site is still within the pixel.

Table 4.1 Match of the image pixel and position of ground station

Day (Granule)	Scan line	Frame line	Center of pixel	Station position	Distance between (m)	Ozone (cm-atm)	Water vapor (g cm^{-2})
65	1752	789	74.1205°S, 109.665°W	74.1215°S, 109.674°W	294.869	0.2370	0.9623
70	957	643	71.7395°S, 115.135°W	71.7439°S, 115.1315°W	503.095	0.3423	1.073
78	874	1222	74.2611°S 104.676°W	74.2554°S 104.704°W	1053.674	0.3199	0.607

4.3 Surface Reflectance from Ground Measurements

Ground measurements are used to assess the accuracy of MODIS-derived reflectance in discrete reflective spectral bands. The time to make the daily *in situ* measurements was in line with the overpass time schedule for the Terra satellite obtained. Study sites are shown in Figure 4.2, with the Julian day indicated. The cruise track is shown in the inset

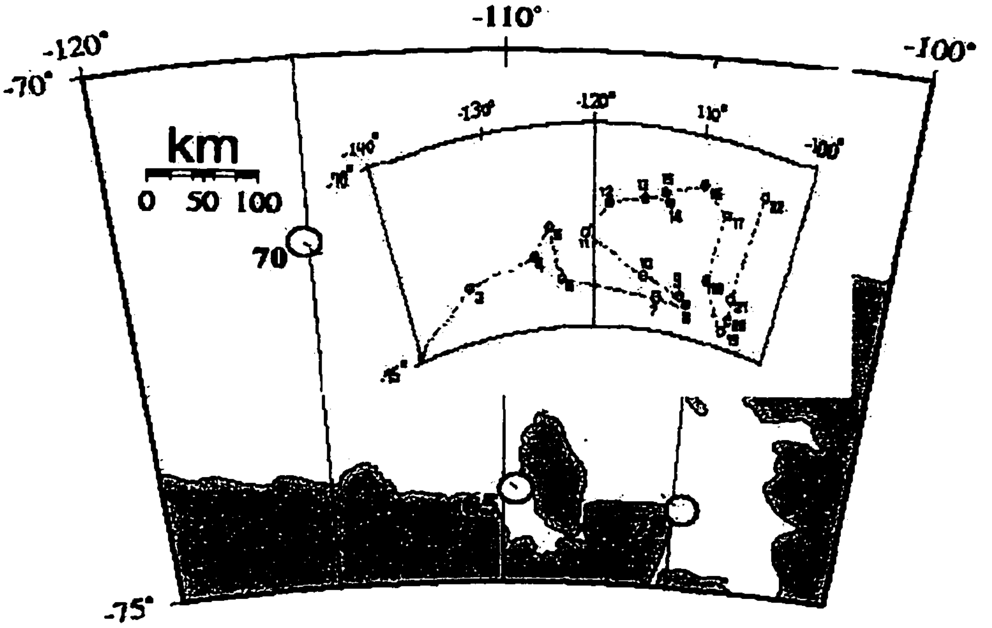

Figure 4.2 Field study sites on the pack ice in the Amundsen Sea. Numbers are Julian days in 2000. Inset map shows the NBP-01 cruise track and ice station (open cycle) number in the Amundsen and Bellingshausen seas. The first two ice stations in the Ross Sea are not shown.

map, with the ice station number explicitly noted. As many ice types as possible were taken as platforms for the reflectance measurements. For thin ice, the measurements were carried out from a Zodiac inflatable. Ice types on which the measurements were made included landfast ice, multiyear year (MY) ice, first year (FY) young white ice, new ice 5-10cm thick including cemented pancake ice and young grey ice, new ice 2-4 cm thick including pancake ice and nilas.

4.3.1 Direct Ground Measurement

Spectral albedo and directional reflectance of snow and sea ice were measured at each ice station. Spectral albedo was measured using a high-spectral-resolution fiber optic spectroradiometer manufactured by Analytical Spectral Devices, Inc. (ASD). The spectroradiometer measures spectral reflectance and spectral radiance at 512 spectral bands from 333.65nm to 1064.9nm, with a spectral resolution of 3nm. Sixteen of the 36 bands of the Terra MODIS are in 512 channels in the visible and near-infrared (VNIR) region. The spectral albedo measurement was performed with the spectroradiometer and a remote cosine receptor (RCR) of a hemispherical field of view (FOV). The instrument setup was the same as described previously [Zhou *et al.*, 2001]. The spectral albedo was acquired by measuring the downwelling spectral irradiance, followed immediately by measuring the upwelling spectral irradiance using the RCR. To reduce the system errors and errors caused by the fluctuations of the radiation field, several samples, each being the average of 10 scans, for both upwelling and downwelling spectral irradiances were collected.

Among the 22 ice stations, 14 measurements of spectral albedo were made, of which 7 were on MY ice floes, 3 on new grey ice (5-10cm thick), 1 on first-year (FY) young white ice, 2 on new ice (2-4cm thick) and one on landfast ice. The cruise was a multi-purpose mission. Time allocated to each science group was limited at each ice station. Exhaustive reflectance measurements on all ice types at one ice station within one imagery pixel were not possible. The ice in the Amundsen Sea was predominantly multi-year ice (survived at least one summer) in the later summer/ early autumn of the year.

Young white ice was seldom seen during the cruise. New ice began to form at this stage. Thus the number of measurements on young white ice and new ice was very limited. As the Ross and Amundsen seas are the least studied areas in the southern ocean, we do not have many data available in literature with which we can compare our measurements. However, from our 7 measurements for multi-year ice, the maximum deviation of spectral albedo is 3.8% at 1.06 μm. For first-year ice, the variation of spectral albedo in a specific region is expected to be smaller than multi-year ice because first-year ice is less heterogeneous [Gogineni *et al.*, 1992]. Therefore, the contribution to the concentration-correction of *in situ* reflectance by variation of spectral albedo of young white ice and new ice is deemed to be small. Thus, the average of measured data for the same ice type on the whole cruise is used to calculate the ground reflectance at 1km satellite spatial resolution. Reflectance obtained this way is also called ice concentration weighted or ice concentration corrected ground reflectance at satellite spatial resolution. The average of the measurements for any ice type was taken as the representative spectral albedo of that ice type.

Table 4.2 Look-up table for the concentration-correction of reflectance in MODIS bands covered by the ground spectroradiometer.

MODIS band	MY	FY white	New ice (5-10cm)	New ice (2-4cm)
1	0.951	0.685	0.356	0.169
2	0.883	0.653	0.314	0.100
3	0.920	0.685	0.296	0.176
4	0.935	0.697	0.346	0.183
8	0.881	0.687	0.256	0.175
9	0.913	0.685	0.278	0.175
10	0.925	0.686	0.310	0.178
11	0.933	0.692	0.335	0.181
12	0.934	0.696	0.344	0.183
13	0.949	0.680	0.353	0.164
14	0.950	0.679	0.354	0.162
15	0.935	0.668	0.341	0.133
16	0.867	0.649	0.306	0.092
17	0.826	0.638	0.279	0.060
18	0.815	0.626	0.240	0.007
19	0.813	0.626	0.239	0.010

For this study, only four types of ice are typical for the ice stations of day 65, 70 and 78 (Figure 4.2), and the spectral albedo of these ice types is shown in Figure 4.3. Based on these measurements, the spectral albedos of bands corresponding to the MODIS sensor are extracted and put into a look-up table (LUT) for the calculation of the ground bidirectional reflectance at the spatial resolution of 1km. This LUT is given in Table 4.2 and will be used in section 2.2 to calculate ice concentration weighted ground reflectance. Within the ice types shown in Figure 4.3, MY ice is generally associated with deepest snow and fine snow grain size, and thus has the highest spectral albedo. New ice (2-4 cm thick) including pancake ice and nilas seldom has snow on the surface and often has liquid water on surface. It has the lowest spectral albedo. Directional reflectance measurements were carried out using the spectroradiometer and a fore-optic sensor of 3° field of view. The measurement of bidirectional reflectance proceeded in a similar fashion to that previously described by Zhou and Li (2000a). At each fixed viewing zenith angle (beginning at nadir), measurements were carried out in the azimuth domain at 10° intervals from the forward scattering direction in the principal plane (relative azimuth angle $\varphi=180°$) to the backward scattering direction ($\varphi=0°$). After each scan in the azimuth, the viewing zenith angle was increased by 10° for a new scan in the azimuth as far as 80°. The same viewing geometry as the MODIS sensor is later interpolated from the set of measurements at multiple view angles after the satellite viewing geometry has been retrieved from the MODIS radiometric calibration product (L1B) so that the *in situ* and satellite-retrieved reflectance can be directly compared without the necessity of viewing geometry correction [Jin and Simpson, 2000].

The ice concentration was estimated by observation from the bridge of the research vessel. According to the technique of ship-based observation of sea ice characteristics [Worby and Allison, 1999], a maximum of three dominant ice types and open water (OW) were identified for one observation. Ice type, ice concentration and open water concentration were recorded. For stations where more than three ice types were present, the most optically (visually) similar types were grouped and amalgamated into one of the three categories. Data obtained by ship-based observation were blended with images

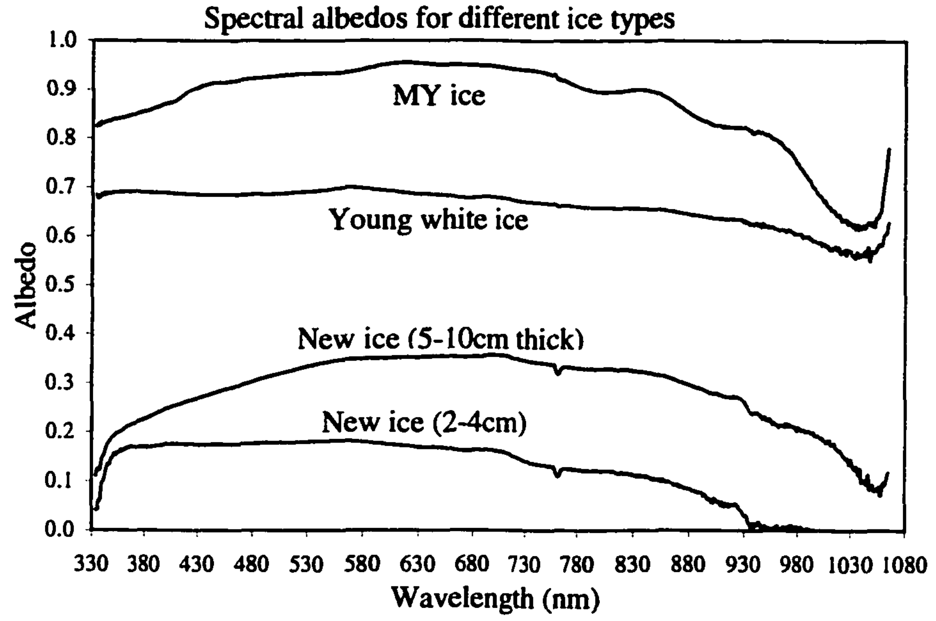

Figure 4.3 Spectral albedo for different ice types measured in the Ross, Amundsen and Bellingshausen seas during the 2000 cruise. Each curve corresponds to the average of all measurements on the same ice type.

Table 4.3 Ice types and concentrations at each of the three daily stations

Day station	*65*	*70*	*78*
Primary ice type (concentration)	MY (6/10)	MY (4/10)	Young grey ice (3.5/10)
Second ice type (concentration)	Young white ice (3/10)	New ice (5-10cm) (3/10)	—
Third ice type (concentration)	New ice (5-10cm) (1/10)	—	—
OW concentration	0/10	3/10	6.5/10

Notes: MY=multiyear ice; OW=open water. Ice concentration of a specific type of ice is the areal coverage of the ice type over the whole area visible, expressed in tenths.

taken coincidentally using a digital camera and the final types and concentration data for each measurement site were obtained. The data for the three measurement sites are given in Table 4.3. Measurements of spectral albedo and bidirectional reflectance were taken on the primary (highest concentration) ice type floe. For the site of day 65, ice concentration was 10/10. Reflectance was measured on the multi-year ice that was the dominant type (6/10). Young white ice (3/10) was the second ice type. New ice (nilas) (5-10 cm thick) only accounted for 1/10. As both the young white ice and MY ice are very reflective, this site was characterized as a very reflective surface. On the site of day 70, only two ice types existed. MY ice was the dominant (4/10) over the new ice (nilas and pancake ice) (5-10 cm thick). Measurements were made on the MY ice. The site of day 78 was the simplest of the three. Only one ice type existed. Ice concentration of the young grey ice was just 3.5/10, as obtained from the average of the observation and images. Along with the measurements of spectral albedo and bi-directional reflectance, visibility and snow and ice surface temperature were also recorded.

4.3.2 Ice-concentration-corrected In Situ Reflectance

A simulated pixel often contains more than one type of sea ice. A reflectance measurement was usually taken on one representative ice floe. Based on the statistical results of spectral albedo measurements for various sea ice types shown above, the concentration-correction scheme of the *in situ* reflectance is as follows

$$R_{correct} = f_1 R_{measured} + f_2 R_2 + f_3 R_3 + (1 - f_1 - f_2 - f_3) R_{water} \tag{4.6}$$

where $R_{correct}$ is the *in situ* reflectance corrected for ice concentration, $R_{measured}$ is the directly measured reflectance at a specific viewing angle on the primary ice type. f_1, f_2, f_3 are the concentrations of the primary, secondary and tertiary ice types respectively. R_2, R_3, and R_{water} are the reflectances of the secondary ice type, tertiary ice type, and open water respectively. The fourth term on the right hand side is from the contribution of open water. R_2, R_3, and R_{water} are, however, not available at each site. To circumvent the unavailability, the general spectral albedo database presented in Figure 4.2 is used for replacement. Spectral albedo of water is taken from Allison *et al.* (1993). This simplification is equivalent to neglecting the anisotropy of reflectance of the secondary and tertiary ice types and open water. Although this can cause deviations of the calculated reflectance from the actual reflectance [Greuell and de Ruyter de Wildt, 1999; Knap and Reijmer, 1998; Warren *et al.*, 1998], when insufficient knowledge of anisotropy of the surface is available, isotropic reflectance is assumed. For this reason, it is still widely used in the conversion of narrowband satellite reflectance to broadband albedo [Knap *et al.*, 1999; Gratton *et al.*, 1993; Duguay and LeDrew, 1992]. In any event, errors resulting from the isotropic assumption in concentration-corrected reflectance in Equation (4.6) depend largely on the representativity of the primary ice type within the pixel on which *in situ* reflectance was made. The higher the concentration of the primary ice type, the smaller the errors resulted from this simplification.

Differences between the directional reflectances directly measured and concentration-weighted for the three sites are shown in Figure 4.4. At the station of day 65, ice concentration was 10/10, with the primary ice type being the dominant one (Table 4.3). The correction is mainly at the blue light bands. The average correction of the 16 bands is 8.5%, with largest correction (16.5%) in band 8 (412 nm) and smallest correction (3.3%) in band 17 (905 nm). At the measurement site on day 70, ice concentration was 7/10, with primary ice type (MY ice) 4/10 and new ice (5-10cm thick) 3/10. The average

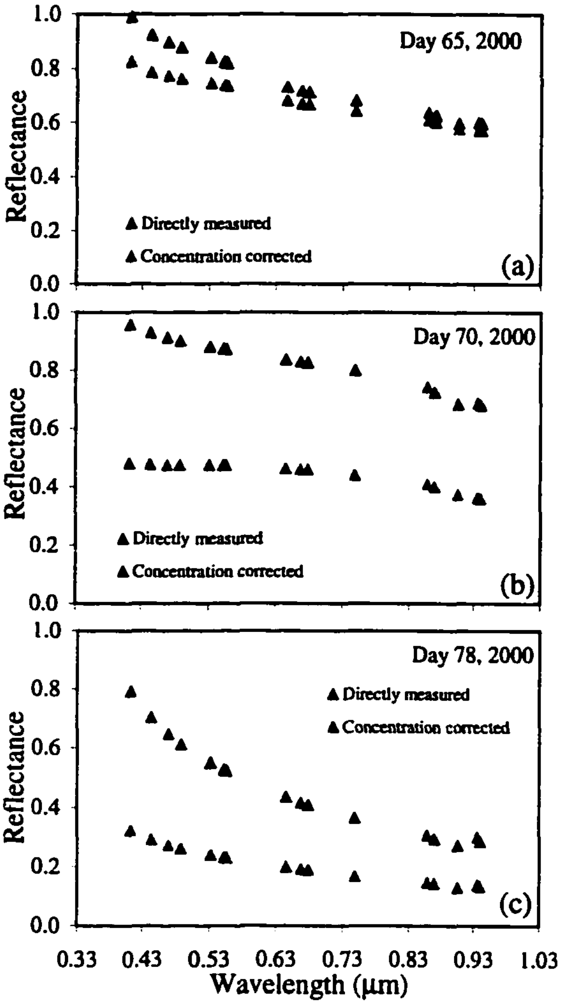

Figure 4.4 Directly-measured and concentration-weighted bidirectional reflectances for the four ground sites shown in Figure 4.2. Panels (a), (b) and (c) correspond to Days 65, 70 and 78, 2000, respectively.

correction for the 16 bands is 46.3%, with the largest correction (49.8%) at band 8 (412nm) and least correction (44.6%) at band 14 (678nm). The ice-concentration correction for this site is remarkable because the concentration of the primary ice type is small (4/10), even though the measurement was made on the most reflective type of ice. The shapes of the spectral reflectance before and after the concentration correction are quite similar if the primary ice type is overwhelmingly dominant in reflection. For the site of day 78, ice concentration was only 3.5/10, and the correction is large for all bands as it is for the day 70 site. As only one ice type is available, correction for this case is simple. The average correction from the directly measured reflectance is 55.3%, with the largest correction (59.3%) at band 8 (412nm) and the smallest (51.7%) at band 16 (869nm). The shapes of the spectral reflectance curves before and after the concentration correction are similar, just as day 70.

4.4 Ground Reflectance Retrieved from MODIS Data

Once the station pixel is located in the MODIS granule, the scaled integer (SI) value of the pixel can be obtained from the SDSs along with the reflectance scale and offset from the SDSs attributes and solar zenith angle from the global attributes of the granule. Then, reflectance can be calculated from Equation (4.7). Reflectance obtained this way is just the apparent reflectance at the top of the atmosphere (TOA), without atmospheric corrections. However, atmospheric disturbance of the reflectance measured at satellite platforms is far from negligible (as much as 20% is possible [Stroeve *et al.*, 1997]), especially for shortwave bands. To compare with the ground measurements, atmospheric effects must be removed from the apparent reflectance. In the rest of the present section, the apparent reflectance is derived first from the MODIS VNIR bands. Then atmospheric effects are corrected by using the 6S radiative transfer algorithm [Tanre *et al.*, 1992; Vermote *et al.*, 1997a; 1997b; 1997c] to obtain the surface reflectance.

4.4.1 Retrieval of Reflectance and Viewing and Illumination Geometrical Parameters

After the scan line number and the frame number of the pixel is found using the direct matching algorithm, the apparent spectral reflectance of band B for the pixel can be obtained with

$$\rho^B = R^B_{scale}(SI^B - R^B_{offset}) / \cos\theta_0 \tag{4.7}$$

where R^B_{scale}, R^B_{offset} are reflectance scale and reflectance offset for band B that are stored as metadata attributes of SDSs [Guenther *et al.*, 1998]. θ_0 is the solar zenith angle at the pixel. SI^B is the scaled integer value of the SDSs stored in the L1B granule files of the pixel for band B. Along with solar azimuth angle, sensor zenith angle and sensor azimuth angle, solar zenith angle is one of the L1B HDF-EOS SWATH metadata stored as global attributes (MODIS Characterization and Support Team (MCST) 2000). These parameters are necessary variables to retrieve apparent reflectance and perform atmospheric corrections to obtain the ground reflectance from satellite sensor data. As bands 13 and 14 are two sets of the same spectral channel (one for high gain and the other for low gain, when the two channels for each band are not saturated), the average is taken as representative.

To display the global and SDSs attributes, a public domain HDF reader program, HDF Inspector available on line at http://www.space-research.pt/ is used. Using HDF Inspector, viewing and illumination geometrical parameters are retrieved from the three days' granules. Results are shown in Table 4.4. Using WebWinds [Elson *et al.*, 2000], SI^B values are retrieved and thus the spectral reflectance is obtained from Equation (4.7). The apparent reflectances for the three stations are shown in Figure 4.5. Table 4.4 lists the valid band numbers whose SI values are usable for the station pixels. MODIS bands cover 20 VNIR bands. However, bands 8 through 19 are for study of ocean colour, phytoplankton and biogeochemistry. These bands are generally in high gain mode. Thus for high reflective surfaces, the sensors of these bands are saturated, and the SI values in L1B products are negative and unusable. For day 65's granule, usable bands include band 1 through 9, band 17 to band 19, and band 26. Sensors of bands 10 through 16 are

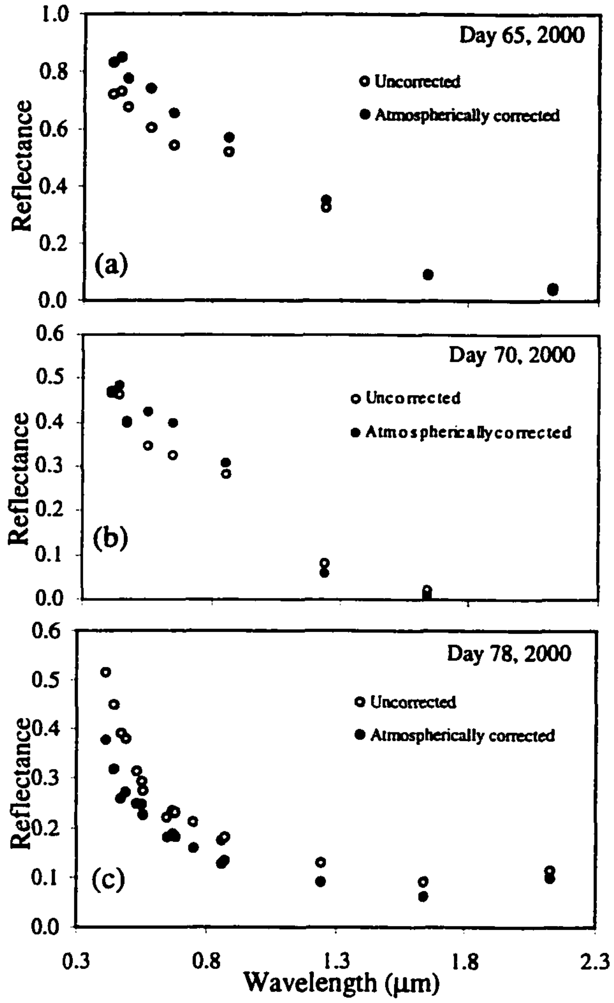

Figure 4.5 Comparison of bidirectional reflectances retrieved from MODIS L1B products with and without atmospheric corrections. Panels (a), (b) and (c) correspond to Days 65, 70 and 78, 2000, respectively.

saturated. For day 70's granule, only sensors of bands 13 to 15 are saturated because of lower ice concentration for the station pixel. But for band 7 (2.13 μm), the data are unusable due to the failure of the aggregation algorithm from 500m to 1km spatial resolution. For day 78's granule, due to the low reflectivity of the pixel, all the 20 bands are usable, with no bands saturated.

Table 4.4 MODIS data summary for the ground (day) station pixels

Day (granule)	Start of the granule (UTC time)	Solar zenith	Solar azimuth	Sensor zenith	Sensor azimuth	Valid Bands
65	16:15	73.758°	50.016°	10.032°	-62.632°	13
70	16:35	74.292°	50.738°	03.216°	112.082°	16
78	17:25	75.13°	25.78°	51.00°	-83.88°	20

4.4.2 Retrieval of Atmospheric Parameters

Atmospheric parameters such as total-ozone burden, temperature and moisture profiles and atmospheric water vapor are retrieved from MODIS MOD07_L2 products. These products are at 5km×5km spatial resolution, while the reflectance value is retrieved from MODIS L1B product at 1-km spatial resolution. Once the scan line and sample line of the location of the ground site (n_s and n_f) are found, as done in section 3, location of the ground site (n_s' and n_f') in the MOD07_L2 images is obtained by inverse mapping of Equation (4.1). Just as is done for the retrieval of directional reflectance, the atmospheric parameters are retrieved [Menzel and Gumley, 1998]. Total ozone contents and total column precipitable water vapor retrieved from infrared channels are shown in Table 4.1. Ozone burden ranges from 0.237 cm-atm (day 65) to 0.3423 cm-atm (day70) and water vapor ranges from 0.607 g cm^{-2} (day 78) to 1.073 g cm^{-2} (day 70).

4.4.3 Atmospheric Correction of Retrieved Reflectance from MODIS Data

The retrieved apparent spectral reflectance from MODIS data deviates from the ground reflectance due to gaseous absorption and scattering by atmospheric molecules, water vapor and aerosols. Without atmospheric correction, Hall *et al.* (1990) showed that the ground reflectance retrieved from Landsat images was 5-20% higher than the apparent reflectance over the Forbindels glacier in Greenland. In order to obtain the ground reflectance from the apparent reflectance, atmospheric effects need to be corrected with radiative transfer models. The 6S radiative transfer model is believed to be accurate over a variety of different surfaces [Mithchell and O'Brien, 1993] and thus is widely used for atmospheric correction [Stroeve *et al.*, 1997; Lucht *et al.*, 2000a; 2000b]. Atmospheric correction of the MODIS satellite reflectance for this study was performed using the 6S radiative transfer model [Vermote *et al.*, 1997a; 1997b] with a few modifications. The apparent reflectance obtained in section 4.1 is atmospherically corrected in the following way:

1) The 6S algorithm is extended to include the 20 MODIS VNIR bands of our concern. This involves updating and supplementing the relative spectral response (RSR) (normalized to unity at peak) for each band. The Terra MODIS relative spectral response L1B Look-Up Table (LUT) which contains the in-band RSRs for each sensor of all 36 spectral bands can be downloaded from the MODIS Characterization Support Team (MCST) homepage mcstftp.gsfc.nasa.gov using the ftp utility. For the purpose of atmospheric correction, the average RSRs of all the detectors for each band is taken as the RSR for that band.

2) The standard Arctic summer atmospheric profile (pressure, temperature, ozone and humidity) is selected as the atmospheric profile model, with the specific profile modified so that total ozone contents and total column precipitable water vapor are equal to those retrieved from the MOD07_L2 products (section 4.2). Maritime aerosol model is chosen for aerosol with meteorological visibility ranging from 30 km (day 65), 15 km (day 70), to 40 km (day 78) recorded from the ship's bridge immediately before occupation of each ice station. This corresponds to aerosol optical depths of 0.20, 0.32, and 0.17, respectively, at 0.55 μm.

3) With the MODIS-retrieved apparent reflectance, terrestrial parameters (solar zenith and azimuth angles), viewing geometrical parameters (viewing zenith and azimuth

angles) from L1B products, and atmospheric parameters (ozone burden and water content) retrieved from MOD07_L2 products as inputs, the corrected reflectance is obtained by running the 6S code band by band.

Reflectances at the three measurement sites shown in Figure 4.2 before and after atmospheric correction are shown in Figure 4.5. Panels (a), (b), and (c) correspond respectively to day 65, 70 and 78. For the satellite-derived reflectance of the MY ice dominated site of day 65 (Figure 4.5a), the average change due to atmospheric correction is 13.8% with the maximum change being 22.6% at band 4 (0.555 μm) and the minimum change 2.9% at band 6 (1.64μm). At the site of day 70, where MY ice floated in new ice and open water background, the visibility was low compared with other days, but the correction is almost the same. The average atmospheric correction is 13.0%, with the maximum change being 25.3% at band 5 (1.24 μm) and the minimum change 0.8% at band 8 (0.412 μm). For day 78 with only 3.5/10 young ice concentration, the average atmospheric correction is 24.0%, with the maximum change being 33.9% at band 3 (0.469 μm) and the minimum change 13.0% at band 7 (2.13 μm). Reflectances of all bands shown in Figure 4.5c after atmospheric correction are smaller than uncorrected values.

For a glacier surface, the atmospheric correction based on the Dave and Gazdag (1970) method results in a 5-20% increase in reflectance for the Landsat TM bands [Hall *et al.*, 1989; 1990]. At the site of day 65, ground conditions were comparable to but still more heterogeneous than a glacier ice surface. The increase of reflectance due to atmospheric correction ranges from 2.9% to 22.6%.

4.5 Comparison of *In Situ* Measurements with MODIS-derived Reflectance

MODIS-derived and *in situ* reflectances have been compared in order to assess the utility of the MODIS reflective bands for obtaining realistic reflectance measurements of snow and sea ice in the polar regions. From the above sections, the *in situ* measured bidirectional reflectance at the three sites on sea ice floes under clear sky conditions are ice concentration-weighted or corrected based on the spectral reflectance measurements of different types of ice and ice concentration observations at the measurement site. The MODIS-derived reflectances concurrently acquired with the *in situ* measurements are atmospherically corrected with the atmospheric parameters used for the correction retrieved from MOD07_L2 products for the same granules. Comparison of the *in situ* measurements with the satellite-derived reflectances is shown in Figure 4.6. In this section, *in situ* reflectance is referred to as the concentration-corrected ground-based measurement while satellite-derived reflectance is referred to as the atmospherically corrected space-based reflectance. Figures 4.6a to 4.6c correspond to day 65, 70 and 78 respectively. The best agreement occurs for day 65 (Figure 4.6a). The MODIS-retrieved reflectances are generally larger than the ground measurements for the available MODIS bands. For this site, the average difference between *in situ* and satellite-derived reflectances is 4.8%, with the largest discrepancy 11.6% at band 9 (0.443μm) and the smallest difference 0.2% at band 9 (0.858 μm). For day 70 (Figure 4.6b), good agreement occurs for bands in visible regions but the agreement deteriorates at near-infrared bands. The average difference between the ground- and space-based measurements is about 8.2%. The best agreement is within 1.2% at band 10 (0.488 μm) and the worst is 25.1%, at band 2 (0.858 μm). In the visible regions, MODIS-derived reflectances are larger than the *in situ* measurements, but the differences are small. In the near infrared regions, MODIS-derived reflectances are smaller than ground measurements, and the differences are much larger than those in the visible bands. In the case of day 78 (Figure 4.6c), the MODIS-retrieved reflectances in the visible spectrum regions are larger while in the near infrared regions they are smaller than the *in situ* measured reflectances. For this site, the average difference between the *in situ* and satellite-derived reflectances is 6.2%, with the largest discrepancy (16.9%) at band 8 (0.412 μm) and the smallest discrepancy (0.8%) at band 4 (0.555μm).

One of the error sources is the error in estimation of concentrations of different ice types. To see the effect of the errors in ice concentration estimate on the comparison of MODIS-derived and *in situ* reflectances, let's take the site of day 78 as an example. As there was only one type of ice available at the site, sensitivity study of the reflectance to

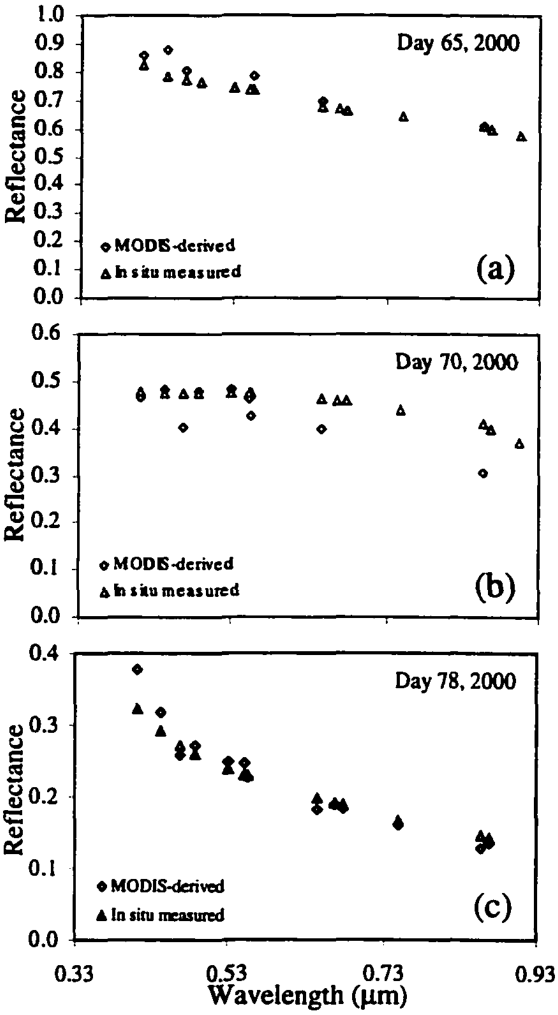

Figure 4.6 Comparison of bidirectional reflectance of *in situ* measurements and MODIS-derived data. Panels (a), (b) and (c) correspond to Days 65, 70 and 78, 2000, respectively.

the ice concentration should be more straightforward than other cases. Had the ice concentration been 5/10 instead of 3.5/10, the average difference between *in situ* and space measurements would be increased from 6.2% to 22.4% with the largest discrepancy (30.1%) at band 2 (0.858 µm) and the smallest discrepancy (12.5%). This result is shown in Figure 4.7. Much worse agreement occurs when the ice concentration is 5/10. Because of the very complicated topography and ice types mixture, errors in ice classification contribute greatly to the discrepancy.

4.6 Discussion and Conclusions

Within this investigation, bi-directional reflectance and spectral albedo measurements were performed on the snow and sea ice surface in the Amundsen sea, Antarctica, coincident with MODIS overpasses, to assess the discrepancy between the *in situ* and MODIS-derived surface reflectance of the snow and sea ice and thus allow for assessment of the accuracy of a satellite-retrieved albedo. *In situ* reflectance measurements were ice concentration-corrected so that the average reflectance of the 1km simulated ground pixel was compared with atmospheric-corrected reflectance retrieved from MODIS 1km products. Atmospheric correction of the MODIS data was performed using the 6S radiative transfer model with extension to all MODIS solar spectral bands.

A sensitivity study of satellite-retrieved reflectances for clear sky conditions was conducted by Stroeve *et al.* (1997) using the 6S model. A 50% change in aerosol amount can lead up to errors of as much as 3.3%, while for 50% uncertainty in ozone concentration, the error is about 1.5%. Uncertainties in water vapor content have the least effect on the satellite measurement. Discrepancy between satellite-derived and *in situ* measurements is common. For instance, AVHRR polar pathfinder-derived surface albedos and ground measured values differ on average by 10%, with worst cases exceeding 38% [Stroeve *et al.*, 2001].

The cruise we participated was a multi-purpose mission and the time allocated to each science group was limited at each ice station. We were not able to make surface

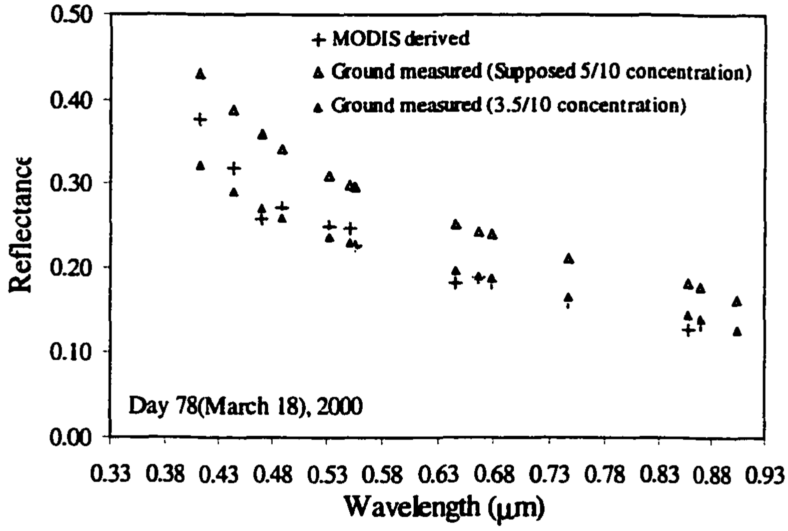

Figure 4.7 Dependence of *in situ* bidirectional reflectance on ice concentrations when there is only one ice type, as on Day 78, 2000. Atmospherically-corrected bidirectional reflectance derived from MODIS data on day 78 is also shown for comparison.

reflectance measurements on all the main ice types at each ice station. To estimate the possible effect of the variation of the spectral albedo of young white ice on the concentration-corrected *in situ* reflectance for the ice station of day 65, we take the maximum deviation of spectral albedo of multi-year ice (see section 2.1) as the maximum representative range of variation. If we take MODIS band 4 (553.6 nm) as an example, the error resulting from the variation of spectral reflectance of young white ice is expected to be smaller than 1.0%. Reflectance of new ice (5-10 cm) is generally very low (0.2-0.3). When the measurements for the MODIS validation were made on the dominant and most reflective MY ice, errors resulting from the uncertainty of spectral albedo of new ice (5-10 cm) are even less. For instance, the same analysis for young white ice was applied to new ice for station 70 and the error is less than 0.83% of the concentration-corrected reflectance of band 4. Analyses for the other bands resulted in similar conclusions. From these analyses we can see that the error in the concentration-corrected reflectance resulting from the variation of spectral albedo of the second or tertiary ice type is less than 1.0%.

Anisotropic reflectance is believed to be an important source in errors in satellite-retrieved albedo data [Jin and Simpson, 2000; Stroeve *et al.*, 1997; Steffen, 1996; Knap and Reijmer, 1998]. Consequently it is routinely corrected for the retrieval of the surface albedo from satellite measurements. However, for this study, the comparison is with the bi-directional reflectance and the illumination and viewing geometry are the same for both the satellite and *in situ* measurements. Anisotropy is already included in both the MODIS-retrieved and *in situ* data. Errors due to anisotropy occur when the surface reflectance is ice-concentration-corrected using albedo (isotropic reflectance) instead of bidirectional reflectance for the secondary and tertiary ice types, as is done in section 4.3.2. However, anisotropic correction is still controversial [De Abreu *et al.*, 1994]. In fact, application of the anisotropic correction factor [Taylor and Stowe, 1984a; 1984b] obtained at TOA to ground reflectance can result in corrected albedo exceeding 1, especially for very reflective surfaces such as snow-covered first-year, multi-year and landfast ice. Given the heterogeneous features of the ice surface in the Amundsen Sea, Taylor and Stowe's (1984a; 1984b) method may not be appropriate [De Abreu *et al.*, 1994]. As noted in section 4.3.2, errors due to anisotropy depend largely on the representativity of the primary ice type within the simulated pixel. The more representative the primary ice type on which the reflectance is measured, the less are errors due to uncertainty in anisotropy, as were the cases of day 65 and 78, 2000.

The main challenge in satellite data validation is to attain adequate ground sampling of observed bio- and/or geophysical variables that exhibit spatial and temporal variance at the sub-pixel scale of a satellite sensor. This problem is even more serious for the sea ice pack in the polar oceans than land surface because of the constant dynamical behavior of sea ice in the ice pack [Geiger *et al.*, 1998; Hibler, 1979]. For validation of sea ice products, one important source of errors is the uncertainty of concentrations of different ice types. For instance, taking the atmospheric parameter of Day 78 and supposing the surface consists of only MY ice and open water, an assumed 5/10 of ice concentration instead of 3.5/10 can result in errors of as much as 33.5%. In addition, the ice-concentration correction is made with the albedo of the minor ice types taken from the other stations. This can result in errors that depend on the surface composition. Ice concentration was estimated from the research vessel-based observations and field digital images. An alternative method of classification of the ground surface types is expected if higher spatial resolution multispectral images such as TM and/or ETM+ or ASTER data are available so that by appropriate classification algorithms the coarse spatial resolution pixel can be spectrally unmixed [Barnsley *et al.*, 2000; Lucht *et al.*, 2000a; 2000b]. Considering that the validation is on the sea ice, a very dynamic earth surface which can drift at a velocity from 4.3 km/day to 21.6 km/day [Kottmeier, 1992], nearly continuous motion and deformation of sea ice due to winds and currents require near-perfect concurrent acquisitions of high-resolution images for MODIS validation. The probability that an ice station covered by MODIS could also be semi-concurrently covered by a sensor with a narrower swath is equal to the ratio of the swath of that particular sensor to that of MODIS. For Landsat sensors, the probability was around 8% (185km/2330km). For ASTER, the probability was around 2.6 % (60km/2330km) (the side looking capability of ASTER is not considered due to the unpredictability of the ship's position on a given date). For a specific ice station, the location of the station in a MODIS image is indicative of the possible availability of ASTER image because ASTER is on the same satellite as MODIS is. On Day 70, the frame number (643, see Table 4.1) is close to the central frame (677). This means there might be a concurrent ASTER image to cover the station if ASTER was on at the time. For days 65 and 78, the availability of ASTER images is zero because the ice stations were far from the central frame of the MODIS image. Search of the Landsat and ASTER archives (http://edcsns17.cr.usgs.gov/EarthExplorer and http://asterweb.jpl.nasa.gov/gettingdata) indicated that no high-resolution satellite data such as TM or ETM+ from Landsat 5 and Landsat 7 and ASTER data were concurrently or semi-concurrently (within 3 days) acquired with the MODIS data used for the present study.

In this study, the *in situ* and MODIS-derived reflectances have been obtained and compared to assess the utility of the MODIS bands for obtaining realistic reflectances measurements from space. Agreement depends on the representativeness of the ice station in the corresponding MODIS pixel, appropriate correction for atmospheric effects, ground anisotropy, inhomogeneity, variability of topography, and the accuracy of the sub-pixel proportions of the ice types in the pixel. Comparison between MODIS-derived and *in situ* reflectances shows that a good agreement could be achieved (with discrepancy being 0.8-16.9%, average difference within 6.2%) when the pixel is one ice type and the measurement was taken on the dominant ice floe (as on Day 78) or when the ice concentration was 10/10 with the most coverage similar in reflectivity (as on day 65, with discrepancy range being 0.2-11.6%, and the average agreement within 4.8%). For the pixel that contains more than one ice type (day 70) that are substantially distinct in surface reflectance, worse agreement (discrepancy range is 0.8-25.3%, average discrepancy is as much as 13.0%) occurred. With the ground site very inhomogeneous and surface topography very variable, the discrepancy can be as large as 30% [Hall *et al.*, 1990]. Comparison for such conditions can be very difficult or even incomparable. We therefore conclude that:

1) The best agreement between in situ and MODIS measurements occurred when the ground is dominated by one ice type and has high concentration. A perfect comparison between the *in situ* and satellite-retrieved reflectances is expected on a large and homogeneous ice floe under clear sky conditions.

2) Simultaneity is a necessity for the *in situ* and space-based measurements to avoid ground truth drift when validation is on a moving surface feature such as sea ice. There is no "permanent" ground truth in validation of sea ice products. Synchronization becomes more important for sea ice product validation than for land surface products where "permanent" ground truth exists.

3) To avoid errors resulting from ice-concentration-correction, an accurate determination of ice concentration and ice types is very important in deriving ground reflectance of a simulated pixel from *in situ* measurements when a pixel covers several

optically-distinctive ice types. The more homogeneous the ground surface and the less variable the ground topography, the better the agreement between the *in-situ* and satellite-derived reflectance.

Acknowledgments

For the research activities involved in the chapter, we are grateful for the logistical support provided by the National Science Foundation and the Antarctic Support Associates personnel aboard the R/V Nathaniel B. Palmer. We are indebted to George A. Riggs (Research and Data Systems Corporation, USA) for providing the overpass time schedule of Terra satellite so that ground measurements could be carried out concurrently with MODIS. We acknowledge Kim Morris (University of Alaska Fairbanks, USA) for organizing the hourly ice observations and providing the final version of the observation record. We thank Nazmi Z. El Saleous (University of Maryland and NASA Goddard Space Flight Center, USA) for ordering all the MODIS granules used for this study from the Goddard DAAC and coordinating the process of the L1B products to generate Level 2 products from the MODIS Data Processing System (MODAPS). The research involved in this chapter was supported by the National Aeronautics and Space Administration under grant NAG5-6338.

CHAPTER 5*

Absorption and Scattering of Solar Radiation by Large Snow Composite Grains using the Geometrical Optics Method

ABSTRACT. Absorption of solar radiation by snow grains in the near-infrared part of the solar spectrum can not be neglected when computing radiative properties of snow. Thus, a geometrical optics method is developed to compute scattering and absorption cross section of particles of arbitrary complex refractive index assuming large snow meltclusters (1 cm-order), observed ubiquitously in the snow cover during summer, can be characterized as spheres, one may compute absorption and scattering efficiencies, and the scattering phase function on the basis of this geometrical optics method. The number of internal reflections and transmissions are truncated based on the ratio of incident irradiance at the n-th interface to the initial incident irradiance within a specific optical ray. Phase functions for both near- and far-field are directly calculated at a specific scattering angle using a hybrid algorithm based on the bisection and Newton-Raphson methods. With these methods the absorption and scattering properties of a single particle can be calculated for any wavelength in the solar spectrum or microwave region. This "Geometrical Optics Method for SNOW" code (GOMsnow) is tested against Wiscombe's Mie scattering code (MIE0) for a range of size parameters. It can be combined with MIE0 to calculate the single scattering properties of snow grains of any size.

---

* This chapter is based on material published by Zhou and Li (2002b).

5.1 Introduction

To model the surface reflectance of snow cover using radiative transfer, we need basic optical properties of individual snow grains. For small spherical particles such as water cloud, the optical properties can be computed exactly from Mie theory [Wiscombe, 1979; 1980] and parameterized as a function of liquid water path and grain size [Hu and Stamnes, 1993]. For non-spherical particles, unlike the spherical case, where the exact Mie theory is available, no benchmarked computational techniques are generally available, although research on light scattering by non-spherical particles is being actively pursued [Liou and Takano, 1994; Mishchenko et al., 1996; Rother and Schmidt, 1996; Mishchenko, 2000]. Grains in wet snow or liquid-saturated snow (liquid water content, LWC, ≥7%) tend to be cohesionless spherical particles [Colbeck, 1979]. Thus, single scattering properties of snow grains can be obtained using Mie scattering theory [Wiscombe, 1979; 1980; van de Hulst, 1957; Bohren and Huffman, 1983]. However, for moist or low liquid content (<7%) snow, grains tend to form multigrain clusters. Clusters of grains are widely observed in snow covers [Bager, 1962; Sturm et al., 1998; Massom, et al., 1998]. Due to frequent melt-refreezing cycles, summer snow cover on Antarctic sea ice is characterized by ubiquitous icy clusters, ice lenses, ice layers, and percolation columns, with grain size of 1 cm-order [Hass, 2001; Morris and Jeffries, 2001; Massom et al., 2001]. Centimeter-scale icy nodules in snow were also observed in winter, after a surface thaw-freeze event [Massom et al., 1997; 1998]. It has been found that the albedo is correlated with snow composite grain size of 1 cm-order instead of the single grains of 1 mm-order that make up composite grains (Chapter 3). This indicated that composite grains such as meltclusters may play an important role in the radiative properties of summer snow cover. Retrieval algorithms based on the comparison between measured radiance or reflectance data from satellite sensors and those obtained from radiative transfer modeling need the scattering properties of the target particles [Nakajima and Nakajima, 1995]. To understand the interaction of electromagnetic radiation with snow grains and its role in the remote sensing of snow cover, it is imperative to obtain the single scattering properties of the composite grains ubiquitously observed in summer snow cover.

In principle, the single scattering properties can be calculated using Mie theory for spheres of any size. But the Mie solutions are expansions on the size parameter $x = 2\pi a/\lambda$, where a is the radius of spherical scatterers and λ is the wavelength of the incident radiation. Numerous complex terms are needed for the general solutions for large values of x [Kokhanovsky and Nakajima, 1998]. For this reason, available Mie codes can be used for $x < 20000$. For large values of x, the best method is the ray optics approximation [van de Hulst, 1957; Nussenzveig, 1992]. In the framework of this approach, the scattering characteristics are represented as expansions with the parameter λ/a, so that only a few terms should be calculated to obtain a converged solution. The geometrical optics method has been extensively used in scattering of radiation not only from spherical particles [van de Hulst, 1957], but also from non-spherical particles [Nakajima et al., 1998]. Calculation from a Monte Carlo code based on the geometrical optics method shows that differences in simulated radiances between the GOM and the Mie calculation decrease as the size parameter increases even when the magnitude of the two phase functions at the scattering angle are almost the same [Nakajima et al., 1998]. It is expected that results from the geometrical optics approach will converge to those of Mie theory when the size/wavelength ratio becomes sufficiently large [van de Hulst, 1957].

The purpose of this chapter is to summarize the development of a practical and fast code (GOMsnow) using a geometrical optics method for calculation of absorption coefficients, scattering coefficients and phase functions for both near- and far-field absorption and scattering of solar radiation by grains within a snow cover. For simplicity, the shape of snowmelt clusters or composite grains is characterized as spherical. There are two main reasons that justify this simplification. First, it is questionable to adopt one particular shape as representative for snow grains in snow cover. Besides, with time evolution, metamorphism makes all kinds of snow grains round off. Second, Grenfell and Warren (1999) found that a nonspherical ice particle can be represented by a collection of independent spheres that has the same volume-to-surface-area ratio as the nonspherical particle, based on a finding by Hansen and Travis (1974) that dispersive media with different particle size distributions but the same values of the effective radius have approximately the same light scattering and absorption characteristics. For the complex refractive index $\hat{m}$ of snow and ice, data are primarily taken from the updated compilation by Warren (1984). Measurements by Kou et al. (1993) of the imaginary part of the complex refractive index for polycrystalline ice in the 1.45-2.50-μm region agree well with Warren's compilation. Discrepancies between the two data sets in this spectral region occur mainly near 1.50-, 1.85- and 2.50-μm, with the largest discrepancy near 1.85-μm. Gaps in the data at ultraviolet wavelengths in the 0.25- to 0.40-μm region were filled by Perovich and Govoni (1991). The temperature dependence of the refractive index of ice for λ<100 μm is deemed to be negligible for most temperatures that would be found on Earth [Warren, 1984a]. With the spectral complex refractive index available, the spectral dependence of the optical properties of a single snow grain can be calculated using GOMsnow.

5.2 Radiative Transfer Equations and Single Scattering Properties

The general equation for radiation at wavelength λ in a dispersive medium may be written as

$$\begin{aligned}\cos\theta\frac{d\mathrm{I}_\lambda(\tau,\theta,\varphi)}{d\tau} = -\mathrm{I}_\lambda(\tau,\theta,\varphi)+\frac{\omega_0}{4\pi}\int_0^{2\pi} d\varphi'\int_0^{\pi} d\theta' P(\tau;\theta,\varphi;\theta',\varphi')\mathrm{I}_\lambda(\theta',\varphi')\sin\theta' \\ +S_{\lambda,extn}(\theta,\varphi)\end{aligned} \tag{5.1}$$

where $\mathrm{I}_\lambda(\tau,\theta,\varphi)$ is the radiance, τ is the optical depth [Kokhanovsky, 1999; Thomas and Stamnes, 1999]. $S_{\lambda,extn}(\theta,\varphi)$ is the external source such as blackbody emission or the solar pseudo-source.

$$P(\tau;\mu,\varphi;\mu',\varphi')=\frac{4\pi C_{sca}^d(\tau;\mu,\varphi;\mu',\varphi')}{C_{sca}}=\frac{4\pi C_{sca}^d(\tau,\Theta)}{C_{sca}}$$

is the phase function. $\mu=\cos\theta$. C_{sca}^d is the differential scattering cross-section. For isotropic media, the value of $C_{sca}^d(\tau;\mu,\varphi;\mu',\varphi')$ depends only on the scattering angle Θ:

$\Theta = \arccos\left(\mu\mu' + \sqrt{1-\mu^2}\sqrt{1-\mu'^2}\cos(\varphi-\varphi')\right)$, thus $C_{sca}^{d}(\tau;\mu,\varphi;\mu',\varphi') = C_{sca}^{d}(\tau,\Theta)$. The physical meaning of $P(\tau;\mu,\varphi;\mu',\varphi')$ is that it is the probability of a photon scattering from the direction $\Omega' = (\theta',\varphi')$ to the direction $\Omega = (\theta,\varphi)$. $C_{sca} = C_{ext} - C_{abs}$ is the total scattering cross section:

$$C_{sca} = 2\pi\int_0^\pi d\Theta C_{sca}^{d}(\tau,\Theta)\sin\Theta$$

The total extinction coefficient σ_{ext} and the absorption coefficient σ_{abs} depend on the number concentration of particles n and their absorption cross-section C_{abs} and scattering cross-section C_{sca} [Bohren and Barkstrom, 1974; Thomas and Stamnes, 1999; Kokhanovsky, 1999]

$$\sigma_{ext} = nC_{ext},\quad \sigma_{sca} = nC_{sca},\quad \sigma_{abs} = nC_{abs},\qquad C_{ext} = C_{sca} + C_{abs} \tag{5.2}$$

where C_{ext} is the extinction cross-section. $\omega_0 \equiv \sigma_{sca}/\sigma_{ext} = \sigma_{sca}/(\sigma_{abs} + \sigma_{sca})$ is the single-scattering albedo. The phase function is thus expressed in terms of the scattering cross section and differential scattering cross-section

$$P(\tau;\mu,\varphi;\mu',\varphi') = \frac{4\pi C_{sca}^{d}(\tau,\Theta)}{C_{sca}} = \frac{2C_{sca}^{d}(\tau,\Theta)}{\int_0^\pi d\Theta C_{sca}^{d}(\tau,\Theta)\sin\Theta} \tag{5.3}$$

Obviously, the phase function satisfies the normalization function

$$\frac{1}{4\pi}\int P(\tau;\Theta,\Psi)d\Omega = 1,$$

where $d\Omega = \sin\Theta d\Theta d\Psi$ is the element of solid angle. Based on the phase function, the asymmetry factor is defined as

$$g = \langle\cos\Theta\rangle = \frac{1}{4\pi}\int P(\tau;\Theta,\Psi)\cos\Theta d\Omega \tag{5.4}$$

5.3 Single Scattering Properties – Formalism

Scattering by a particle is actually the sum of the reflection and refraction plus the Fraunhofer diffraction. Reflection and refraction make the outgoing (scattered) light distributed in all directions dependent on the optical properties of the particles. The diffraction pattern is more or less a narrow and intense lobe around the forward scattering direction, Θ = 0°. Diffraction depends on the form and size of the particle but is independent of the optical properties of the particle, and is thus a purely geometric effect.

The general forms of the electromagnetic field $(\mathbf{E}, \mathbf{H})$ plane electromagnetic waves, which is a solution of the Maxwell equations, are

$$\mathbf{E} = \mathbf{E}_0 e^{i(\mathbf{k}\cdot\mathbf{x} - \omega t)} \tag{5.5}$$

where $\mathbf{k} = k\hat{e}$ is the complex wave vector ($\hat{e}$ is a unit vector in the propagation direction), and the wave propagates along space vector $\mathbf{x}$. The wave frequency is ω and t is time. The wave number k is

$$k = \frac{\omega \hat{m}}{c} = \frac{2\pi \hat{m}}{\lambda} = \omega\sqrt{\varepsilon\mu} = \frac{2\pi m'}{\lambda} + i\frac{2\pi m''}{\lambda} \tag{5.6}$$

where $\hat{m}$ is the complex refractive index of snow. Inserting Equation (5.6) into Equation (5.5), the electric field takes the form

$$\mathbf{E} = \mathbf{E}_0 e^{-\frac{2\pi m''}{\lambda}z} e^{i\left(\frac{2\pi m'}{\lambda}z - \omega t\right)} = \mathbf{E}_0 e^{-\gamma_1 z} e^{i(\gamma_2 z - \omega t)}, \quad \gamma_1 = \frac{2\pi m''}{\lambda}, \quad \gamma_2 = \frac{2\pi m'}{\lambda} \tag{5.7}$$

where γ_1 and γ_2 are absorption constant and phase constant, respectively [Hallikainen and Winebrenner, 1992]. $z = \hat{e}\cdot\mathbf{x}$. λ is the wavelength and ω the angular frequency of the incident electromagnetic (EM) wave, c the speed of light *in vacuo*, ε the complex permittivity and μ the permeability of the medium. Radiative transfer processes of electromagnetic waves (radiation) by snow are simplified as the scattering and absorption of plane waves by snow grains. The Poynting vector of a plane wave is

$$\mathbf{S} = \frac{1}{2}\mathrm{Re}\{\mathbf{E}\times\mathbf{H}^*\} = F_\lambda \hat{\mathbf{e}} \tag{5.8}$$

where

$$F_\lambda = \frac{1}{2}\mathrm{Re}\left\{\sqrt{\frac{\varepsilon}{\mu}}\right\}|\mathbf{E}_0|^2 \exp\left(-\frac{4\pi m'' z}{\lambda}\right)$$
$$= \frac{m'}{2Z_0}|\mathbf{E}_0|^2 \exp(-\beta z), \quad \beta = \frac{4\pi m''}{\lambda} = 2\gamma_1, Z_0 = \sqrt{\mu_0 / \varepsilon_0}$$

where F_λ is the amplitude of the Poynting vector (it is also called the spectral irradiance or energy flux at wavelength λ). Z_0 is the impedance of free space, its dimensions are energy per unit area, time and wavelength. β is the absorption coefficient. Note that for energy flux, the attenuation constant due to absorption is called the absorption coefficient, while for the EM field, it is called the absorption constant.

5.3.1 Truncation of the Number of Rays Emerging from a Sphere

Each snow particle is assumed to be internally homogeneous and axisymmetric, and is assumed to reside in air. For a snow grain whose radius is much larger than the wavelength of the incident wave, we adopt the ray tracing method to calculate the single scattering properties [van de Hulst, 1957; Bohren and Huffman, 1983]. Supposing the incident wave is p-polarized, p = // or ⊥ indicates that the wave is parallel- or perpendicular-polarized. Reflection and transmission occurs only at an interface between media with different indices of refraction. Figure 5.1 illustrates absorption and scattering by a spherical snow grain in the geometrical optics picture. The initial ray separates into reflected and refracted sub-rays after it hits the particle surface. Energy contained in each ray decreases rapidly as it propagates by reflection and refraction. The thickness of the arrowed lines denote this debasement of energy in each ray. All rays emerging from the central grain will participate in the same process with the other grains, resulting in multiple scattering. Here, we concentrate only on the single-scattering properties of snow grains. With full knowledge of single-scattering properties, multiple scattering can be treated using radiative transfer theory (cf. chapter 6). At the jth interface, which is defined as the order of interface between the particle and the incident light ray, assuming the incident electric field is $E_{p,i}^j$, the reflected ($E_{p,r}^j$) and transmitted ($E_{p,t}^j$) electric fields are [Hecht, 1998]

$$E_{p,r}^j = r_p^j E_{p,i}^j, \qquad E_{p,t}^j = t_p^j E_{p,i}^j \tag{5.9}$$

where

$$r_p^j = r_p(\Theta_i, \Theta_t, \hat{m}) = r_p, \quad t_p^j = t_p(\Theta_i, \Theta_t, \hat{m}) = t_p, \quad j = 1$$

$$r_p^j = r_p(\Theta_t, \Theta_i, 1/\hat{m}), \quad t_p^j = t_p(\Theta_t, \Theta_i, 1/\hat{m}), \quad j > 1$$

The reflection coefficients r_p and transmission coefficients t_p are complex and complicated for absorbing and scattering media. Following the discussion for wave reflection and transmission of metallic film of Born and Wolf (1980) (p.628-631), and setting $\hat{m}\cos\Theta_t = u + iv, (i = \sqrt{-1})$, r_p and t_p take the following form (see Appendix A)

$$\begin{cases} r_{//}(\Theta_i, \Theta_t, \hat{m}) = \dfrac{\left[(m'^2 - m''^2)\cos\Theta_i - u\right] + i(2m'm''\cos\Theta_i - v)}{\left[(m'^2 - m''^2)\cos\Theta_i + u\right] + i(2m'm''\cos\Theta_i + v)} \\ t_{//}(\Theta_i, \Theta_t, \hat{m}) = \dfrac{2(m' + im'')\cos\Theta_i}{\left[(m'^2 - m''^2)\cos\Theta_i + u\right] + i(2m'm''\cos\Theta_i + v)} \end{cases} \qquad (5.10a)$$

$$\begin{cases} r_{\perp}(\Theta_i, \Theta_t, \hat{m}) = \dfrac{(\cos\Theta_i - u) - iv}{(\cos\Theta_i + u) + iv} \\ t_{\perp}(\Theta_i, \Theta_t, \hat{m}) = \dfrac{2\cos\Theta_i}{(\cos\Theta_i + u) + iv} \end{cases} \qquad (5.10b)$$

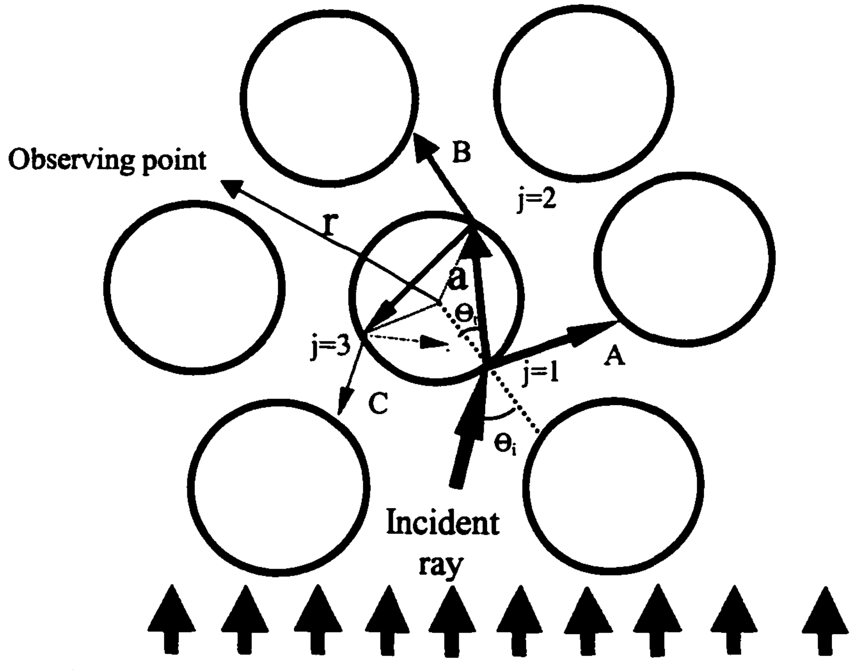

Figure 5.1 Ray tracing diagram. Incident rays will propagate by separation of reflection and refraction. Energy contained in each ray decreases rapidly as it propagates. Rays such as A, B and C, etc. emerging from the scatterer will experience the same process with other scatterers, resulting in multiple scattering. The weight of each arrow denotes the energy content contained in the ray.

and

$$\begin{cases} r_p(\Theta_t, \Theta_i, 1/\hat{m}) = -r_p(\Theta_i, \Theta_t, \hat{m}) \\ t_p(\Theta_t, \Theta_i, 1/\hat{m}) = \dfrac{(u+iv)}{\cos\Theta_i} t_p(\Theta_i, \Theta_t, \hat{m}) \end{cases} \tag{5.10c}$$

with

$$\begin{cases} u = \dfrac{\sqrt{2}}{2}\left\{\left[\left(m'^2 - m''^2 - \sin^2\Theta_i\right)^2 + 4m'^2 m''^2\right]^{\frac{1}{2}} + \left(m'^2 - m''^2 - \sin^2\Theta_i\right)\right\}^{\frac{1}{2}} \\ v = \dfrac{\sqrt{2}}{2}\left\{\left[\left(m'^2 - m''^2 - \sin^2\Theta_i\right)^2 + 4m'^2 m''^2\right]^{\frac{1}{2}} - \left(m'^2 - m''^2 - \sin^2\Theta_i\right)\right\}^{\frac{1}{2}} \end{cases}$$

where Θ_i is the incident angle(real), Θ_t is the refraction angle (complex).

Between two consecutive interfaces, the ray travels a path length of

$$\begin{aligned} \xi &= \left|2a\cos\Theta_t\right| \\ &= \frac{2a}{m'^2 + m''^2}\sqrt{(um' + vm'')^2 + (vm' - um'')^2} \end{aligned}$$

where a is the radius of the spherical snow grain. The incident electric field at the jth interface (j ≥ 2) is related to the reflected electric field at the (j-1)th interface (j > 2) or transmitted field when j = 2 by the following relations

$$\begin{aligned} E_{p,i}^j &= e^{-\gamma_1\xi}E_{p,t}^{j-1} = e^{-\beta\xi/2}E_{p,t}^{j-1}, \qquad j = 2 \\ E_{p,i}^j &= e^{-\gamma_1\xi}E_{p,r}^{j-1} = e^{-\beta\xi/2}E_{p,r}^{j-1}, \qquad j > 2 \end{aligned}$$

At the jth interface,

$$\begin{aligned} E_{p,i}^j &= \begin{cases} E_{p,i}, & j = 1 \\ t_p \prod_{l=2}^{j}\left(r_p^l\right) e^{-\beta\xi(j-1)/2} E_{p,i} = t_p\left(-r_p\right)^{j-2} e^{-\beta\xi(j-1)/2} E_{p,i}, & j \geq 2 \end{cases} \\ E_{p,t}^j &= \begin{cases} t_p E_{p,i}, & j = 1 \\ t_p^j E_{p,i}^j = \dfrac{(u+iv)}{\cos\Theta_i}\left(t_p\right)^2\left(-r_p\right)^{j-2} e^{-\beta\xi(j-1)/2} E_{p,i}, & j \geq 2 \end{cases} \\ E_{p,r}^j &= \begin{cases} r_p E_{p,i}, & j = 1 \\ r_p^j E_{p,i}^j = t_p\left(-r_p\right)^{j-1} e^{-\beta\xi(j-1)/2} E_{p,i}, & j \geq 2 \end{cases} \end{aligned} \tag{5.11}$$

Rays emerging from the surface of the sphere are called scattered rays. They include reflected and transmitted rays. From Equation (5.11), we obtain the scattered field near the surface of the sphere (near field, r = a)

$$E_{p,s}^{j} = \varepsilon_p^j E_{p,i}, \qquad \varepsilon_p^j = \begin{cases} r_p, & j = 1 \\ \dfrac{(u+iv)}{\cos\Theta_i}(t_p)^2(-r_p)^{j-2} e^{-\beta\xi(j-1)/2}, & j \geq 2 \end{cases} \tag{5.12}$$

The rays reflected from the first interface is the only reflected radiation and the other rays are transmitted radiation. The angle of the emergent ray at the jth interface from the sphere that deviates from the incident direction is [van de Hulst, 1957; Glantschnig and Chen, 1981]

$$\Theta'(j,\Theta_i) = 2(j-1)|\Theta_t| - 2\Theta_i - (j-2)\pi, \qquad j = 1,2,\ldots \tag{5.13a}$$

which defines the scattering angle Θ in the interval (0, π) by

$$\Theta' = l \cdot 2\pi + q\Theta \tag{5.13b}$$

where l is an integer and $q = \pm 1$. The complex refraction angle Θ_t is obtained from the law of refraction as

$$\begin{aligned} \Theta_t &= \sin^{-1}\left[\frac{(m'-im'')\sin\Theta_i}{m'^2+m''^2}\right] \\ &= -i\ln\left\{ i\frac{(m'-im'')\sin\Theta_i}{m'^2+m''^2} + \sqrt{1-\left[\frac{(m'-im'')\sin\Theta_i}{m'^2+m''^2}\right]^2} \right\} \end{aligned} \tag{5.14}$$

where the other root of inverse sine function of complex argument in obtaining Θ_t is discarded based on the physical refraction process. For any incident ray, l is the nearest integer of $\frac{\Theta'}{2\pi}$ and $fra\left(\frac{\Theta'}{2\pi}\right)$ is the remainder of $\frac{\Theta'}{2\pi}$, i.e.

$$l = \begin{cases} \mathrm{int}\left(\dfrac{\Theta'}{2\pi} + 0.5\right) & if\ \dfrac{\Theta'}{2\pi} \geq 0 \\ \mathrm{int}\left(\dfrac{\Theta'}{2\pi} - 0.5\right) & if\ \dfrac{\Theta'}{2\pi} < 0 \end{cases} \tag{5.15a}$$

with int(a) = 0 if $|a| < 1$, or int(a) = the integer part of a, disregarding the fractional part if $|a| > 1$. $fra\left(\frac{\Theta'}{2\pi}\right)$ can be expressed as

$$fra\left(\frac{\Theta'}{2\pi}\right)=\frac{\Theta'}{2\pi}-l$$

from which we have

$$q=\begin{cases}+1, & if \quad fra\left(\frac{\Theta'}{2\pi}\right)>0\\ -1, & if \quad fra\left(\frac{\Theta'}{2\pi}\right)\leq 0\end{cases} \tag{5.15b}$$

This way, the scattering angle for each ray emerging from the sphere is determined. The monotonical relationships between the scattering angle (Θ) and the incident angle (Θ_i) at the first five interfaces (j = 1, 2, ..., 5) for λ = 0.5 μm are shown in Figure 5.2. At a specific interface for any incident angle, the scattering angle of the ray is independent of the size of the ice sphere.

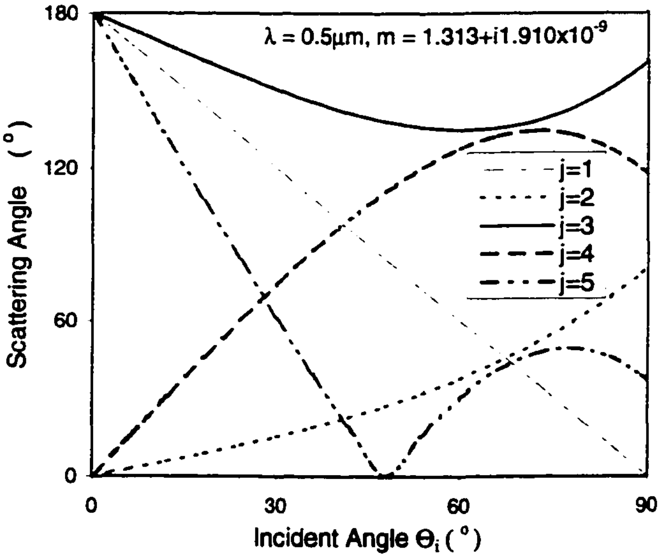

Figure 5.2 Relationship between outgoing angle Θ at a specific interface j and incident angle Θ_i. The five curves correspond to the first five interfaces once a light ray enters an ice sphere. The wavelength for each case is λ = 0.5 μm and refractive index m = $1.313+i1.910\times10^{-9}$.

Differentiation of Θ' and Θ with respect to Θ_i by use of Snell's law yields

$$\frac{d\Theta}{d\Theta_i} = q\frac{d\Theta'}{d\Theta_i} = 2q\left[(j-1)\left|\frac{\cos\Theta_i}{u+iv}\right| - 1\right] \tag{5.16}$$

Inserting Equation (5.10) into Equation (5.8), we can obtain the incident, transmitted or reflected irradiances at the jth interface. The irradiance absorbed between the (j-1)th and jth interfaces is

$$F_{j-1,j}(\Theta_i, m) = \left|t_p\right|^2 \left(R_p\right)^{j-2} e^{-\beta\xi(j-2)}\left(1-e^{-\beta\xi}\right)m' F_0 \tag{5.17}$$

where $F_0 = \frac{1}{2Z_0}\left|E_{p,i}\right|^2$ is the incident irradiance on the sphere.

Assume the incident radiation is unpolarized, the total absorbed energy (summed over all ray paths and integrated over the sphere surface for all incident angles) is then [Bohren and Huffman, 1983]

$$\begin{aligned} W_{abs} &= \int_0^{\pi/2}\int_0^{2\pi} \sum_{j=2}^{N} F_{j-1,j}(\Theta_i, m)\left|\cos\Theta_t\right| a^2 \sin\Theta_i d\Theta_i d\Psi_i \\ &= 2\pi a^2 F_0 \int_0^1 T(\mu_i)\sum_{j=2}^{N}\left(\mathrm{R}e^{-\beta\xi}\right)^{j-2}\left(1-e^{-\beta\xi}\right)\mu_i d\mu_i \end{aligned} \tag{5.18}$$

where

$$\begin{aligned} T &= \frac{1}{2}\left(T_{//} + T_{\perp}\right), \quad with \quad T_p = \frac{m'\sqrt{\left(um'+vm''\right)^2 + \left(vm'-um''\right)^2}}{\left(m'^2+m''^2\right)\cos\Theta_i}\left|t_p\right|^2 \\ R &= \frac{1}{2}\left(R_{//} + R_{\perp}\right), \quad with \quad R_p = \left|r_p\right|^2 \end{aligned} \tag{5.19}$$

where $\mu_i = \cos\Theta_i$, R is the reflectance and T is the transmittance. For spherical particles with arbitrary absorption coefficient, sum over the interface number is, theoretically, to infinite. However, based on the strength of the incident electric field at the jth interface, the series can be truncated at some value, for instance N, at which interface the electric field is so weak compared with the incident field that further calculation does not make any difference. Supposing the truncation is made when the ratio of the irradiance or energy flux at the jth interface to that incident at the first interface (j = 1) is equal to some small tolerance number ς, we can obtain the maximum number N of interfaces to be summed over in Equation (5.18). Supposing

$$R = |r|^2 ,\ T = \frac{m'\sqrt{(um'+vm'')^2 + (vm'-um'')^2}}{(m'^2+m''^2)\cos\Theta_i}|t|^2 ,$$

where

$$t = \sqrt{0.5\left(t_{//}{}^2 + t_{\perp}{}^2\right)}$$
$$r = \sqrt{0.5\left(r_{//}{}^2 + r_{\perp}{}^2\right)}$$

and replacing r_p and t_p with r and t in Equation (5.11), and combining with Equation (5.8), N is found to be

$$N(\Theta_i) = \frac{\beta\xi + 2\ln|t| - 2\ln R - \ln\varsigma}{\beta\xi - \ln R} \tag{5.20}$$

Thus, summation over j in Equation (5.18) is from 2 to N. The relationship of N to incident angle for the case of green light λ = 0.5 μm is shown in Figure 5.3a for an ice sphere of radius a = 1 cm. The same calculation for λ = 2.0 μm shows that N = 2 for all incident angles. Glantschnig and Chen (1981) compared the angular scattering diagrams using the results from geometrical optics approximation with N = 2 for λ = 0.49 μm with the exact Mie calculation. They found that for $\Theta_i \leq 60°$, the agreement is reasonable, and at grazing or near grazing angles, the geometrical optics theory does not give good results. From Figure 5.3a, we can see that for the green light N increases rapidly with increasing incident angle when it is greater than about 80°. This illustrates that the approximation N = 2 is not enough for the calculation of light scattering by weak absorbing scatterers at large incident angles. The relationship of N with wavelength λ is shown in Figure 5.3b for $\Theta_i = 60°$. For visible light, ice is very weakly absorbing, and attenuation is weaker so that a greater number of ray paths is needed, while for near infrared ice is strongly absorbing and only 1 or 2 paths are necessary to extinguish the transmitted radiation.

5.3.2 Absorption

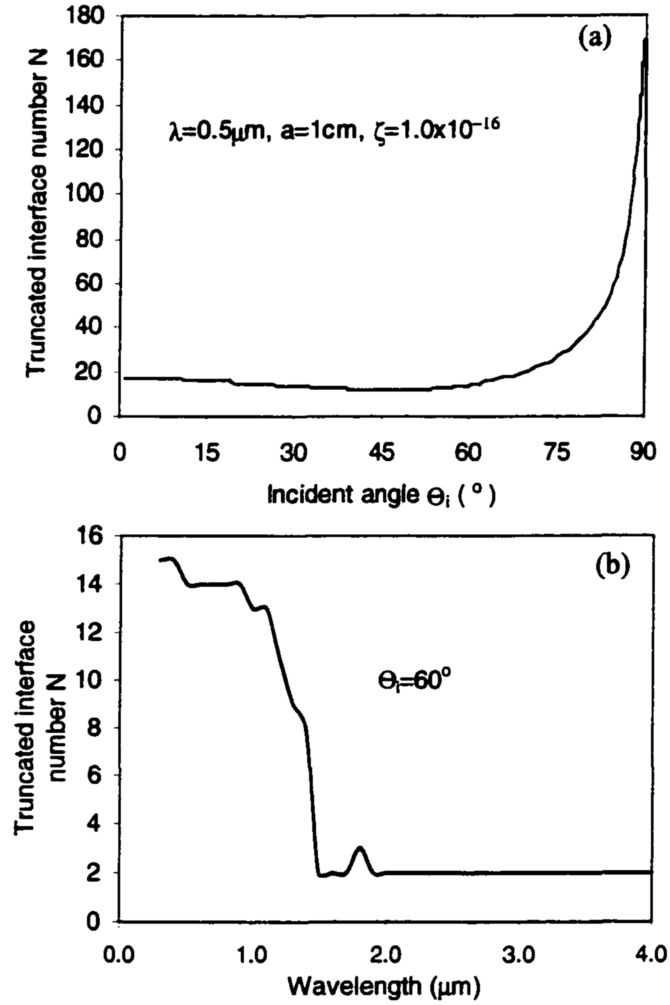

Figure 5.3 (a) Maximum number N versus incident angle for the truncation in the sum series of the calculation of absorption efficiency for an ice sphere with radius $a = 1$ cm and truncation tolerance $\varsigma = 1.0\times10^{-16}$ for wavelength $\lambda = 0.5$ μm; and (b) the maximum number N versus wavelength λ for the truncation in the sum series of the calculation of absorption efficiency of an ice sphere with radius $a = 1$ cm and truncation tolerance $\varsigma = 1.0\times10^{-16}$ for incidence angle $\Theta_i = 60°$.

From the total energy absorbed and the initial incident irradiance, the absorption cross-section and absorption efficiency are obtained as (N→∞)

$$\begin{aligned} C_{abs} &= \frac{W_{abs}}{F_0} = 2\pi a^2 \int_0^1 T(\mu_i) \sum_{j=2}^{N} \left(\mathrm{R}e^{-\beta\xi}\right)^{j-2} \left(1-e^{-\beta\xi}\right) \mu_i d\mu_i \\ &= 2\pi a^2 \int_0^1 T(\mu_i) \frac{1-\exp(-\beta\xi)}{1-\mathrm{R}\exp(-\beta\xi)} \mu_i d\mu_i \end{aligned} \qquad (5.21a)$$

$$Q_{abs} = \frac{C_{abs}}{\pi a^2} = 2 \int_0^1 T(\mu_i) \frac{1-\exp(-\beta\xi)}{1-\mathrm{R}\exp(-\beta\xi)} \mu_i d\mu_i \qquad (5.21b)$$

The total energy scattered by a large sphere includes the diffracted, reflected, and transmitted components. Thus, the scattering cross-section of a large sphere can be written as [Bohren and Huffman, 1983]

$$C_{sca} = \frac{\sum_{j=1}^{N} W_{sca}^{j}}{F_0} = C_{dif} + C_{ref} + C_{tra} \qquad (5.22)$$

5.3.3 Near-field Scattering

Scattered rays at the first interface are exclusively the reflected component. All emerging rays from the second interface on are included in the transmitted component. In the same manner as obtaining Equation (5.21), using Equation (5.8), Equation (5.12) and Equation (5.19), we can derive components of Equation (5.22) for unpolarized incident radiation as follows

$$C_{ref} = \frac{W_{sca}^{1}}{F_0} = 2\pi a^2 \int_0^1 R(\mu_i) \mu_i d\mu_i \qquad (5.23a)$$

$$C_{tra} = \frac{\sum_{j=2}^{N} W_{sca}^{j}}{F_0} = \pi a^2 \sum_{j=2}^{N} \int_0^1 \left[T_{//}^2(\mu_i) R_{//}^{j-2}(\mu_i) + T_{\perp}^2(\mu_i) R_{\perp}^{j-2}(\mu_i)\right] e^{-\beta\xi(j-1)} \mu_i d\mu_i \qquad (5.23b)$$

Equation (5.23a) has the same form as the case of a non-absorbing sphere [Bohren and Huffman, 1983]. For the near field, the diffraction is Fresnel diffraction. Fraunhofer diffraction will occur when the viewing distance r > a²/λ [Hecht, 1998]. For the incident plane waves, we will neglect the Fresnel diffraction.

Considering the energy distribution of the scattered ray in the scattering direction (scattering angle), the irradiance of the scattered ray at the sphere surface from the jth interface is expressed as the following, which is expanded to absorbing medium from non-absorbing [van de Hulst, 1957; Glantschnig and Chen, 1981; Liou and Hansen, 1971]

$$F_p(j,\Theta_i,\Theta)=\frac{-F_0\left|\varepsilon_p^j\right|^2\cos\Theta_i a^2\sin\Theta_i d\Theta_i d\Psi}{a^2\sin\Theta d\Theta d\Psi}=F_0\left|\varepsilon_p^j\right|^2 D \tag{5.24}$$

with

$$D(j,\Theta_i,\Theta)=\frac{\sin(2\Theta_i)}{4\left|(j-1)\frac{\cos\Theta_i}{\sqrt{u^2+v^2}}-1\right|\cdot\sin\Theta}$$

D is the geometrical divergence factor. Equation (5.16) and Snell's law have been used in deriving the above equation. Rainbows appear when $\frac{d\Theta}{d\Theta_i}=0$, under which $F_p(j,\Theta_i,\Theta)$ has a localized peak [Liou and Hansen, 1971]. This can be readily seen from Equation (5.24). In snow pack, a rainbow can be difficult to observe, but a localized peak exists at rainbow angles Θ_i^{rb}. For visible light, the imaginary part of the refractive index can be neglected, thus

$$\Theta_i^{rb}=\sin^{-1}\left(\sqrt{\frac{(j-1)^2-m'^2}{(j-1)^2-1}}\right).$$

For the general case,

$$\Theta_i^{rb}=\sin^{-1}\left\{\left[\frac{(j-1)^4-\left(m'^2-m''^2\right)-\left\{(j-1)^4\left[\left(m'^2+m''^2\right)^2-2\left(m'^2-m''^2\right)+1\right]-4m'^2m''^2\right\}^{1/2}}{(j-1)^4-1}\right]^{1/2}\right\}$$

Table 5.1 shows the rainbow angles for a spherical snow grain at any interface for 7 visible channels from blue to red (0.4-0.7 μm). Rainbow angle-widths Δ, which is defined as the scattering angle difference between λ = 0.4 μm and λ = 0.7 μm for any of the rainbow series, are also shown. Most scattered energy is contained in the j = 1 to 4 components [Liou and Hansen, 1971]. Thus primary (j = 3) and secondary (j = 4) rainbows are the most important power peaks. The angle difference between the primary and secondary rainbows versus wavelength is shown in Figure 5.4. At λ ≈ 0.52 μm, the angle difference has a minimum, indicating the primary and secondary rainbows within snow are nearest at λ ≈ 0.52 μm.

Table 5.1 Incident angles (Θ_i) and scattering angles (Θ) at which rainbows appear for each visible channel (λ) at the j-th interface. Primary and secondary, etc. rainbows correspond to j = 3, 4, etc. The angle-width (Δ) of each rainbow is also shown.

	j = 3		4		5		6	
λ (μm)	Θ_i(°)	Θ(°)	Θ_i(°)	Θ(°)	Θ_i(°)	Θ(°)	Θ_i (°)	Θ(°)
0.40	60.20	135.90	72.28	132.74	77.16	46.83	79.88	37.20
0.45	60.42	135.34	72.4	133.75	77.25	48.25	79.95	35.38
0.50	60.58	134.93	72.49	134.49	77.31	49.28	80.00	34.07
0.55	60.70	134.61	72.56	135.05	77.36	50.07	80.03	33.06
0.60	60.79	134.36	72.61	135.50	77.39	50.70	80.07	32.26
0.65	60.87	134.15	72.66	135.88	77.43	51.22	80.09	31.59
0.70	60.94	133.97	72.69	136.02	77.45	51.68	80.11	31.01
Δ		1.94		3.46		4.85		6.19

From scattering theory [van de Hulst, 1957], the scattered irradiance at a distance r from the scatterer center is associated with incident irradiance through the differential scattering cross section $C_p^d(j,\Theta_i,\Theta)$ by

$$F_p(j,\Theta_i,\Theta)=\frac{C_p^d(j,\Theta_i,\Theta)}{r^2}F_0$$

Comparing this with Equation (5.24), we have the differential scattering cross section at the surface of the sphere

$$C_p^d(j,\Theta_i,\Theta)=a^2\left|\varepsilon_p^j\right|^2 D(j,\Theta_i,\Theta) \qquad (5.25)$$

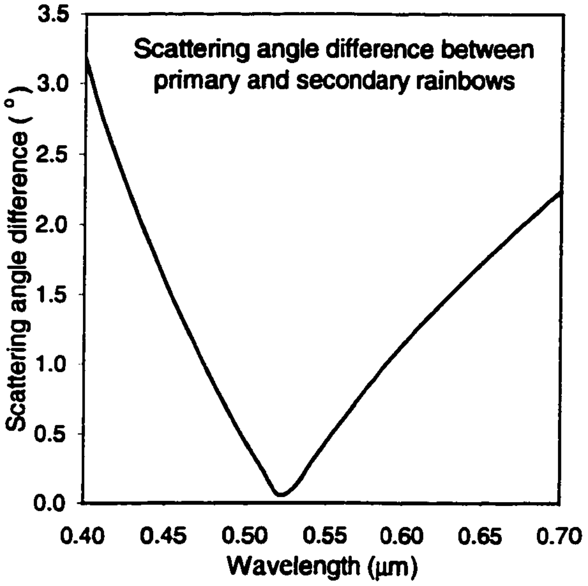

Figure 5.4 Scattering angle difference between primary and secondary rainbows versus wavelength. The primary and secondary rainbows are closest at λ = 0.52 μm.

For unpolarized natural light, the phase function (see Equation (5.3)) is thus

$$P(\Theta)=\frac{2\pi}{C_{sca}}\sum_{j,\Theta_i}\sum_{p}C_p^d(j,\Theta_i,\Theta) \tag{5.26a}$$

with

$$C_{sca}=\pi a^2\int_0^{\pi}\sum_{j,\Theta_i}\left[\left|\varepsilon_{//}^j\right|^2+\left|\varepsilon_{\perp}^j\right|^2\right]D(j,\Theta_i,\Theta)\sin\Theta d\Theta \tag{5.26b}$$

and the asymmetry factor g is (see. Equation (5.4)) [van de Hulst, 1957]

$$\begin{aligned} g &= \langle\cos\Theta\rangle \\ &= \frac{\pi}{C_{sca}}\int_0^{\pi}\sum_{j,\Theta_i}\sum_{p}C_p^d(j,\Theta_i,\Theta)\cos\Theta\sin\Theta d\Theta \end{aligned} \tag{5.26c}$$

$\sum_{j,\Theta_i}$ in Equation (5.26) is to sum over all sets of (j, Θ_i) that make up an emergent light ray with outgoing angle Θ. This guarantees that the irradiances of rays emerging at the same scattering angle for a specific incident angle but from different interfaces, and those for a specific interface but from different incident angles, are added up. The extinction cross section is determined by

$$C_{ext} = C_{sca} + C_{abs} \tag{5.27}$$

Equations (5.22), (5.23), (5.26) and (5.27) constitute the main equations for near field scattering by large absorbing particles.

5.3.4 Far-field Scattering

For far-field scattering, the absorption is the same as expressed in Equation (5.21). Fraunhofer diffraction will be included in the calculation of scattering cross section. The irradiance of the scattered ray at the sphere surface from the jth interface is expressed as [van de Hulst, 1957; Glantschnig and Chen, 1981]

$$F_p(j,\Theta_i,\Theta) = \frac{F_0\left|\varepsilon_p^j\right|^2 \cos\Theta_i a^2 \sin\Theta_i d\Theta_i d\Psi}{r^2 \sin\Theta d\Theta d\Psi} = \frac{a^2}{r^2} F_0\left|\varepsilon_p^j\right|^2 D \tag{5.28}$$

From which the differential scattering cross section due to reflection and transmission $C_p^d(j,\Theta_i,\Theta)$ has the same form as Equation (5.25). Summing over all emerging rays from the same scattering angle we have the differential scattering cross section due to reflection and transmission for each incident light ray

$$C_p^d(\Theta_i,\Theta) = \sum_{j,\Theta_i} C_p^d(j,\Theta_i,\Theta) \tag{5.29}$$

The scattering cross section due to reflection and transmission of natural light is

$$\begin{aligned} C_{sca}^{rt} &= \int_{4\pi} C_p^d(\Theta_i,\Theta) d\Omega \\ &= \pi \int_0^{\pi} d\Theta \sin\Theta \sum_{j,\Theta_i}\sum_{p} C_p^d(j,\Theta_i,\Theta) \end{aligned} \tag{5.30}$$

Substituting Equation (5.29) and (5.30) into Equation (5.3), we obtain the phase function of scattering due to reflection and transmission for natural light and it has the same form as Equation (5.26a).

$$P^{n}(\Theta_i,\Theta)=\frac{2\pi\sum_{p}C_p^d(\Theta_i,\Theta)}{C_{sca}}=\frac{2\pi}{C_{sca}}\sum_{p}\sum_{j,\Theta_i}C_p^d(j,\Theta_i,\Theta) \tag{5.31}$$

The asymmetry factor for this phase function is the same as Equation (5.26c)

Scattering amplitude functions expressed in terms of $C_p^d(j,\Theta_i,\Theta)$ are [van de Hulst, 1957; Glantschnig and Chen, 1981]

$$\left|S_p^n(j,\Theta_i,\Theta)\right|=\sqrt{C_p^d(j,\Theta_i,\Theta)} \tag{5.32}$$

The scattering amplitude function due to Fraunhofer diffraction for both polarizations is given by Glantschnig and Chen (1981)

$$S_p^{dif}(\Theta)=x^2\left[\frac{J_1(x\sin\Theta)}{x\sin\Theta}\right],\quad x=\frac{2\pi a}{\lambda} \tag{5.33}$$

where $J_1(x)$ is the first order Bessel function. From Equation (5.33) we have the differential cross section of Fraunhofer diffraction

$$C_p^{dif}(\Theta)=\left|S_p^{dif}(\Theta)\right|^2/k^2=a^2x^2\left[\frac{J_1(x\sin\Theta)}{x\sin\Theta}\right]^2=\frac{a^2J_1^2(x\sin\Theta)}{\sin^2\Theta} \tag{5.34}$$

The scattering cross section due to Fraunhofer diffraction is [van de Hulst, 1957]

$$C^{dif}=\int\frac{1}{2}\sum_{p}C_p^{dif}(\Theta)d\Omega=2\pi a^2\int_0^\pi\frac{J_1^2(x\sin\Theta)}{\sin\Theta}d\Theta=\pi a^2 \tag{5.35}$$

The phase function resulting from the Fraunhofer diffraction is (see Equation (5.3))

$$P^{dif}(\Theta)=\frac{4J_1^2(x\sin\Theta)}{\sin^2\Theta} \tag{5.36}$$

from which the asymmetry factor due to diffraction is derived as

$$g^{dif}=\frac{1}{4\pi}\iint P^{dif}(\Theta)\cos\Theta d\Omega=2\int_0^\pi J_1^2(x\sin\Theta)\cot(\Theta)d\Theta \tag{5.37}$$

Based on Equation (5.32) and Equation (5.33), the full scattering amplitude functions are calculated by

$$S_p(\Theta_i,\Theta)=S_p^{dif}(\Theta)+\sum_{j,\Theta_i}S_p^n(j,\Theta_i,\Theta) \tag{5.38}$$

The total differential scattering cross section due to reflection, transmission and diffraction can be obtained from Equations (5.29) and (5.34)

$$\begin{aligned}C^d_{sca}(\Theta_i,\Theta) &= \frac{1}{2}\sum_p \left(C^d_p(\Theta_i,\Theta)+C^{dif}_p(\Theta)\right)\\ &= \frac{1}{2}\sum_{j,\Theta_i}\sum_p C^d_p(j,\Theta_i,\Theta)+\frac{a^2J_1^2(x\sin\Theta)}{\sin^2\Theta}\end{aligned} \tag{5.39}$$

The phase function is easily obtained if we insert Equation (5.39) into Equation (5.3), considering Equation (5.35). It takes the form

$$P(\Theta_i,\Theta)=\frac{2\sum\limits_{j,\Theta_i}\sum\limits_p \left|\varepsilon_p^j\right|^2 D(j,\Theta_i,\Theta)+\frac{4J_1^2(x\sin\Theta)}{\sin^2\Theta}}{1+\int_0^\pi d\Theta\sin\Theta\sum\limits_{j,\Theta_i}\sum\limits_p\left(\varepsilon_p^j\right)^2D(j,\Theta_i,\Theta)} \tag{5.40}$$

The asymmetry factor then takes on the following form (from Equation (5.4))

$$g=\frac{\int_0^\pi d\Theta\cos\Theta\sin\Theta\left\{\sum\limits_{j,\Theta_i}\sum\limits_p\left(\varepsilon_p^j\right)^2D(j,\Theta_i,\Theta)+\frac{2J_1^2(x\sin\Theta)}{\sin^2\Theta}\right\}}{1+\int_0^\pi d\Theta\sin\Theta\sum\limits_{j,\Theta_i}\sum\limits_p\left(\varepsilon_p^j\right)^2D(j,\Theta_i,\Theta)} \tag{5.41}$$

Equations (5.21), (39-41) form the set of equations of single scattering properties for far-field scattering calculated by the geometrical-optics method.

5.4 Single Scattering Properties – Calculations

Based on the formalism in section 5.3, numerical calculation is carried out in this section. For integration involved, if only the integral value is concerned, Gauss-Legendre quadrature method is used.

5.4.1 Absorption Efficiency

First we calculate the integral value of Equation (5.21) using Gaussian quadratures. The abscissas and weights of the Gauss-Legendre n-point quadrature formula are calculated within (-1, 1), then the actual integration interval is scaled to obtain the integral value [Davis and Rabinowitz, 1984]. Comparison of the results with exact Mie

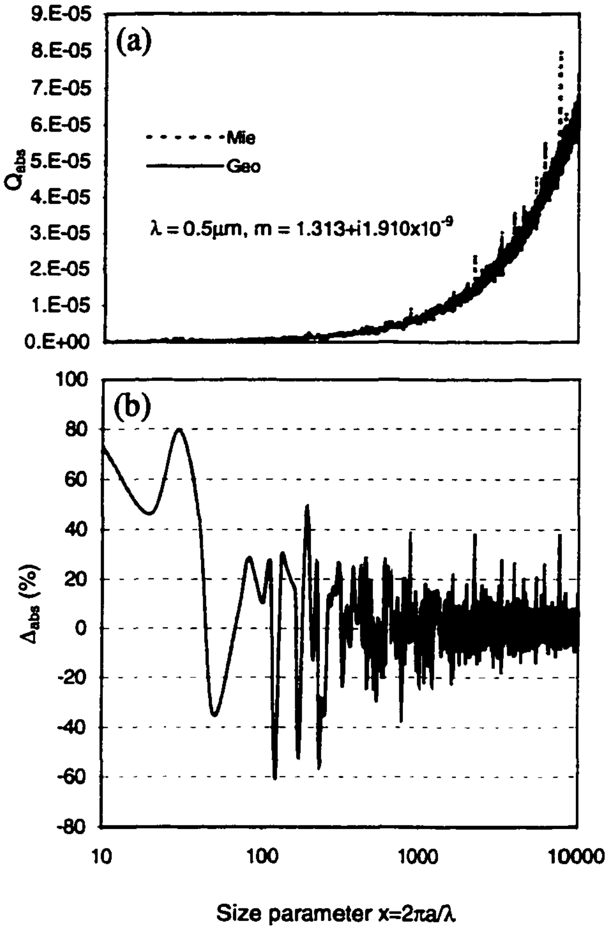

Figure 5.5 (a) Absorption efficiency versus size parameter $x = 2\pi a/\lambda$ for wavelength $\lambda = 0.5$ μm corresponding to refractive index $m = 1.313+i1.910\times10^{-9}$. Absorption efficiency is calculated using Mie scattering theory (dashed curve) and the geometrical optics method (solid line). (b) Difference factor $\Delta = \frac{Q_{abs}^{Mie} - Q_{abs}^{Geo}}{Q_{abs}^{Mie}} \times 100\%$ versus size parameter.

calculation [Wiscombe, 1980] is shown in Figure 5.5 and Figure 5.6. The variation of the absorption efficiency Q_{abs} with particle size parameter $x = 2\pi a/\lambda$ for wavelength $\lambda = 0.5$ μm is shown in Figure 5.5a. The dashed curve is the absorption efficiency Q_{abs} calculated using Mie theory [Wiscombe, 1980] and the solid curve is that from the geometrical optics method (GOM). To assess the deviation of the calculation of GOM from that of the Mie calculation, an absorption efficiency difference factor is defined as

$$\Delta_{abs} = \frac{Q_{abs}^{Mie} - Q_{abs}^{Geo}}{Q_{abs}^{Mie}} \times 100\% \tag{5.42}$$

The variation of Δ_{abs} with x for $\lambda = 0.5$ μm is shown in Figure 5.5b. The average difference factor for size parameter x from 10 to 10^4 is 1.46% due to many extremely narrow peaks (ripple structure). If these peaks are ignored, the difference should be smaller [Bohren and Huffman, 1983]. For large particles with x from 5000 to 10,000, the average is 1.03%. As x increases, the difference factor decreases to zero. Variation of absorption efficiency for a more absorbing band such as $\lambda = 2.0$ μm is shown in Figure 5.6. The results for $\lambda = 2.0$ μm is obtained using the same procedure as for $\lambda = 0.5$ μm. As the size parameter increases, Q_{abs} approaches an asymptotic value as indicated by results from both Mie calculation and the geometrical optics method (Figure 5.6a). The results from GOM converge to Mie results when the size parameter increases. Average Δ_{abs} versus x is shown in Figure 5.6b. From this figure it is readily seen that the deviation of GOM from Mie results approaches zero as $x > 4000$. Δ_{abs} decreases monotonically with size parameter when $x > 30$, with a maximum of Δ_{abs} occurring at $x \approx 30$. For $x \geq 220$, $\Delta_{abs} < 5\%$. For x from 10 to 10000, the average difference factor is 0.6%, and for large particles with x from 5000 to 10000, the average difference factor is 0.13%.

5.4.2 Near-field Scattering

From Equation (5.23), the scattering efficiency takes the form [Bohren and Huffman, 1983]

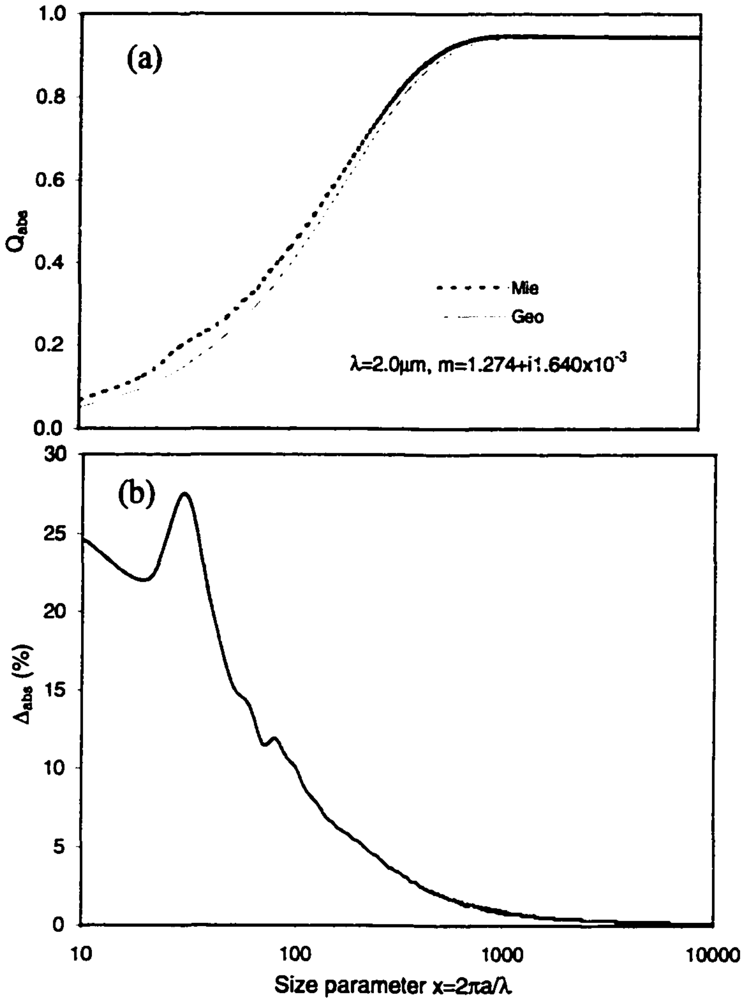

Figure 5.6 (a) Absorption efficiency versus size parameter x = 2πa/λ for wavelength λ = 2.0 μm corresponding to refractive index m = 1.274+i1.640x10^{-3}. Absorption efficiency is calculated using Mie scattering theory (dashed curve) and the geometrical optics method (solid line). (b) Difference factor $\Delta_{abs} = \frac{Q_{abs}^{Mie} - Q_{abs}^{Geo}}{Q_{abs}^{Mie}} \times 100\%$ versus size parameter.

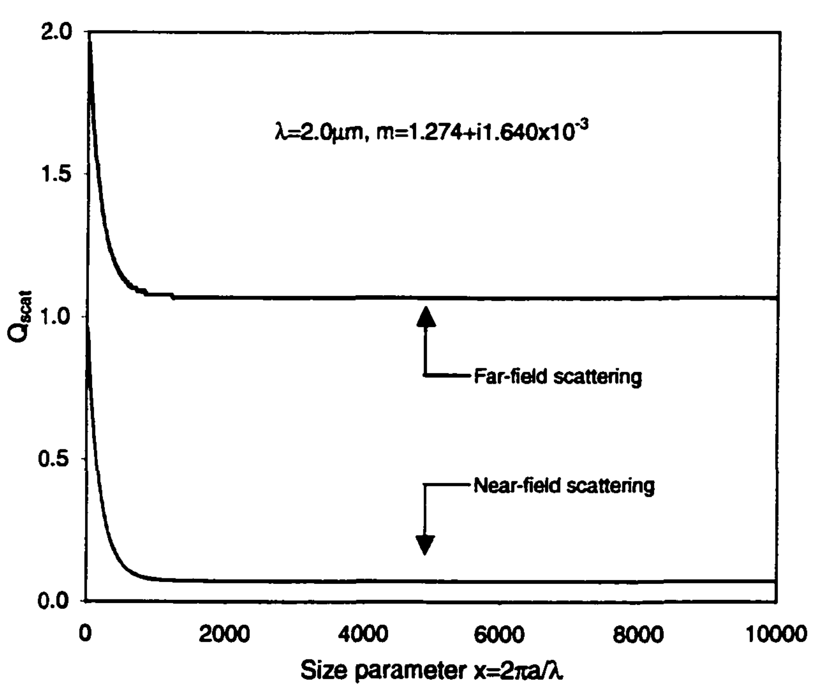

Figure 5.7 Near-field scattering efficiency versus size parameter x = 2πa/λ for wavelength λ = 2.0 μm. The far-field scattering efficiency for λ = 2.0 μm is also included for comparison. The difference between far-field and near-field scattering efficiencies is due only to Fraunhofer diffraction.

$$Q_{sca} = 2\int_0^1 R(\mu_i)\mu_i d\mu_i + \sum_{j=2}^{N} \int_0^1 \left[T_{//}^2(\mu_i)R_{//}^{j-2}(\mu_i) + T_{\perp}^2(\mu_i)R_{\perp}^{j-2}(\mu_i)\right] e^{-\beta\xi(j-1)}\mu_i d\mu_i \quad (5.43)$$

Using the same procedure as in the previous section, the integration of (5.43) can be obtained. For visible light, for instance λ = 0.5 μm, $Q_{sca} \approx 1.0$ for any x because the absorption is very small (Figure 5.5). For the near-infrared spectrum, the scattering efficiency decreases with size parameter and approaches an asymptotic value. For instance, Figure 5.7 shows the variation of the near-field scattering efficiency with the size parameter x = 2πa/λ for wavelength λ = 2.0 μm. The far-field scattering efficiency for λ = 2.0 μm (section 5.4.3) is also included for comparison. If the interference for near-field is neglected, the difference between the far-field and near-field scattering efficiencies are exclusively due to Fraunhofer diffraction.

The phase function Equation (5.26a) and the asymmetry factor g can be written in the following forms when they are combined with Equation (5.25)

$$P(\Theta)=\frac{2\sum_{j,\Theta_i}\sum_{p}\left|\varepsilon_p^j\right|^2 D(j,\Theta_i,\Theta)}{\int_0^\pi \sum_{j,\Theta_i}\left(\left|\varepsilon_{//}^j\right|^2+\left|\varepsilon_{//}^j\right|^2\right)D(j,\Theta_i,\Theta)\sin\Theta d\Theta} \tag{5.44a}$$

$$g=\frac{\int_0^\pi \sum_{j,\Theta_i}\sum_{p}\left|\varepsilon_p^j\right|^2 D(j,\Theta_i,\Theta)\cos\Theta\sin\Theta d\Theta}{\int_0^\pi \sum_{j,\Theta_i}\left(\left|\varepsilon_{//}^j\right|^2+\left|\varepsilon_{\perp}^j\right|^2\right)D(j,\Theta_i,\Theta)\sin\Theta d\Theta} \tag{5.44b}$$

From Equation (5.13) we have

$$\cos\Theta=\cos\left[2(j-1)\left|\Theta_i\right|-2\Theta_i-(j-2)\pi\right] \tag{5.45}$$

For a given scattering angle Θ, we need to find all the sets of (j, Θ_i) that satisfy Equation (5.45), so that the right hand side (RHS) of Equation (5.45) can be evaluated. The method to obtain (j, Θ_i) is as follows: First, scan the j from 1 to N, and for each j solve Equation (5.45) for all possible roots of Θ_i. Then, substitute each set of (j, Θ_i) in Equation (5.44). Summing up all the results gives the phase function.

To solve the intractable trigonometric equation (5.45), let's first transform it into a polynomial equation, which is easier to solve. Setting $S=\tan\left(\frac{\Theta_i}{2}\right)\in[0,1]$, so that $\sin\Theta_i=\frac{2S}{1+S^2}$, $\cos\Theta_i=\frac{1-S^2}{1+S^2}$, Equation (5.45) becomes

$$f(S)=\frac{(-1)^{j-2}}{\left(1+S^2\right)^2}\left\{\left(1-6S^2+S^4\right)\cos\left[2(j-1)\left|\Theta_i\right|\right]+4S\left(1-S^2\right)\sin\left[2(j-1)\left|\Theta_i\right|\right]\right\}-\cos\Theta=0 \tag{5.46}$$

with

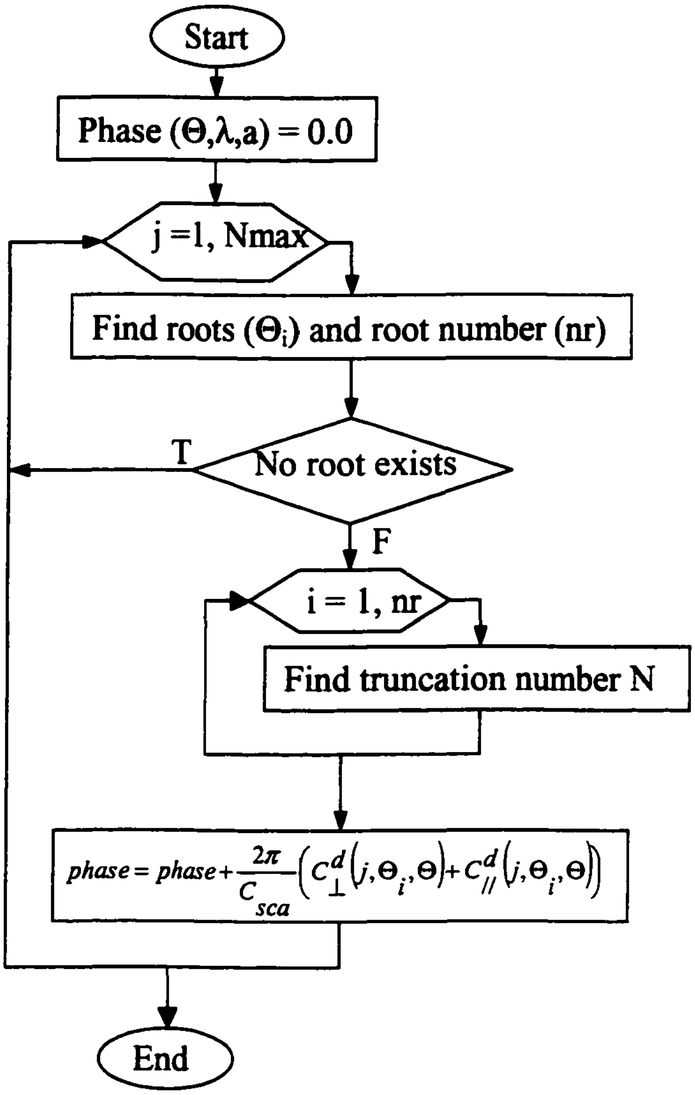

Figure 5.8 Flow chart for the calculation of the phase function of near-field scattering. T = True, F = False. Root-finding is based on a combination of bracketing method and a hybrid algorithm of bisection and Newton-Raphson methods. Interface number is determined by Eq. (5.20).

$$\Theta_t = \sin^{-1}\left(\frac{1}{\hat{m}}\frac{2S}{1+S^2}\right) = -i\ln\left[i\frac{1}{\hat{m}}\frac{2S}{1+S^2} + \sqrt{1-\left(\frac{1}{\hat{m}}\frac{2S}{1+S^2}\right)^2}\right]$$

To find the roots (S) of Equation (5.46) for a given scattering angle Θ, we adopt the following methods. First, we bracket the roots then utilize a hybrid algorithm of bisection and Newton-Raphson methods [Press et al., 1992]. From section 5.3.1 (Figure 5.2), we have seen that for each incident angle there exists an outgoing angle for a specific interface. But the opposite is not true. As the solution S is within [0,1], we calculate brackets for a maximum number of possible roots for n (= nmax) distinct intervals, each of which contains at most one root for each interface. Try and error method is used to find nmax. The number of interfaces is infinite if no truncation is made. The core procedure of calculating the phase function of near-field scattering is shown in Figure 5.8. Given the wavelength, the size (radius) of a sphere, and the scattering angle Θ, scan the interface number j to a reasonable large value jmax (larger than interface number, section 5.3.1). For each interface, search all the possible roots. Appropriate redirection is performed in order to include all possible sets of (j, Θ_i) in the calculation of phase function and asymmetry factor (Equation (5.44)). The phase function versus scattering angle of near field scattering is shown in Figure 5.9 for a snow grain of 1 cm. The black solid line is for wavelength λ = 0.5 μm and light solid line is for λ = 2.0 μm. For the visible light channel, the rainbows (peaks) appear at angles as shown in Table 5.1. However, for near infrared channels, the transmitted energy is attenuated so quickly that almost no energy is available to reach the third interface where the primary rainbow is expected to appear. Thus, the phase function for the near-infrared spectrum is much smoother than for the visible channels. To compare the results from GOMsnow code developed in this chapter with those from the Monte Carlo code [Nakajima et al., 1998], which deals with non-absorbing medium, Figure 5.10 shows the phase function for refractive index $\hat{m}$ = 1.333 + i 0.0. The data from the Monte Carlo code are taken from Table 1 of the paper by Kokhanovsky and Nakajima (1998). The results show that the agreement between the two codes is remarkably good for scattering by a non-absorbing medium.

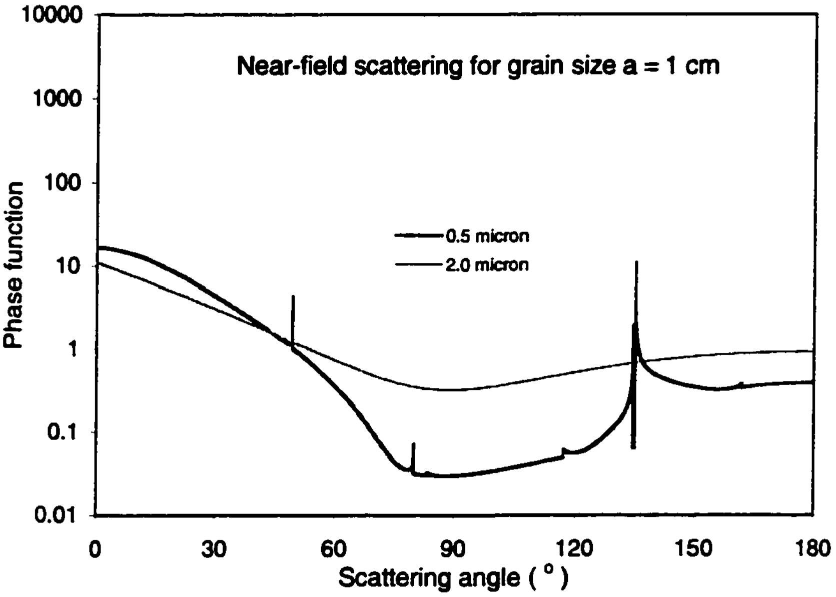

Figure 5.9 Phase function of near-field scattering versus scattering angle Θ for snow grains of a = 1 cm for wavelength λ = 0.5 μm and 2.0 μm. Each peak in the visible curve corresponds to the position of a rainbow.

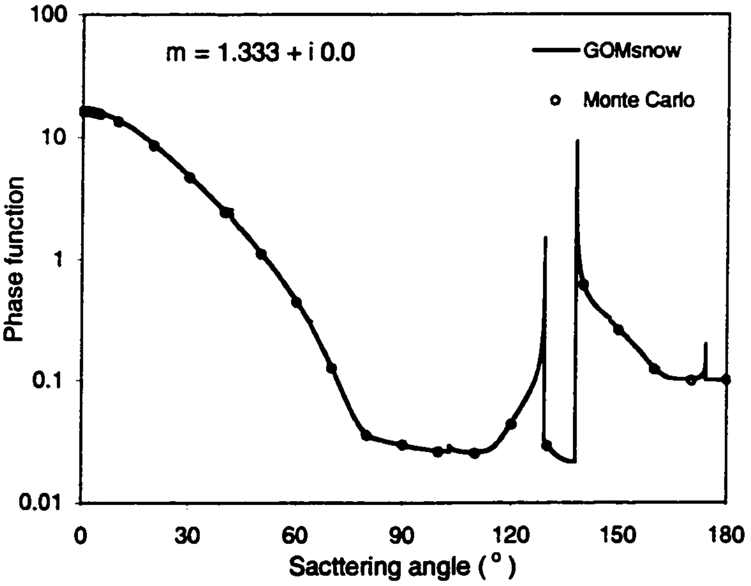

Figure 5.10 Comparison of the phase function calculated with GOMsnow with that from a Monte Carlo code [Kokhanovsky and Nakajima, 1998; Nakajima et al., 1998] for the non-absorbing case of $\hat{m}$ = 1.333 + i 0.0.

5.4.3 Far-field Scattering

The scattering efficiency for far field scattering takes the form

$$Q_{sca}^{F} = Q_{sca}^{N} + 1 \tag{5.47}$$

The phase function and asymmetry factor g are from Equations (5.40)-(5.41)

$$P(\Theta_i, \Theta) = \frac{\left[2\sum_{j,\Theta_i}\sum_{p}\left|\varepsilon_p^j\right|^2 D(j,\Theta_i,\Theta) + \frac{4J_1^2(x\sin\Theta)}{\sin^2\Theta}\right]}{1 + \int\sum\left[\left|\varepsilon_{//}^j\right|^2 + \left|\varepsilon_{\perp}^j\right|^2\right]D(j,\Theta_i,\Theta)\sin\Theta d\Theta} \tag{5.48}$$

$$g = \frac{\int_0^\pi d\Theta\cos\Theta\sin\Theta\left\{\sum_{j,\Theta_i}\sum_{p}\left|\varepsilon_p^j\right|^2 D(j,\Theta_i,\Theta) + \frac{2J_1^2(x\sin\Theta)}{\sin^2\Theta}\right\}}{1 + \int_0^\pi\sum_{j,\Theta_i}\left[\left|\varepsilon_{//}^j\right|^2 + \left|\varepsilon_{\perp}^j\right|^2\right]D(j,\Theta_i,\Theta)\sin\Theta d\Theta} \tag{5.49}$$

Following the same procedure as in the previous section to find all the sets of (j, Θ_i) for a given scattering angle, scattering efficiency, asymmetry factor and phase function can be evaluated. For visible light, whose absorption in snow is negligible, the scattering efficiency is about 2.0. For the near-infrared spectrum, for instance λ = 2.0 μm, the absorption is much larger than the visible, the scattering efficiency is well below 2.0. The size parameter dependence of Q_{scat} is shown in Figure 5.11. When x ≥ 1300, Q_{scat} is almost constant. To compare results from GOMsnow with those from Mie scattering calculation, Figure 5.11a shows the Q_{scat} versus size parameter x from both GOM and Mie calculations. The inset of Figure 5.11a shows the results for x up to 10000. Differences between GOM and Mie are only visible at small x values. Figure 5.11b shows the relative deviation of GOM calculation from Mie calculation. For x ≥ 110, the relative deviation is smaller than 5%. For x ≥ 350, the relative deviation is smaller than 1%. Combined with the comparisons for other wavelengths we conclude that the scattering efficiency calculated using GOMsnow agrees well with Mie calculation for x as small as 300.

Phase functions of far field scattering are shown in Figure 5.12. For comparison, the phase functions of near-field scattering are also shown. Figure 5.12a is for λ = 0.5 μm

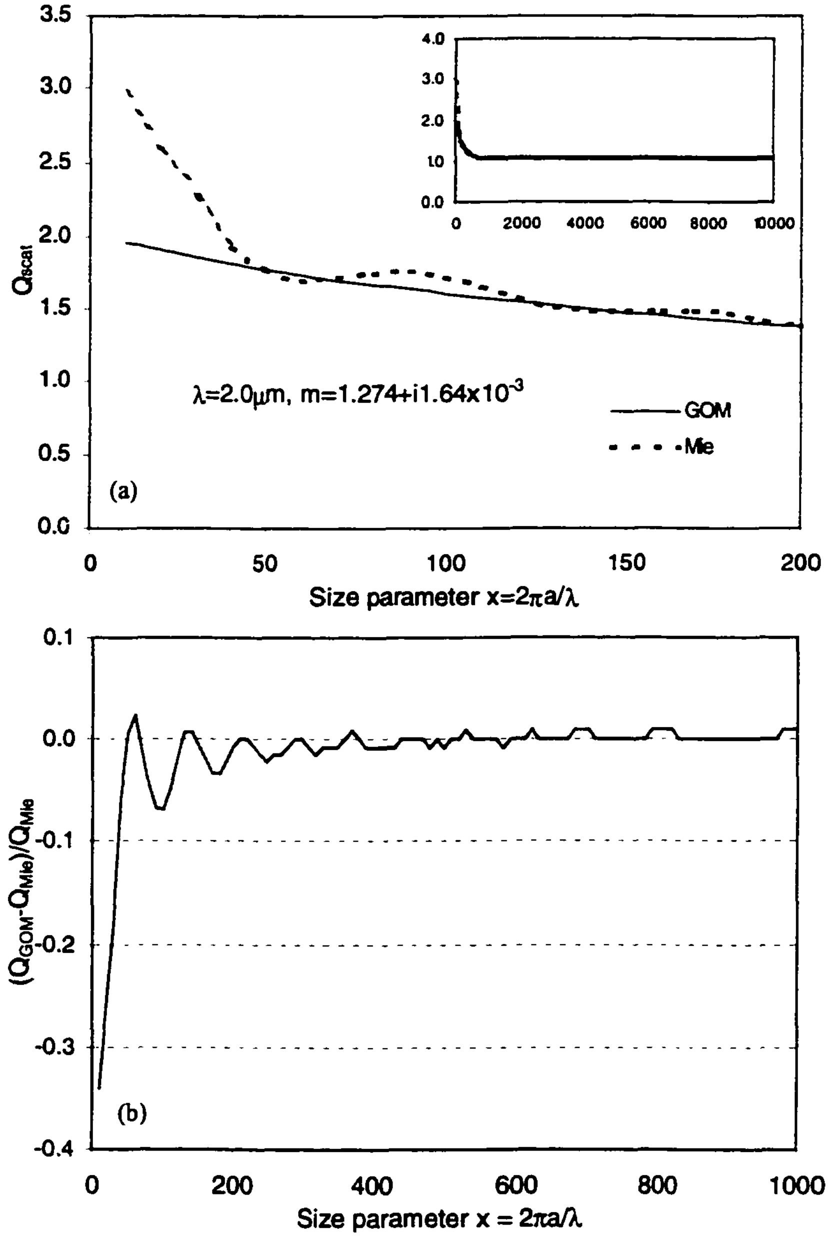

Figure 5.11 (a) Far-field scattering efficiency versus size parameter x = 2πa/λ for wavelength λ = 2.0 μm. In the inset, the size parameter extends to 1000. The difference between Mie and GOM calculations is very small except for small size parameter (<200). (b) The deviation of the scattering coefficient calculated by GOMsnow from that by Mie0. For x ≥ 110, the deviation is smaller than 5%.

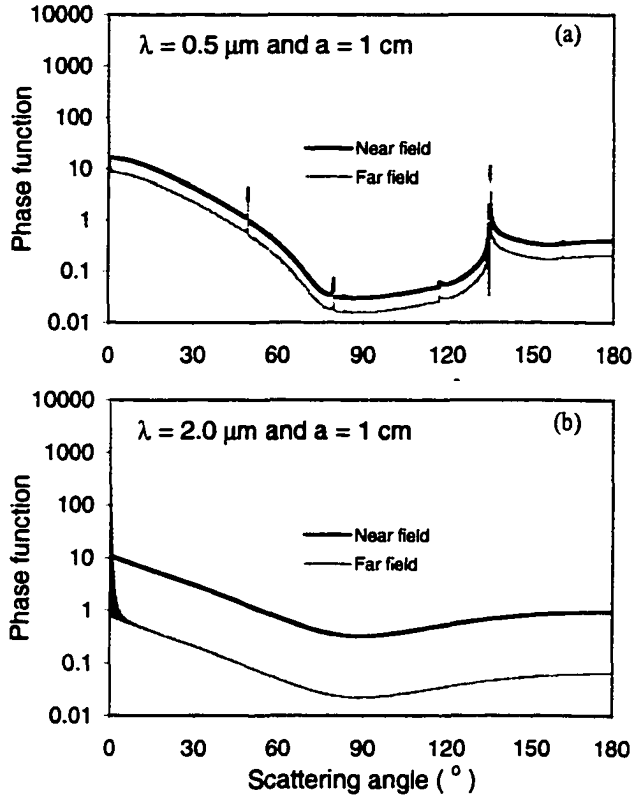

Figure 5.12 Phase function of far-field scattering versus scattering angle Θ for snow grains of a = 1 cm for wavelength (a) λ = 0.5 μm and (b) λ = 2.0 μm. For comparison, near-field results are also shown. Each peak appears in the visible curve corresponding to the position of the rainbow. Strong forward scattering due to Fraunhofer diffraction appears in far-field scattering phase function.

and Figure 5.12b is for λ = 2.0 μm. For the same wavelength, the structure of phase function for near- and far-field are similar, except in the forward scattering direction where there is a strong forward scattering for far-field scattering due to Fraunhofer diffraction. The difference between different channels for far-field scattering is similar to the case for near-field scattering. In the visible light region, multiple rainbows appear while in the near infrared region, no "rainbows" are observed for the same reason as described in section 5.4.2.

5.5 Discussion and Conclusions

The absorption efficiency, scattering efficiency and scattering phase function for both near- and far-field scattering are calculated for large snow grains on the basis of the geometrical optics method (GOM). Both the incident and scattered radiation fields are assumed to be time-harmonic. The code GOMsnow is developed to calculate these single-scattering properties. Comparison of results from GOMsnow with Mie0 indicate that the GOMsnow can be used for $x \geq 300$. Spectral dependence of these properties is obtained based on the spectral complex refractive index database of ice [Warren, 1984; Kou et al., 1993; Perovich and Govoni, 1991]. The phase function is calculated directly using a hybrid algorithm of bisection and Newton-Raphson methods [Press et al., 1992]. Comparison between GOMsnow code and a Monte Carlo code [Nakajima, 1998; Kokhanovsky and Nakajima, 1998] indicates that the agreement is remarkably good. Detailed scattering patterns can be constructed using GOMsnow. Rainbow angles appearing in the phase function agree well with analytical results [van de Hulst, 1957; Liou and Hansen, 1971]. Due to the difference of absorption or the imaginary part of the complex refractive index between the visible region and the near infrared region within the solar spectrum, rainbows mainly appear in the visible spectrum, where absorption is so weak that there exists at least one internal reflection. Rainbows seldom appear in the near-infrared spectrum, where absorption is large enough for the refracted portion of the energy to decrease to a negligible level without any internal reflection. Phase function calculations for both near- and far-field scatterings show that the angular distribution of the scattered light intensity of near-infrared channels by large snow grains is more evenly distributed than visible light.

GOMsnow was tested against a Monte Carlo code [Nakajima et al., 1998; Kokhanovsky and Nakajima, 1998]. Results from GOMsnow agrees well with Mie0 code [Wiscombe, 1979; 1980] for size parameter ≥ 200. GOMsnow and Mie0 codes can be combined to calculate single scattering properties for any wavelength from ultraviolet to microwave. The size parameter is unlimited for GOMsnow when size parameter ≥ 200. The code is computationally efficient and the computing time is almost independent of size parameter, while for Mie0 code the size parameter is limited (< 20000) and computing-time is intensive when the size parameter is large. The calculated angular scattering patterns agree well with Mie calculation for any incident angle, rather than only good for the incident angle ≤ 60° using geometrical optics method as obtained by Glantschnig and Chen (1981). This is because the number of internal reflections truncated based on the truncation tolerance number (see section 5.3.1) is a dynamic parameter that depends on the incident angle, while Glantschnig and Chen's calculation was based only on $N = 2$.

The GOMsnow code is a computer program written in ANSI 77 standard FORTRAN to calculate the absorption coefficients, scattering coefficients and phase function for both near- and far-field scattering of unpolarized radiation by snow grains in the solar spectrum, as well as at thermal infrared and microwave wavelengths. For general purposes, the three input parameters are wavelength of the light in meters, radius of the snow grain in meters and scattering angle in radians. If only absorption and scattering coefficients are needed, only wavelength and radius of the snow grain are inputs, and the scattering angle can be set to any value. The code and associated information can be downloaded by ftp anonymously to ftp.gi.alaska.edu. The files are in /pub/xzhou directory.

ACKNOWLEDGMENTS

The research involved in this chapter was supported by the National Aeronautics and Space Administration under grant NAG5-6338 to the University of Alaska Fairbanks.

CHAPTER 6

Effects of Vertical Inhomogeneity on Snow Spectral Albedo and Its Implication for Remote Sensing of Snow

ABSTRACT. The spectral albedo of snow is modeled using a multi-layer model based on the multiple scattering radiative transfer code DISORT with the single scattering parameters calculated using the Mie scattering code Mie0 and the geometrical optics method code GOMsnow. Spectral albedo versus snow depth for various snow grain-sizes and densities indicates that albedo approaches an asymptotic value at a very shallow snow depth (~ 3 cm) for the near infrared wavelengths while in the visible, the albedo of a snowpack overlying a black base increases very rapidly with snow thickness when it is smaller than 5 cm. A thickness of 5 cm is enough for the snowpack to be semi-infinite for near-infrared radiation. In the visible, the semi-infinite depth can be as large as 50 cm for a natural snow cover, depending on grain-size and density, but the top 5-10 cm layer is the most important layer. Two snowpacks with the same average grain-size, but with different vertical distributions of grain-size within the very top few centimeters can yield quite different spectral albedos, especially at longer wavelengths. Radiation at near-infrared wavelengths is not only more sensitive to the grain-size for a vertically homogeneous snowpack but also even more sensitive to the grain-size in the upper layers for a vertically heterogeneous snowpack than visible radiation. The visible light is sensitive to snow properties within a much larger snow-depth range than near-infrared radiation. As expected, the vertical structure of density does not affect the semi-infinite spectral albedo. But it does affect the semi-infinite depth. The modeled spectral albedo computed from the multi-layer model agrees better with the measured albedo when the measured composite grain-size rather than the measured single grain-size is adopted. Using a two-layer model, with the top layer comprised of the observed fine grains and the bottom layer of the coarse composite grains, the modeled spectral albedo can be fitted to

the measurements quite well, but the required composite grain-size is twice the measured composite grain-size.

6.1 Introduction

A homogeneous layer of snow is defined as a snow layer in which the three-dimensional skeletal arrangement of ice grains, which can be single ice crystals or groupings of several ice crystals, is characterized by the grains (shape, dimensions, crystallographic orientation), the bonds (area), the coordination number [Watanabe, 1993] (including the bond's spatial distributions relative to the grain), and the spatial arrangement of chains formed by several grains that obey the same statistical distributions [Salm, 1982]. It is common for a natural snowpack to be composed of layers of different types of snow, and each of which is more or less a homogeneous layer [Colbeck, 1991]. Generally, a seasonal snow cover is highly stratified with many layers, each layer has its own physical, optical, thermal and mechanical properties due to the initial snow condition and thermal history. A snow cover has a stratified structure because the snow cover is deposited in a series of uniform snowfall periods at the time of deposition. Subsequent metamorphosis, which is mainly determined by varying weather conditions, load and arrangement of ice particles, may have almost the same effect on each layer, so that the homogeneous nature of that layer is preserved in the lifetime of the snow cover.

A stratified structure is ubiquitously observed in the snow cover on sea ice [Sturm et al., 1998; Morris and Jeffries, 2001]. Snow grain-size was observed to increase generally from about 0.1 mm for new snow cover at the top of snow to about 5 mm at the bottom in winter [Sturm et al., 1998] or even larger than 15 mm in summer [Morris and Jeffries, 2001], but not necessarily every homogeneous layer above has smaller grain-size than layers below. Similar stratification has also been observed on snowpacks on land [Grenfell et al., 1994; Aoki et al., 2000], except that the grain-size below the very top layers is smaller than in the snowpack on sea ice.

For remote sensing of snow, physical and optical properties are the main concerns. In the following study of the interaction of solar radiation with snow, the definition of a homogeneous snow layer is simplified to be a snow layer of the same effective snow grain-size, density and texture. In a natural snow cover, the average snow grain-size and density show a remarkable variation from the top layers to the bottom layers [Aoki et al., 2000; Morris and Jeffries, 2001]. This vertical inhomogeneity of the snow physical parameters is expected to affect the outcomes of the interaction of solar radiation with the snow cover, and thus the signals received by optical instruments such as MODIS aboard the Terra and Aqua satellites, or the MEdium Resolution Imaging Spectrometer (MERIS) aboard the European Space Agency (ESA) satellite ENVISAT. Understanding the effect of the vertical structure of a snowpack on the reflectance of snow is required for correct interpretation of snow albedo measurements from both ground-based instruments and satellite sensors.

Modeling efforts of snow spectral albedo were comprehensively reviewed by Wiscombe and Warren (1980) and Warren (1982). Using a simple analytical model based on the delta-Eddington approximation [Joseph et al., 1976], Wiscombe and Warren (1980) studied the dependence of the spectral albedo on snow grain-size (or age), liquid water content (through increase of effective snow grain-size), solar zenith angle, cloud cover (through changing the effective incidence angle), snow thickness, and snow density. A common difficulty in simulating the snow spectral reflectance of a natural snowpack using a single grain-size is that a good agreement in the near-infrared of the model with measurement destroys the model's good agreement in the visible, and *vice versa*. Thus, using the grain-size of the snow surface of a homogeneous snowpack, the modeled near-infrared albedo may agree well with measurements of a natural snow cover, while the modeled visible albedo is consistently higher than the measured values [Grenfell and Maykut, 1977; Kuhn and Siogas, 1978; Wiscombe and Warren, 1980; Knap et al., 1999]. The discrepancy in the visible region is often attributed to impurities in the snow (soot, dust) [Warren and Wiscombe, 1980; Knap et al., 1999; Aoki et al., 2000]. However, Antarctic snow is generally considered to be very clean. For instance, Kumai (1976) found that the impurity (clay minerals) concentration at the South Pole was 15 ng/g. Murozumi et al. (1969) found that the impurity (terrestrial dust) at Byrd Station, West Antarctica, was 2 ng/g. Warren and Clarke (1990) found near the South Pole that impurity (soot) in snow far from the station was 0.1-0.3 ng/g. Thus, impurities are generally neglected in modeling of Antarctic snow reflectance [Grenfell et al., 1994]. All comparisons of measured spectral albedo with modeling for pure snow indicate that a single homogeneous layer model for a natural snowpack cannot explain the observations. Thus, Grenfell et al. (1994) introduced a two-layer model: a very thin layer of very fine grain-size snow on top of a thick layer of much larger grain-size snow. The two-layer model can fit observations very well, though more research is needed in the interpretation and applicability of the model.

Grenfell et al.'s (1994) measurements were carried out at South Pole and Vostok in summer, when the air temperature rarely rises above -20°C. The snow is cold and dry so that snow metamorphism proceeds very slowly. Therefore the snow grain-size at the top of the snowpack is very fine (20 - 100 μm) and the largest grain-size at lower layers is also fine (0.2 - 0.5 mm). The snowpack on sea ice in summer is quite different. The air temperature is around 0°C, liquid-water content in the snow can increase from dry or moist at the top to wet and slushy at the bottom due to melting from the top and flooding from the bottom [Jeffries et al., 1994; 2001]. Snow metamorphism proceeds quickly, resulting in much larger snow grain-size in the snowpack over sea ice than the snowpack on the Antarctic continent. Formation of composite grains, including clustered single crystals (6cl) and melt-freeze polycrystalline particles (6mf) [Colbeck et al., 1990] makes the summer snowpack on sea ice a very special snow cover that has coarse (1.0-2.0 mm) or even extremely coarse (> 5 mm) grain-size. Morris and Jeffries (2001) found that snow composite grains comprise most of the snowpack on sea ice in summer while individual single grains account for only a small portion.

This chapter focuses on the use of a multi-layer snow model to compute the spectral albedo of snow on sea ice, the effect of the vertical inhomogeneity of a snowpack on the reflectance, and comparisons of the modeling with highly resolved spectral albedo measurements (spectral resolution: 3 nm) in the 0.33-1.06 μm spectral region on summer snowpacks on sea ice in the Ross Sea, Antarctica.

6.2 Radiative Transfer Modeling Formulation

The general equation for radiation at wavelength λ in a dispersive medium is written in vector form [Chandrasekhar, 1950; Papanicolaou and Burridge, 1975; Kokhanovsky, 1999]:

$$\begin{aligned}\frac{d\bar{\mathrm{I}}_\lambda(\theta,\varphi)}{dL} &= -\hat{\sigma}_{ext}\bar{\mathrm{I}}_\lambda(\theta,\varphi) + \int_0^{2\pi} d\varphi' \int_0^{\pi} d\theta' \sin\theta' \hat{\sigma}^d_{sca}(\theta,\varphi;\theta',\varphi')\bar{\mathrm{I}}_\lambda(\theta',\varphi') \\ &\quad + \bar{S}_{\lambda,extn}(\theta,\varphi)\end{aligned} \tag{6.1}$$

where $\bar{\mathrm{I}}$=(I,Q,U,V) is the Stokes vector, dL is the distance traversed by the radiation, $\hat{\sigma}_{ext}$ is the extinction matrix, and $\hat{\sigma}^d_{sca}$ is differential scattering matrix. $\bar{S}_{\lambda,extn}$ is the external source function of the Stokes vector. The second term of the right hand side in Equation (6.1) is the internal source due to multiple scattering into the direction **Ω** = (θ, φ) from all other directions **Ω**' = (θ', φ').

It is relatively easy to find simple expressions for the external source function in some limiting cases, for example, the blackbody radiation when local thermodynamic equilibrium is reached. The source function is defined as the ratio of the emission coefficient j_λ to the absorption coefficient k_λ at a given point of the radiation field. According to Kirchhoff's law, the coefficient of emission j_λ of any matter in local thermodynamic equilibrium is connected with its coefficient of absorption k_λ through the relation

$$j_\lambda = k_\lambda(1-\omega_0)B_\lambda(T)$$

Thus, the source function

$$\bar{S}_{\lambda,extn}/\sigma_{ext} = j_\lambda / k_\lambda = (1-\omega_0)B_\lambda(T)$$

where

$$B_\lambda(T) = \frac{2hc}{\lambda^5\left(e^{hc/\lambda KT}-1\right)}$$

is the Plank function, T the absolute temperature, K (=1.380662 x 10-23 J deg^{-1}) the Boltzmann's constant, h (=6.626075 x 10^{-34} Js) the Planck's constant and c the speed of light.

For optical remote sensing, our concern is in the visible, near infrared and infrared spectrum. Let's denote the vertical coordinate as z, with z = 0 being the top of the scattering and absorbing medium. Direction of z is downward. The polar angle θ is defined as the angle between the inverse direction of the z axis and the light traveling direction. This configuration is shown in Figure 6.1. We also simplify Equation (6.1) by ignoring the polarization of the spectral radiation. The optical depth is

$$d\tau = \sigma_{ext}(z)dz. \tag{6.2}$$

From Figure 6.1, we can see that dL = dz/cos(π-θ) = -secθ dz. The radiative transfer equation now becomes

$$\begin{aligned}\cos\theta\frac{d\mathrm{I}_\lambda(\tau,\theta,\varphi)}{d\tau} = \mathrm{I}_\lambda(\tau,\theta,\varphi) - \frac{\omega_0}{4\pi}\int_0^{2\pi} d\varphi' \int_0^{\pi} d\theta' P(\tau;\theta,\varphi;\theta',\varphi')\mathrm{I}_\lambda(\theta',\varphi')\sin\theta' \\ -(1-\omega_0)B_\lambda(T)\end{aligned} \tag{6.3}$$

where the phase function

$$P(\tau;\mu,\varphi;\mu',\varphi') = \frac{4\pi C_{sca}^d(\tau,\Theta)}{C_{sca}} = \frac{2C_{sca}^d(\tau,\Theta)}{\int_0^{\pi} d\Theta C_{sca}^d(\tau,\Theta)\sin\Theta} \tag{6.4}$$

is the probability of a photon scattering from the direction **Ω**'= (0', φ') to the direction **Ω** = (θ, φ). $C_{sca} = C_{ext} - C_{abs}$ is the total scattering cross-section.

$$C_{sca} = 2\pi\int_0^{\pi} d\Theta C_{sca}^d(\tau,\Theta)\sin\Theta$$

The phase function satisfies the normalization function

$$\frac{1}{4\pi}\int P(\tau;\Theta,\Psi)d\Omega = 1,$$

where $d\Omega = \sin\Theta d\Theta d\Psi$ is the element of solid angle. Based on the phase function, the asymmetry factor is defined as

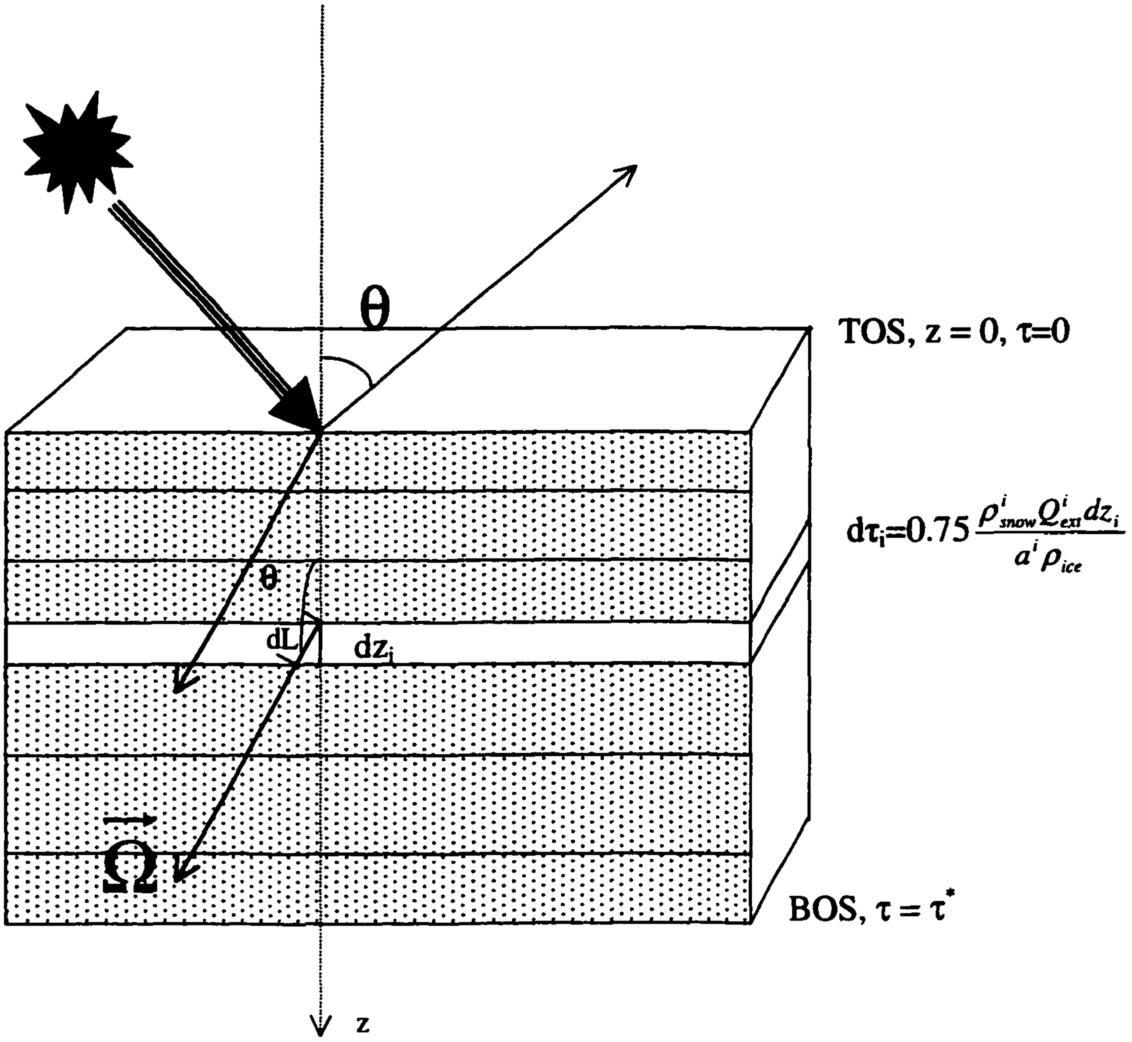

Figure 6.1 Optical geometry of radiation transport in snowpack. TOS = Top Of Snow; BOS = Bottom Of Snow.

$$g = \langle \cos\Theta \rangle = \frac{1}{4\pi} \int P(\tau;\Theta,\Psi)\cos\Theta d\Omega \tag{6.5}$$

The total extinction coefficient σ_{ext} and the absorption coefficient σ_{abs} depend on the number concentration of particles n and their absorption cross-section C_{abs} and scattering cross-section C_{sca} [Bohren and Barkstrom, 1974]:

$$\sigma_{ext} = nC_{ext}, \quad \sigma_{sca} = nC_{sca}, \quad \sigma_{abs} = nC_{abs}, \qquad C_{ext} = C_{sca} + C_{abs} \tag{6.6}$$

where C_{ext} is the extinction cross-section. $\omega_0 \equiv \sigma_{sca}/\sigma_{ext} = \sigma_{sca}/(\sigma_{abs} + \sigma_{sca})$ is the single-scattering albedo.

Two ideal cases are worth considering. The first is that the medium is perfectly absorbing, i.e., $\omega_0 = 0$. Equation (6.2) is reduced to

$$\cos\theta \frac{dI_\lambda(\tau,\theta,\varphi)}{d\tau} = I_\lambda(\tau,\theta,\varphi) - B_\lambda(T) \tag{6.7}$$

This is the case for local thermodynamic equilibrium. Supposing the radiation travels from z = 0 (τ=0) to point z = Z (τ=τ), the solution is

$$I_\lambda(\tau,\theta,\varphi) = I_{\lambda 0}(\theta,\varphi)e^{-\tau/\cos\theta} + B_\lambda(T)(1 - e^{-\tau/\cos\theta})$$

with $\tau = \int_0^Z \sigma_{ext}(z)dz$.

The second case is the perfect scattering medium, i.e., $\omega_0 = 1$. Equation (6.2) is then reduced to

$$\cos\theta \frac{dI_\lambda(\tau,\theta,\varphi)}{d\tau} = I_\lambda(\tau,\theta,\varphi) - \frac{1}{4\pi}\int_0^{2\pi} d\varphi' \int_0^{\pi} d\theta' P(\tau;\theta,\varphi;\theta',\varphi')I_\lambda(\theta',\varphi')\sin\theta' \tag{6.8}$$

The main parameters of Equation (6.8) are the optical thickness τ, the single scattering albedo ω_0, and the phase function $P(\tau;\mu,\varphi;\mu',\varphi')$. The single scattering and absorption properties have been discussed in Chapter 5. Outputs from the MieO and GOMsnow codes are input into Equation (6.3) so that the radiance at any angle can be calculated.

What we want to calculate is the radiance (or intensity) at any angle. For remote sensing, the fundamental distinction between upward ($0 \le \theta \le \pi/2$, $0 \le \mu \le 1$) and downward directions ($\pi/2 \le \theta \le \pi$, $-1 \le -\mu \le 0$) is recognized so that Equation (6.2) splits into two [Thomas and Stamnes, 1999]

$$\begin{aligned}\mu\frac{dI_\lambda^{\uparrow}(\tau,\mu,\varphi)}{d\tau} &= I_\lambda^{\uparrow}(\tau,\mu,\varphi)-\frac{\omega_0}{4\pi}\int_0^{2\pi}d\varphi'\int_0^1 d\mu' P(\tau;\mu,\varphi;\mu',\varphi')I_\lambda^{\uparrow}(\mu',\varphi')\\ &-\frac{\omega_0}{4\pi}\int_0^{2\pi}d\varphi'\int_0^1 d\mu' P(\tau;\mu,\varphi;-\mu',\varphi')I_\lambda^{\downarrow}(\mu',\varphi')\\ &-(1-\omega_0)B_\lambda(T)\end{aligned} \tag{6.9a}$$

$$\begin{aligned}-\mu\frac{dI_\lambda^{\downarrow}(\tau,\mu,\varphi)}{d\tau} &= I_\lambda^{\downarrow}(\tau,\mu,\varphi)-\frac{\omega_0}{4\pi}\int_0^{2\pi}d\varphi'\int_0^1 d\mu' P(\tau;-\mu,\varphi;\mu',\varphi')I_\lambda^{\uparrow}(\mu',\varphi')\\ &-\frac{\omega_0}{4\pi}\int_0^{2\pi}d\varphi'\int_0^1 d\mu' P(\tau;-\mu,\varphi;-\mu',\varphi')I_\lambda^{\downarrow}(\mu',\varphi')\\ &-(1-\omega_0)B_\lambda(T)\end{aligned} \tag{6.9b}$$

In Equation (6.9) and the following discussion, $0 \le \mu \le 1$, so that $I_\lambda^{\uparrow}(\tau,\mu,\varphi)=I_\lambda(\tau,\mu,\varphi)$, and $I_\lambda^{\downarrow}(\tau,\mu,\varphi)=I_\lambda(\tau,-\mu,\varphi)$.

For radiative transfer in the solar spectrum, at any level of optical thickness, it is convenient to distinguish the direct component of the radiance from the diffuse component, especially for the retrieval of reflectance at the ground surface from remotely sensed data. For the upward radiance, there is no direct component, unless specular reflection is taken into account, which is not done here. While for the downward radiance, there are direct and diffuse components. Therefore,

$$I_\lambda^{\uparrow}(\tau,\mu,\varphi)=I_{\lambda,df}^{\uparrow}(\tau,\mu,\varphi) \tag{6.10a}$$

$$I_\lambda^{\downarrow}(\tau,\mu,\varphi)=I_{\lambda,dr}^{\downarrow}(\tau,\mu,\varphi)+I_{\lambda,df}^{\downarrow}(\tau,\mu,\varphi) \tag{6.10b}$$

where subscripts *dr* and *df* correspond to the direct and diffuse components of the radiance, respectively.

The direct component of the downward radiance $I_{\lambda,dr}^{\downarrow}(\tau,\mu,\varphi)$ satisfies the following equation

$$-\mu\frac{dI_{\lambda,dr}^{\downarrow}(\tau,\mu,\varphi)}{d\tau}=I_{\lambda,dr}^{\downarrow}(\tau,\mu,\varphi)$$

The solution to it is

$$I_{\lambda,dr}^{\downarrow}(\tau,-\mu_0,-\mu,\varphi-\varphi_0)=F_\lambda^S e^{-\tau/\mu_0}\delta(\mu-\mu_0)\delta(\varphi-\varphi_0) \tag{6.11}$$

where F_λ^S is the spectral irradiance at the top of the atmosphere. The incidence solar angles are (μ_0, φ_0).

Substituting Equations (6.7) - (6.8) into Equation (6.5), we obtain the following equations for the diffuse components of upward and downward radiances

$$\begin{aligned}\mu\frac{dI^{\uparrow}_{\lambda,df}(\tau,\mu,\varphi)}{d\tau} &= I^{\uparrow}_{\lambda,df}(\tau,\mu,\varphi)-\frac{\omega_0}{4\pi}\int_0^{2\pi}d\varphi'\int_0^1 d\mu' P(\tau;\mu,\varphi;\mu',\varphi')I^{\uparrow}_{\lambda,df}(\mu',\varphi')\\ &-\frac{\omega_0}{4\pi}\int_0^{2\pi}d\varphi'\int_0^1 d\mu' P(\tau;\mu,\varphi;-\mu',\varphi')I^{\downarrow}_{\lambda,df}(\mu',\varphi')\\ &-\frac{\omega_0}{4\pi}P(\tau;\mu,\varphi;-\mu_0,\varphi_0)F_\lambda^S e^{-\tau/\mu_0}\\ &-(1-\omega_0)B_\lambda(T)\end{aligned} \tag{6.12a}$$

$$\begin{aligned}-\mu\frac{dI^{\downarrow}_{\lambda,df}(\tau,-\mu,\varphi)}{d\tau} &= I^{\downarrow}_{\lambda,df}(\tau,-\mu,\varphi)-\frac{\omega_0}{4\pi}\int_0^{2\pi}d\varphi'\int_0^1 d\mu' P(\tau;-\mu,\varphi;\mu',\varphi')I^{\uparrow}_{\lambda,df}(\mu',\varphi')\\ &-\frac{\omega_0}{4\pi}\int_0^{2\pi}d\varphi'\int_0^1 d\mu' P(\tau;-\mu,\varphi;-\mu',\varphi')I^{\downarrow}_{\lambda,df}(\mu',\varphi')\\ &-\frac{\omega_0}{4\pi}P(\tau;-\mu,\varphi;-\mu_0,\varphi_0)F_\lambda^S e^{-\tau/\mu_0}\\ &-(1-\omega_0)B_\lambda(T)\end{aligned} \tag{6.12b}$$

In the following sections, the main task is to solve Equation (6.12) for $I^{\uparrow}_{\lambda,df}(\tau,\mu,\varphi)$ and $I^{\uparrow}_{\lambda,df}(\tau,\mu,\varphi)$ using the discrete-ordinate (DISORT) algorithm [Stamnes et al., 1988]. Then, substituting these with Equation (6.11) into Equation (6.10), we obtain the upward and downward radiances at any optical thickness level and any viewing angle.

Let's take the principal plane, which is defined as the vertical plane intercepting the sun, as the reference plane for the azimuth, i.e., $\varphi_0 = 0$. Supposing at some level of τ, the radiance $I_\lambda(\tau, \mu, \varphi)$ is obtained, the following important quantities can be calculated. The net monochromatic energy flux or irradiance is

$$\begin{aligned}F_\lambda(\tau,\mu_0) &= \int_\Omega I_\lambda(\tau;\mu,\varphi;\mu_0)\mu d\Omega\\ &= F_\lambda^{\uparrow}(\tau,\mu_0)-F_\lambda^{\downarrow}(\tau,\mu_0)\end{aligned} \tag{6.13}$$

This is an important quantity for energy deposition within snow, resulting in the internal melting of the snowpack. The monochromatic upward and downward fluxes or spectral irradiances are

$$\begin{aligned} F_\lambda^\uparrow(\tau,\mu_0) &= \int_0^{2\pi} d\varphi \int_0^1 d\mu \mu I(\tau,\mu_0,+\mu,\varphi-\varphi_0) \\ &= \int_0^{2\pi} d\varphi \int_0^1 d\mu \mu I_\lambda^\uparrow(\tau,\mu_0,\mu,\varphi-\varphi_0) \end{aligned} \tag{6.14}$$

$$\begin{aligned} F_\lambda^\downarrow(\tau,\mu_0) &= \int_0^{2\pi} d\varphi \int_0^1 d\mu \mu I_\lambda(\tau,\mu_0,-\mu,\varphi-\varphi_0) \\ &= \int_0^{2\pi} d\varphi \int_0^1 d\mu \mu I_\lambda^\downarrow(\tau,\mu_0,-\mu,\varphi-\varphi_0) \end{aligned} \tag{6.15}$$

The spectral albedo is then

$$\alpha_\lambda(\tau,\mu_0) = \frac{F_\lambda^\uparrow(\tau,\mu_0)}{F_\lambda^\downarrow(\tau,\mu_0)} \tag{6.16}$$

The bidirectional reflectance distribution function (BRDF) $\rho_\lambda(\tau;-\mu',\varphi';\mu,\varphi)$ is defined as the ratio of the upward infinitesimal radiance in direction (μ,φ) to the downward infinitesimal spectral irradiance in direction (μ',φ') [Nicodemus, et al., 1977; Ahmad and Deering, 1992; Ramon and Santer, 2001], i.e.

$$\begin{aligned} \rho_\lambda(\tau;-\mu',\mu,\varphi-\varphi') &= \frac{dI_\lambda^\uparrow(\tau,-\mu',\mu,\varphi-\varphi')}{dF_\lambda^\downarrow(\tau,-\mu',-\mu_0,\varphi'-\varphi_0)} \\ &= \frac{d^2 I_\lambda^\uparrow(\tau,-\mu',\mu,\varphi-\varphi')}{\mu' I_\lambda^\downarrow(\tau,-\mu',-\mu_0,\varphi'-\varphi_0) d\mu' d\varphi'} \end{aligned} \tag{6.17}$$

Now let's derive the relation between the spectral albedo α_λ and the BRDF. First, the directional-hemispherical reflectance (or "black-sky" albedo) [d'Entremont et al., 1999] or direct-beam albedo [Wiscombe and Warren, 1980]), $\alpha_\lambda^{d-h}(\tau,\mu_0)$, is the albedo only for the directional incident radiation. The spectral albedo at the top of the atmosphere (TOA) is an example:

$$\alpha_\lambda^{d-h}(\mu_0) = \frac{\int_0^1 d\mu \int_0^{2\pi} d\varphi \mu I_\lambda^\uparrow(-\mu_0,\mu,\varphi-\varphi_0)}{\int_0^1 d\mu' \int_0^{2\pi} d\varphi' \mu' I_\lambda^\downarrow(-\mu_0,-\mu',\varphi'-\varphi_0)} \tag{6.18}$$

For the sole directional incident radiation in the direction (μ_0, φ_0),

$$I_\lambda^{\downarrow}(-\mu_{0,}-\mu',\varphi'-\varphi_0)=F_\lambda^S\delta(\mu'-\mu_0)\delta(\varphi'-\varphi_0) \tag{6.19}$$

where F_λ^S is the downward spectral irradiance. From Equation (6.17) and (6.19), we have

$$\begin{aligned} I_\lambda^{\uparrow}(-\mu_0,\mu,\varphi-\varphi_0) &= \int_0^1 d\mu'\int_0^{2\pi} d\varphi'\rho_\lambda(-\mu',\mu,\varphi-\varphi')\mu' I_\lambda^{\downarrow}(-\mu_0,-\mu',\varphi'-\varphi_0) \\ &= \mu_0 F_\lambda^S \rho_\lambda(-\mu_0,\mu,\varphi-\varphi_0) \end{aligned} \tag{6.20}$$

Substituting Equations (6.19) - (6.20) into Equation (6.18) yields

$$\alpha_\lambda^{d-h}(\mu_0)=\int_0^1 d\mu\int_0^{2\pi} d\varphi\mu\rho_\lambda(-\mu_0,\mu,\varphi-\varphi_0) \tag{6.21}$$

This is the relationship between the directional-hemispherical reflectance and BRDF. Equation (6.21) indicates that when the diffuse part of the incident radiation is negligible (for instance, at near-infrared for very clear sky), integration of surface BRDF over the up hemisphere results in the surface spectral albedo.

On the other hand, if the incident radiation is diffuse and perfectly uniform, i.e., the radiance at any incident angle is the same, the albedo defined in Equation (6.16) is called the bi-hemispherical reflectance. As it provides the spectral albedo under conditions of perfectly uniform illumination, it is also called "white-sky" albedo [d'Entremont et al., 1999], or the diffuse albedo [Wiscombe and Warren, 1980]. For completely diffuse illumination, Equation (6.19) becomes

$$I_\lambda^{\downarrow}(-\mu',\varphi')=F_\lambda^S/\pi. \tag{6.22}$$

and Equation (6.17) takes the form as

$$\begin{aligned} I_\lambda^{\uparrow}(\mu,\varphi) &= \int_0^1 d\mu'\int_0^{2\pi} d\varphi'\rho_\lambda(-\mu',\mu,\varphi-\varphi')\mu' I_\lambda^{\downarrow}(-\mu',\varphi') \\ &= \frac{F_\lambda^S}{\pi}\int_0^1 d\mu'\int_0^{2\pi} d\varphi'\rho_\lambda(-\mu',\mu,\varphi-\varphi')\mu' \end{aligned} \tag{6.23}$$

Substituting Equations (6.22) - (6.23) into Equation (6.18), we obtain the diffuse albedo as

$$\begin{aligned} \alpha_\lambda^{h-h} &= \frac{1}{\pi}\int_0^1 d\mu\int_0^{2\pi} d\varphi\int_0^1 d\mu'\int_0^{2\pi} d\varphi'\mu\mu'\rho_\lambda(-\mu',\mu,\varphi-\varphi') \\ &= 2\int_0^1 d\mu\int_0^{2\pi} d\varphi\int_0^1 d\mu'\mu\mu'\rho_\lambda(-\mu',\mu,\varphi-\varphi') \end{aligned} \tag{6.24}$$

Comparison between Equations (6.18) and (6.21) shows that if we integrate the solar zenith angle (incident angle) of the direct albedo, the diffuse albedo is obtained. That is

$$\alpha_\lambda^{h-h} = 2\int_0^1 d\mu'\mu'\alpha_\lambda^{d-h}(\mu') \tag{6.25}$$

For general cases, where the incident radiation at a specific optical thickness contains both directional and diffuse parts, the spectral albedo is calculated from Equation (6.16). For real cases, the diffuse part may not be perfectly isotropic. From Equation (6.17), we have

$$I_\lambda^\uparrow(-\mu_0,\mu,\varphi-\varphi_0) = \int_0^1 d\mu'\int_0^{2\pi} d\varphi'\rho_\lambda(-\mu',\mu,\varphi-\varphi')\mu' I_\lambda^\downarrow(-\mu_0,-\mu',\varphi'-\varphi_0) \tag{6.26}$$

With Equations (6.14) - (6.16) and Equation (6.26), the spectral albedo takes the form

$$\alpha_\lambda(\tau,-\mu_0) = \frac{\int_0^{2\pi} d\varphi\int_0^1 d\mu\int_0^{2\pi} d\varphi'\int_0^1 d\mu'\mu\mu'\,\rho_\lambda(\tau,-\mu',\mu,\varphi-\varphi')I_\lambda^\downarrow(\tau,-\mu_0,-\mu',\varphi'-\varphi_0)}{\int_0^{2\pi} d\varphi'\int_0^1 d\mu'\mu' I_\lambda^\downarrow(\tau,-\mu_0,-\mu',\varphi'-\varphi_0)} \tag{6.27}$$

With Equation (6.21), the above equation can also be written as

$$\alpha_\lambda(\tau,-\mu_0) = \frac{\int_0^{2\pi} d\varphi\int_0^1 d\mu\mu\alpha_\lambda^{d-h}(\tau,-\mu)I_\lambda^\downarrow(\tau,-\mu_0,-\mu,\varphi-\varphi_0)}{\int_0^{2\pi} d\varphi\int_0^1 d\mu\mu I_\lambda^\downarrow(\tau,-\mu_0,-\mu,\varphi-\varphi_0)} \tag{6.28}$$

Inserting Equations (6.10b) and (6.11) into Equation (6.28), and supposing the fraction of direct irradiance in the total downward irradiance is

$$R(\tau,-\mu_0) = \frac{\mu_0 F_\lambda^S e^{-\tau/\mu_0}}{\int_0^{2\pi} d\varphi\int_0^1 d\mu\mu I_\lambda^\downarrow(\tau,-\mu_0,-\mu,\varphi-\varphi_0)} \tag{6.29}$$

yields

$$\begin{aligned}\alpha_\lambda(\tau,-\mu_0) &= R(\tau,-\mu_0)\alpha_\lambda^{d-h}(\tau,-\mu_0)\\ &+\frac{R(\tau,-\mu_0)}{\mu_0 F_\lambda^S e^{-\tau/\mu_0}}\int_0^{2\pi} d\varphi\int_0^1 d\mu\mu\alpha_\lambda^{d-h}(\tau,-\mu)I_{\lambda,df}^\downarrow(\tau,-\mu_0,-\mu,\varphi-\varphi_0)\end{aligned} \tag{6.30}$$

The downward diffuse radiance $I_{\lambda,df}^\downarrow(\tau,-\mu_0,-\mu,\varphi-\varphi_0)$ is the solution of Equation (6.12). Once the BRDF at each layer (specific τ) is calculated (cf. Equation (6.17)), the direct albedo can be obtained from Equation (6.21), then the spectral albedo of that layer can be accurately calculated by Equation (6.30). A few simplified cases are worth noting. Assume the diffuse part of the downward radiance is perfectly isotropic, i.e.,

$$I^{\downarrow}_{\lambda,df}(\tau,-\mu_0,-\mu,\varphi-\varphi_0)=I^{\downarrow}_{0\lambda,df}(\tau,-\mu_0) \tag{6.31}$$

The total downward irradiance [see Equation (6.29)] is then

$$F^{\downarrow}_{\lambda}(\tau,-\mu_0)=\frac{\mu_0 F^{S}_{\lambda} e^{-\tau/\mu_0}}{R(\tau,-\mu_0)}=\mu_0 F^{S}_{\lambda} e^{-\tau/\mu_0}+\pi I^{\downarrow}_{0\lambda,df}(\tau,-\mu_0)$$

from which $I^{\downarrow}_{0\lambda,df}(\tau,-\mu_0)$ is obtained

$$I^{\downarrow}_{0\lambda,df}(\tau,-\mu_0)=\frac{1-R(\tau,-\mu_0)}{\pi R(\tau,-\mu_0)}\mu_0 F^{S}_{\lambda} e^{-\tau/\mu_0} \tag{6.32}$$

Substituting Equations (6.31) - (6.32) into Equation (6.30), we obtain

$$\alpha_{\lambda}(\tau,-\mu_0)=R(\tau,-\mu_0)\alpha^{d-h}_{\lambda}(\tau,-\mu_0)+(1-R(\tau,-\mu_0))\alpha^{h-h}_{\lambda}(\tau,-\mu_0) \tag{6.33}$$

This relation is widely used to calculate the actual albedo from direct albedo and diffuse albedo [Wiscombe and Warren, 1980; Lewis and Barnsley, 1994]. From the derivation above we can see that this relation is true only for the case that the downward radiation consists of direct beam and diffuse radiation that is isotropic. However, if the downward diffuse part is not perfectly uniform, the exact expression for the spectral albedo is Equation (6.30).

All-wave albedo can be obtained by integrating the spectral albedo over the whole solar spectrum.

$$\alpha(\tau,-\mu_0)=\int \alpha_{\lambda}(\tau,-\mu_0)d\lambda \tag{6.34}$$

From the above discussion, we can see that for remotely sensed radiative properties at the ground surface, the radiance distribution and the BRDF are basic quantities for the derivation of radiative quantities such as spectral albedo and all-wave albedo.

The optical depth for each homogeneous layer within the snowpack is

$$\tau^{i}=\sigma^{i}_{ext}d^{i}_{snow}=\frac{3Q^{i}_{ext}\rho^{i}_{snow}d^{i}_{snow}}{4a^{i}\rho_{ice}} \tag{6.35}$$

where a^i, ρ_{snow}^i and d_{snow}^i are the snow grain-size, the density and the depth of the ith layer. Q_{ext}^i is the corresponding extinction efficiency. $\rho_{ice} = 0.917$ g/cm^3 is the density of pure ice. Equation (6.6) and $C_{ext} = \pi a^2 Q_{ext}$ have been used in obtaining Equation (6.35).

6.3 Sensitivity Study I: Vertically Homogeneous Snow Cover

Light transmitted into a snowpack will attenuate with snow depth. An optically semi-infinite depth is defined as the snow depth at or beyond which scattering and absorption of solar radiation do not affect the snow surface spectral albedo. The minimum depth h_{CSD} for a snow cover to be optically semi-infinite is called the critical snow depth (CSD), which is defined as the minimum depth that satisfies

$$\frac{d\alpha_\lambda}{dh}\bigg|_{h_{CSD}} = 0$$

where α_λ is the albedo at wavelength λ, and h is the snow depth. This is too strict a definition. For practical usage, we control the numerical calculation of CSD by using the definition of the effective semi-infinite depth, i.e., the depth h_{CSD}^{eff} at which the difference between the albedo $\alpha_\lambda(h_{CSD}^{eff})$ and $\alpha_\lambda(\infty)$ for an optically infinite snowpack is within 1% [Wiscombe and Warren, 1980]. CSD and effective semi-infinite depth are treated as the same thing in the following discussion. Both of them are also called the 99% cutoff depth. Any depth beyond the critical snow depth but not infinite is a semi-infinite depth.

Suppose a snowpack that has many layers is so deep that the solar radiation at any wavelength can not "see through" the bottom of the snowpack, the number of layers for the albedo calculation should be smaller than the total layers of the whole snowpack. CSD is calculated by iteration with variable integral space step, depending on wavelength due to the much lower penetrating power of near-infrared radiation than the visible. Calculation of CSD for the near-infrared needs finer space steps in the iteration calculation. Once the effective semi-infinite depth is determined, the number of layers can be readily obtained. We also study two cases that discriminate the direct-beam incident radiation from the diffuse.

6.3.1. Spectral Semi-infinite Depth of Snow: Vertically Homogeneous Snow Cover

Beyond the effective semi-infinite depth, the albedo for a specific wavelength will be constant, regardless of the depth. The scattering and absorptive properties of snow are wavelength-dependent; the depth required for a snow cover to be optically semi-infinite is thus also wavelength-dependent. To study the spectral semi-infinite depth, we use the DISORT algorithm [Stamnes et al., 1988] along with Equation (6.35) to solve Equations (6.12) and (6.30) so that the spectral albedo for any depth of the snowpack is obtained. For the sensitivity study, the base of the snow cover is assumed to be a black surface, and the reflectivity is thus zero. But in modeling the measured spectral albedo of the snowpack on sea ice (cf. section 6.5), the albedo of bare first-year sea ice is assumed [Perovich, 1996] if the snow-ice interface is not flooded, but if the base of the snowpack is slush, the albedo of nilas is assumed [Allison et al., 1993], as the spectral albedo for slush is not available. Because nilas surface generally is a mixture of ice and liquid water, like slush, they should have similar albedos, just a little bit higher than that of water. Even though, the effect of the base on the surface reflectance depends ultimately on the thickness of the overlying snowpack. For the incident radiation, we study two ideal cases in detail. The first case is that the incident radiation is a direct beam, and the second case is that the incident radiation is diffuse and perfectly uniform.

Figure 6.2 gives the direct-beam spectral albedo versus snow depth for various wavelengths ($\lambda_1 \ldots \lambda_5 = 0.5, 0.75, 1.0, 1.25$ and 1.5 μm), snow grain-size ($a = 2$ mm and 8 mm), and density ($\rho = 400$ and 800 kg m^{-3}). The solar zenith angle is $\theta_0 = 60°$. Comparison of Figure 6.2a and Figure 6.2b shows the effect of densification or compaction (while keeping the grain-size constant) on direct-beam spectral albedo. For near-infrared bands λ_3 (1.0 μm), λ_4 (1.25 μm), and λ_5 (1.5 μm), 3 cm depth of snow is enough for the albedo of these bands to be saturated. Thus beyond 3 cm depth, increase of depth does not have any effect on albedo. For the visible band λ_1 (0.5 μm) and near-infrared band λ_2 (0.75 μm), the depth of snow required for the albedo to approach the

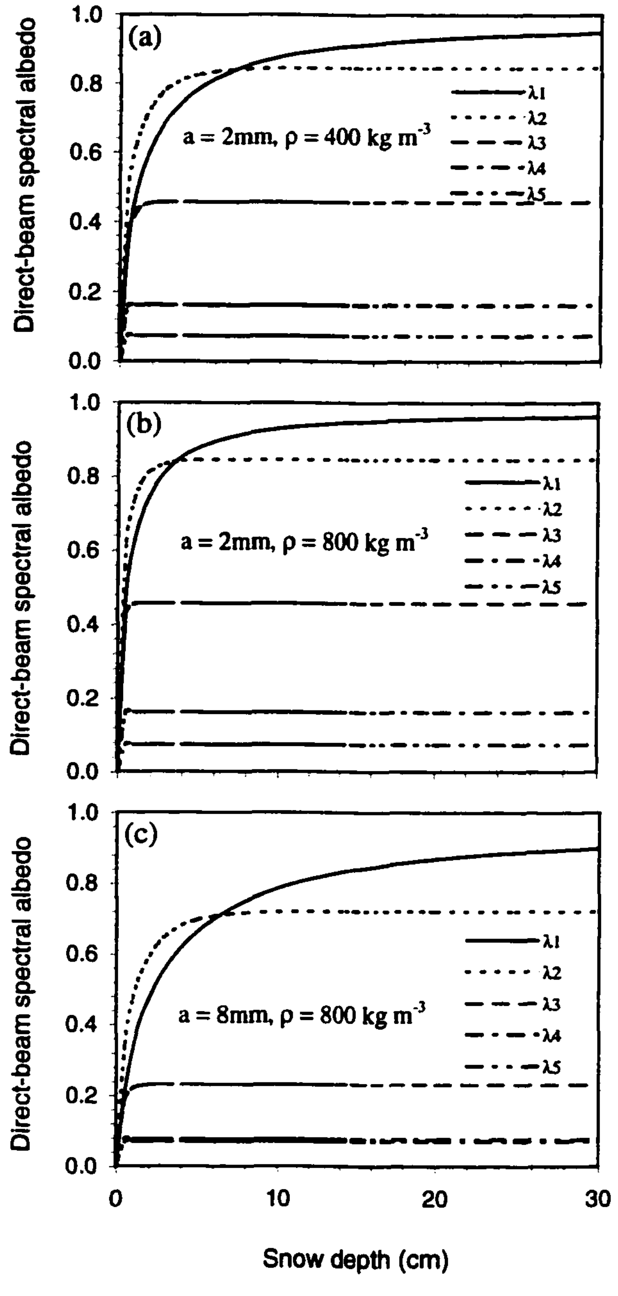

Figure 6.2 Variation of spectral direct-beam albedo with snow depth of a homogeneous snow cover for five spectral bands: λ_1 =0.5 μm, λ_2 = 0.75 μm, λ_3 = 1.0 μm, λ_4 = 1.25 μm, and λ_5 = 1.5 μm. The bottom boundary of the snow cover is assumed to be optically black. The solar zenith angle θ_0 = 60°. (a) Snow grain-size a = 2 mm, density ρ = 400 kg m^{-3}; (b) Snow grain-size a = 2 mm, density ρ = 800 kg m^{-3}; (c) Snow grain-size a = 8 mm, density ρ = 800 kg m^{-3}.

asymptotic value decreases when the snow density is increased. That is, an increase of density (compaction) decreases the semi-infinite depth of the snow. This can be seen more clearly for band λ_2 (0.75 μm). Figure 6.2c is for snow of the same density as in Figure 6.2b but a larger grain-radius (a = 8 mm) to illustrate the effect of grain-size on the direct-beam spectral albedo. Comparison between Figure 6.2b and Figure 6.2c shows that the albedo decreases for all bands when the grain-size increases. When the grain-radius is very large (a = 8 mm), the albedo of the near-infrared (NIR) bands λ_4 (1.25 μm) and λ_5 (1.5 μm) approaches almost the same value when the snow depth is larger than 1 cm. This is because single scattering plays a dominant role at large grain-sizes. Rays of radiation at these bands transmitted to a single grain are completely absorbed within the grain. The decrease of albedo due to the increase of grain-size is also significant for the others NIR bands (λ_2 and λ_3), while for the visible band λ_1 (0.5 μm), the decrease is observable, but not as great as for the NIR bands. Another effect of density that can be seen from Figure 6.2b and Figure 6.2c is the increase of semi-infinite depth. The depth required for the albedo to approach an asymptotic value increases when the grain-size increases, which is clearly seen for band λ_1 (0.5 μm) and band λ_2 (0.75 μm).

Figure 6.3 gives the diffuse counterpart of Figure 6.2. All conditions for Figure 6.3 are the same as for Figure 6.2, except that the incident radiation is diffuse rather than direct. The difference between Figure 6.3 and Figure 6.2 is very small because the solar zenith angle $\theta_0 = 60°$ is not large enough to show a difference [Wiscombe and Warren, 1980].

From the above calculations, we can see that for a snowpack overlying a black surface the albedo for a specific spectral band saturates as the snow depth increases. Beyond a particular depth, increase of snow depth does not affect the albedo any more and the snow cover is thus optically semi-infinite. The increase of albedo with snow depth is very rapid for thin snow cover. From the above calculations we can see that within a typical snow-density range the spectral albedo versus snow depth for various snow grain-sizes and densities indicates that the albedo approaches an asymptotic value at a very shallow snow depth (~ 3 cm) for the near infrared wavelengths while for

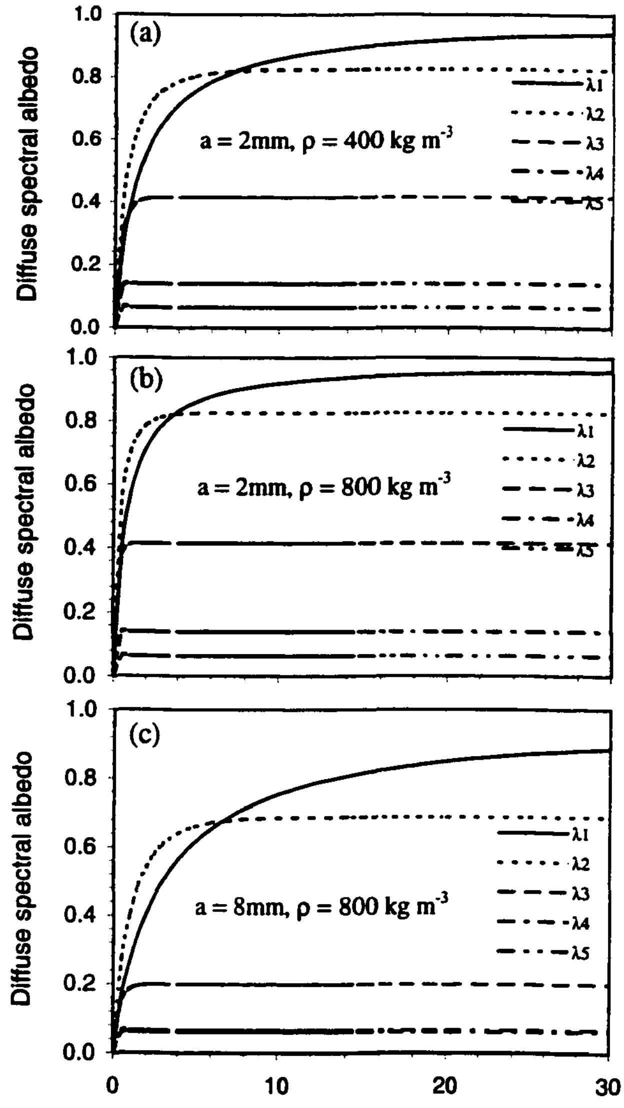

Figure 6.3 Variation of spectral diffuse albedo with snow depth of a homogeneous snow cover for five spectral bands: λ_1 =0.5 μm, λ_2 = 0.75 μm, λ_3 = 1.0 μm, λ_4 = 1.25 μm, and λ_5 = 1.5 μm. The bottom boundary of the snow cover is assumed to be optically black. Incident radiation is assumed to be isotropically diffuse. (a) Snow grain-size a = 2 mm, density ρ = 400 kg m^{-3}; (b) Snow grain-size a = 2 mm, density ρ = 800 kg m^{-3}; (c) Snow grain-size a = 8 mm, density ρ = 800 kg m^{-3}.

the visible, albedo increases very rapidly with depth within 5 cm depth of snow. The top 10 cm also plays a very important role in determining the albedo in the visible. For a snowpack of 100 cm thickness with 1mm grain-size and 300 kg m^{-3} density, the top 3 cm and 10 cm of the snow contribute about 87% and 97%, respectively, to the albedo at wavelength $\lambda = 0.5$ μm. Even for the extreme case when the snow grain-size is very large (8 mm) and the density is small (300 kg m^{-3}), the top 10 cm of the snow cover can still account for 65% of the albedo at 0.5 μm. If the density is larger or the grain-size is smaller, the contribution of the top 10 cm of the snow to the overall albedo will be greater. This happens because the increase of density or decrease of grain-size will decrease the semi-infinite depth. If the semi-infinite depth is ≤ 10 cm, then the overall albedo is wholly contributed by the top 10 cm. These results are corroborated by the conclusion that the all-wave albedo is significantly correlated with the snow parameters only within the top 9 cm snow cover (cf. Chapter 3).

Figure 6.4 shows the critical snow depths required for a snowpack to be semi-infinite versus wavelength for different combinations of grain-size and density when the incident light is a direct beam with incident zenith angle $\theta_0 = 60°$. For a fine-grained snowpack, the maximum critical depth (about 8.5 cm) occurs at around 0.5 μm (Figure 6.4a). Figure 6.4b is for an older snowpack compared with the case of Figure 6.4a. The grain-size is larger ($a = 2$ mm) but the density is the same. The effect of snow density on the semi-infinite depth can be seen by comparing Figure 6.4c and Figure 6.4b. Figure 6.4d is for a snowpack that has the same density as Figure 6.4c but the grain-radius is very large ($a = 8$ mm) (composite grains or depth hoar). For a snowpack of medium density ($\rho = 400$ kg m^{-3}), increase of grain-radius from 0.2 mm to 2 mm (Figure 6.4a to Figure 6.4b), the maximum semi-infinite depth at 0.5 μm increases from 8.5 cm to about 42 cm. While for an old or compacted snowpack ($\rho = 800$ kg m^{-3}), increase of grain-radius from 2 mm to 8 mm (Figure 6.4c to Figure 6.4d), the maximum semi-infinite depth at 0.5 μm increases from about 22 cm to about 53 cm. Enlargement of grain-size increases the critical depth, but mainly in the visible region. For near-infrared wavelengths > 1.0 μm, snow of 5 cm depth will be deep enough to be semi-infinite. Increase of snow density but with constant

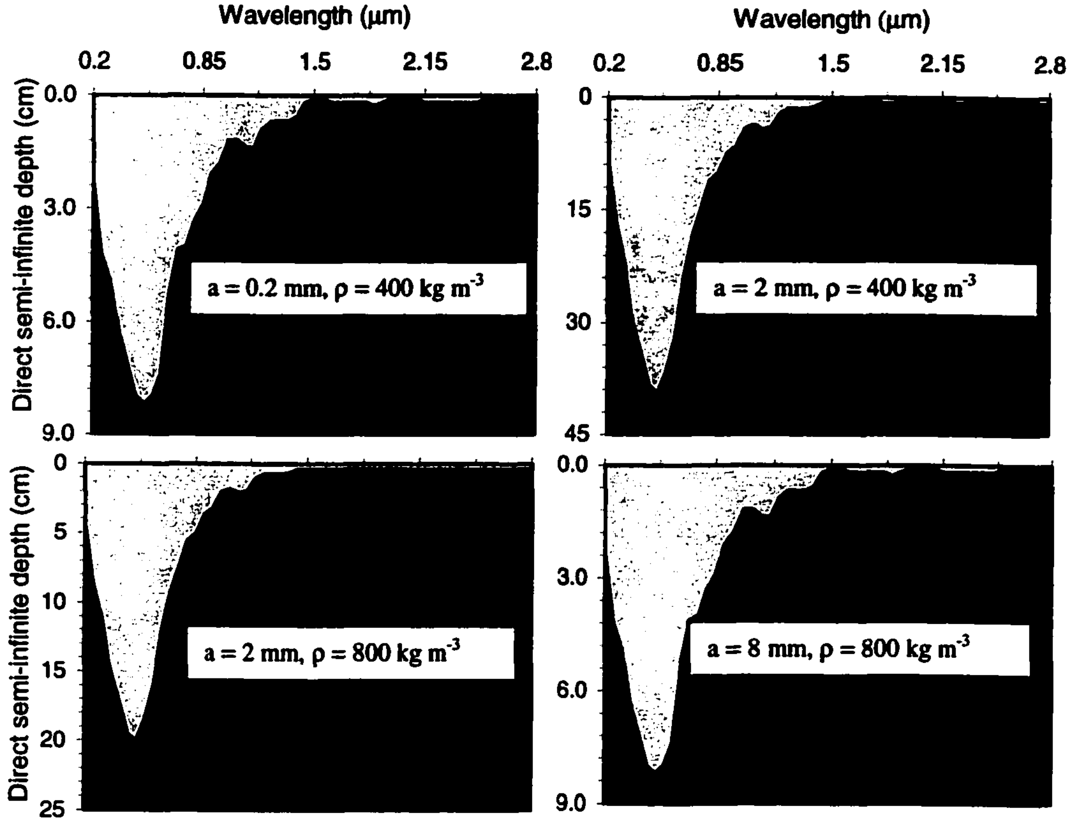

Figure 6.4 Spectral critical snow depth for direct-beam incident radiation. The snow cover is treated as semi-infinite when the snow depth exceeds the critical depth. The solar zenith angle θ_0 = 60°. (a) Snow grain-size a = 0.2 mm, density ρ = 400 kg m^{-3}; (b) Snow grain-size a = 2 mm, density ρ = 400 kg m^{-3}; (c) Show grain-size a = 2 mm, density ρ = 800 kg m^{-3}; (d) Snow grain-size a = 8 mm, density ρ = 800 kg m^{-3}.

grain-size (from Figure 6.4b to Figure 6.4c) will decrease the critical depth. This is because increasing density will increase the optical depth (cf. Equation (6.32)) for the same snow layer and thus enhance the extinction of the light rays within the snow. The consequence is that the light has less penetration power into the snow cover.

Figure 6.5 is the diffuse counterpart of Figure 6.4. The incident radiation is assumed to be uniformly diffuse. For the same snowpack, the difference between the direct-beam case and the diffuse incidence case is small for the same reason discussed above. The effects of grain-size and density on the snow semi-infinite depth seen in Figure 6.4 for the direct-beam case can also be inferred from Figure 6.5 for the diffuse incidence case: increasing grain-size enhances the semi-infinite depth and increasing density decreases the semi-infinite depth.

Although the snow semi-infinite depth in the visible is as large as 40 cm when the grain-radius is 2 mm and $\rho = 400$ kg m^{-3}, the dependence of snow albedo on snow depth is not linear. From Figures 6.2 and 6.3, it is noted that the snow albedo quickly saturates for the top few centimeters of the snowpack for the near-infrared wavelengths, and the rate of increase of the albedo with snow depth is largest for the top few centimeters in the visible region. To see the non-linearity of the contribution of snow depth to albedo, we calculated the minimum snow depth required to achieve 90% of the corresponding direct-beam semi-infinite albedo, i.e., the 90% albedo saturation depth. The results are shown in Figure 6.6. All parameters for Figure 6.6 are the same as Figure 6.4 except the calculation is controlled by 90% saturation instead of 99% as was done for Figure 6.4. Comparison with Figure 6.4 indicates that the 90% albedo-saturation depth is much smaller than the snow semi-infinite depth. For new snow with fine grain-size (Figure 6.4a and Figure 6.6a), the critical snow depth is about 9 cm, but only 2 cm is needed for all wavelengths to achieve at least 90% of the semi-infinite value of albedo. In fact, 2 cm of snow has already been semi-infinite for all wavelengths beyond $\lambda = 0.9$ µm. For the case of larger snow grain-radius ($a = 2$ mm), to achieve 99% of the semi-infinite albedo, a maximum depth of about 42 cm (Figure 6.4b) is required for a snowpack of $a = 2$mm and $\rho = 400$ kg m^{-3}, while only about 9 cm is required (Figure 6.6b) for all wavelengths to achieve at

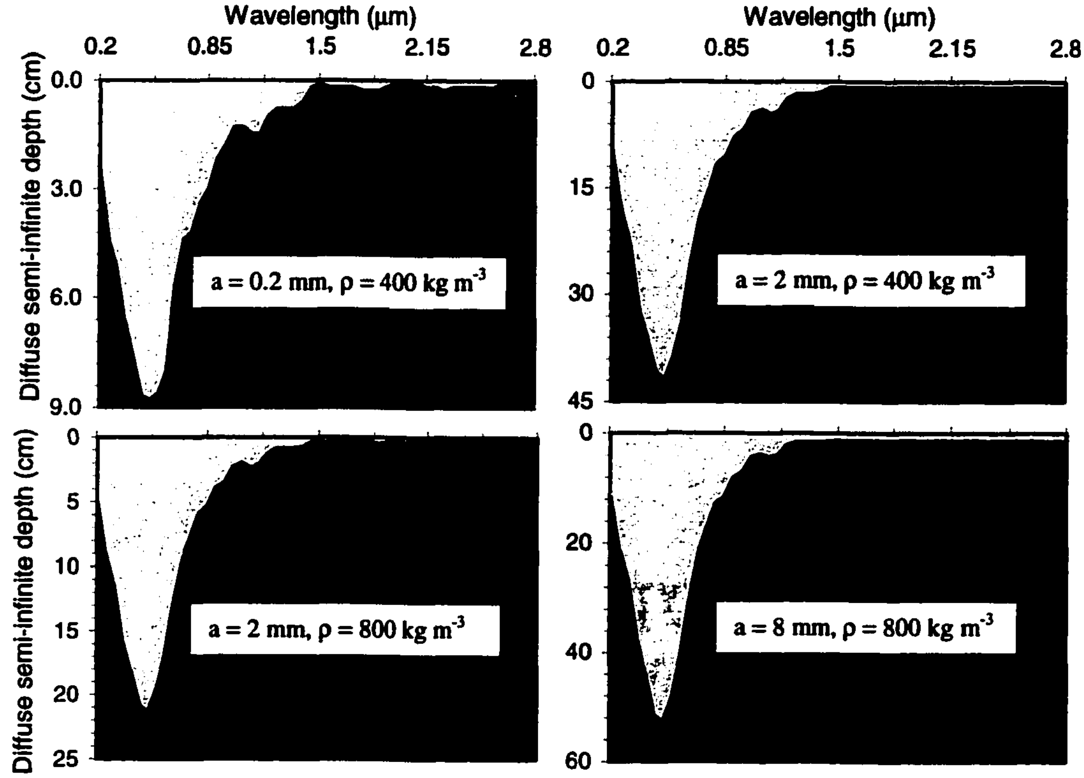

Figure 6.5 Spectral critical snow depth for diffuse incident radiation. The snow cover is treated as semi-infinite when the snow depth exceeds the critical depth. (a) Snow grain-size a = 0.2 mm, density ρ = 400 kg m^{-3}; (b) Snow grain-size a = 2 mm, density ρ = 400 kg m^{-3}; (c) Snow grain-size a = 2 mm, density ρ = 800 kg m^{-3}; (d) Snow grain-size a = 8 mm, density ρ = 800 g m^{-3}.

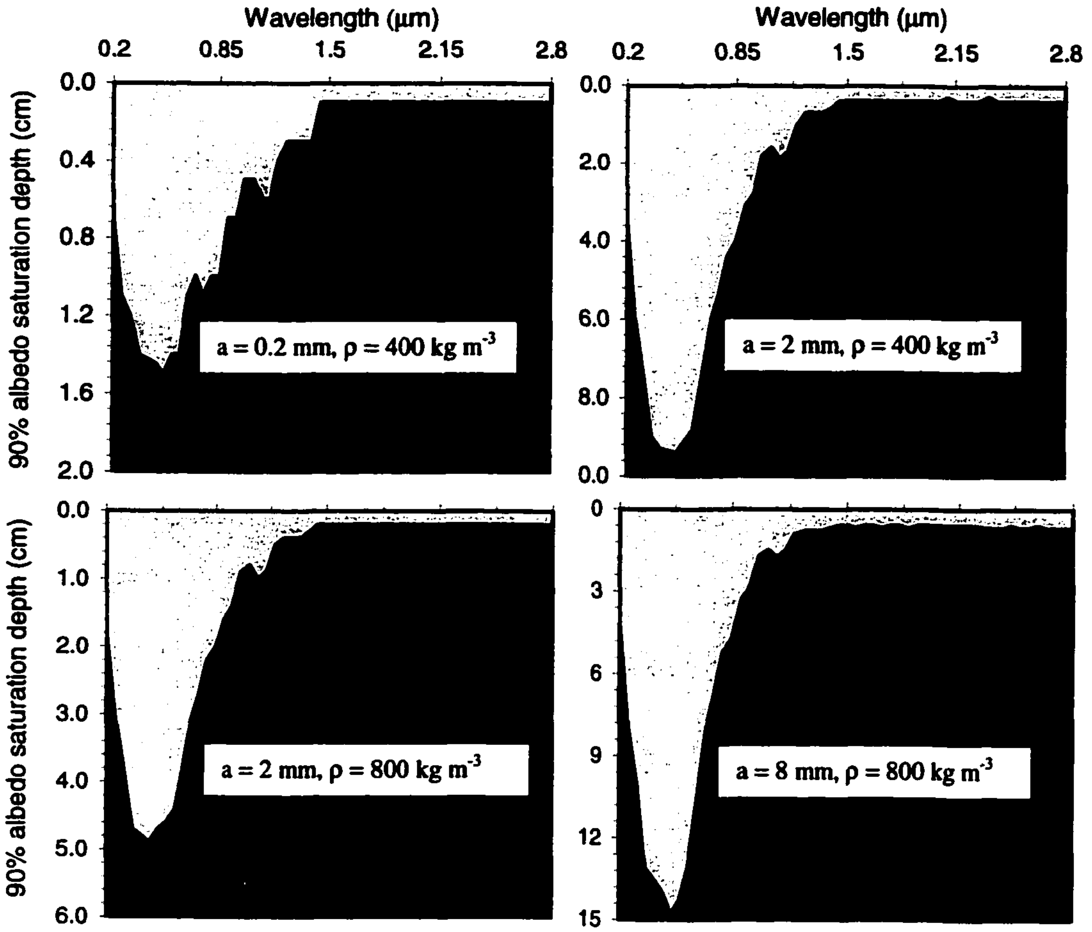

Figure 6.6 Spectral 90% albedo saturation depth for direct-beam incident radiation. A 90% albedo saturation depth is the snow depth required for the albedo to achieve 90% of the semi-infinite albedo. The solar zenith angle $\theta_0 = 60°$. (a) Snow grain-size a = 0.2 mm, density ρ = 400 kg m^{-3}; (b) Snow grain-size a = 2 mm, density ρ = 400 kg m^{-3}; (c) Snow grain-size a = 2 mm, density ρ = 800 kg m^{-3}; (d) Snow grain-size a = 8 mm, density ρ = 800 kg m^{-3}.

least 90% of the semi-infinite albedo. As in the case of new snow of fine grains, for the 9 cm snow cover all near-infrared wavelengths are 100% albedo-saturated for all wavelength beyond $\lambda = 0.9$ μm. Consequently, it is expected that the top 9 cm of snow contributes significantly to the all-wave albedo for this case. Compaction or densification (Figures 6.6b - 6.6c) by a factor of two will further decrease the 90% albedo saturation depth from 9 cm to less than 5 cm. The decrease of snow depth required to achieve 90% albedo from that to achieve 99% albedo is even more significantly for the case of large composite (meltclusters etc.) grain-size (a = 8 mm) and large density (Figures 6.5b and 6.6d). 90% albedo can be achieved by at most 15 cm, while to achieve 99% of the semi-infinite albedo, a snow depth of 53 cm is required. A calculation is also carried out for a snowpack of grain-size a = 1mm and density $\rho = 300$ kg m^{-3}: for wavelength $\lambda = 0.5$ μm, the semi-infinite depth (99% cut-off depth) is about 21 cm, but the top 10cm of snow contributes 97% and the top 3 cm alone contributes 87%, which indicates the snow layer of 11 cm below a depth of 10 cm only contributes 2% to the albedo at the surface. This is understandable if we estimate the probability that a photon that contributes to this 2% must travel through the top 10 cm and interact with the lower 11 cm without being absorbed. The photon is most probably bounced back within the top 10 cm snow layer. The optical depth for the top 10 cm of snow is about $\tau = 49$ (cf. Equation (6.35)). Without modification by multiple scattering, the probability that the photon reaches a depth of 10 cm (cf. Equation (6.8)) is very small ($\approx e^{-\tau} \approx 5.2\times10^{-22}$). This only demonstrates that within the semi-infinite depth, the closer to the surface the snow layers, the greater they contribute to the albedo.

6.3.2. Depth of a Homogeneous Snow Cover MODIS Land Bands Can Sense

For visible and near-infrared (VNIR) sensors on a satellite, knowledge of the snow penetration depth for each VNIR channel is important for correct interpretation of retrieved snow parameters such as snow grain-size retrieved from these sensors. As shown above, the depths with the albedo cut off at 99% or 90% of the semi-infinite

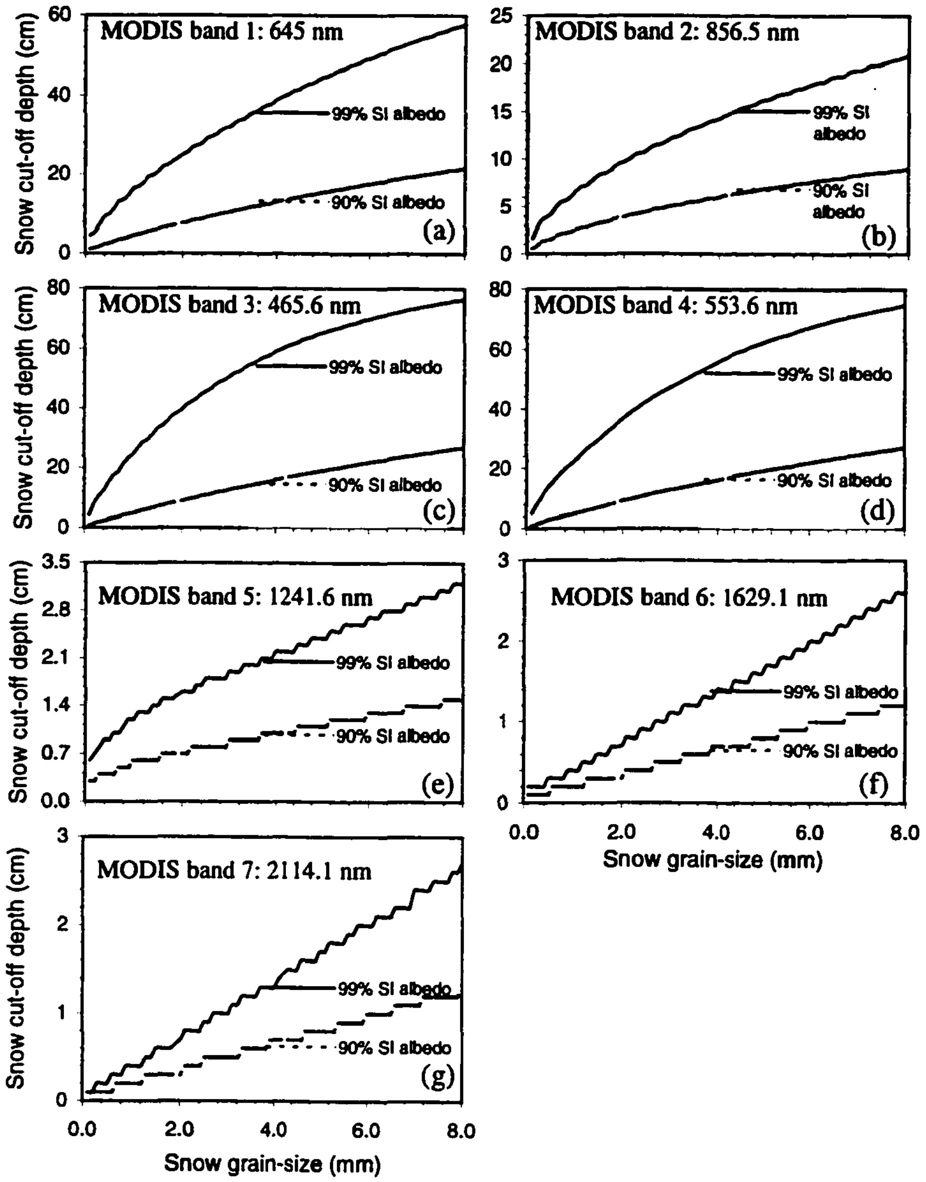

Figure 6.7 Critical snow depth and 90% albedo saturation depth versus snow grain-size for MODIS land bands (band1 to band 7) for direct-beam incident radiation. SI stands for semi-infinite. A 90% albedo saturation depth is the snow depth required for the albedo to achieve 90% of the SI albedo. The solar zenith angle $\theta_0 = 60°$. Snow density $\rho = 400$ kg m^{-3}. (a)-(g) correspond to MODIS band 1 to 7.

albedo vary according to wavelength. This cut-off depth also depends on the snow density and snow grain-size. Figure 6.7 shows the snow cut-off depth versus the snow grain-size for MODIS land bands for a snow cover with density $\rho = 400$ kg m^{-3}. The solar zenith angle is $\theta_0 = 60°$. For visible bands (bands 1, 3 and 4), the 99% cut-off depth or critical snow depth varies from 5 cm for new snow ($a = 0.1$ mm) up to 75 cm for snow meltclusters ($a = 8$ mm). But the 90% cut-off depth does not exceed 20 cm. For NIR band 2, the critical depth can be 20 cm, and the 90% cut-off depth is less than 7 cm. For the other 3 NIR bands, the critical depth is below 3 cm. These results suggest that for the NIR channels of the MODIS land bands, the reflectance received is due to the very top 3 centimeters of snow, while for the visible channels, snow as deep as 75 cm can contribute to the reflectance for old snow with grain-size as large as 8 mm, although it is mostly due to the top 20 cm for snow. For smaller grain-sizes, the corresponding cut-off depth is reduced.

6.3.3. Depth of a Homogeneous Snow Cover That Snow Grain-size Retrieving Band Can Sense

For snow grain-size retrieval, Nolin and Dozier (2000) successfully used the 1.03 μm band to obtain the snow effective optical grain-size. The grain-size should be the average of the snow-critical-depth layer. Figure 6.8 shows the snow critical depth for various combinations of snow grain-size and density for this band. The top curve is for a density of 100 kg m^{-3}, which represents a new snow cover. The bottom curve is for a snow density of 800 kg m^{-3}, which represents a well metamorphosed snowpack or firn. This plot should cover the variations of density and grain-size of a natural snow cover. As snow of small grain-size is generally associated with smaller density, grain-size retrieved from this band should lie in the lower left part of the plot. For old snow with snow density generally larger than 300 kg m^{-3}, the snow critical depth is not very sensitive to the snow grain-size and density. For all cases that have snow density larger than 300 kg m^{-3} and snow grain-size between 0 to 2.5 mm, the retrieved grain-size will represent a top snow layer of less than 5.2 cm.

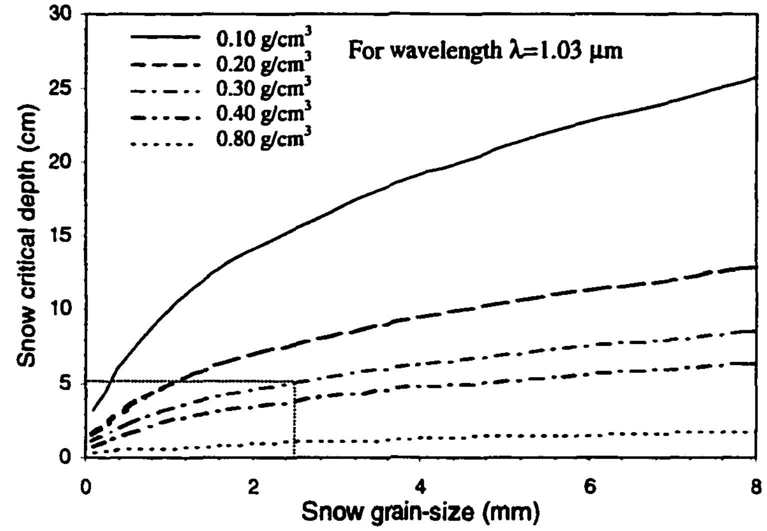

Figure 6.8 Critical snow depth of grain-size retrieving band λ = 1.03 μm [Nolin and Dozier, 2000] for ranges of natural snow density and grain-size. For snow of a specific density, the retrieved snow grain-size represents an average grain-size within the critical depth.

6.4 Sensitivity Study II: Vertically Inhomogeneous Snow Cover

6.4.1. Effect of Vertically Inhomogeneous Grain-size on Spectral Semi-infinite Albedo

To separate the effect of grain-size on albedo from other factors such as density and depth, let's simplify a snowpack as a snow cover having vertically constant density but vertically stratified grain-size. The whole snow cover is assumed optically semi-infinite for all wavelengths and is subdivided into layers having different grain-sizes. Each sub-layer is treated as a homogeneous layer. Figure 6.9 shows the effect of different stratifications of grain-size on the semi-infinite spectral albedo in the visible and near-infrared. The snow cover is assumed to be 1 m thick with a constant density (ρ = 300 kg m^{-3}) from the snow surface to the bottom, with the top 6 cm being stratified and the bottom 94 cm being a homogeneous layer of grain-radius a = 1 mm. The top 6 cm is assumed to be stratified with 6 homogeneous layers each 1 cm thick and having different snow grain-sizes. Two cases of stratification are studied. Stratification case A (Figure

6.9a) is for a snowpack with grain-radius increasing from 0.1 mm at the top to 5 mm at 6 cm, i.e., the gradient of snow grain-size with respect to the depth from the surface is positive. This case represents the ideal case of a natural snow cover. Aging and metamorphism result in increasing grain-size with depth. But, for a real snowpack, intermittent snowfalls and warm weather may make the snow cover interweaved with layers of various grain-sizes. Stratification case B is for a snowpack that has the reverse profile of case A for the top 6 cm, i.e., the grain-size decrease with depth. Snow grain-size is constant from 7 cm to the bottom (1 m) for both cases. The vertical grain-size profiles for these two cases are shown in Figure 6.9a and Figure 6.9b. Figure 6.9c is for the diffuse spectral albedo of the two cases, while Figure 6.9d is for the direct-beam (solar zenith angle $\theta_0 = 56°$). The semi-infinite depths for the two stratification cases are also calculated and shown in Figure 6.9e and Figure 6.9f. Figure 6.9e is for diffuse incidence and Figure 6.9f is for the direct-beam. For each figure (Figures 6.9c - 6.9f), the solid curve is for stratification case A, and the dashed curve is for stratification case B. The difference of albedo due to the two stratification cases is negligible for the visible light within 0.3 - 0.6 μm. For wavelengths longer than 0.6 μm, the difference increases with wavelength. The longer the wavelength, the smaller the spectral albedo for stratification B compared with case A. Although the average grain-size is the same for the top 6 cm for the two stratification cases, different vertical distributions of grain-size result in quite different spectral albedos. Both Figure 6.9e and Figure 6.9f show that the semi-infinite depths for stratification case A and B are very close within 0.3 - 0.8 μm and larger than 6 cm, the spatial scale of inhomogeneity of the snowpack. For wavelengths longer than 0.8 μm, the difference between different stratification cases is obvious. Beyond 0.85 μm, the semi-infinite depth for case A is smaller than 3 cm while for case B it was between 4 and 6 cm. If we attempt to retrieve the snow grain-size using the 1.03 μm band, it is expected that the retrieved grain-size is quite different although the mean grain-size is the same for the top 6 cm for both cases. The semi-infinite depths for both case A and case B at 1.03 μm do not exceed 6 cm. The grain-size retrieved from

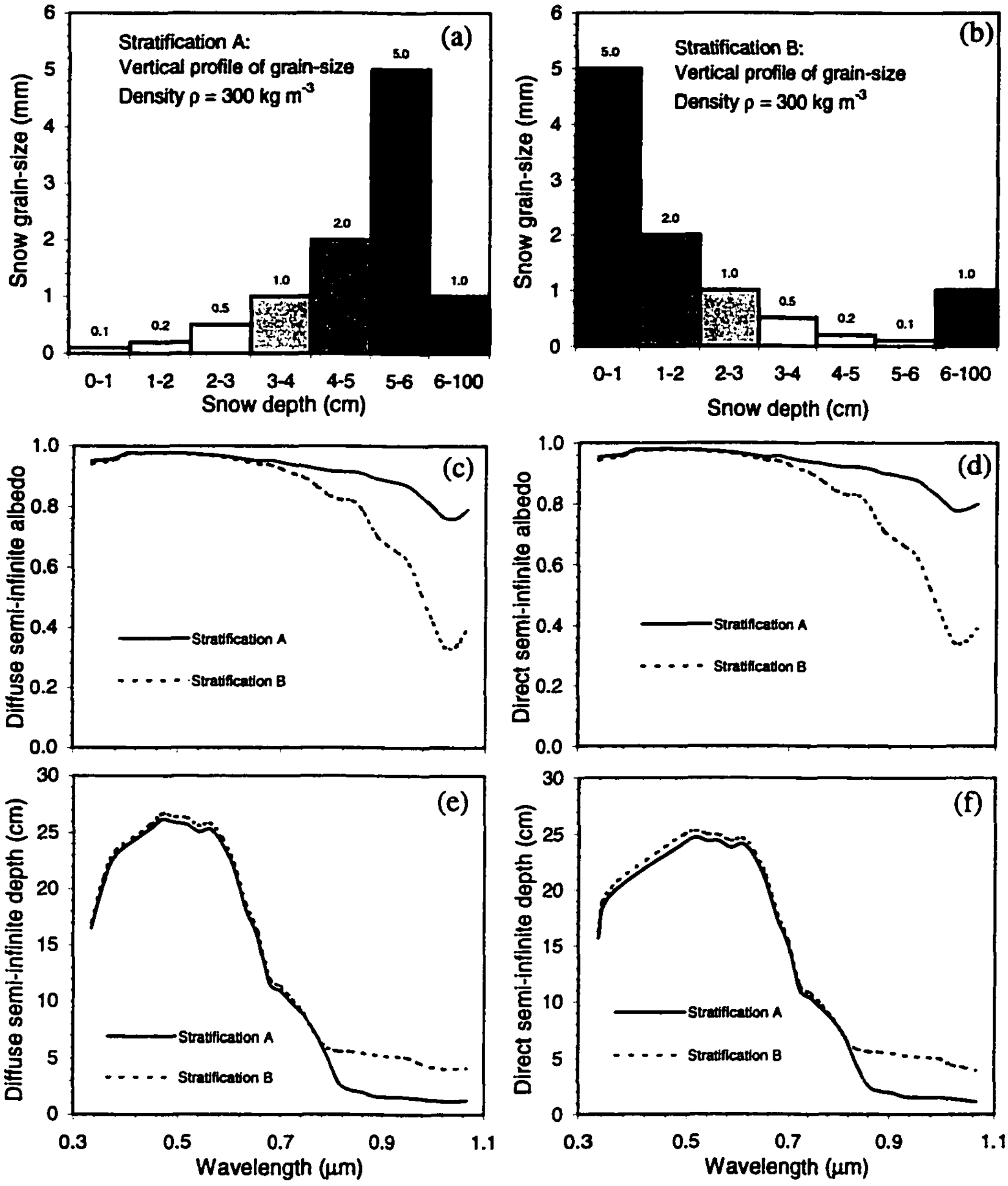

Figure 6.9 Effect of vertical profiles of snow grain-size on semi-infinite albedo and semi-infinite snow depth for a snowpack of constant density (ρ = 300 kg m^{-3}). (a) Vertical profile of grain-size for stratification A: the grain-size increases with depth until 6 cm depth. (b) Vertical profile of grain-size for stratification B: grain-size decreases with depth until 6 cm depth. For both (a) and (b), the number above each column is the grain-size in mm and the grain-size from 6 cm to 100 cm is constant. Diffuse (c) and direct-beam (d) spectral semi-infinite albedo for stratification case A and case B. Diffuse (e) and direct-beam (f) spectral semi-infinite depths for stratification case A and case B.

Case A is only from the top 2 cm (see Figures 6.9e - 6.9f for Case A), while from case B it is from the top 5 cm; thus the retrieved grain-size for case A is apparently much smaller than that retrieved for case B. Grain-size retrieved from near-infrared channels represents a homogeneous snow layer of very shallow depth. The smaller the grain-size at the top of the real snowpack, the thinner the representative homogeneous snow layer. This indicates that the near-infrared wavelengths are not only more sensitive than the visible to grain-size but also more sensitive to the grain-size in the top layers, resulting in a bifurcation of the spectral albedo for cases A and case B when the wavelength increases (Figures 9c and 9d).

6.4.2. Effect of Vertically Inhomogeneous Snow Density on Spectral Semi-infinite Albedo

The effect of the vertical inhomogeneity of the snow density is studied by adopting a snowpack with constant grain-size, but different densities from the top to the bottom of the snowpack. Figure 6.10 shows the effect of different stratifications of snow density on the semi-infinite spectral albedo in the visible and near-infrared region. As for Figure 6.9, the snowpack for Figure 6.10 is also assumed to have a total depth of 1 m, which is deep enough for the snow cover to be treated as optically semi-infinite. The top 6 cm is stratified as follows: 6 homogeneous layers each being 1 cm thick and having different densities. The grain-radius is assumed to be a = 0.5 mm. These cases are similar to those in Figure 6.9, with the grain-size replaced by the density. Stratification case C and case D are shown in Figure 6.10a and Figure 6.10b, respectively. For case C, the density increases from the top to 6 cm depth, and case D is the reverse of case C, i.e., the density decreases with the depth. The spectral diffuse and direct-beam semi-infinite albedos are shown in Figures 6.10c and 6.10d, respectively, for both case C and case D. From these figures we can see that the vertical structure of density does not affect the semi-infinite spectral albedo, which is expected based on the result of Warren and Wiscombe (1980), Bohren and Barkstrom (1974) and Bohren and Beschta (1979). But it will affect the spectral albedo if the snow depth is not semi-infinite for a particular wavelength. The spectral diffuse and direct-beam semi-infinite depths are shown in Figures 6.10e and

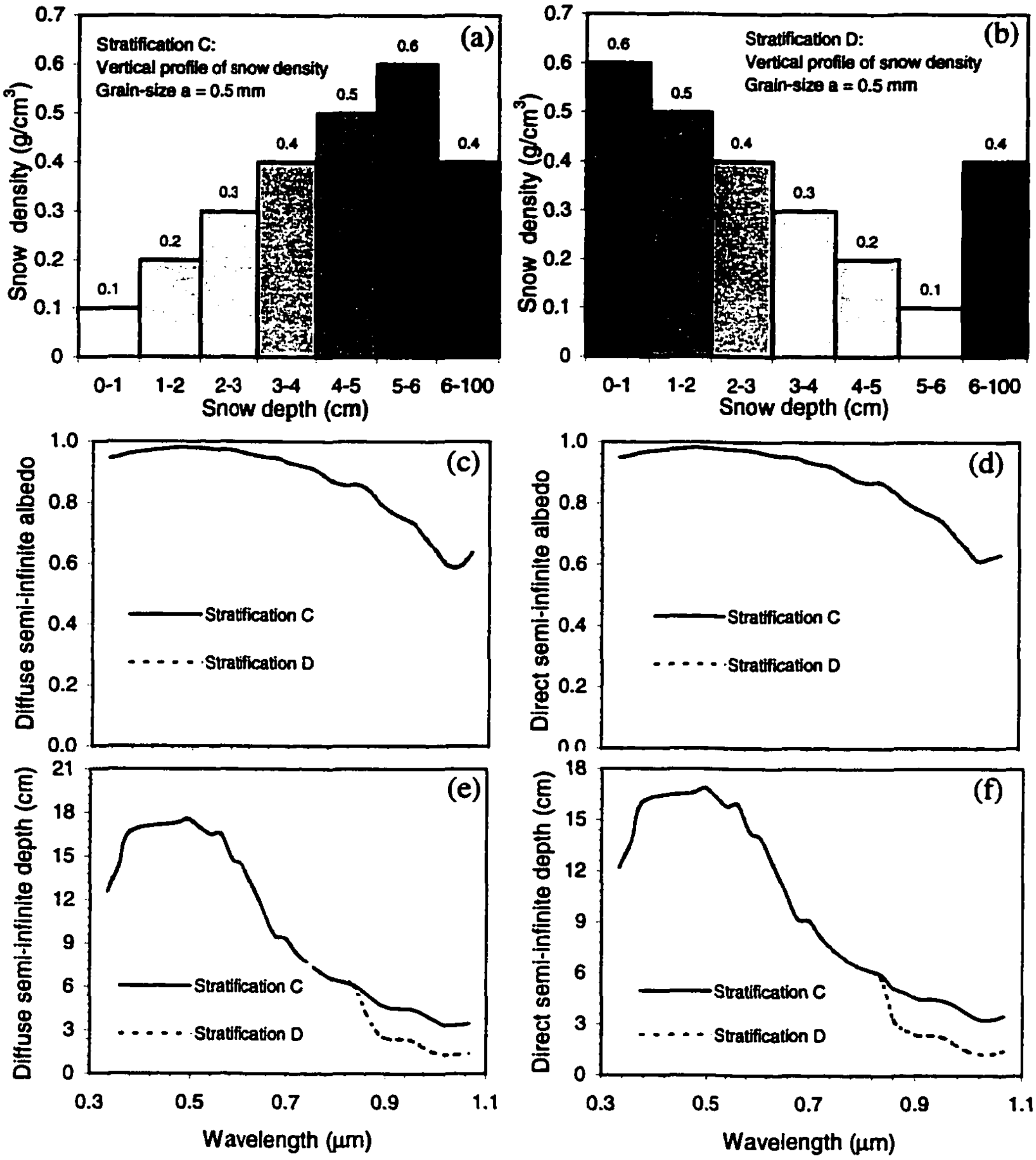

Figure 6.10 Effect of vertical profiles of snow density on semi-infinite albedo and semi-infinite snow depth for a snowpack of constant grain-size (a = 0.5 mm). (a) Vertical profile of density for stratification C: the density increases with depth until 6 cm depth. (b) Vertical profile of density for stratification D: density decreases with depth until 6 cm. For both (a) and (b), the number above each column is the density in kg m^{-3} and the density from 6 cm to 100 cm is constant. Diffuse (c) and direct-beam (d) spectral semi-infinite albedo for stratification case C and case D. Diffuse (e) and direct-beam (f) spectral semi-infinite depths for stratification case C and case D.

6.10f. The effect of the density structure can be seen in both figures. For wavelength $\lambda \leq$ 0.84 μm, both density profiles result in almost the same semi-infinite depths. For wavelength $\lambda > 0.84$ μm, stratification case D results in a much smaller semi-infinite depth than stratification case C because the increase of optical depth with geometrical depth is faster within the top layers for case D, which has higher density at the top, than for case C, which has lower density at the top. The remote sensing implication of the effect of density structure on the snow spectral albedo is that, if $\lambda = 1.03$ μm is used to retrieve the snow grain-size, the result will be representative of 3.3 cm of snow cover for case C and only 1.3 cm of snow cover for case D. Therefore, it is expected that snow parameters retrieved from near-infrared channels will represent deeper snow cover for new snow than wind packed snowpack which has higher density in the top layers, though the snow grain-size for these cases are the same.

6.5 Comparison of Modeled Spectral Albedo with Measurements

For cruise NBP99-1, most measurements of spectral albedo and bidirectional reflectance were carried out under cloudy conditions but with the solar disk visible. For clear sky conditions, the solar position helped us to shade the direct beam using a light baffle so that the incident diffuse spectral irradiance was measured. Along with the total incident spectral irradiance, the direct portion can also be obtained. In the following discussion, we will focus on a comparison of modeling results with measurements under clear-sky conditions.

The measurements under clear-sky conditions were taken on Julian day 8 (ice station 5) of NBP99-1 cruise (cf. Figure 2.1). Measurements and modeling results for the snow cover of ice station 5, NBP99-1 cruise are compared in Figure 6.11. The site had a snow depth of 12 cm, below which was slush. The measurements of snow grain size and density were done in 3 cm thick layers, but the grain-size at the very top of 5 to 10 mm was closely examined, because a large change in grain-size even in the top 5 mm can significantly impact the pattern of spectral albedo of snow cover [Grenfell et al., 1994]. Vertical profiles of the grain-size for both composite grains and single grains that make up the composite grains, and density of the snowpack are shown in Figure 6.11a. The density of the top 1 cm snow was not measured and was estimated as the average of typical new snow (133 kg m^{-3}) and the measured density of the top 3 cm. The downwelling spectral irradiance and the ratio of the diffuse to the total irradiance are shown in Figure 6.11b. The data in Figures 6.11a - 6.11b are used as inputs to the multi-layer radiative transfer model. The solar zenith angle was 56°. The measured and calculated spectral albedos are shown in Figure 6.11c. Several cases are modeled. One is for measured large composite grains, while the second case is for the measured single grains that are subunits of the composite grains. The measurement from sensors between 1043.44 nm and 1064.90 nm are not very reliable because their irradiance measurements fluctuated considerably compared to sensors at other wavelengths. Comparison of the two cases with the measurement shows that the modeled albedo agrees fairly well with the measurement when the input snow grain-size is taken as the measured composite grain-size. The modeled result is on average 2.8% (maximum 4.7%) higher than the measurement. The modeled albedo is on average 9.1% (maximum 13.7%) higher than the measured if the input grain-size is taken as the measured single grain-size. The discrepancy between the measurements and the modeling results is smaller with composite grain-size than with single grain-size. This corroborates the finding that the all-wave albedo is more significantly correlated with the composite grain-size rather than the single grain-size (cf. Chapter 3). Figure 6.11c also includes the modeled result of the two-layer model that best fits the measured spectral albedo [Grenfell et al., 1994]. The two-layer model consists of an upper layer of 1 cm thickness with measured grain-radius of 0.2 mm (individual single grains) and a lower layer of 11 cm thickness with grain-radius of 5 mm (composite grains). The upper layer represents recent snow and controls the spectral albedo in the near-infrared region. The lower layer represents metamorphosed (melt-refreeze) old snow that along with base reflectivity, controls the spectral albedo in the visible. A twelve-centimeter depth is not thick enough for the snowpack to be semi-infinite in the visible region. Thus, the bottom surface (slush in this case) plays some role in determining the spectral albedo in the visible. The effective

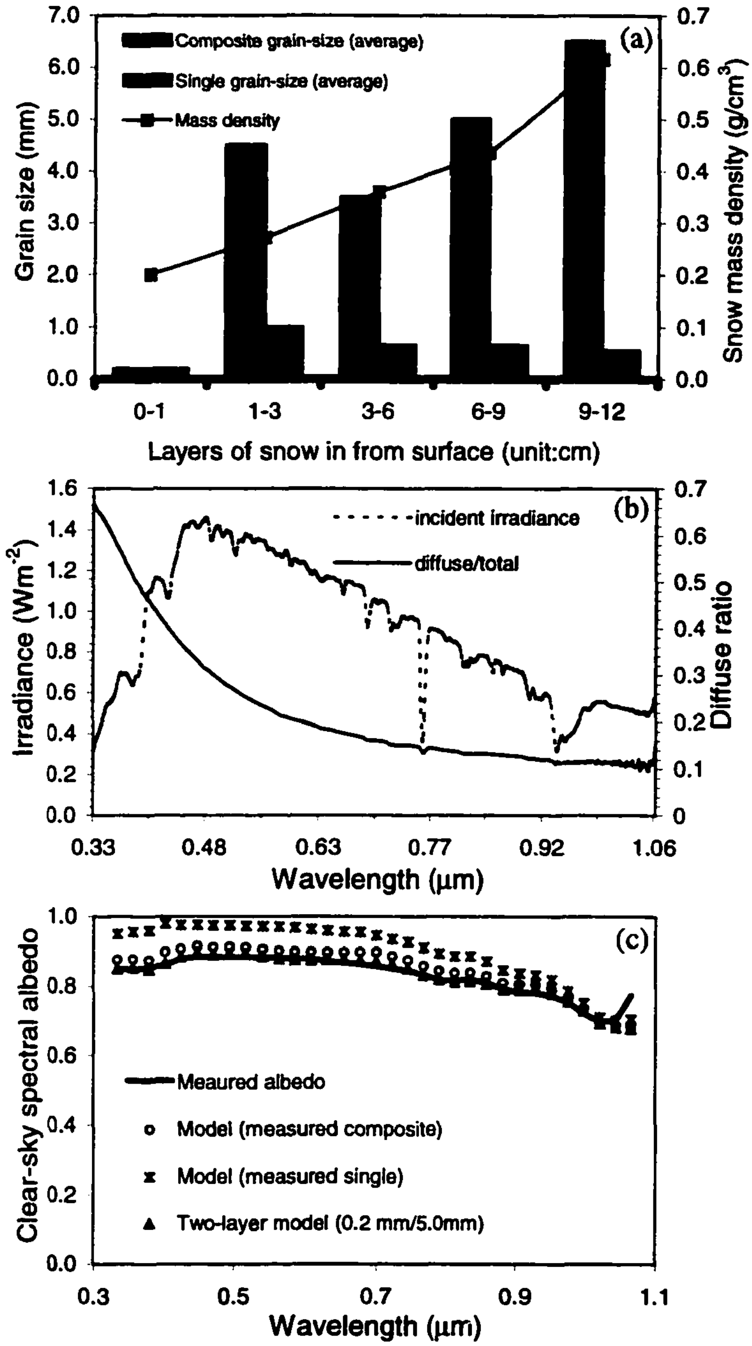

Figure 6.11 Comparison of modeled spectral albedo with measured spectral albedo. (a) Vertical profile of composite and single grain-size and snow density. (b) Incident spectral irradiance and ratio of diffuse to total irradiance. Solar zenith angle $\theta_0 = 56°$. (c) Measured spectral albedo and modeled results. A two-layer model (0.2 mm/ 5.0 mm) is also used to simulate the measurement.

average grain-radius derived from the grain-size measured in the field for the snowpack (cf. Equation (3.2c)) is 2.44 mm.

This means that to fit the measurements using the two-layer model, a grain-size about twice as large as the measured value is needed. The modeled spectral albedo from the multi-layer model agrees better with the measured result when the measured composite grain-size is used than when the measured single grain-size is used. Using the composite grain-size, modeled results agree fairly well with the measured ones, but it is still generally higher than the measurements in the visible. The discrepancy may be due to the following two factors which are not taken into account in the modeling: 1) biomass, which is absorptive in the visible region and exists in the snowpack, especially at the snow-ice interface and in slush; and 2) snow grain-grain connectivity [Itagaki and Lemieux, 1993], which provides paths for the light that passes through grain-neck enabling light to travel from one grain to the other, without being reflected, will reduce the single scattering albedo and increase the asymmetry factor, both of which reduce the albedo. We did not consider these factors, mainly due to the unavailability of information required to quantify these processes.

6.6 Discussion and Conclusions

The investigation is focused on the effect of vertical structure of homogeneous and inhomogeneous snowpacks on the snow spectral albedo using a multi-layer radiative transfer model. The computed spectral albedo versus snow depth for a homogeneous snowpack with various values of naturally occurring snow grain-sizes and density values indicates that albedo approaches an asymptotic value for a very shallow snow depth (~ 3 cm) at near-infrared wavelengths, while in the visible, the albedo of a snowpack overlying a black surface increases very rapidly with depth for the snow depth within 5 cm. A thickness of 5 cm is enough for the snowpack to be semi-infinite for near-infrared radiation. In the visible, the top 10 cm is found to be the most important, even though the critical snow depth may be much larger than 10 cm when the grain-size is large and the density is small. For instance, at wavelength $\lambda = 0.5$ μm for a snowpack with 1mm grain-size and 300 kg m^{-3} density, the semi-infinite depth is about 21 cm, but the top 3 cm and 10 cm of the snow cover contribute about 87% and 97%, respectively, to the albedo of a snowpack of 100 cm. In the visible region, the semi-infinite depth is much larger than that in the near-infrared. But the contribution of the lower part of the snowpack is much smaller than that if it is placed at the top. For a snowpack, the contribution of the top 10 cm (or any value that is smaller than the effective semi-infinite depth) snow layer to the overall albedo of the snowpack depends on the grain-size and density within the layer: the smaller the grain-size or the larger the density, the larger the contribution.

For MODIS visible bands (bands 1, 3 and 4) (cf. Figure 6.7), the 99% cut-off depth or critical depth varies from 5 cm for new snow (a = 0.1 mm) up to 75 cm for snow meltclusters (a = 8 mm). But the 90% cut-off depth does not exceed 20 cm. For MODIS NIR band 2 (856.5 nm), the critical depth can be 20 cm and the 90% cut-off depth is less than 7 cm. For the other NIR land bands (band 5, 6 and 7) (cf. Figure 6.7), the critical depth is smaller than 3 cm. These results suggest that for these NIR channels, the reflectance received by the MODIS sensors is due to the very top 3 centimeters of snow, while for the visible channels, snow as deep as 75 cm can contribute to the reflectance, although most of it is due to the top 20 cm for snow grain-size as large as 8 mm. For smaller grain-sizes, the corresponding cut-off depth is reduced. For a natural snowpack, the semi-infinite depth can be much reduced because the top snow layers are generally associated with new or recent snow of fine grain-size.

While the near-infrared albedo of a natural snowpack is very sensitive to the physical parameters of the very top layers of the snow (< 5 cm), the visible albedo is sensitive to snow physical parameters of much deeper snow layers. Thus, not only the top layers should be examined in very high resolution, the snow stratification should be also recorded and snow grain-size and snow density should be measured within each snow stratum for the whole snowpack. Grain-size retrieved from remote-sensing near-infrared channels represents the weighted average of a snow layer within a particular depth (semi-infinite depth) with heavier weights associated with upper layers. The smaller the grain-size at the top of the real snowpack, the thinner the representative snow layer.

Studies of the effect of the vertical inhomogeneity of the snow grain-size on the spectral albedo shows that although the average grain-sizes may be the same for two snowpacks, different vertical distributions of grain-size within the very top few centimeters can result in quite different spectral albedos, especially at longer wavelengths. This is because radiation at near-infrared wavelengths is not only more sensitive than visible light to grain-size, but also more sensitive to the grain-size in the upper layers of the snow. The visible light is sensitive to snow parameters within a much larger depth range than NIR. As expected, the vertical structure of the density alone does not affect the semi-infinite spectral albedo. But it does affect the semi-infinite depth. A snow profile that has smaller density at the top has a larger semi-infinite depth, especially for longer wavelengths. The contribution of a top layer with specified depth (e.g. 10 cm) to the overall spectral reflectance of the whole snowpack depends on the grain-size and density: the smaller the grain-size or the larger the density, the larger the contribution.

The simulated spectral albedo from a multi-layer snow model agrees better with the measured results when the measured composite grain-size rather than when the measured single grain-size is used. The composite grain-size leads to modeled results that agree fairly well with the measured ones, but that are 2.8% on average higher than the measurements in the visible. Biomass, ubiquitously observed in the summer snowpack on sea ice in the South Ocean, especially at the snow-ice interface, and snow grain-grain connectivity [Itagaki and Lemieux, 1993], may play an important role in reducing this gap. Connectivity of snow particles allows light to transmit through the bonds of the connected grains [Itagaki and Lemieux, 1993], reducing the single scattering albedo and increasing the forwarding scattering, both of which reduce the albedo. The scattering behavior of connected snow grains may approach that of single larger particles [Vedernikova and Kabanov, 1974]. The effect of connectivity is equivalent to an increase in grain size. This is consistent with the result of the two-layer model, which requires about twice the measured composite grain-size to fit very well the measured spectral albedo.

CHAPTER 7

Summary

Ground measurements, satellite data analysis and radiative transfer modeling of optical remote sensing of snow and ice are presented in the thesis.

Radiative parameters (all-wave albedo, spectral albedo and bidirectional reflectance) were measured of the summer/fall snow-covered pack ice in the Ross, Amundsen and Bellingshausen seas, Antarctica, along with observations of snow physical parameters at the measurement sites. Data analyses showed (Chapter 2, 3) that

- All-wave albedo is variable (0.70-0.86) over the Ross Sea pack ice and similar to those inferred from observations in the East Antarctica (0.65-0.85) [Allison et al., 1993].
- All-wave albedo was observed to be lower at the margin of the pack ice than in the central pack ice. Over the central ice pack, it was observed that the higher the latitude south, the higher the all-wave albedo, the lower the surface temperature and the smaller the snow density.
- Clear- and cloudy-sky albedos measured at the same ice floe indicate that the average increase due to clouds is 1.4%, with the largest increment being 4.0%. The average increase of 1.4% in all-wave albedo corresponds to the average decrease of 23% in downwelling irradiance due to clouds. The increase of albedo due to clouds measured by others is between 5-11% [Liljequist, 1956; Hanson, 1960; Weller, 1968]. Strong absorption by clouds of near-infrared wavelength, at which snow is less reflective than the visible, is the cause of the increase of all-wave albedo under cloudy conditions.
- No major difference was observed between spectral albedos under clear-sky and cloudy conditions. But the differences between various ice floes are significant in both the spectral distribution and amplitude at a specific wavelength, depending

on surface conditions such as snow grain-size (age), snow depth, vertical stratification, etc.

- The snow composite grain-size of the top 3 cm of the snow cover was observed to decrease with latitude south, but no such relation was observed for single grain-size.
- All-wave albedo was observed to be significantly correlated with the composite grain-size for snow depth of up to 9 cm, beyond which the correlations are not significant: the smaller the composite grain-size, the higher the all-wave albedo. No such correlation was observed for single grain-size.

In situ snow reflectance and spectral albedos were obtained concurrently with MODIS in the Ross, Amundsen and Bellingshausen seas. These measurements were dedicated to validation of MODIS snow and sea ice products in the Southern Ocean. The site-positions were accurately identified in the clear-sky MODIS L1B granules using a combination of small angle approximation and direct matching algorithms. The reflectance data corresponding to the ground-site pixels were retrieved and atmospherically corrected. Ground measurements were sampled at the same viewing geometry as MODIS and corrected for ice concentration. Comparison between the *in situ* and MODIS data shows that:

- The atmospheric corrections for MODIS bands varied between 0.8% and 33.9%, depending on spectral band, atmospheric conditions, and ground surface conditions. For the most homogeneous and reflective surface (10/10 ice concentration, visibility 30 km, ozone 0.237 cm-atm, water vapor 0.962 g cm^{-2}), the average atmospheric correction is the smallest (13.8%, varying between 22.6% and 2.9%). For the most heterogeneous and least reflective surface (3.5/10 ice concentration, visibility of 40 km, ozone of 0.320 cm-atm, water vapor of 0.607 g cm^{-2}), the average atmospheric correction is the largest (average 24.0%, varying between 33.9% and 13.0%).

- To solve the pixel mixture problem, which is especially serious in sea ice remote sensing, an ice-concentration correction of *in situ* measurements should be made so that the *in situ* and space-borne measurements can be compared.
- The best agreement between the *in situ* and MODIS measurements was found when the ground had 10/10 ice-concentration or was dominated by one ice type. A good comparison between the *in situ* and satellite-retrieved reflectances is expected for large and homogeneous ice floes under clear-sky condition.
- Simultaneity is a necessity for the *in situ* and space-based measurements to avoid ground truth drift when validation is on a moving surface feature such as sea ice. There is no "permanent" ground truth in validation of sea ice products. Synchronization is more imperative for sea-ice product validation than for land surface products where "permanent" ground truth exists.
- To avoid errors resulting from ice-concentration correction, an accurate determination of ice concentration is important in deriving ground reflectance of a simulated pixel from the *in situ* measurements when a pixel covers several optically-distinct ice types. It is expected that the more homogeneous the ground surface and the less variable the ground topography, the better the agreement between the *in-situ* and satellite-derived reflectances.
- There exists a difficulty in unmixing the coarse MODIS pixel using high-resolution satellite data in validating sea ice products due to scarcity of concurrent or near-concurrent high-resolution satellite data covering the same site.

Radiative transfer modeling provides a theoretical background for quantitative remote sensing. Modeling of the interaction of solar radiation with snow involves the calculation of absorption and single scattering properties (single scattering albedo and phase function) as inputs to solve the radiative equation and calculate radiative parameters (all-wave albedo, spectral albedo, bidirectional reflectance, etc.) by taking multiple scattering into account. Based on the observation that large composite snow grains in the summer snow cover on sea ice have an important effect on the reflectance of the snow surface in the VNIR regions, and the difficulty of Mie calculation for large size parameters, a

FORTRAN code (GOMsnow) was developed to calculate the absorption and scattering efficiencies, and the scattering phase function using a geometrical optics method.

- GOMsnow tested against a Monte Carlo code [Nakajima, 1998; Kokhanovsky and Nakajima, 1998]. Results from GOMsnow agree well with the Mie0 code [Wiscombe, 1979; 1980] for size parameter ≥ 200. GOMsnow and Mie0 codes can be combined to calculate single scattering properties for any wavelength from ultraviolet to microwave. The size parameter is unlimited for GOMsnow when size parameter ≥ 200. The code is computationally efficient and the computing time is almost independent of size parameter, while for Mie0 code the size parameter is limited (< 20000) and computing-time is intensive when the size parameter is large.
- The calculated angular scattering patterns agree well with Mie calculation for any incident angle, rather than only good for the incident angle ≤ 60° using geometrical optics method as obtained by Glantschnig and Chen (1981). This is because the number of internal reflections truncated based on the truncation tolerance number (see section 5.3.1) is a dynamic parameter that depends on the incident angle, while Glantschnig and Chen's calculation was based only on $N = 2$.

The single scattering calculations (GOMsnow and Mie0) are used as input to the multiple scattering code DISORT [Stamnes et al., 1988; 2000] in a multi-layer model for snow reflectance to investigate the influence of vertical stratification on the spectral albedo and its possible implication for optical remote sensing.

- For a natural snowpack over sea ice, 1 to 3 cm depth of snow is enough for the albedo to reach a constant value when the wavelength is longer than 1.0 μm. For visible light, the albedo reaches 90% of its semi-infinite values when the snow depth is 10 cm.
- Grain-size retrieved from near-infrared bands is representative for the very top few centimeters (≤ ~5 cm) of the snow.

- The albedo in the near-infrared (≥0.7 μm) is sensitive not only to grain-size but also to the grain-size at upper layers, while that in visible wavelengths (0.4-0.7 μm) is sensitive to the grain-size of much greater depths.
- For two snowpacks with the same average grain-sizes, different vertical distributions of grain-size within the very top few centimeters can result in quite different spectral albedos, especially at longer wavelengths.
- Comparison of the measurements of spectral albedo with radiative transfer calculation for both the single and composite grain-size when the vertical profiles are considered shows that the composite grain-size gives better agreement. This corroborates the conclusion that the all-wave albedo is significantly correlated with the snow composite grain-size rather than the single grain-size from the analyses of all-wave albedo with snow grain-size.

Future work could include but is not limited to 1) detailed measurements of snow grain size using stereographic method and detailed measurements of the vertical stratification of snow parameters such snow grain-size, density, organic or inorganic impurities in a high vertical spatial resolution, especially for the top snow layers. Such measurements will provide more accurate input to radiative transfer models and thus enable more meaningful comparisons between modeled and measured reflectnace (albedo) data. (there are very few or no impurity measurements in the snowpack on the sea ice in the southern oceans). 2) Detailed measurement of optical properties of the biomass present in the snowpacks on sea ice, especially at the interface between snow and sea ice are required to quantify the effect of biomass on the reflectance of snow, especially for the visible light. 3) Measurements of radiative quantities using a spectroradiometer with broader spectral range (0.28-2.5 μm) are needed to conduct more detailed comparisons of measurement with radiative transfer modeling in the near-infrared region. 4) Research on techniques to derive more accurately the ice concentration at moderate resolution (e.g., MODIS 1 km) pixel to unmix the pixel, and establishment of a complete database of spectral albedo for various ice types in a specific region and at a specific season are required, so that ground reflectance measurement for snow and sea ice can be accurately ice-concentration-corrected. 5) Modeling the effect of snow connectivity [Itagaki and Lemieux, 1993] on phase function and reduction of single scattering albedo and observing the effect of connectivity of snow particles on the reflectance of snow; 6) retrieving the stratifications of snow grain-size using multiple channels ranging from the near-infrared to the visible. Modeling results and their comparison with measurements suggest this approach is feasible, based on the conclusion that remote sensed data at longer wavelengths in the NIR region bring information of snow layers of smaller depth.

APPENDIX A

Geometrical Optics of Absorptive Media

At the boundary of two different media (different complex refractive index), the coefficient of reflection (transmission) r_p (t_p), where p is the polarization, is defined as the ratio between the amplitudes of reflected (refracted) wave and the incident wave. The reflection and transmission geometry is shown in Figure A1. Here we consider two wave modes: TE mode and TM mode. TE wave is also called the vertically polarized ($p = \perp$) wave, of which the electric vector is perpendicular to the plane of incidence; and TM wave is also called the parallel polarized ($p = //$) wave, of which the electric field is parallel to the plane of incidence.

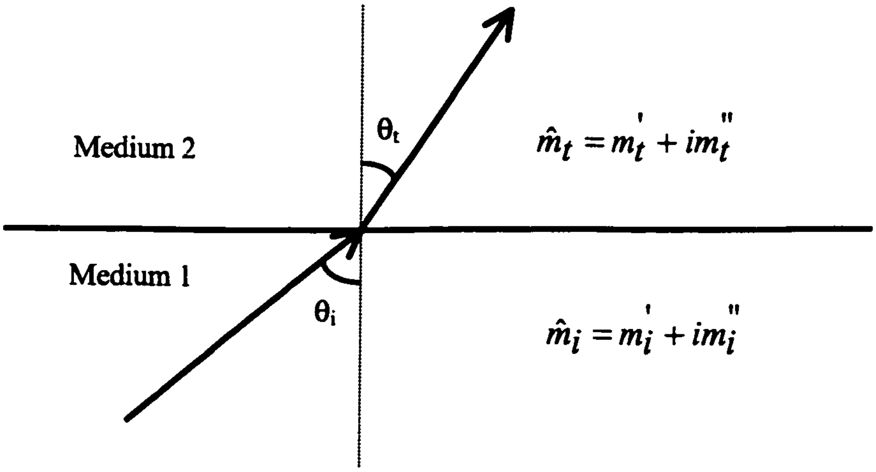

Figure A.1 Geometry of reflection and transmission of wave at absorbing medium interfaces. Complex indices of medium 1 and 2 are denoted by $\hat{m}_i$ and $\hat{m}_t$.

A1. Non-absorbing Media

If all the media are non-absorbing, the reflection and transmission coefficients are given by the Fresnel formulae [Liou and Hansen, 1971; Born and Wolf, 1980]

$$\begin{cases} r_{\perp}(\theta_i,\theta_t,m_i,m_t)=\dfrac{m_i\cos\theta_i-m_t\cos\theta_t}{m_i\cos\theta_i+m_t\cos\theta_t} \\ t_{\perp}(\theta_i,\theta_t,m_i,m_t)=\dfrac{2m_i\cos\theta_i}{m_i\cos\theta_i+m_t\cos\theta_t} \end{cases} \tag{A.1}$$

$$\begin{cases} r_{//}(\theta_i,\theta_t,m_i,m_t)=\dfrac{m_t\cos\theta_i-m_i\cos\theta_t}{m_t\cos\theta_i+m_i\cos\theta_t} \\ t_{//}(\theta_i,\theta_t,m_i,m_t)=\dfrac{2m_i\cos\theta_i}{m_t\cos\theta_i+m_i\cos\theta_t} \end{cases} \tag{A.2}$$

A2. Absorbing Media

If all the media are absorbing, i.e., the refractive index if any of the media is complex, the Fresnel formulae have the same forms as above but with real refractive index m$_i$ and m$_t$ replaced by complex refractive index $\hat{m}_i$ and $\hat{m}_i$ respectively, and the law of refraction is also the same, i.e.

$$\hat{m}_i\sin\theta_i=\hat{m}_t\sin\theta_t \tag{A.3}$$

Following Born and Wolf (1980) (p.628-633), we also define

$$\hat{m}_i\cos\theta_i=u_i+iv_i \tag{A.4a}$$

$$\hat{m}_t\cos\theta_t=u_t+iv_t \tag{A.4b}$$

For the problem, θ$_i$, $\hat{m}_i$ and $\hat{m}_t$ are known, and we are trying to find r$_p$ and R$_p$ and T$_p$. For incident medium, we have

$$u_i=m_i'\cos\theta_i, \qquad v_i=m_i''\cos\theta_i \tag{A.5}$$

To obtain u$_t$ and v$_t$, squaring (A.4b) and using (A.3), we have

$$(u_t+iv_t)^2=\hat{m}_t^{\,2}-\hat{m}_i^{\,2}\sin^2\theta_i$$

Equating real and imaginary parts in both sides of the above equation gives

$$\begin{cases} u_t^2 - v_t^2 = \Delta = m_t'^2 - m_t''^2 - \left(m_i'^2 - m_i''^2\right)\sin^2\theta_i \\ u_t v_t = \Gamma = m_t' m_t'' - 2m_i' m_i'' \sin^2\theta_i \end{cases} \tag{A.6}$$

The solution of Equation (A.6) is readily found to be

$$\begin{cases} u_t = \dfrac{\sqrt{2}}{2}\left[\left(\Delta^2 + 4\Gamma^2\right)^{\frac{1}{2}} + \Delta\right]^{\frac{1}{2}} \\ v_t = \dfrac{\sqrt{2}}{2}\left[\left(\Delta^2 + 4\Gamma^2\right)^{\frac{1}{2}} - \Delta\right]^{\frac{1}{2}} \end{cases} \tag{A.7}$$

Thus, the reflection and transmission coefficients, reflectivity and transmissivity are given by

$$\begin{cases} r_\perp\left(\theta_i, \theta_t, \hat{m}_i, \hat{m}_t\right) = \dfrac{\hat{m}_i\cos\theta_i - \hat{m}_t\cos\theta_t}{\hat{m}_i\cos\theta_i + \hat{m}_t\cos\theta_t} = \dfrac{(u_i - u_t) + i(v_i - v_t)}{(u_i + u_t) + i(v_i + v_t)} \\ t_\perp\left(\theta_i, \theta_t, \hat{m}_i, \hat{m}_t\right) = \dfrac{2\hat{m}_i\cos\theta_i}{\hat{m}_i\cos\theta_i + \hat{m}_t\cos\theta_t} = \dfrac{2u_i + i2v_i}{(u_i + u_t) + i(v_i + v_t)} \end{cases} \tag{A.8a}$$

$$\begin{cases} r_{//}\left(\theta_i, \theta_t, \hat{m}_i, \hat{m}_t\right) = \dfrac{\hat{m}_t\cos\theta_i - \hat{m}_i\cos\theta_t}{\hat{m}_t\cos\theta_i + \hat{m}_i\cos\theta_t} = \dfrac{a + ib}{c + id} \\ t_{//}\left(\theta_i, \theta_t, \hat{m}_i, \hat{m}_t\right) = \dfrac{2\hat{m}_i\cos\theta_i}{\hat{m}_t\cos\theta_i + \hat{m}_i\cos\theta_t} = \dfrac{2(e + if)}{c + id} \end{cases} \tag{A.8b}$$

with

$$\begin{aligned} a &= u_i\left(m'^2_t - m''^2_t\right) - u_t\left(m'^2_i - m''^2_i\right) - 2\left(v_i m'_t m''_t - v_t m'_i m''_i\right) \\ b &= v_i\left(m'^2_t - m''^2_t\right) - v_t\left(m'^2_i - m''^2_i\right) + 2\left(u_i m'_t m''_t - u_t m'_i m''_i\right) \\ c &= u_i\left(m'^2_t - m''^2_t\right) + u_t\left(m'^2_i - m''^2_i\right) - 2\left(v_i m'_t m''_t + v_t m'_i m''_i\right) \\ d &= v_i\left(m'^2_t - m''^2_t\right) + v_t\left(m'^2_i - m''^2_i\right) + 2\left(u_i m'_t m''_t + u_t m'_i m''_i\right) \\ e &= u_i\left(m'_i m'_t - m''_i m''_t\right) - v_i\left(m'_i m''_t + m'_t m''_i\right) \\ f &= u_i\left(m'_i m''_t + m'_t m''_i\right) + v_i\left(m'_i m'_t - m''_i m''_t\right) \end{aligned}$$

Now let's derive the specific case that the absorbing medium in vacuum or air. Two cases are considered: wave incident from air to absorbing medium and wave traveling from absorbing medium to air. First we consider wave propagates from air to absorbing medium. In this case, $m'_i = 1, m''_i = 0$, $\hat{m}_t = \hat{m} = m' + im''$ is the relative complex refractive index of the medium, and $\hat{m}_t \cos\theta_t = u + iv$. Inserting these into Equation (A.8), we have

$$\begin{cases} r_\perp(\theta_i,\theta_t,\hat{m}) = \dfrac{\cos\theta_i - \hat{m}\cos\theta_t}{\cos\theta_i + \hat{m}\cos\theta_t} = \dfrac{(\cos\theta_i - u) - iv}{(\cos\theta_i + u) + iv} \\ t_\perp(\theta_i,\theta_t,\hat{m}) = \dfrac{2\cos\theta_i}{\cos\theta_i + \hat{m}\cos\theta_t} = \dfrac{2\cos\theta_i}{(\cos\theta + u) + iv} \end{cases} \tag{A.9a}$$

$$\begin{cases} r_{//}(\theta_i,\theta_t,\hat{m}) = \dfrac{\hat{m}\cos\theta_i - \cos\theta_t}{\hat{m}\cos\theta_i + \cos\theta_t} = \dfrac{\left[(m'^2 - m''^2)\cos\theta_i - u\right] + i(2m'm''\cos\theta_i - v)}{\left[(m'^2 - m''^2)\cos\theta_i + u\right] + i(2m'm''\cos\theta_i + v)} \\ t_{//}(\theta_i,\theta_t,\hat{m}) = \dfrac{2\cos\theta_i}{\hat{m}\cos\theta_i + \cos\theta_t} = \dfrac{2(m' + im'')\cos\theta_i}{\left[(m'^2 - m''^2)\cos\theta_i + u\right] + i(2m'm''\cos\theta_i + v)} \end{cases} \tag{A.9b}$$

with

$$\begin{cases} u = \dfrac{\sqrt{2}}{2}\left[\left(\Delta^2 + 4\Gamma^2\right)^{\frac{1}{2}} + \Delta\right]^{\frac{1}{2}} \\ v = \dfrac{\sqrt{2}}{2}\left[\left(\Delta^2 + 4\Gamma^2\right)^{\frac{1}{2}} - \Delta\right]^{\frac{1}{2}} \end{cases}$$

$$\begin{cases} \Delta = m'^2 - m''^2 - \sin^2\theta_i \\ \Gamma = m'm'' \end{cases}$$

From above, we can easily obtain the results for wave propagating from medium to air. What we most concern is that the wave propagates from air into absorbing medium and then emerging from the medium to air. For this case, the incident angle at the medium-air interface is just the refractive angle at the air-medium interface. Thus we have

$$\begin{cases} r_p(\theta_t,\theta_i,1/\hat{m}) = -r_p(\theta_i,\theta_t,\hat{m}) \\ t_p(\theta_t,\theta_i,1/\hat{m}) = \dfrac{(u+iv)}{\cos\theta_i} t_p(\theta_i,\theta_t,\hat{m}) \end{cases} \tag{A.9c}$$

REFERENCES

Ackley, S. F., Mass-balance aspects of Weddell Sea pack ice. *J. Glaciol.*, **24**(90), 391-405, 1979.

Ackley, S. F., M. A. Lange, and P. Wadhams, Snow cover effects on Antarctic sea ice thickness. *CRREL Monogr.*, **90-1**, 16-21, 1990.

Ahmad, S. P., and D. W. Deering, A simple analytical function for bidirectional reflectance. *J. Geophys. Res.*, **97**(D17), 18,867-18,886, 1992.

Allison, I., R. E. Brandt, and S. G. Warren, East Antarctic sea ice: albedo, thickness distribution, and snow cover. *J. Geophys. Res.*, **98**(C7), 12,417-12,429, 1993.

Arctowski, H., Les glaces: glace de mer et banquises, In *Results du voyage du S. Y. Belgica en 1897-1898-1899. Rapports Scientifiques*, **Vol. 5**, Antwerp, J. E. Buschmann, 3-55, (Transl., NTIS AD 881 363), 1908.

Armstrong, R. L., Metamorphism in subfreezing seasonal snow cover: The role of thermal and vapor pressure conditions. Ph.D. thesis, Dept. Geography, Univ. Colorado, Boulder, 1985.

Armstrong, R. L., A. Chang, A. Rango, and E. Josberger, Snow depths and grain-size relations with relevance for passive microwave studies. *Ann. Glaciol.*, **17**, 171-176, 1993.

Andreas, E. L., and S. F. Ackley, On the differences in ablation seasons of Arctic and Antarctic sea ice. *J. Atmos. Sci.*, 39, 440-447, 1982.

Aoki, T., T. Aoki, M. Fukabori, A. Hachikubo, Y. Tachibana, F. Nishio, Effects of snow physical parameters on spectral albedo and bidirectional reflectance of snow surface. *J. Geophys. Res.*, **105** (D8), 10,219-10,236, 2000.

Aoki, T., T. Aoki, M. Fukabori, Y. Tachibana, Y. Zaizen, F. Nishino, and T. Oishi, Spectral albedo observation on the snow field at Barrow, Alaska. *Polar Meteorol. Glaciol.*, **12**, 1-9, 1998.

Bader, H., R. Haefeli, E. Bucher, J. Neher, O. Eckel and C. Thams, Snow and its metamorphism. *SIPRE Translation 14*, 1954.

Bager, H., Physics and Mechanics of Snow as a Material. U. S. Army Cold Region Research and Engineering Lab., Hanover, N. H., P.8, 1962.

Barnsley, M. J., P. D. Hobson, A. H. Hyman, W. Lucht, J.-P. Muller, and A. H. Strahler, Characterizing the spatial variability of broadband albedo in a semidesert environment for MODIS validation. *Remote Sens. Environ*, **74**, 58-68, 2000.

Bates, R. L., and J. A. Jackson (Ed.), Glossary of Geology. 2nd ed., American Geological Institute, Falls Church, Va., 1980.

Bensen, C. S., Stratigraphic studies in the snow and firn of the Greenland ice sheet. *SIPRE Res. Rep. 70*, 1962.

Bernier, P. Y., Microwave remote sensing of snowpack properties: potential and limitations. *Nord. Hydrol.*, **18**(1), 1-20, 1987.

Bohren, C. F., and B. R. Barkstrom, Theory of the optical properties of snow. *J. Geophys. Res.*, **79**(30), 4527-4535, 1974.

Bohren, C. F., and R. L. Beschta, Snowpack albedo and snow density. *Cold Reg. Sci. Technol.*, **1**, 47-50, 1979.

Bohren, C. F., and D. R. Huffman, Absorption and Scattering of Light by Small Particles. Wiley, New York, NY, 1983.

Born, M. and E. Wolf, Principles of Optics. Sixth (Corrected) Edition, Oxford, Pergamon Press, 1980.

Bourdelles, B., and M. Fily, Snow grain-size determination from Landsat imagery over Terre Adelie, Antarctic. *Ann. Glaciol.*, **17**, 86-92, 1993.

Brandt, R. E., T. C. Grenfell, and S. G. Warren, Optical properties of snow. *Antarct. J. US*, **26**, 272-275, 1991.

Brandt, R. E., and S. G. Warren, Solar-heating rates and temperature profiles in Antarctic snow and ice. *J. Glaciol.*, **39**, 99-110, 1993.

Brandt, R. E., and S. G. Warren, Temperature measurements and heat transfer in near-surface snow at the South Pole. *J. Glaciol.*, **43**(144), 339-351, 1997.

Brest, C. L., Seasonal albedo of an urban/rural landscape from satellite observations. *J. Climate Appl. Meteor.*, **26**, 1169-1187, 1987.

Brest, C. L. and S. N. Goward, Deriving surface albedo measurements from narrow band satellite data. *Int. J. Remote Sensing*, **8**(3), 351-367, 1987.

Carlson, R.W., Arakelian, T., and W. D. Smythe, Spectral reflectance of Antarctic snow: "Ground truth" and spacecraft measurements. *Antarct. J. U. S.*, **27**, 296-298, 1992.

Carlson. R. W., and T. Arakelian, Spectral bidirectional reflectance and energy absorption rates of Antarctic snow. *Antarct. J. U. S.*, **28**, 256-258, 1993.

Carroll, J. J. and B. W. Fitch, Effects of solar elevation and cloudiness on snow albedo at the south pole. *J. Geophys. Res.*, **86**(C6), 5271-5276, 1981.

Chandrasekhar, S., Radiative Transfer. Oxford: Oxford University Press, 1950.

Chang, A. T. C., J. L. Foster, D. K. Hall, A. Rango and B. K. Hartline, Snow water equivalent determination by microwave radiometry. National Aeronautics and Space Administration. Goddard Space Flight Center, Greenfield, MD. (Technical Memorandum 82074), 1981.

Chang, A. T. C., J. L. Foster, and D. K. Hall, Nimbus-7 SMMR derived global snow cover parameters. *Ann. Glaciol.*, 9, 39-44, 1987a.

Chang, A. T. C., and 6 others, Estimating snowpack parameters in the Colorado River basin. International Association of Hydrological Sciences Publication 166 (Symposium at Vancouver 1987 – Large Scale Effects of Seasonal Snow Cover), 343-352, 1987b.

Chernigovski, N. T., Radiational properties of the central Arctic ice cover. In Fletcher, J. O., B. Keller and S. M. Olenicoff, *eds. Soviet data on the Arctic heat budget and its climatic influence*. Rand Corporation, 151-173. (Research Memorandum RM-5003-PR), 1966.

Chýlek, P., V. Ramaswamy, and V. Srivastava, Albedo of soot-contaminated snow. *J. Geophys. Res.*, **88**(C15), 10837-10843, 1983.

Colbeck, S. C., Grain clusters in wet snow. *J. Colloid Interface Sci.*, **72**(3), 371-384, 1979.

Colbeck, S. C., Thermodynamics of snow metamorphism due to variations in curvature. *J. Glaciol.*, **26** (94), 291-301, 1980.

Colbeck, S. C., An overview of seasonal snow metamorphism. *Rev. Geophys. Space Phys.*, **20**(1), 45-61, 1982.

Colbeck, S. C., Statistics of coarsening in water-saturated snow. *Acta Metall.*, **34**, 347-352, 1986.

Colbeck, S. C., A review of the metamorphism and classification of seasonal snow cover crystals. International Association of hydrological Science Publication 162 (Symposium at Davos 1986 – Avalanche Formation, Movement and Effects), 3-34, 1987.

Colbeck, S., E. Akitaya, R. Armstrong, H. Gubler, J. Lafeuille, K. Lied, D. McClung, and E. Morris, *The International Classification for Seasonal Snow on the Ground*, 23 pp., Int. Comm. On Snow and Ice of the Int. Assoc. of Sci. Hydrol., Gentbrugge, Belgium, 1990.

Colbeck, S. C., The layered character of snow covers. *Rev. Geophys.*, **29**(1), 81-96, 1991.

Comiso, J. C., Sea ice effective microwave emissivities from satellite passive microwave and infrared observations. *J. Geophys. Res.*, **88**(C12), 7686-7704, 1983.

Conway, H., A. Gades, C. F. Raymond, Albedo of dirty snow during conditions of melt. *Water Resour. Res.*, **32**(6), 1713-1718, 1996.

Dave, J. V., and Gazdag, J., A modified Fourier transform method for multiple scattering calculations in a plane-parallel atmosphere. *Appl. Opt.*, **9**, 1457-1466, 1970.

Davis, P. J., and P. Rabinowitz, Methods of numerical integration. Second edition, Academic Press, Orlando, FL, pp.481-483, 1984.

Davis, R. E., and J. Dozier, Stereological characterization of dry alpine snow for microwave remote sensing. *Adv. Space Res.*, **9**(1), 245-251, 1989.

Davis, R. E., A. W. Nolin, R. Jordan, and J. Dozier, Towards predicting temporal changes of the spectral signature of snow in visible and near-infrared wavelengths. *Ann. Glaciol.*, **17**, 143-148, 1993.

De Abreu, R. A., D. G. Barber, K. Misurak, and E. F. LeDrew, Spectral albedo of snow-covered first-year and multi-year sea ice during spring melt. *Ann. Glaciol.*, **21**, 337-342, 1995.

De Abreu, R. A., J. Key, J. A. Maslanik, M. C. Serreze, and E. F. LeDrew, Comparison of *in situ* and AVHRR-derived broadband albedo over Arctic sea ice. *Arctic*, **47**(3), 288-297, 1994.

d'Entremont, R. P., C. B. Schaaf, W. Lucht, and A. H. Strahler, Retrieval of red spectral albedo and bidirectional reflectance using AVHRR HRPT and GEOS satellite observations of the New England region. *J. Geophys. Res.*, **104**(D6), 6229-6239, 1999.

Dey, B., D. C. Goswami, and A. Rango, Utilization of satellite snow-cover observations for seasonal stream flow estimates in the Western Himalayas. *Nordic Hydrology*, **14**, 257-266, 1983.

Dirmhirn, I., and F. D. Eaton, Some characteristics of the albedo of snow. *J. Appl. Meteor.*, **14**, 375-379, 1975.

Dozier, J., S. R. Schneider, and D. F. McGinnis, J., Effect of grain size and snowpack water equivalence on visible and near-infrared satellite observations of snow. *Water Resour. Res.*, **17**, 1213-1221, 1981. .

Dozier, J., Snow reflectance from LANDSAT-4 thematic mapper. *IEEE Trans. Geosci. Remote Sens.*, **GE-22** (3), 323-328, 1984.

Dozier, J. and D. Marks, Snow mapping and classification from Landsat Thematic Mapper data. *Ann. Glaciol.*, **9**, 97-103, 1987.

Dozier, J., Spectral signature of alpine snow cover from the Landsat Thematic Mapper. *Remote Sens. Environ.*, **28**, 9-22, 1989.

Drinkwater, M. R., and V. Lytle, ERS-1 SAR and field-observed austral fall freeze-up in the Weddell Sea, Antarctica. *J. Geophys. Res.*, **102**(C6), 12,593-12608, 1997.

Duguay, C. R., and E. F. LeDrew, Mapping surface albedo in the east slope of the Colorado Front Range, U.A.S., with Landsat Thematic Mapper. *Arctic and Alpine Research*, **23**, 213-223, 1991.

Duguay, C. R. and E. F. LeDrew, Estimating surface reflectance and albedo from Landsat-5 Thematic Mapper over rugged terrain. *Photogramm. Eng. Remote Sens.*, **58**(5), 551-558, 1992.

Eicken, H., H. Fischer, and P. Lemke, Effects of the snow cover on Antarctic sea ice and potential modulation of its response to climate change. *Ann. Glaciol.*, **21**, 369-376, 1995.

Elson, L., M. Allen, J. Goldsmith, M. Orton and W. Weibel, An example of a network-based approach to data access, visualization, interactive analysis and distribution. 2000. Documentation and software of WbWinds are available online at http://webwinds.jpl.nasa.gov.

Fetterer, F., N. Untersteiner, Observations of melt ponds on Arctic sea ice. *J. Geophys. Res.*, **103**(C11), 24,821-24,835, 1998.

Fily, M., B. Bourdelles, J. P. Dedieu, and C. Sergent, Comparison of *in situ* and Landsat Thermatic Mapper derived snow grain characteristics in the Alps. *Remote Sens. Environ.*, **59**, 452-460, 1997.

Foster, J. L., D. K. Hall, A. T. C. Chang, and Rango, An overview of passive microwave snow research and results. *Rev. Geophys. Space Phys.*, **22**(2), 195-208, 1984.

Garrity, C., Characterization of snow on floating ice and case studies of brightness temperature changes during the onset of melt. In *Microwave Remote Sensing of Sea Ice, Geophys. Monogr. Ser., vol. 68*, edited by F. Carsey, pp. 313-328, AGU, Washington, D. C., 1992.

Geiger, C. A., W. D. Hibler III, and S. F. Ackley, Large scale sea ice drift and deformation: Comparison between models and observations in the western Weddell Sea during 1992. *J. Geophys. Res.*, **103**(C10), 21,893-21,913, 1998.

Glantschnig, W. J., and S.-H. Chen, Light scattering from water droplets in the geometrical optics approximation. *Appl. Opt.*, **20**(14), 2499-2509, 1981.

Gogineni, S. P., R. K. Moore, T. C. Grenfell, D. G. Barber, S. Digby and M. drinkwater, The effects of freeze-up and melt processes on microwave signatures. In: *Microwave remote sensing of sea ice* (F. D. Carsey, editor), Geophysical Monograph **68**, American Geophysical Union, Washington, 329-341, 1992.

Gratton, D. I., P. J. Howart, and D. J. Marceau, Using Landsat-5 Thematic Mapper and digital elevation data to determine the net radiation field of a mountain glacier. *Remote Sens. Environ.*, **43**, 315-331, 1993.

Green, R. O., and J. Dozier, Inversion for surface snow grain size and liquid water from AVIRIS spectra. In *Summaries of the Sixth Annual JPL Airborne Earth Science Workshop,* **Volume 1**. AVIRIS Workshop (R. O. Green, Ed.), JPL Publication 96-4, Jet Propulsion Laboratory, Pasadena, CA, pp.127-134, 1996.

Grenfell, T. C., and G. A. Maykut, The optical properties of ice and snow in the Arctic Basin. *J. Glaciol.*, **18**(80), 445-463, 1977.

Grenfell, T. C., D. K. Perovich, Spectral albedos of sea ice and incident solar irradiance in the southern Beaufort Sea. *J. Geophys. Res.*, **89**, 3573-3580, 1984.

Grenfell T. C., S. G. Warren, P. C. Mullen, Reflection of solar radiation by the Antarctic snow surface at ultraviolet, visible, and near-infrared wavelengths. *J. Geophys. Res.*, **99**(D9), 18,669-186,84, 1994.

Grenfell, T. C., and S. G. Warren, Representation of a nonspherical ice particle by a collection of independent spheres for scattering and absorption of radiation. *J. Geophys. Res.*, **104**(D24), 31,697-31,709, 1999.

Greuell, W., and de Ruyter de Wildt, M., Anisotropic reflectance by melting glacier ice: Measurements and parameterizations in Landsat TM bands 2 and 4. *Remote Sens. Environ.*, **70**, 265-277, 1999.

Guenther, B., G. D. Godden, X. Xiong, E. J. Knight, S.-Y. Qiu, H. Montgomery, M. M. Hopkins, M. G. Khayat, and Z. Hao, Prelaunch algorithm and data format for the Level 1 calibration products for the EOS-AM1 Moderate Resolution Imaging Spectroradiometer (MODIS). *IEEE Trans. Geosci. Remote Sensing*, **36** (4), 1142-1151, 1998.

Gutman, G., A simple method for estimating monthly mean albedo of land surfaces from AVHRR data. *J. Appl. Meteorol.*, **27**, 973-988, 1988.

Haas, C., The seasonal cycle of ERS scatterometer signatures over perennial Antarctic sea ice and associated surface ice properties and processes. *Ann. Glaciol.*, **33**, 69-73, 2001.

Haefliger, M., K. Steffen, and C. Fowler, AVHRR surface temperature and narrow-band albedo comparison with ground measurements for the Greenland ice sheet. *Ann. Glaciol.*, **17**, 49-54, 1993.

Hall, D. K., A. T. C. Chang, J. L. Foster, C. S. Benson, and W. M. Kovalick, Comparison of *in situ* and Landsat derived reflectance of Alaska glaciers. *Remote Sens. Environ.*, **28**(1), 23-31, 1989.

Hall, D. K., R. A. Bindschadler, J. L. Foster, A. T. C. Chang, and H. Siddalingaiah, Comparison of *in situ* and satellite-derived reflectance of Forbindels glacier, Greenland. *Int. J. Remote Sens.*, **11**(3), 493-504, 1990.

Hall, D. K., J. L. Foster, and A. T. C. Chang, Reflectance of snow as measured *in situ* and from space in sub-arctic areas in Canada and Alaska, *IEEE Trans. Geosci. Remote Sens.*, **30**(3), 634-637, 1992.

Hall, D. K., G. A. Riggs, and V. V. Salomonson, Development of methods for mapping global snow cover using Moderate Resolution Imaging Spectroradiometer data. *Remote Sens. Environ.*, **54**, 127-140, 1995.

Hall, D. K., A.B. Tait, J.L.Foster, A.T.C.Chang, M. Allen, Intercomparison of satellite-derived snow-cover maps. *Ann. Glaciol.*, **31**, 369-376, 2000.

Hallikainen, M., and D. P. Winebrenner, The physical basis for sea ice remote sensing. In *Microwave Remote Sensing of Sea Ice, Geophys. Monogr. Ser.*, **vol. 68**, edited by F. Carsey, pp. 29-46, AGU, Washington, D. C., 1992.

Hansen, J. E., and L. D. Travis, Light scattering in planetary atmosphere. *Space Sci. Rev.*, **16**, 527-610, 1974.

Hanson, K. J., Radiation measurements on the Antarctic snowfield, a preliminary report. *J. Geophys. Res.*, **65** (3), 935-946, 1960.

Hanson, K. J., The albedo of sea ice and ice islands in the Arctic Ocean Basin. *Arctic*, **14**(3), 188-196, 1961.

Hecht, E., Optics. Third Edition, Addison Wesley Longman, Inc., Reading, Massachusetts, 1998.

Herber, A., L. W. Thomason, K. Dethloff, P. Viterbo, V. F. Radionov, and U. Leiterer, Volcanic perturbation of the atmosphere in both polar regions: 1991-1994. *J. Geophys. Res.*, **101**, 3921-3928, 1996.

Hibler, W. D. III, Ice dynamics. *CRREL Monograph* **84-3**, 1979.

Hoinkes, H. C., Studies of solar radiation and albedo in the Antarctic (Little America V and South Pole, 1957/58). *Arch. Meteorol. Geophys. Bioklimatol.*, Ser. B, **10**(2), 175-181, 1961.

Hu, B., W. Lucht, and A. H. Strahler, The interrelationship of atmospheric correction of reflectances and surface BRDF retrieval: A sensitivity study. *IEEE Trans. Geosci. Remote Sens.*, **37**(2), 724-738, 1999.

Hu, Y. – X., and K. Stamnes, An accurate parameterization of the radiative properties of water clouds suitable for use in climate models. *J. Climate*, **6**, 728-742, 1993.

Hyvärinen, T., and J. Lammasniemi, Infrared measurement of free-water content and grain size of snow. *Opt. Eng.*, **26**(4), 342-348, 1987.

Itagaki, K., and G. E. Lemieux, Connectivity of snow particles. *Ann. Glaciol.*, **18**, 7-10, 1993.

Jeffries, M. O., A. L. Veazey, K. Morris and H. R. Krouse, Depositional environment of the snow cover on West Antarctic pack-ice floes. *Ann. Glaciol.*, **20**, 33-38, 1994.

Jeffries, M. O., H. R. Krouse, B. Hurst-Cushing, and T. Maksym, Snow ice accretion and snow cover depletion on Antarctic first-year sea ice floes, *Ann. Glaciol.*, **33**, 51-60, 2001.

Jin, Z., and Simpson, J. J., Bidirectional anisotropic reflectance of snow and sea ice in AVHRR channel 1 and 2 spectral regions – Part I: Theoretical analysis. *IEEE Trans. Geosci. Remote Sens.*, **37**, 543-554, 1999.

Jin, Z., and J. Simpson, Bidirectional anisotropic reflectance of snow and sea ice in AVHRR channel 1 and channel 2 spectral regions – Part II: Correction applied to imagery of snow on sea ice. *IEEE Trans. Geosci. Remote Sens.*, **38**(2), 999-1015, 2000.

Jordan, R., A one-dimensional temperature model for a snow cover: Technical documentation for SNTHER.89. *CRREL Spec. Rep.* **91-16**, U. S. Arm Corps of Eng., Hanover, N. H., 1991.

Joseph, J. H., W. J. Wiscombe and J. A. Weinman, The delta-Eddington approximation for radiative flux transfer. *J. Atmos. Sci.* **33**(12), 2452-2459, 1976.

Key, J., and Schweiger, A. J., Tools for atmospheric radiative transfer Streamer and FluxNet, *Computers & Geosciences*, **24**(5), 443-451, 1998.

Knap, W. H., C. H. Reijmer, and J. Oerlemans, Narrowband to broadband conversion of Landsat-TM glacier albedos. *Int. J. Remote Sens.*, **20**(10), 2091-2110, 1999.

Knap, W. H., and C. H. Reijmer, Anisotropy of the reflected radiation field over melting glacier ice: measurements in Landsat TM bands 2 and 4. *Remote Sens. Environ.*, **65**, 93-104, 1998.

Knap, W. H., and J. Oerlemans, The surface albedo of the Greenland ice sheet: satellite derived and *in situ* measurements in the Sondre Stromfjord area during the 1991 melt season. *J. Glaciol.*, **42**,364-374, 1996.

Kneizys, F. X., Shettle, E. P., Abreu, L. W., Chetwynd, J. H., Anderson, G. P., Gallery, W. O., Selby, J. E. A. and Clough, S. A., Users Guide to LOWTRAN7. Environmental Research Papers, No. 1010, AFGL-TR-88-0177, Air Force Geophysics Laboratory, Hanscom AFB, Massachusetts, pp.1-137, 1988.

Kneizys, F.X., Robertson, D.C., Abreu, L.W., Acharya, P., Anderson, G.P., Rothman, L.S., Chetwynd, J.H., Selby, J.E.A., Shettle, E.P., Gallery, W.O., Berg, A., Clough, S.A., Bernstein, L.S., The MODTRAN 2/3 Report and LOWTRAN 7 MODEL, Edited by: L.W. Abreu and G.P. Anderson, Ontar Corporation, pp.1-161, 1996. Available on line at http://imkpcdemo.fzk.de/isys-public/Software-tools/Modtran/science/modrep.htm.

Koepke, P., Removal of atmospheric effects from AVHRR albedos. *J. Appied Meteorology*, **28**(12), 1341-1348, 1989.

Koike, T., and T. Suhama, Passive-microwave remote sensing of snow. *Ann. Glaciol.*, **18**, 305-308, 1993.

Kokhanovsky, A. A., and T Y Nakajima, The dependence of phase functions of large transparent particles on their refractive index and shape. *J. Phys. D: Appl. Phys.*, **31**, 1329-1335, 1998.

Kokhanovsky, A. A., Optics of light scattering media: problems and solutions. Praxis Pblishing ltd, Chichester, UK, 1999.

Kottmeier, C., J. Olf, W. Frieden, and R. Roth, Wind forcing and ice motion in the Weddell sea region. *J. Geophys. Res.*, **97**(D18), 20373-20383,1992.

Kou L., D. Labrie, and P. Chylek, Refractive indices of water and ice in the 0.65- to 2.5-μm spectral range. *Appl. Opt.*, **32** (19), 3531-3540, 1993.

Kuhn, M., L. S. Kundla and L. A. Stroschein, The radiation budget at Plateau Station, Antarctica, 1966-1967. *In* Businger, J. A., *ed. Meteorological studies at Plateau station, Antarctica.* Washington, DC, American Geophysical Union, 41-73. (Antarctic Research Series 25.), 1977.

Kuhn, M., and L. Siogas, Spectroscopic studies at McMurdo, South Pole and Siple Stations during the austral summer 1977-78. *Antarctic J. U. S.*, **13**, 178-179, 1978.

Kuhn, M., Bidirectional reflectance of polar and alpine snow surface. *Ann. Glaciol.*, 6, 164-167, 1985.

Kumai, M., Identification of nuclei and concentrations of chemical species in snow crystals sampled at the South Pole. *J. Atmos. Sci.*, **33**, 833-841, 1976.

Kunzi, K. F., S. Patil, and H. Rott, Snow-cover parameters retrieved from Nimbus-7 Scanning Multi-channel Microwave Radiometer (SMMR) data. *IEEE Trans. Geosci. Remote Sens.*, **GE-20**(4), 452-467, 1982.

Langleben, M. P., Albedo and degree of puddin of a melting cover of sea ice. *J. Glaciol.*, **8**(54), 407-412, 1969.

Langleben, M. P., Albedo of melting sea ice in the southern Beaufort Sea, *J. Glaciol.*, **10**(58), 101-104, 1971.

Leroux C., J. Lenoble, G. Brogniez, J. W. Hovenier and J.F. De Haas, A model for the bidirectional polarized reflectance of snow. *J. Quant. Spectrosc. Radiat. Transfer*, **61**(3), 273-285, 1999.

Leroux C., and M. Fily, Modeling the effect of sastrugi on snow reflectance, *J. Geophys. Res.*, **103**, 25,779-25,788, 1998.

Lewis, P., and M. J. Barnsley, Influence of the sky radiance distribution on various formulations of the earth surface albedo. Paper presented at the Sixth International Symposium on Physical Measurements and Signatures in Remote Sensing, Int. Soc. For Photogram. and Remote Sens., Val d'Isere, France, 1994.

Li, S, X. Zhou, and K. Morris, Measurement of sow and sea ice surface temperature and emissivity in the Ross Sea. IGARSS'99, *IEEE 1999 International Geoscience and Remote Sensing Symposium*, Hamburg, Germany, June 28-July 02, 1999, **Volume 2**, pp.1034-1036, 1999.

Li, S., A model for the anisotropic reflectance of pure snow. M. S. thesis, 60 pp., University of Calif., Santa Barbara, 1982.

Li, S., Z. Wan, and J. Dozier, A component decomposition model for evaluating atmospheric effects in remote sensing. *J. Electromagnetic Waves and Application*, **1**(4), 323-347, 1987.

Li, S., and X. Zhou, Derivation and Comparison of Bi-directional Reflectance Functions of First-year and Multi-year Sea Ice Types in the Southern Ocean. In: *Proc. IEEE 2002 International Geoscience and Remote Sensing Symposium (IGARSS'02) and 24th Canadian Symposium on Remote Sensing*, 24-28 June, Toronto, Canada, Vol. **III**, pp. 1944-1946, 2002a.

Li, S., and X. Zhou, Deriving Reciprocal Kernel Functional Expression of Antarctic Sea Ice Surface BRDF from Field Measurements. In: *Proc. IEEE 2002 International Geoscience and Remote Sensing Symposium (IGARSS'02) and 24th Canadian Symposium on Remote Sensing*, 24-28 June, Toronto, Canada, **Vol. IV**, pp. 2173-2175, 2002b.

Li, W., K. Stamnes, and B. Chen, X. Xiong, Snow grain size retrieved from near-infrared radiances at multiple wavelengths. *Geophys. Res. Lett.*, **28**(9), 1699-1702, 2001.

Li, Z., and L. Garand, Estimation of surface albedo from space: A parameterization for global application. *J. Geophys. Res.*, **99**(D4), 8335-8350, 1994.

Li, Z., and H. G. Leighton, Narrowband to broadband conversion with spatially autocorrelated reflectance measurements. *J. Appl. Meteorol.*, **31**, 421-432, 1992.

Liljequist, G. H., Energy exchange of an Antarctic snowfield. Short-wave radiation (Maudheim, 71°03'S, 10°56'W). *Norwegian-British-Swedish Antarctic Expedition, 1949-52, Sci. Results* II, Pt. 1A, Oslo, Norsk Polarinstitutt, 107 pp, 1956.

Liou, K. N., and J. E. Hansen, Intensity and polarization for single scattering by polydisperse spheres: A comparison of ray optics and Mie theory. *J. Atmos. Sci.*, **28**, 995-1004, 1971.

Liou, K.-N., and Y. Takano, Light scattering by nonspherical particles: Remote sensing and climate implications. *Atmos. Res.*, **31**, 271-298, 1994.

Lucht, W., A. H. Hyman, A. H. Strahler, M. J. Barnsley, P. Hobson, and J.-P. Muller, A comparison of satellite-derived spectral albedos to ground-based broadband albedo measurements modeled to satellite spatial scale for a semidesert landscape. *Remote Sens. Environ.*, **74**, 85-98, 2000a.

Lucht, W., C. B. Schaaf and A. H. Strahler, An algorithm for the retrieval of albedo from space using semiempirical BRDF models. *IEEE Trans. Geosci. Remote Sens.*, **38**(2), 977-998, 2000b.

Male, D. H., and R. J. Granger, Snow surface energy exchange. *Water Resource. Res.*, **17**(3), 609-627, 1981.

Martinec, J., and A. Rango, Parameter values for snowmelt runoff modeling. *J. Hydrol.*, **84**, 197-219, 1986.

Massom, R. A., M. R. Drinkwater, and C. Haas, Winter snow cover on sea ice in the Weddell Sea. *J. Geophys. Res.*, **102**(C1), 1101-1117, 1997.

Massom, R. A., V. I. Lytle, A. P. Worby, and I. Allison, Winter snow cover variability on East Antarctic sea ice. *J. Geophys. Res.*, **103**(C11), 24,837-24,855, 1998.

Massom, R. A., H. Eicken, C. Haas, M. O. Jeffries, M. R. Drinkwater, M. Sturm, A. P. Worby, X. Wu, V. I. Lytle, S. Ushio, K. Morris, P. A. Reid, S. G. Warren, and I. Allison, Snow on Antarctic sea ice. *Rev. Geophys.*, **39**, 413-445, 2001.

Matsubara, K., and S. Kawaguchi, Spectral extinction measurement by sunphotometer at Syowa Station, Antarctica. *Mem. Natl. Inst. Polar Res.*, Spec. Issue, 29, 85-93. 1983.

Mätzler, C., Applications of the interaction of microwaves with the natural snow cover, *Remote Sensing Rev.*, 2(2), 259-387, 1987.

Maykut, G. A., and N. Untersteiner, Some results from a time-dependent thermodynamic model of sea ice, *J. Geophys. Res.*, **76**, 1550-1575, 1971.

Maykut, G. A., The surface heat and mass balance. In *The Geophysics of Sea Ice*, edited by N. Untersteiner, pp. 395-464, NASA ASI Series B: Physics vol. **146**, Plenum Press, New York, 1986.

McNamara, J. P., D. J. Kane, and L. D. Hinzman, An analysis of streamflow hydrology in the Kuparuk River basin, Arctic Alaska: A nested watershed approach. *J. Hydrol.*, **206**(1-2), 39-57, 1998.

McPhee, M. G., S. F. Ackley, P. Guest, B. A. Huber, D. G. Martinson, J. H. Morison, R. D. Muench, L. Padman, and T. P. Stanton, The Antarctic zone flux experiment. *Bull. Am. Meteorol. Soc.*, **77**, 1221-1232, 1996.

Menzel, W. P., and Gumley, L. E., MODIS Atmospheric Profiles Retrieval Algorithm Theoretical Basis Document. *ATBD-MOD-07*, NASA Goddard Space Flight Center, pp.1-38, 1998. Available on line at: http://ltpwww.gsfc.nasa.gov/MODIS-Atmosphere/_docs/atbd_mod07.pdf.

Mishchenko, M. I., L. D. travis, and D. W. Mackowski, T-matrix computations of light scattering by nonspherical particles: A review. *J. Quant. Spectrosc. Radiat. Transfer*, **55** (5), 535-575, 1996.

Mishchenko, M. I., J. M. Dlugach, E. G. Yanovitskij, and N. T. Zakharova, Bidirectional reflectance of flat, optically thick particulate layers: An efficient radiative transfer solution and applications to snow and soil surfaces. *J. Quant. Spectrosc. Radiat. Transfer*, **55**, 409-432, 1999.

Mishchenko, M. I., Calculation of the amplitude matrix for a nonspherical particle in a fixed orientation. *Appl. Opt.*, **39** (6), 1026-1031, 2000.

Mithchell, R. M., and O'Brien, D. M., Correction of AVHRR shortwave channels for the effects of atmospheric scattering and absorption. *Remote Sens. Environ.*, **46**, 129-145, 1993.

Morris, K., and M. O. Jeffries, Seasonal contrasts in snow cover characteristics on Ross Sea ice floes. *Ann. Glaciol.*, **33**, 61-68, 2001.

Morris, K., and M. O. Jeffries, and S. Li, Sea ice characteristics and seasonal variability of ERS 1 SAR backscatter in the Bellingshausen Sea. In *Antarctic Sea Ice: Physical Processes, Interactions and Variability*, Antarct. Res. Ser., vol. **74**, edited by M. O. Jeffries, pp. 213-242, AGU, Washington, D. C., 1998.

Murozumi, M., T. J. Chow, and C. Patterson, Chemical concentrations of pollutant lead aerosols, terrestrial dusts and sea salts in Greenland and Antarctic snow strata. *Geochim. Cosmochim. Acta*, **33**, 1247-1294, 1969.

Nakajima, T. Y., and T. Nakajima, Wide-area determination of cloud microphysical properties from NOAA AVHRR measurements for FIRE and ASTEX regions. *J. Atmos. Sci.*, **52**, 4043-4059, 1995.

Nakajima, T. Y., T. Nakajima, and A. A. Kokhanovsky, Radiative transfer through light scattering media with nonspherical large particles: direct and inverse problems. *Proc. SPIE*, **3220**, 2-12, 1998.

Nicodemus, F. E., J. C. Richmond, J. J. Hsia, I. W. Ginsberg, and T. Limperis, Geometrical considerations and nomenclature for reflectance. *NBS Monogr. 160*, U.S. Department of Commerce/National Bureau of Standards, pp.52, 1977.

Nishihama, M., R. Wolfe, D. Solomon, F. Patt, J. Blanchette, A. Fleig, E. Masuoka, MODIS Level 1A Earth Location: Algorithm Theoretical Basis Document Version 3.0. *SDST-092*, August, 1997. Available on line at:

http://eospso.gsfc.nasa.gov/ftp_ATBD/REVIEW/MODIS/ATBD-MOD-28/atbd-mod-28.pdf.

Nolin, A. W., and J. Dozier, Estimating snow grain size using AVIRIS data, *Remote Sens. Environ.*, **44**, 231-238, 1993.

Nolin, A. W., J. Dozier, and L. A. K. Mertes, Mapping alpine snow using a spectral mixture modeling technique. *Ann. Glaciol.*, **17**, 121-124, 1993.

Nolin, A. W., and J. Dozier, A hyperspectral method for remotely sensing the grain size of snow. *Remote Sens. Environ.*, **74**, 207-216, 2000.

Nussenzveig, H. M., Diffraction Effects in Semiclassical Scattering. London: Cambridge University Press, 1992.

O'Brien, H. W., and R. H. Munis, Red and near-infrared spectral reflectance of snow. *U. S. Army CRREL Research Report* **332**, 18pp., 1975.

Painter, T. H., D. A. Roberts, R. O. Green, and J. Dozier, The effect of grain size on spectral mixture analysis of snow-covered area with AVIRIS data. *Remote Sens. Environ.*, **65**, 320-332, 1998.

Papanicolaou, G. C., and R. Burridge, Transport equations for the Stokes parameters from Maxwell equations in a random media. *J. Math. Phys.*, **16**, 2074-2082, 1975.

Patt, F. S., R. H. Woodward, W. W. Gregg, An automated method for navigation assessment for Earth survey sensors using island targets, *Int. J. Remote Sens.*, **18**(16), 3311-3336, 1997.

Pearson, E. S., and H. O. Hartley (Eds.), Biometrika Tables for Statisticians. **Vol.1**, Third edition, Biometrika Trustees, 1966.

Perovich, D., The optical properties of sea ice. USA Cold Regions Research and Engineering Laboratory, **Monograph 96-1**, 1996.

Perovich, D. K. and J. W. Govoni, Absorption coefficients of ice from 250 to 400 nm. *Geophys. Res. Lett.*, **18**(7), 1233-1235, 1991.

W. H. Press, S. A. Teukolsky, W. T. Vetterling, and B. P. Flannery, Numerical recipes in C: the art of scientific computing. Second edition, Cambridge University Press, pp.350-354, 1992.

Ramon, D., and R. Santer, Operational remote sensing of aerosols over land to account for directional effects, *Appl. Opt.*, **40**(18), 3060-3075, 2001.

Rango, A., and K. I. Itten, Satellite potentials in snow-cover monitoring and runoff prediction. *Nord. Hydrol.*, **7**, 209-230, 1976.

Rango, A., V. V. Salomonson, and J. L. Foster, Seasonal streamflow estimation in the Himalaya region employing meteorological satellite snow cover observations. *Water Resour. Res.*, **14**, 359-373, 1977.

Rango, A., and J. Morrinec, Application of snowmelt-runoff model using Landsat data. *Nord. Hydrol.*, **10**, 225-238, 1979.

Rango, A., An international perspective on large-scale snow studies. *Hydrol. Sci. J.*, **30**, 225-238,1985.

Reijmer, C. H., R. Bintanja, and W. Greuell, Surface albedo measurements over snow and blue ice in thematic mapper bands 2 and 4 in Dronning Maud Land, Antarctica. *J. Geophys. Res.*, **106** (D9), 9661-9672, 2001.

Rother, T., and K. Schmidt, The discretized Mie-formalism for plane wave scattering on dielectric objects with non-separable geometries. *J. Quant. Spectrosc. Radiant. Transfer*, **55**, 615-625, 1996.

Rott, H., Remote sensing of snow. *International Association of Hydrological Sciences (IAHS) Publication,* **166**, (Symposium at Vancouver 1987 – Large Scale Effects of Seasonal Snow Cover), 279-290, 1987.

Rusin, N. P., Meteorologicheskiy I radiatsionyy rezhim Antarktidy. Leningrad, Gidrometeorologischeskoye Izdatel'stvo, 1961. [English translation: Meteorological and Radiational Regime of Antarctica. *Jerusalem, Israel Program for Scientific Translations*, 1964, 355 pp.].

Salm, B., Mechanical properties of snow, *Rev. Geophys. Space Phys.*, **20**(1), 1-19, 1982.

Saunders, R. W., The determination of broad band surface albedo from AVHRR visible and near-infrared radiance. *Int. J. Remote Sens.*, **11**(1), 49-67, 1990.

Schlatter, T. W., The local surface energy balance and subsurface temperature regime in Antarctica. *J. Appl. Meteorol.*, **11**, 1048-1062, 1972.

Schwander, H., B. Mayer, A. Ruggaber, A. Albold, G. Seckmeyer, and P. Koepke, Method to determine snow albedo values in the ultraviolet for radiative transfer modeling. *Appl. Opt.*, **38**(18), 3869-3875, 1999.

Sellers, W. D., A global climate model based on the energy balance of the Earth-Atmosphere system. *J. Appl. Meteorol.*, **8**, 392-400, 1969.

Shaw, G. E., Atmospheric turbidity in the polar regions. *J. Appl. Meteor.*, **21**, 1080-1088. 1982.

Shi, J., R. E. Davis, J. Dozier, Stereological determination of dry-snow parameters for discrete-scatter microwave modeling. *Ann. Glaciol.* **17**, 295-299, 1993.

Shiobara, M., M. Tanaka, T. Nakajima and H. Ogawa, Spectral measurements of direct solar radiation and the sky brightness distribution at Syowa Station, Antarctica. In: *Atmospheric Radiation, Progress and Prospects, Proc. Beijing Int. Radiation Symp.*, Beijing, China, 629-637, 1986.

Sommerfeld, R. A., and E. LaChapelle, The classification of snow metamorphism, *J. Glaciol.*, 9, 3-17, 1970.

Spichkin, V. A., Role of evaporation in the surface ablation of sea ice, Sovetskaia Antarkticheskaia Ekspeditsiia, 1955. *Sov. Antarct. Exped. Inf. Bull., 6, 16-17.* *[*Transl. From *Inform. Byull. Sov. Antarkt. Eksped. 55),* 1967.

Squire, V. A., P. Wadhams, and S. C. Moore, Surface gravity wave processes in the winter Weddell Sea. *EOS Trans.*, AGU, **67**(44), 1005, 1986.

Stamnes, K., S.-C. Tsay, W. Wiscombe, and K. Jayaweera, Numerically stable algorithm for discrete-ordinate-method radiative transfer in multiple scattering and emitting layered media. *Appl. Opt.*, **27**(12), 2502-2509, 1988.

Stamnes, K., S. C. Tsay, W. Wiscombe and I. Laszlo, A General-Purpose Numerically Stable Computer Code for Discrete-Ordinate-Method Radiative Transfer in Scattering and Emitting Layered Media, *DISORT Report*, **v1.1**, 2000.

Steffen, K., Bidirectional reflectance of snow at 500-600 nm. *IAHS Publ.* **166**, 415-425, 1987.

Steffen, K., Effect of solar zenith angle on snow anisotropic reflectance. In *IRS'96: Current Problems in Atmospheric Radiation, Proceeings of the International Radiation Symposium*, 1996, edited by W. L. Smith and K. Stamnes, pp.41-44, A. Deepak Publishing, 1997.

Stroeve, J.C., J. E. Box, C. Fowler, T. Haran, J. Key, Intercomparison between *in situ* and AVHRR polar pathfinder-derived surface albedo over the Greenland. *Remote Sens. Environ.*, **75**, 360-374, 2001.

Stroeve, J., A. Nolin, and K. Steffen, Comparison of AVHRR-derived and *in situ* surface albedo over the Greenland ice sheet. *Remote Sens. Environ.*, **62**, 262-276, 1997.

Sturm, M., The role of thermal convection in heat and mass transport in the subarctic snow cover. *CRREL Report* **91-19**, USA Cold Regions Research and Engineering Lab., Hanover, New Hampshire, 1991.

Sturm, M., and J. B. Johnson, Thermal conductivity measurements of depth hoar. *J. Geophys. Res.*, **97**, 2129-2139, 1992.

Sturm, M., T. C. Grenfell, and D. K. Perovich, Passive microwave measurements of tundra and taiga snow covers in Alaska, U.S.A.. *Ann. Glaciol.* **17**, 125-130, 1993.

Sturm, M., and C. S. Benson, Vapor transport, grain growth and depth hoar development in the subarctic snow. *J. Glaciol.*, **43**(143), 42-59, 1997.

Sturm, M., K. Morris, and R. Massom, The winter snow cover of the West Antarctic pack ice: Its spatial and temporal variability. In: *Antarctic Sea Ice: Physical Processes, Interactions and Variability*, Antarct. Res. Ser., vol. **74**, M. O. Jeffries (Ed.), pp.1-18, AGU, Washington, D.C., 1998.

Tait, A. B., D. K. Hall, J. L. Foster, and R. L. Armstrong, Utilizing multiple datasets for snow-cover mapping. *Remote Sens. Environ.*, **72**, 111-126, 2000.

Tait, A., D. Hall, J. Foster, A. Change, and A. Klein, Detection of snow cover using millimeter-wave imaging radiometer (MIR) data. *Remote Sens. Environ.*, **68**, 53-60, 1999.

Tanré, D., C. Deroo, P. Duhaut, M. Herman, and J. J. Morcrette, Description of a computer code to simulate the satellite signal in the solar spectrum: the 5S code. *Int. J. Remote Sens.*, **11**(4), 659-668, 1990.

Tanré, D., B. N. Holben, and Y. J. Kaufman, Atmospheric correction algorithm for NOAA-AVHRR products: theory and application. *IEEE Trans. Geosci. Remote Sens.*, **30**, 231-250, 1992.

Taylor, V. R. and L. L. Stowe, Reflectance characteristics of uniform Earth and cloud surfaces derived from Nimbus 7 ERBE. *J. Geophys. Res.*, **89**, 4987-4996, 1984.

Thomas, G. E., and K. Stamnes, Radiative Transfer in the Atmosphere and Ocean. Cambridge University Press, 1999.

Tucker, W. B., III, D. K. Perovich, A. J. Gow, W. F. Weeks, and M. R. Drinkwater, Physical properties of sea ice relevant to remote sensing. In: *Microwave remote sensing of sea ice* (F. D. Carsey, editor), Geophysical Monograph **68**, American Geophysical Union, Washington, 9-28, 1992.

van de Hulst, H. C., Light Scattering by Small Particles. Wiley, New York, NY, 1957.

Vedernikova, E. A., and M. V. Kabanov, Scattering of optical radiation by a system of closely spaced scatterers. *Opt. Spectrosc.*, **37**, 71-74, 1974.

Vermote, E. F., N. E. Saleous, C. O. Justice, Y. J. Kaufman, J. L. Privette, L. Remer, J. C. Roger, and D. Tanré, Atmospheric correction of visible to middle-infrared EOS-MODIS data over land surface: Background, operational algorithm and validation. *J. Geophys. Res.*, **102**(D14), 17131-17141, 1997a.

Vermote, E., D. Tanré, J. L. Deuzé, M. Herman, and J. J. Morcrette, Second Simulation of the Satellite Signal in the Solar Spectrum (6S). 6S User Guide Version2, July, 1997b. Code and documentaions are available online at ftp://kratmos.gsfc.gov/pub/6S.

Vermote, E., D. Tanré, J. L. Deuzé, M. Herman, and J. J. Morcrette, Second simulation of the satellite signal in the solar spectrum, 6S: An overview. *IEEE Trans. Geosci. Remote Sens.*, **35**(3), 675-686, 1997c.

Wadhams, P., M. A. Lange, and S. F. Ackley, The ice thickness distribution across the Atlantic sector of the Antarctic Ocean in midwinter. *J. Geophys. Res.*, **92**(C13), 14,535-14,552, 1987.

Walker, A. E., and B. E. Goodison, Discrimination of a wet snow cover using passive microwave satellite data. *Ann. Glaciol.*, **17**, 307-311, 1993.

Warren, S. G., and W. J. Wiscombe, A model for the spectral albedo of snow. II: Snow containing atmospheric aerosols. *J. Atmos. Sci.*, **37**, 2734-2745, 1980.

Warren, S. G., Optical properties of snow. *Rev. Geophys. Space Phys.*, **20**(1), 67-89, 1982.

Warren, S. G., Optical Constants of Ice from the Ultraviolet to the Microwave. *Appl. Opt.*, **23**, 1206-1225, 1984a.

Warren, S. G., Impurities in snow: effects on albedo and snowmelt. *Ann. Glaciol.*, **5**, 177-179, 1984b.

Warren, S. G., and A. D. Clarke, Soot in the atmosphere and snow surface of Antarctica. *J. Geophys. Res.*, **95**, 1811-1816, 1990.

Warren, S. G., R. E. Brandt, P. O. Hinton, Effect of surface roughness on bidirectional reflectance of Antarctic snow. *J. Geophys. Res.*, **103**(E11), 25,789-25,807, 1998.

Warren, S. G., I. G. Rigor, N. Untersteiner, V. F. Radionov, N. N. Bryazgin, Y. I. Aleksandrov, and R. Colony, Snow depth on Arctic sea ice. *J. Clim.*, **12**, 1814-1829, 1999.

Washington, W. M. and C. L. Parkinson, An Introduction to Three-Dimensional Climate Modeling, University Science Books, Mill Valley, CA, 422 pp., 1986.

Watanabe, Z., Proposition of a net-like model of snow. *Ann. Glaciol.*, **18**, 72-78, 1993.

Weller, G., Heat-energy transfer through a four-layer system: Air, snow, sea ice, sea water. *J. Geophys. Res.*, **73**, 1209-1220, 1968.

Wendler, G., The "radiation paradox" on the slopes of the Antarctic continent. *Polarforschung*, **56**(1/2), 33-41, 1986.

Williams, F., Reasoning with Statistics, How to Read Quantitative Research. Fourth edition, Holt, Rinehart and Winston, Inc., 1992.

Winther, J.-G., and D. K. Hall, Satellite-derived snow coverage related to hydropower production in Norway—present and future. *Int. J. Remote Sens.*, **20** (15-16), 2991-3008, 1999.

Wiscombe, W. J., Mie scattering calculations: Advances in technique and fast, vector-speed computer codes. *NCAR Technical Note, NCAR/TN-140+STR*, National Center for Atmospheric Research, Boulder, Colo., 1979.

Wiscombe, W. J., Improved Mie scattering algorithms. *Appl. Opt.*, **19**(9), 1505-1509, 1980.

Wiscombe, W. J., and S. G. Warren, A model for the spectral albedo of snow. I: Pure snow. *J. Atmos. Sci.*, **37**(12), 2712-2733, 1980.

Woolf, H. M., On the computation of solar elevation angles and the determination of sunrise and sunset times, *NASA Tech. Memo. X-1646*, National Aeronautics and Space Administration, Washington, D. C., 1968.

Worby A. P., N. L. Bindoff, V. I. Lytle, I. Allison, and R. A. Massom, Winter ocean/sea ice interactions studied in the East Antarctic. *EOS*, **77**(46), 453, 456-457, 1996.

Worby A., and I. Allison, A technique for making ship-based observations of Antarctic sea ice thickness and characteristics, part I, Observational techniques and results. *Res. Rep. 14*, pp.1-23, Antarctic CRC, Hobart, Tasmania, Australia, 1999.

Wordie, J. M., Shackleton Antarctic Expedition, 1914-1917: The natural history of pack ice as observed in the Weddell Sea. *Trans. R. Soc. Edinburgh*, **52**, 795-829, 1921.

Wydick, J. E., P. A. Davis, and A. Gruber, Estimation of broadband planetary albedo from operational narrowband satellite measurements. *NOAA Technical Report NESDIS* **27**, pp. 1-32, 1987.

Yamanouchi, T., Variations of incident solar flux and snow albedo on the solar zenith angle and cloud cover at Mizuho Station, Antarctica. *J. Meteorol. Soc. Jpn.*, **61**(6), 879-893, 1983.

Yen, Y. C., Review of thermal properties of snow, ice and sea water, *CRREL Rep.* **8-10**, U. S. Army Corps of Eng., Hanover, N. H., 1981.

Zhou, X., S. Li, and K. Morris, Measurement of all-wave and spectral albedos of snow-covered summer sea ice in the Ross Sea, Antarctica. *Ann. Glaciol.*, **33**, 267-274, 2001.

Zhou, X., and S. Li, Sub-pixel Correction in Comparison between *In Situ* and Satellite Derived Spectral Reflectance. In: *Proc. IEEE 2002 International Geoscience and Remote Sensing Symposium (IGARSS'02) and 24th Canadian Symposium on Remote Sensing*, 24-28 June 2002, Toronto, Canada, **Vol. II**, pp.976-978, 2002a.

Zhou, X., and S. Li, Phase Functions of Large Snow Meltclusters Calculated Using the Geometrical Optics Method. In: *Proc. IEEE 2002 International Geoscience and Remote Sensing Symposium (IGARSS'02) and 24th Canadian Symposium on Remote Sensing*, 24-28 June 2002, Toronto, Canada, **Vol. VI**, pp.3576-3578, 2002b.

Zhou, X., and S. Li, Comparison between *in situ* and MODIS-derived spectral reflectances of snow and sea ice in the Amundsen sea, Antarctica. Submitted to *Int. J. Remote Sens.*, 2002c.

Zhou, X., and S. Li, Measurement of BRDF of snow and sea ice in the Ross and Amundsen Seas by the visible and near-infrared channels of MODIS. In: *Proc. IEEE 2000 International Geoscience and Remote Sensing Symposium (IGARSS'00)*, 24-28 July 2000, Hawaii, USA, pp.1567-1569, 2000a.

Zhou, X., and S. Li, Concentration determination of sea ice pressure ridges in the Ross Sea based on radar backscatter and object delineation methods. In: *Proc. IEEE 2000 International Geoscience and Remote Sensing Symposium (IGARSS'00)*, 24-28 July 2000, Hawaii, USA, pp.1323-1325, 2000b.

Zhou, X., and S. Li, Summer and Winter Snow and Sea Ice Surface Spectral Directional Reflectance and Albedo Measured in the Ross Sea. In: *Proc. IEEE 1999 International Geoscience and Remote Sensing Symposium (IGARSS'99)*, June 28-July 2, 1999, Vol. I, Hamburg, Germany, 104-106, 1999.